UNIVERSITY OF SOUTHAMPTON
FACULTY OF PHYSICAL AND APPLIED SCIENCES
PHYSICS AND ASTRONOMY

A Multi-Wavelength, Hubble Space Telescope Study of Two Globular Clusters

by

Grace Samantha Thomson

Thesis for the degree of Doctor of Philosophy
February 15, 2013

UNIVERSITY OF SOUTHAMPTON

ABSTRACT

FACULTY OF PHYSICAL AND APPLIED SCIENCES

PHYSICS AND ASTRONOMY

Doctor of Philosophy

A MULTI-WAVELENGTH, HUBBLE SPACE TELESCOPE STUDY OF TWO GLOBULAR CLUSTERS

by Grace Samantha Thomson

Globular clusters (GCs) are among the densest and oldest stellar aggregates in the Galaxy, and are thought to date from around the time that the Galaxy first formed. The high central densities that characterise GCs lead to frequent stellar interactions and the formation of exotic stellar populations, making GCs excellent laboratories for studying the stellar dynamics of dense environments. The ability to observe many stars which are equidistant and (approximately) the same age makes GCs invaluable in understanding stellar structure and evolution.

This thesis describes surveys of two Galactic GCs: far- and near-ultraviolet data from the Advanced Camera for Surveys (ACS) on-board the *Hubble Space Telescope* (*HST*) were used to study the core region of M 80, and far-ultraviolet to I-band data from the Space Telescope Imaging Spectrograph (STIS), ACS and the Wide Field Camera 3 (WFC3) on-board *HST* were used to carry out an in-depth, multi-wavelength survey of NGC 6752. In both studies, the properties of key stellar populations resident in globular clusters are investigated.

In M 80, it was discovered that the fainter (redder) blue straggler stars are more centrally concentrated than the brighter (bluer) ones. This is contrary to expectations, and suggests that blue stragglers might get a 'kick' at formation, before settling back towards the core. In a search for counterparts to known X-ray sources in M 80, one X-ray source was shown to be the remnant of the classical nova T Scorpii. This source was undergoing a dwarf nova outburst during the observations. A variability study of the GC also revealed three variable sources, including an RR Lyrae that was observed around maximum brightness, an SX Phoenicis star with a ≈ 55 minute period, and a longer period variable which might be another RR Lyrae or a Cepheid variable.

In NGC 6752, two known cataclysmic variables were revealed to be dwarf novae (DNe), which underwent outbursts during the observations. This takes the number of known DNe in NGC 6752 to three, more than any other cluster. Some of the global parameters describing NGC 6752 were also investigated. A new estimate of the cluster's centre position was determined and used to show that the stellar density profile cannot be fit using a single 'King' profile, indicating that the cluster is in a core-collapsed state. Finally, a search for broadening in the main-sequence of the colour-magnitude diagram found evidence of small-scale broadening, suggesting the presence of multiple populations. A radial trend in the level of observed broadening was also suggested, with more broadening found in the core than the outer parts of the cluster.

CONTENTS

APPENDICES

LIST OF TABLES

LIST OF FIGURES

DECLARATION

I, Grace Samantha Thomson, declare that the thesis entitled *A Multi-Wavelength, Hubble Space Telescope Study of Two Globular Clusters* and the work presented in the thesis are both my own, and have been generated by me as a result of my own original research. I confirm that:

- this work was done wholly or mainly while in candidature for a research degree at this University;
- where any part of this thesis has previously been submitted for a degree or any other qualification at this University or any other institution, this has been clearly stated;
- where I have consulted the published work of others, this is always clearly attributed;
- where I have quoted from the work of others, the source is always given. With the exception of such quotations, this thesis is entirely my own work;
- I have acknowledged all main sources of help;
- where the thesis is based on work done by myself jointly with others, I have made clear exactly what was done by others and what I have contributed myself;
- parts of this work have been published as:
    - A far-ultraviolet variability survey of the globular cluster M80, 2010, MNRAS, 406, pp. 1084-1093
    - A multiwavelength survey of NGC 6752: X-ray counterparts, two new dwarf novae and a core-collapsed radial profile, 2012, MNRAS, 423, pp. 2901-2916

Grace Samantha Thomson, February 15, 2013

ACKNOWLEDGEMENTS

First, of course, thank you to my supervisor, Christian Knigge, for introducing me to the wonders of all things globular cluster related. Thank you for all the support over the last few (not quite four!) years, and for continually encouraging me to try "one last thing" to make sense of my (often rather obscure) data.

Thanks to Andrea Dieball, for your never-ending patience and for all you have taught me. To Tom Maccarone, for being all-knowing and checking up on me when I needed it most. To Tony Bird, also for never-ending patience, and for just making things work. If it weren't for you, I'd still be compiling DOLPHOT... and to Simon Harris, without whom, getting through a PhD would be (even) more painful.

To Sades, the "bestest, most beautious" office mate in all the world, for generally being "lovelly", for all the tea and tales and talking. I'm so glad I picked your office. To Lizbo and Lee, with apologies for making you share as if you're one person, thanks for all the distractions, gossip, laughs, exceptionally classy nights out in Hamble, and hugs when I needed them most. To those who have gone before - especially Mark Peacock (with extra thanks for being my LA-buddy and not actually crashing the car), Tony Wilkinson, Elme and Martin - thanks for showing me how it's done. To Tanana, Jack, Seb, Dan and Dan, and everyone that I've forgotten to mention, thanks for making it all a lot less like work.

To my family, thank you for all the support through my many years of studying, and for always understanding that I had to do it, even if you didn't understand what "it" was. To Mum, thank you for "doing lunch", "proper hugs" and generally keeping me sane. To Daddy, thank you for always knowing the right time to send a little encouragement, and thank you for showing me the stars. I bet you didn't know what you were letting yourself in for when you made up names for the "seven sisters"; I hold you entirely responsible! To Enna, George and little Theo, thank you for making sure I remember the important things in life. To my parents and grandparents, thank you for instilling in me the importance of education and doing my best, and thank you for always thinking it was good enough.

Finally, to my wonderful husband, Dessie. For supporting me, always, in so many ways, I am more grateful than you will ever know. Who would have thought that first time we met that this is where we'd be in 5 1/2 years...? From leaving America to finishing my PhD, via a wedding(!), being with you has made everything more fun, and I'm looking forward to starting our next adventure together. Your drive to succeed and your thirst to understand is inspirational, and all of your questioning has, I'm sure, made me a better scientist. Thank you for being so understanding when work has threatened to get in the way of real life, and thank you for always being able to make me smile when I need it most (and when I don't). Thank you, most of all, for always believing in me; especially when I didn't. I love you.

Grace Samantha Thomson, February 15, 2013

> It's friendlier with two.
>
> A. A. MILNE (1882 – 1956)

For Des

Remember, nil desperandum: That means don't let the .... get you down.

JOHN THOMSON (1921 – 2008)

Grace, my girl, you can do anything.

ALBERT HENRY NAYLER (1928 – PRESENT)

For my part, I know nothing with any certainty, but the sight
of the stars makes me dream.

VAN GOGH (1853 – 1890)

1

An Introduction to Globular Clusters

This thesis describes observational investigations into several aspects of globular clusters. In this chapter, I give an overview of the astrophysics of globular cluster systems, highlighting key issues that will be researched in detail throughout the thesis.

In Section 1.1, I introduce globular clusters and their role in our understanding of cosmology, galaxy formation and stellar evolution. I describe their main observational characteristics in Section 1.2, although a detailed look at the stellar populations they contain will be deferred to Chapter 2. In Section 1.3, I outline the mechanisms involved in the formation and evolution of globular clusters, including an in-depth look at the recent discovery that, rather than being formed all at once, the stars contained in clusters are actually made up of multiple generations of stars with distinct properties.

1.1 Globular Clusters

Globular clusters (GCs[1]) are tightly bound, roughly spherical collections of up to 10^6 stars. Figure 1.1 shows a well known example, 47 Tuc. GCs are found in the

---

[1] See Appendix A for a full list of the abbreviations used in this thesis.

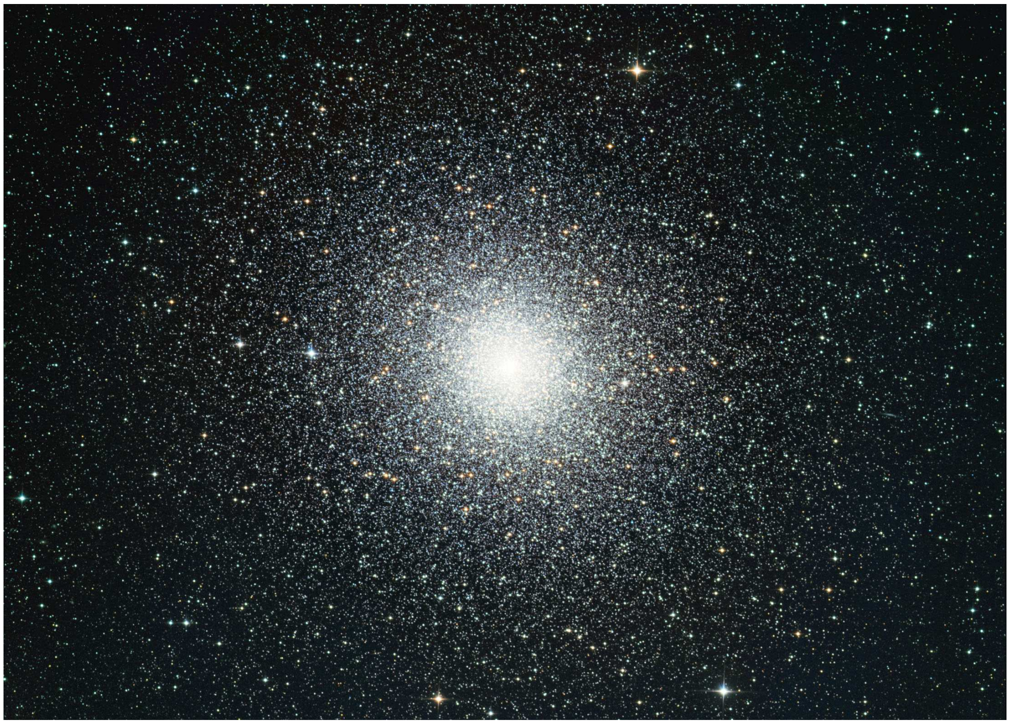

Figure 1.1: The globular cluster 47 Tuc (NGC 104). Image credit: Dieter Willasch.

haloes of galaxies, and are fairly common: over 150 are known in the Milky Way (Harris, 1996; 2010 edition); between 400 and 950 are thought to reside in the Andromeda galaxy (Peacock et al., 2010), and over 10000 are thought to exist in giant elliptical galaxies like M 87 (Strader et al., 2011).

A defining feature of GCs is their high central stellar density. On average, GCs contain 0.4 stars per cubic parsec, but this rises to $10^4 - 10^5$ stars per cubic parsec in the core of the cluster (Freire et al., 2003). By contrast, the average stellar density in the solar neighbourhood is around 1 star per cubic parsec.

GCs are also among the oldest known objects in the Universe, with measured ages of around $10 - 13$ Gyrs, depending on the measurement method used (see, for example Mendel et al. 2007; Marin-Franch et al. 2009), and are made up of Population II stars. In fact, the age of GCs is of interest in terms of both cosmology and galactic astronomy: the age of the oldest GC places a strong lower limit on the age of the Universe itself, while possible variations in GC age in different parts of the Milky Way might hold clues regarding the formation of the Galaxy.

GCs have long been important tools in astrophysics research. For example, the fact that they are bright enough and extend far enough from the Galactic plane to be observed even on the far side of the Galactic core allowed Shapley (1918) to demonstrate that the Galaxy is far larger than previously thought and to estimate the position of the Sun relative to the centre of the Galaxy.

The ability to study large groups of stars which are equidistant and formed at (approximately) the same time also makes GCs invaluable laboratories for understanding stellar structure and evolution. Much of our current knowledge about the changes that happen as stars evolve away from the main-sequence, for example, was gleaned from comparisons between theoretical predictions and observations of stars in GCs. More information about the stellar populations found in GCs and the stellar evolutionary phases associated with them can be found in Chapter 2.

The high stellar densities in the cores of GCs make interactions between stars inevitable, leading to the creation of exotic stellar populations such as blue stragglers (BSs), cataclysmic variables (CVs), low-mass X-ray binaries (LMXBs) and other close binary systems, as well as destroying or altering primordial binary systems. Studies of GCs can, therefore, give a great deal of information about the stellar dynamics of dense environments. The close binary systems found in GCs are explained in more detail in Sections 2.1.9 and 2.3.

On the other hand, studying the close binary population can also tell us something about the cluster as a whole, as the binding energy of just a few close binaries can approach that of the GC. By transferring their orbital energy to single stars via dynamical interactions, close binaries can influence the dynamical evolution of the cluster (see, for example, Elson et al. 1987 and Hut et al. 1992). If only a few close binaries reside in a GC, long-term interactions will dominate the evolution of the GC. Alternatively, if there is a large close binary population, frequent and violent interactions will heat the cluster and cause expansion and evaporation on shorter time-scales. Understanding the number and nature of close binaries in a GC is important in learning about GC evolution, a topic which still provokes much debate (Williams et al., 2012). GC evolution is discussed in more detail in Section 1.3.

1.2 Observational Characteristics of Globular Clusters

1.2.1 Spatial Distribution and Metallicity

Within the Milky Way, GCs are easily divided into two distinct populations: the majority, which are metal-poor ($[\mathrm{Fe/H}] \approx -1.59\,\mathrm{dex}$) form a roughly spherical halo distribution about the Galaxy (e.g. Ashman & Zepf 1998), while others, with higher metallicities of $[\mathrm{Fe/H}] > -0.8\,\mathrm{dex}$ can be described as a 'thick disk' population (Zinn, 1985). The orbits of GCs making up the halo population do not participate in the general rotation of the Galaxy; GC orbits are highly elliptical, and some are even retrograde compared to the Galaxy's rotation (Rodgers & Paltoglou, 1984). The 'disk' GCs have a flattened distribution and rotate about the Galactic centre (Zinn, 1985). The disk extends to $\approx 2\,\mathrm{kpc}$ from the plane of the Galaxy, making it much thicker than the 0.4 kpc thick disc made up of Population I stars (Armandroff, 1989). These GCs' orbits are much more circular than those of the halo GCs, and are in the direction of the Galactic rotation, although slightly slower than the Population I disk (e.g. Brodie & Strader 2006). It is commonly accepted that disk GCs formed a little later than halo GCs, and that their higher metal abundance is due to enrichment of the gas cloud by reactions in earlier generations of stars (Forbes et al., 1997). The precise difference in age between disk and halo GCs, and between individual GCs themselves is a topic of debate. In principle, it can give insight into key time-scales in the formation of the Galaxy (see, for example, Harris 1991).

GCs are found around nearly all galaxies, from giant elliptical galaxies to dwarf galaxies. In nearly all cases, GCs extend to larger radii from the centre of the galaxy than galactic field stars, making GCs excellent tools to study the dynamics of galaxies, including, for example, their dark matter content (e.g. Spitler & Forbes 2009). As in the Milky Way case, GCs in other galaxies can be divided into redder and bluer clusters (e.g. Brodie & Strader 2006). This bi-modality might be due to differences in metal abundance or age, or both. This suggests that there have been (at least) two major star-forming periods in the early development of the Galaxy (Brodie & Strader, 2006), a significant discovery in the context of galaxy formation.

1.2.2 The Morphology of Globular Clusters

The image of the GC 47 Tuc in Figure 1.1 illustrates the high stellar density and spherical shape that characterise GCs. On closer inspection, however, variations in the overall shape can be found between individual GCs and and between the GCs residing in different galaxies. Clusters in the Milky Way and M 31 are typically oblate spheroids (with ellipticities of 0.07 ± 0.04 and 0.09 ± 0.04, respectively; Goodwin 1997; Staneva et al. 1996), while those in the Magellanic Clouds are more elliptical in shape (Large and Small Magellanic Cloud GCs have average ellipticities of 0.16 ± 0.05 and 0.19 ± 0.06, respectively; Staneva et al. 1996). Nevertheless, the shapes are so close to spherical that the assumption that a GC can be modelled as a sphere for the purposes of ascertaining its radial profile is valid. It has been sug-

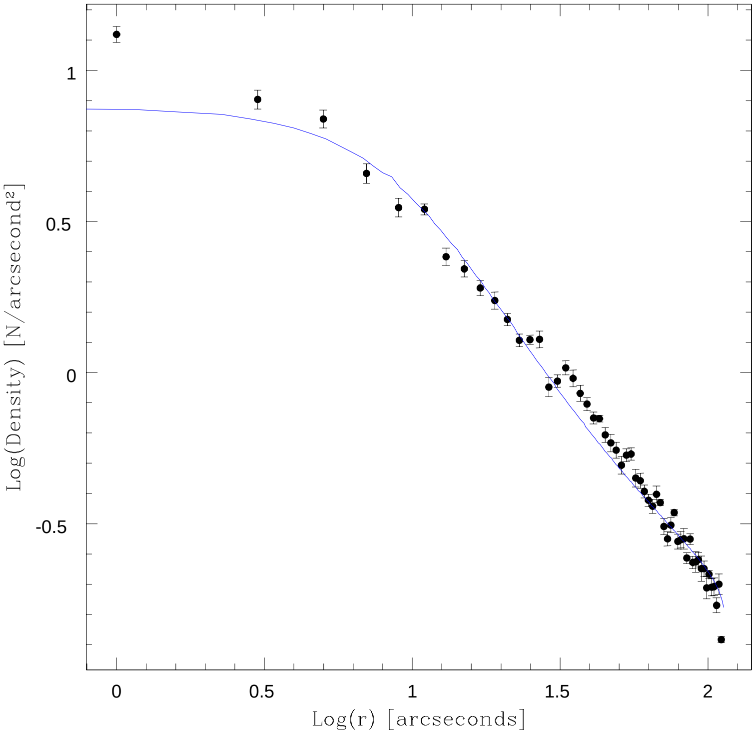

Figure 1.2: The radial profile of globular cluster NGC 6752. This shows the stellar density as a function of distance from the cluster centre. The blue line shows the best-fitting radial profile model. More information on the construction of this profile and its implications can be found in Chapter 4.

gested that tidal interactions with the host galaxy can reduce the ellipticity of a GC, making it more spheroidal in shape (Goodwin, 1997); more massive host galaxies destroy velocity anisotropies more efficiently, resulting in more spherical clusters.

The morphology of a GC is described using a number of parameters which can be derived from the radial profile of the cluster. Figure 1.2 shows the radial profile (in this case, the stellar density profile) of a GC. As one would expect from Figure 1.1, the stellar density (and luminosity) decreases with increasing distance from the centre.

The distance from the core at which the surface brightness has fallen to half of its core value is the core radius, r_c.

An alternative quantity is the half-light radius, r_h, defined as the radius from within which half of the integrated light of the cluster is received. It should be noted that this radius includes light from stars in the outer part of the cluster along the observer's line of sight. Instead, the half-mass radius, r_m is often used by theorists. This is the radius containing half of the mass of the GC.

The final characteristic radius is the tidal radius, r_t, which is the distance from the cluster centre at which the gravitational influence of the GC is equal to that of the galaxy. The radial profile of a GC is truncated at this distance, as stars beyond this radius can be stripped away from the cluster (see Section 1.3.3.2).

The concentration parameter, defined by

$$c \equiv \log_{10}(r_t/r_c),$$

gives a useful, distance-independent indication of the morphology of the cluster. Typically, GCs have concentration parameters of $0.5 < c < 3$ (Harris, 1996; 2010 edition). A high concentration parameter ($c \gtrsim 2-2.5$) indicates that the GC's core radius is very small compared to the tidal radius; such a GC may be undergoing core-collapse. A discussion of the implications of different values of c is given in Section 1.3.3.

The measured values of the parameters governing the morphology of a particular GC depends on a number of factors, including, for example, mass segregation, tidal stripping and relaxation time (see Section 1.3.3.2). As such, the dynamical processes affecting the radial profile are still not well modelled, even nearly 50 years after the first basic and seminal model was put forward by King (1966). The King model assumes that all the stars have the same mass (a 'single mass model'). It takes into account two key characteristics of GCs: relaxation through two-body encounters and stripping of stars due to the galactic tidal field. The model assumes that the GC can be well-described by an isothermal sphere which is truncated due to tidal stripping. King models tend to be good descriptions of GCs, except at very small and very large radii, where deviations are found either in the form of central cusps, or overly extended tidal radii.

Many authors have attempted to find better models to fit the overall shape of GC radial profiles; in King-Michie models (Michie, 1963; King, 1966), the King model was extended to include anisotropic velocity dispersion; Gunn & Griffin (1979) used 'multi-mass' King models to try to model the globular cluster M 3. Others have used different fitting functions to attempt to describe GC profiles, such as Wilson models (Wilson, 1975; McLaughlin & van der Marel, 2005) or power-law models (McLaughlin & van der Marel, 2005), but these are not based on any underlying, physical picture of GCs. Even more recently, Williams et al. (2012) used theoretically derived, maximum entropy equilibrium models known as DARKexp models to suggest that collisionless dynamics might be the dominant mechanism shaping GC radial profiles (except in the very centre). They caution, however, that the good fits achieved using their model might be related to the ability of the model to fit to a very complex system, rather than because of the dynamical mechanisms it described. For now, King (1966) models remain the most popular method for describing GC profiles.

In the following sections, I describe the evolution of a globular cluster, and how its radial profile changes over time.

1.3 The Life of a Globular Cluster

1.3.1 Globular Cluster Formation

There is, at present, no widely accepted theory describing the formation mechanism (or mechanisms) of GCs. A wide ranging assortment of scenarios have been proposed, but as yet the phenomenon remains poorly understood (see Brodie & Strader (2006) for a review).

It is generally believed that GCs form from giant molecular clouds in regions of denser-than-average interstellar medium (Larson, 1993). For a formation model to be considered successful, it must explain observational characteristics such as the spatial distribution of GCs, with the metallicity differences discussed in Section 1.2.1.

The vast age of GC stars leads to the belief that they formed at approximately the same time as their host galaxies; GCs provide something of a 'snapshot' of early conditions, so they are useful tools in studying and constraining theories of galaxy formation (Harris & Racine, 1979; Harris, 1991).

Early models for GC formation struggled to establish where GC formation came in the chronology of galaxy formation: Peebles & Dicke (1968) suggested that GCs actually pre-date galaxies, forming in conditions unique to the early Universe. It is difficult to reconcile a cosmological GC origin with the observed spatial distribution, however. The fact that comparatively metal-rich GCs lie predominantly in the disk of the galaxy, with metal-poor counterparts in the halo, suggests that galaxy formation must pre-date GC formation. Furthermore, cosmologically created GCs would be expected to form with a halo of dark matter. Since there is strong evidence that no such halo exists (Moore, 1996), 'primary' formation models, in which GCs form prior to their host galaxies, have largely been ruled out.

'Secondary' formation models assume that GCs formed concurrently with their host galaxies. Fall & Rees (1985) suggested that the molecular clouds that become GCs form through thermal instabilities in proto-galaxies. They argued that cooling of a gas cloud in such a scenario would become inefficient at around 10^4 K, equating to a Jeans mass of around $10^6\,M_\odot$, which is the median mass of GCs. There are, however, a number of ways in which cooling can continue below this characteristic temperature (Ashman, 1990; Ashman & Zepf, 1998), and the low probability of the cloud remaining at $\approx 10^4$ K for a sufficient time has become a major problem for this model. Furthermore, the comparatively high metallicity of GCs found in large elliptical galaxies and in the disk of the Milky Way suggest that the protocluster clouds were enriched with metals before the clusters formed. The presence of metals increases the efficiency of the cooling process (Ashman & Zepf, 2001). As well as allowing molecular clouds to cool to well below the 10^4 K required by the Fall$-$Rees model, this would lead one to expect the mass of GCs to decrease with increasing metallicity (since faster cooling leads to the formation of less massive GCs). Such a trend is ruled out by observations (Djorgovski & Meylan, 1994).

Observations using the *Hubble Space Telescope* (*HST*)[2] have revealed the widespread formation of bright, blue, compact clusters in interacting and merging galaxies (e.g. Holtzman et al. 1992; Whitmore et al. 1999). Galaxy interactions are known to trigger bursts of star formation (‘starbursts’; Hernquist 1989; Barnes & Hernquist 1996; Mihos & Hernquist 1996). Merger-induced starbursts, in turn, play a key role in the hierarchical merging events which are central to galaxy formation (e.g. White & Rees 1978; Cole et al. 2000). It is now generally believed that giant molecular clouds in the high-pressure interstellar medium found in starbursts are the progenitors of both young GCs and at least some of the ‘traditional’ old GCs (Ashman & Zepf, 2001; Beasley et al., 2002). As discussed in Section 1.2.1, GCs with higher metallicity are predominantly found in the disk, whereas lower metallicity GCs are found in the Galactic halo. It has been suggested (e.g. Ashman & Zepf 1992; Beasley et al. 2002) that metal-rich, disk GCs were formed through galaxy mergers. The metal-poor halo GCs are the remnants of the GC population of the merging galaxies; they formed as the merging galaxies formed and are deposited in the halo when the galaxies merge. Clearly, understanding the effects of interaction-induced starbursts can tell us about structural evolution and the history of the Universe, while studying star clusters can shed light on past galaxy mergers.

The size and mass of the young clusters found in nearby, interacting galaxies indicate that they may be analogous to old, previously known GCs (Elmegreen & Efremov, 1997). The main difference between the young and old GC systems lies in their inferred mass functions. Old GCs are known to have a log-normal mass

---

[2] See Appendix B for details of the *Hubble Space Telescope*.

function; in other words, the number of stars contained within old GCs is peaked, with most clusters containing around 10^6 stars. Young stellar clusters, on the other hand, have a mass function that is consistent with a single power law with index -2, down to the detection limit at around $10^4\,M_\odot$, although it is expected that the physical lower mass limit is much lower (Zhang & Fall, 1999; Portegies Zwart et al., 2010); the numbers of stars found in these clusters vary over a wide range, including much lower than the mass at which old GC numbers begin to decline (Ashman & Zepf, 2001). Assuming that the initial cluster mass function is universal, all clusters should be formed according to the -2 power law seen in nearby interacting galaxies. This is contrary to the observed lack of low mass, old, globular clusters (Fall & Zhang, 2001; Elmegreen, 2010), implying that lower mass GCs are being preferentially lost.

There are several ways that GCs can be destroyed. They include the expulsion of gas by young, massive stars (known as “feedback”, which lowers the star formation efficiency of the cluster), mass loss from intermediate and low-mass stars, tidal effects of passing molecular clouds, and stars escaping due to two body relaxation (Fall & Chandar, 2012). It is well known, however, that the high gas densities and tidal shocks that occur in coalescing galaxies can also disrupt star clusters (Spitzer, 1958; Gieles et al., 2006). In general, the likelihood of cluster destruction decreases with increasing cluster mass. Simulations show that the same starbursts caused by interacting galaxies that are thought to give rise to cluster formation actually preferentially destroy lower mass clusters (Kruijssen et al., 2012). Only the most massive clusters are able to survive the rapidly changing gravitational forces that exist in galactic interactions.

According to simulations by Kruijssen et al. (2012), the clusters which survive the starburst events have the characteristics expected for a ‘classical’ GC soon after formation. In the early Universe, starburst events were common, so it is understandable that the GCs that we see today all appear to have similar numbers of stars. This leads to two tantalising prospects: on the topic of GC formation, there are examples of nearby galaxies that have recently undergone interactions and bursts of star formation, which could be searched for traces of rapid destruction of young star clusters; on the wider topic of galaxy formation, these simulations suggest that the majority of a GC’s characteristics were set out at its formation. As they appear to be similar, regardless of the galaxy they reside in, the environments that they formed in must have also been similar. This gives further evidence to the assertion that GCs are fossils from the time when the first stars and galaxies formed.

1.3.2 Multiple Stellar Populations in Globular Clusters

Further complicating the picture, recent developments have shown that GC formation theories must actually allow for not just one star forming event, but several generations, over several hundred million years. A full description of a typical GC colour-magnitude diagram (CMD) and the stellar populations found in GCs will be given in Chapter 2. In this section, I outline the main evidence for multiple generations of stars among different types of stars in some GCs. The reader is referred to Chapter 2 for background information on the stellar populations themselves, and Figure 2.1 for a sample CMD.

Globular clusters were traditionally thought to be good examples of simple single stellar populations. The sharp appearance of their CMD features and the narrowness of the sequences led to the belief that GCs are sets of stars with the same age and chemical composition. This led to the use of GCs in the testing of stellar evolution theories. Many of the aspects of stellar evolution described in Section 2.1 were developed in order to describe the location of stars on a GC's CMD using a single population of stars (see Gratton et al. 2012).

Recent developments in instrumentation and analysis techniques have finally allowed spectroscopy and photometry with sufficient precision to show that the CMD sequences are sometimes broadened (e.g. Milone et al. 2010; Hilker & Richtler 2000) or, in some cases, split (e.g. Bedin et al. 2004; Piotto et al. 2007; Anderson et al. 2009; Milone et al. 2012a), and that the spectra of stars within a given evolutionary stage can be quite different (e.g. Hesser & Bell 1980; Cohen 1999a,b; Gratton et al. 2001; Cavallo et al. 2004). In fact, the stars within a GC differ more than can be explained by a small spread in the ages of stars born within a single star formation epoch, or by small inhomogeneities in the original chemical abundances (see Gratton et al. 2012). It is now widely accepted than the spreads and splits in CMD sequences and the differing chemical abundances measured in spectra of individual stars are tracers of multiple generations of stars, commonly known (and referred to throughout this thesis) as multiple populations (Gratton et al., 2012).

Obviously, understanding the nature and, ultimately, the cause of multiple populations is essential if we are to fully understand the formation and evolution of GCs as a whole. The current multiple populations theory typically involves two generations of stars, which can be described as first (primordial) generation and second generation. The second generation (which is likely to contain many sub-populations) is formed from material polluted by ejecta from a fraction of the first generation population (Gratton et al. 2004 and references therein). Evidence for these different generations of stars can be found in broadening or splitting of CMD sequences, or in their chemical compositions (especially the light elements). As helium enrichment is an indication that matter has been exposed to very high temperatures, second generation stars are expected to be He enriched compared to first generation stars. Helium abundance cannot usually be measured directly, but stars with the same mass but different He abundances can be distinguished based on their photometric properties. Broadened sequences on the colour-magnitude diagram, for example, are tracers of spreads in helium abundance. Evidence of helium enrichment has been found in the main-sequence, red giant branch and horizontal branch of a number of GCs.

It should be noted that the ‘enrichment’ multiple population scenario described above is the ‘standard’ scenario and the one that most current research is focussing on, but there is another kind: some unusual GCs, including ω Cen and NGC 1851, have multiple CMD sequences which are unlikely to be caused by the multiple generation scenario described above. Instead, the sequences in these clusters are attributed to stellar populations with a wider range of ages (e.g. Milone et al. (2008a) suggest an age spread in NGC 1851’s SGB populations of 1 Gyr). These GCs are associated with dwarf galaxies which have merged or are in the process of merging with the Milky Way (Lee et al., 2009; Bekki & Yong, 2012), suggesting that the CMD complexities are linked to the merger events.

In the following subsections, I will outline the evidence for multiple populations in various parts of the CMD (see Figure 2.1 for an example with the stellar populations highlighted). I do this in the order that the stellar populations will be described in Chapter 2, but it should be noted that the first (spectroscopic and photometric) evidence for multiple populations was actually found in red giant stars.

1.3.2.1 Evidence for Multiple Populations: The Main-Sequence

Evidence for multiple populations of main-sequence (MS) stars was found in spectra as early as thirty years ago. Hesser & Bell (1980) found differing CN-band strengths in seven MS stars in 47 Tuc, although the results were not interpreted at the time in terms of multiple populations; instead, they considered alternative possibilities such as multiple proto-cluster gas clouds. Since then, a great deal of research into the spectra of MS stars has found anticorrelations between CN and CH, and correlations between Na and CH in 47 Tuc (e.g. Cohen 1999a,b). In the multiple populations scenario, the CN-weak stars form first. The CN-strong stars form later, enriched by the ejecta of the first generation.

More importantly from the perspective of confirming the presence of multiple populations, Gratton et al. (2001) found Na-O and Mg-Al anticorrelations in MS stars of NGC 6752 and NGC 6397. The temperatures required to produce Na and destroy Mg cannot be reached by low mass MS stars (Arnould et al., 1999), but Ventura et al. (2001) showed that intermediate mass stars ($M = 4-5\,M_{\odot}$) can reach up to 10^8 K during the asymptotic giant branch phase. This allows the complete CNO cycle to operate, leading to oxygen depletion. At the same time, the p-capture process produces aluminium and sodium. This clearly indicates that an external origin was responsible for the chemical composition, and that multiple populations are involved.

Photometric evidence for multiple populations on the MS was found first in ω Cen (Bedin et al., 2004; Villanova et al., 2007). Three MSs have now been found in NGC 2808 (Piotto et al., 2007), and split MSs are known in NGC 6397 (Milone et al., 2012b) and 47 Tuc (Anderson et al., 2009; Milone et al., 2012a). Milone et al. (2010) found a spread, and the suggestion of a split, in the MS of NGC 6752. The search for further evidence of this spread forms part of Chapter 6 of this thesis.

These multiple MSs have been interpreted as evidence of helium enrichment (Piotto et al., 2005; Norris, 2004; D'Antona et al., 2005; Piotto et al., 2007), with the bluer MS up to ≈ 0.3 dex more enriched than the red one. The multiple MSs also correspond to different groups in the previously mentioned Na-O anticorrelation. A current challenge is establishing why different clusters' MSs have such different amounts of He enrichment, and how to obtain helium abundances as high as those observed (for example, 47 Tuc's MS spread requires a variation in helium abundance of just $\Delta Y \approx 0.026$ dex, (Anderson et al., 2009), while NGC 2808's reddest and bluest MSs are best fit with helium abundances of $Y = 0.25$ dex and 0.38 dex (Milone et al., 2012c)).

1.3.2.2 Evidence for Multiple Populations: The Sub-Giant Branch

As in the case of main-sequence populations, the first photometric evidence for a split in the sub-giant branch (SGB) of a globular cluster was found in ω Cen. A spread was found first (e.g. Hilker & Richtler 2000), before a split was detected (Ferraro et al., 2004). The picture is now known to be even more complex, with at least four branches, which are thought to have different ages and metallicities (Villanova et al., 2007). As mentioned above, ω Cen is an unusual cluster, thought to have formed from the nuclei of a dwarf galaxy.

Split sub-giant branches are now known to exist in NGC 6388 (Moretti et al., 2009), 47 Tuc (Anderson et al., 2009), M 22 and M 54 (Piotto, 2009) and NGC 1851 (e.g. Milone et al. 2008a, 2009; Zoccali et al. 2009). The split in NGC 1851 can be explained by an age difference of ≈ 1 Gyr, a difference in CNO abundances, or the merging of two GCs of slightly different ages (Carretta et al., 2011).

In their study of NGC 6752, Milone et al. (2010) found no evidence of broadening in the SGB of the cluster. Appendix C shows preliminary work on this GC which shows hints of broadening, but, as explained in that section, also demonstrates the need for further study of this feature.

1.3.2.3 Evidence for Multiple Populations: The Red Giant Branch

As the red giant branch (RGB) contains the (optically) brightest sources, it is unsurprising that it was among RGB stars that abundance differences pointing to multiple populations were first discovered (Osborn, 1971). Differing abundances of light elements (C, N, O, Na, Al, Mg, Si and F) have been found in many GCs, including M 80 (Cavallo et al., 2004) and NGC 6752 (e.g. Carretta et al. 2007a; Yong et al. 2008), which are of particular interest in this thesis.

The fact that Na-O anticorrelations are found among both (unevolved) MS stars and (evolved) RGB stars shows that anticorrelations cannot be caused by evolutionary processes, and must be present in the original stellar material. The multiple population scenario is considered the only plausible explanation at present (Gratton et al., 2012).

Further evidence is found in the helium abundances of stars on the RGB. Helium-enhanced, second generation RGB stars appear bluer than the first generation sources (Bragaglia et al., 2010). In the red giant branch bump in particular, the second generation appears brighter (Bragaglia et al., 2010). Nataf et al. (2011) found a radial trend in 47 Tuc, with brighter sources in the core where the second generation should dominate (see Section 1.3.2.6).

Multiple RGB populations were found first in the most massive GCs, leading to some speculation that multiple populations were an exotic curiosity only found in the most massive clusters. Spectroscopic evidence, however, now suggests that all GCs surveyed to date exhibit Na-O anticorrelations and, therefore, contain multiple populations.[3] The extension of the Na-O anticorrelation (defined in terms of the interquartile ratio of the abundances; see Carretta et al. 2006), which is determined by parameters such as the amount of polluting material and the mass of the polluters,

---

[3] Exceptions to this are Terzan 7 and Pal 12, but only a few stars have been analysed in these clusters (Sborbone et al., 2005; Cohen, 2004).

does seem to be affected by cluster mass. This implies that GC mass has important implications for the formation and evolution of the cluster. No Na-O anticorrelation has been found in open clusters, indicating that there may be a lower limit on the mass of multiple population hosting GCs, which might be related to the difference between globular and open clusters.

Unlike the Na-O case, spreads in iron abundances have only been found in the most massive GCs (so far) and range from 0.08 dex in NGC 1851 (Yong & Grundahl, 2008) to 1.5 dex in ω Cen (e.g. Norris & Da Costa 1995; Marino et al. 2011a).

In terms of photometry, multiple populations in the RGB are difficult to discern in optical CMDs, since only small spreads are expected. If ultraviolet (UV) wavebands are used, however, the effect is far more obvious. The spread of the RGB is due, in part, to differences in N abundance, and CN and NH bands are both present in the UV, blue and Strömgren filters, making finding multiple RGBs considerably easier in surveys where such filters are used. Broadened or split RGBs have been found in several clusters, although differences between the results have led to some inconsistencies. For example, Lee et al. (2009) claimed that all eight of the GCs that they studied showed evidence of enhanced Ca, indicating pollution due to supernova explosions. Except in the cases of NGC 1851 and M 22, this is controversial (see, for example, Carretta et al. 2010). It has also been reported that RGB stars associated with the second generation are more centrally concentrated; one of the GCs for which this has been suggested is NGC 6752 (Kravtsov et al., 2011).

1.3.2.4 Evidence for Multiple Populations: The Horizontal Branch

The intriguing differences between the horizontal branch (HB) appearances of different GCs will be discussed in detail in Section 2.1.3.

Globular cluster metallicity is known to be the main factor determining HB morphology, but it cannot explain why the horizontal branches of GCs with similar metallicities can look very different. A combination of age and mass (or central density) are the most likely second (and third) parameters driving the differences in HB shape and colour. In particular, more massive GCs are more likely to retain enough first generation material to allow a significant second generation to form (see Section 1.3.2.6), while the second generation, He-enhanced HB sources are bluer (e.g. D'Antona et al. 2005).

Links have been found between the Na-O anticorrelation on the RGB and HB colour (Carretta et al., 2007b; Gratton et al., 2010), which support the multiple generation scenario, since HB stars within GCs of similar metallicities could end up with different levels of He-enhancement (and, thus, different colours). In NGC 6752, blue HB stars were found by Villanova et al. (2009) to be Na poor and O rich, in line with the anticorrelation found elsewhere, and as expected in the multiple population scenario. Marino et al. (2011b) and Villanova et al. (2012) studied the GC M 4, which has both a blue HB and red HB. Again, the blue HB sources were found to be Na poor and O rich, while the opposite was true for red HB sources, which were rich in O and poor in Na. This is further evidence of the presence of multiple populations and their link to HB morphology.

1.3.2.5 Evidence for Multiple Populations: The Asymptotic Giant Branch

Stars with strong CN bands are common among red giant branch stars, but rare among asymptotic giant branch (AGB) stars. This is surprising, as CN bands are usually associated with more mixed material. It has been suggested that CN-strong stars, which are He-enhanced and have low masses (Norris et al., 1981), do not ascend the giant branch for a second time (see Section 2.1.5). One would expect, therefore, that the brightest AGB stars (which are evolved, He poor, HB stars) are Na-poor and O-rich, like their HB counterparts. Na and O measurements of AGB stars are not yet available, but the fact that such measurements of RGB stars have been successfully performed suggests that such measurements should be possible in the near future. This would give much needed clarification on the connection between HB and AGB stars.

1.3.2.6 The Origin of Multiple Stellar Populations

As previously mentioned, understanding the cause of multiple populations is key to understanding globular cluster evolution, and the ability to fully describe the evolution of stars within a GC will help with understanding how well the processes involved in a GC reflect stellar evolution elsewhere.

For a multiple population, GC formation theory to be successful, it must explain two key observational features: the majority of stars in GCs are from the second generation, and that they have chemical compositions rarely found among field stars.

First generation stars make up just 10 – 30% of the observed, current total population (Caloi & D’Antona, 2011; Gratton et al., 2012). The composition of the second generation requires that they formed from ejecta from only a fraction of the first generation stars. This suggests that (unless we adopt a very unrealistic and unusual initial mass function (Smith & Norris, 1982; D’Antona & Caloi, 2004)), the original stellar system (made up of first generation stars) must be around ten times the mass of currently observed GCs (D'Ercole et al., 2008; Bekki, 2011). If this is the case, then a mechanism must be found through which the first generation stars can be preferentially lost, while the second generation remain.

The fact that the second generation contains only a fraction of the "polluting" material available from the first generation implies that it is diluted with unprocessed material. The origin of this combination of processed and unprocessed material remains unclear, although some ideas have been suggested: D'Ercole et al. (2008) suggested that the polluting material might be the ejecta from the most massive AGB stars, which collects at the centre of the cluster, although how successfully the AGB ejecta can be retained within the relatively shallow gravitational potential well of a cluster, and whether AGB ejecta can account for all of the mass of the second generation stars has been questioned (Bekki, 2011); others (e.g. Decressin et al. 2007) have suggested that the source might be the winds of fast-rotating massive stars; most recently, Maccarone & Zurek (2012) proposed that it could come from novae which are powered by accretion of the intra-cluster medium by massive white dwarfs. Which, if any, of these models is responsible for the chemical abundances found in second generation stars is not yet known.

As evidence for multiple populations emerges, thoughts are now turning to the question of whether any single population GCs actually exist. Caloi & D'Antona (2011) suggest that two types of single stellar population GCs should exist: those which were too small to retain enough first generation-ejected material to form a second generation (so are made up of first generation stars only) and those which were so massive that they formed a second generation but failed to lose a significant fraction of the first generation (so remain mainly first generation stars). In their search of 106 GCs, Caloi & D'Antona (2011) found 17 GCs which are candidates for single stellar populations, based on the likelihood of a single population HB. Nine of these are thought to have been massive enough to form a second generation, but did not lose the first generation stars.

Regardless of the details of the process, the observational evidence all seems to imply that GCs formed within massive episodes of star formation, creating clusters much larger than the GCs we observe today, and that most of the original stars have been lost. Much of the Galactic halo may have formed in these same star formation episodes, adding to the significance of GCs in the context of galaxy evolution (Gratton et al., 2012).

While the general multiple generation scenario is able to explain well the spectroscopic and photometric features discovered to date, many aspects of the theory are still unclear and the subject of debate. The nature of the material from which the second generation stars form is not yet understood. The time-scales over which the star forming periods took place is not yet clear. Finally, understanding of the connection between the different evolutionary phases, the link between photometric and spectroscopic features, and understanding of the connection between multiple populations and more complicated CMD features such as HB morphology are really in their infancy.

Ever more precise photometry and larger spectroscopic surveys are key to obtaining a true picture of the extent and nature of multiple populations, while further developments in theoretical models are required to explain the physical mechanisms at work.

1.3.3 Globular Cluster Evolution

After a globular cluster has formed, and survived the tidal forces which threaten it in its early development, there are two major processes at play: mass segregation (or core-collapse) and evaporation.

1.3.3.1 Mass Segregation and Core-Collapse

In a globular cluster of sufficient age, encounters between stars will have redistributed the initial star kinetic energies, trying to drive the stars in a GC towards equipartition. As this happens, the most massive stars slow down and move towards the centre of the cluster, while less massive stars, which have higher velocities for the same kinetic energy, move towards the outer region. This process is called mass segregation (e.g. Elson et al. 1987; Heggie & Hut 2003). The central stars then occupy a smaller volume, making the core region more densely crowded. In turn, the shrinking of the core speeds up the energy transfer process, so the core contracts further and the GC halo expands more quickly, in a process known as core-collapse (e.g. Elson et al. 1987; Hut et al. 1992; Heggie & Hut 2003).[4]

Core-collapse can be delayed by the presence of a even a small population of primordial binary systems. When a star passes close to a binary system, the binary pair's orbit tends to contract, releasing energy. Once the energy released from primordial binaries contained within a cluster is exhausted (i.e. the binaries are all

---

[4] The phenomenon in which removal of energy from the core leads to stars dropping into lower orbits, moving faster, and therefore having more energy is sometimes referred to as gravothermal instability (Ashman & Zepf, 1998). Note that this can also happen in single mass models and is not dependent on mass segregation.

disrupted or ejected), core-collapse proceeds (Heggie & Hut, 2003).

By contrast, tidal shocks caused by the GC repeatedly passing through the plane of a spiral galaxy tends to speed up core-collapse. As the GC passes through the disk (or the galactic bulge), the gravitational shock gives energy preferentially to stars in the outer parts of the cluster (Ostriker et al., 1972). This allows more stars to escape (see Section 1.3.3.2), but also adds to the velocity dispersion in the core and accelerates core-collapse (Gnedin et al., 1999).

The fact that GCs do not contain infinitely dense cores indicates that something must happen to reverse the process. It turns out that the system is able to sustain itself (see Heggie & Hut 2003). The high stellar densities in the central region of a core-collapsed cluster lead to frequent interactions, including three body interactions in which two single stars form a binary system, with a third star acting as a catalyst. In such an encounter, the single (catalyst) star gains kinetic energy, and the newly formed binary system is then more likely to undergo further interactions. When another single star passes close to the binary, the binary system's orbit shrinks, and the binary is said to 'harden'. The binary system loses gravitational energy, while the kinetic energy of the passing star increases. Similarly, as core density rises, existing binary systems are also more likely to interact with passing single (or binary) stars. In fact, mass segregation causes primordial binaries to accumulate in the cluster core, increasing the efficiency of binary-binary interactions. Close encounters between binary systems may dissolve one of the binaries, leaving a binary and two single stars, or may harden both binary systems, leading to the release of energy. The increase in available energy means that core-collapse happens in reverse; stars move outwards from the core, lowering the core density, and the core expands further. This is sometimes known as a post-core-collapse bounce phase (Heggie & Hut, 2003).

Observationally, the evolutionary stage of a GC can be determined from its radial profile. As explained in Section 1.2.2, the radial profile (whether constructed in terms of surface brightness or stellar density) demonstrates that, in general, the stellar density increases with decreasing distance from the core. In a pre-core-collapse cluster, this increase continues down to a certain distance from the core, and then flattens. Recent models have shown that a cluster which has undergone post-core-collapse bounce may be indistinguishable, based on its radial profile, from a pre-collapse cluster (Heggie & Giersz, 2009). A GC that is undergoing core-collapse, or in a post-core-collapse bounce phase can be identified by a continual increase in luminosity all the way to the GC centre. It should be noted, however, that such a 'cusp' can also indicate the presence of a central black hole. This is discussed further in Section 1.4.

Numerically, as explained in Section 1.2.2, the dynamical status of a GC can be described in terms of its concentration parameter, $c = \log_{10}(r_t/r_c)$. A concentration parameter of $c \gtrsim 2-2.5$ is considered to be on the verge of collapsing, undergoing core-collapse, or post-core-collapse (Meylan & Heggie, 1997).

There is, as yet, no clear way to determine whether a cluster is about to undergo core-collapse, in the process of doing so, or in a post-collapse bounce phase, either from the slope of the cusp in a radial profile, or from its concentration parameter. It is possible, however, to distinguish whether GCs are in this group of phases or not. Fitting radial profiles to single-mass King models, which are characterised by values of r_t and r_c, can give an indication of whether the entire cluster can be defined using one value of c, or if different values are needed to describe the core and outer regions. If multiple King models are needed to reproduce the radial profile of a cluster, it can be thought of as in one of the core-collapse phases. This is investigated in the case of NGC 6752, in Chapter 4.

1.3.3.2 Evaporation

While mass segregation and core-collapse dominate the dynamics of the central region of the cluster, the overall size of the cluster is affected by evaporation.

Evaporation occurs when stars in the outer part of the cluster have enough kinetic energy to be removed entirely from the cluster's gravitational influence (i.e. its velocity exceeds the escape velocity of the cluster, $v_{star} > v_{esc}$). It is one of the ways in which a GC can be destroyed. In isolation, this will happen through two-body relaxation as a cluster tries to move towards equipartition (Spitzer, 1940), as previously discussed (see Section 1.3.3.1), but the presence of an external gravitational field makes the process happen quicker. In Section 1.2.2, I defined the tidal radius as the radial distance at which the gravitational force of the GC is equal to its host galaxy. As a GC orbits a galaxy, stars outside this radius will be captured by the galaxy and stripped away. The external gravitational field can be introduced in a more dramatic way in the form of tidal shocking.

Tidal shocking, also known as disk shocking, has already been mentioned in the context of its affect on core-collapse rates. It occurs when the GC passes through the disk (Ostriker et al., 1972) or bulge (Gnedin & Ostriker, 1997) of a galaxy and is well known to increase the rate at which stars are lost from the outskirts of the cluster (Kundic & Ostriker, 1995). This tidal stripping effect is self-limiting; as a GC loses mass and becomes more compact, the importance of tidal shocks diminishes.

The time-scales on which evaporation and tidal shocking occur can be interpreted as indicating the characteristic time-scale over which a GC will be destroyed. There are three key time-scales to consider in the context of GCs: the crossing time, relaxation time and evaporation time.

The crossing time of a cluster is the typical time taken for a star to travel a distance equal to the characteristic size of the cluster. This is usually taken to be the half-mass radius, r_m (see Section 1.2.2). The crossing time is given by

$$t_{cross} \approx \frac{r_m}{v},$$

where v is the typical velocity of a cluster member ($\approx 10\,\mathrm{km/s}$; Benacquista 2006). Typically, $t_{cross} \approx 10^5$ years (Padmanabhan, 2001).

The relaxation time of a gravitationally bound system is defined as the characteristic time taken for the component stars to interact with one another enough that they lose all history of their original velocity. Once this occurs, in theory, the stars all have equal kinetic energy. It is related to the number and strength of the interactions taking place within the cluster, so depends on the average length of time that a star takes to cross the system, as well as the number of stars contained within the system. The mean relaxation time can be shown to be

$$t_{relax} \approx \frac{0.1N}{\ln N} t_{cross}.$$

(Binney & Tremaine, 1987). In a GC, the relaxation time is typically less than 10^{10} years, at least out to the half-mass radius. By contrast, the relaxation time of an elliptical galaxy is generally longer than this, except in the innermost few parsecs (Elson et al., 1987), so the relaxation process is far more important in the evolution of a GC than a galaxy. Of course, stars moving towards the gravitational centre of the cluster, as well as interactions between individual stars mean that GCs cannot ever be truly ‘relaxed’.

The evaporation time of a globular cluster is the time taken for a cluster to dissolve by losing stars whose kinetic energy is high enough for them to escape. This high-end tail of the distribution of speeds is replenished by relaxation. The evaporation time is given by

$$t_{evap} = \frac{t_{relax}}{\gamma},$$

where γ is the fraction of stars which escape in one relaxation time. For an isolated system, assuming that the system is virialised, this turns out to give an evaporation time of

$$t_{evap} \approx 136 \times t_{relax}$$

(Benacquista, 2006). As previously discussed, the evaporation time can be shortened considerably by tidal stripping due to interactions with the disk or bulge of the host galaxy.

The characteristic time-scales of globular clusters differ significantly from each other as follows: $t_{cross} \ll t_{relax} \ll t_{evap}$. On short time-scales, interactions between stars are important, whereas relaxation and evaporation become important at around the typical current age of GCs.

1.4 Open Questions in Globular Cluster Astrophysics

Globular clusters have been studied for centuries, and have long been recognised by both observers and theorists as of great importance in the understanding of topics from stellar evolution to cosmology. There is, however, still much to learn. In fact, it could be argued that recent developments in instrumentation and analysis techniques are showing us just how little we truly understand these fascinating systems. Far from being simple, single stellar populations as we once thought, GCs have recently been revealed to consist of multiple populations of stars. This adds to the already ongoing debate around how they formed, and how they tie in with galaxy evolution. Related to this is the fact that the better instruments become, the more thoroughly we are able to study distant, extra-galactic clusters, and the more we have to start trying to understand what GC spatial distribution can tell us about galaxy structure, and what we can learn from correlations between GC parameters and those of the host galaxies themselves.

While large, ambitious surveys like ‘the ACS survey of Galactic globular clusters’ (Sarajedini et al. 2007; see also Piotto et al. 2002; Rosenberg et al. 2000) can be very useful in studying a number of globular clusters in a self-consistent way, in reality, studies of individual clusters are still the most common method for attempting to amass sufficient data to answer some of the big questions surrounding GC astrophysics. This thesis focuses on two such studies.

In this section, I summarise some of key questions surrounding GC astrophysics, and highlight some of the ways in which the work described in this thesis might help to answer them.

1.4.1 Globular Cluster Formation

An ongoing and important topic of research is that of formation mechanisms, which can be divided, broadly, into three topics: the likely link to star forming regions in interacting galaxies; the possible link to dwarf galaxies and the involvement of multiple stellar populations.

As discussed in Section 1.3.1, it is generally believed that globular clusters form in periods of rapid star formation (starbursts). In these starburst regions, the interstellar medium is particularly dense, allowing GCs to form from giant molecular clouds. In the last few years, it has become widely accepted that the young, blue clusters residing in starburst regions such as the Magellanic clouds and galaxy mergers are likely counterparts to the classic, old GCs. Studies of such clusters, in particular in interacting galaxies, will allow us to finally determine the time-scale on which star formation occurs in the progenitor cloud, and confirm or disprove the theory that the fact that all (old) GCs have approximately the same mass (as opposed to the range of masses found in young clusters) because only the most massive clusters are able to survive disruption in the same star formation bursts that form them. It is clear that as GC formation is closely linked to galaxy formation and mergers, investigating GCs will inevitably help us to learn about the galaxies that they reside in.

In order to fully understand the mechanisms governing GC formation, we must also get answers to many questions regarding the nature and origin of multiple stellar populations residing in GCs. Only in the last few years have astronomers come to accept that GCs are made up of multiple generations of stars, but recent observations have shown that multiple populations appear ubiquitous; a key question now is whether or not any GCs exist whose stars can be considered to be a single stellar population. Current theories are able to explain observational evidence in each individual part of the CMD (i.e. broadened sequences and chemical inhomogeneities), but work to track the different generations through the complete evolutionary track of a CMD (from the MS, through the sub and red giant branches, for instance) is just beginning.

The true multiple population picture is likely to impact on other areas of GC astrophysics: the multiple population scenario is likely to be related to the so-called ‘second parameter problem’, through which the horizontal branch morphology appears to be related to age, metallicity, or cluster mass. The relative importance of these parameters in determining the shape and extent of the horizontal branch is not yet established.

Furthermore, multiple population theory may also be linked to even more complex stellar evolution questions: a recent study by Haggard et al. (2010) found a population of nine X-ray emitting stars which lie to the red of the red giant branch in the CMD. These may be a class of X-ray emitting binary systems, or may be linked to the metal-rich red giant branch. It is not known why this population is prone to producing X-ray-bright sources.

Finally, it is not yet understood how the different generations of stars form, and what their presence tells us about the wider topic of early galaxy formation. While most multiple population clusters appear to be of the 'enrichment' type, others, such as ω Cen and NGC 1851 have spreads in age and metallicity that are too large for such a scenario to work. These clusters are thought to be linked to dwarf galactic nuclei, as discussed below.

Work to investigate the presence of multiple stellar populations in GCs tends to be taking place on a cluster-by-cluster basis, because high precision photometry is required, which often leads to approaches being tailored to each specific cluster. To this end, part of this work (see Chapter 6) focuses on a search for broadening in the main sequence of the globular cluster NGC 6752. Searches for evidence of multiple stellar populations in more GCs, and deeper searches in those known to harbour multiple populations will likely be needed before comparisons can be drawn and theories surrounding the true nature of multiple populations can be refined.

It has been suggested that there is a link between dwarf galaxies and halo GCs. Freeman (1993) suggested that in the early Universe, GCs form as the nuclei of dwarf galaxies, and are then accreted into the galactic halo as their host galaxies merge onto larger structures. A recent study by Georgiev et al. (2009) supports this claim, at least for GCs which exhibit extreme horizontal branches (see Section 2.1.3). Marin-Franch et al. (2009) propose that the nature of the multiple stellar populations found in a GC might tell us something about the GCs origins as an accreted satellite. Bekki & Yong (2012) interpret the presence of the stellar halo around the Galactic GC NGC 1851 (found by Olszewski et al. 2009) as evidence that it formed in the centre of a (now defunct) dwarf galaxy. Brodie et al. (2011), however, studied the GC population of M 87 and found that its ultra-compact dwarfs, which are thought to be the stripped nuclei of dwarf galaxies, are a distinct population from GCs. Establishing the extent of a link between dwarf galaxies and GCs is important in the context of both GC and galaxy formation.

1.4.2 Globular Cluster Evolution

As well as helping to understand galaxy formation, studies of globular clusters can also aid in the understanding of galaxies' subsequent evolution. A key tool in this investigation is the initial mass function (IMF: the number distribution of stars as a function of mass). Theories suggest, for example, that the characteristic mass of GCs will increase with lower GC metallicities (Paust et al., 2010). GCs provide a way to probe whether the IMF changes with metallicity, and a number of studies have investigated correlations between the present day mass function and factors such as metallicity, spatial position in the Galaxy, central surface brightness and central density (Capaccioli et al., 1993; Djorgovski et al., 1993; Paust et al., 2010). As demonstrated by the fact that some of these surveys appear to have contradictory results (for example, Capaccioli et al. 1993 and Djorgovski et al. (1993) find correlations with metallicity and location, whereas Paust et al. 2010 do not), determining even the present day mass function in GCs is difficult. However, such studies are undoubtedly informing the theories concerning the IMF of the Milky Way. In turn, understanding the IMF of the galaxy and any potential connection with GC location might help explain the chemical compositions of GCs and why they differ.

1.4.3 Black Holes

An exciting topic of research concerns the possibility of black holes residing in GCs. The possibility of the existence of black holes of various masses in GCs is discussed in detail in the context of stellar populations in Section 2.3. Here, I focus on the effect of a central black hole on the overall morphology of its host GC.

The presence of an intermediate mass black hole (IMBH) is one of the causes of higher than expected luminosity or stellar density in the very core of a cluster (Baumgardt et al., 2005; Noyola & Gebhardt, 2006). In order to establish the presence of an IMBH in a cluster centre, the slope of the radial profile must be measured very accurately, as the observable difference between the influence of an IMBH and a collapsed core is subtle. Furthermore, the black holes in question have masses of just a few hundred to thousand $M_\odot$ (Goldsbury et al., 2010), so the region in which stars are observably influenced would be small. It is vitally important, therefore, to know the location of the cluster centre to a great degree of precision. Noyola et al. (2008) and Anderson & van der Marel (2010) independently searched the radial profile of ω Cen for signs of a central IMBH. The centre positions that they used differed by just $12''$, but they drew very different conclusions: Noyola et al. (2008)

claim to have found evidence for an IMBH, while Anderson & van der Marel (2010) found, at most, a shallow central cusp which does not suggest evidence of a black hole. Accurately locating the cluster centre is key if radial profiles are to be used in searching for the presence of central black holes.

1.4.4 Radial Profile

As explained in Section 1.2.2, the radial density or brightness profile of a GC can tell us about its evolutionary state. Radial profiles can identify clusters which are undergoing core-collapse, through the presence of a central peak. At present, however, there is no way to determine if a cluster is about to undergo core-collapse, currently collapsing, or in a post-collapse bounce phase. New work even suggests that a pre-collapse GC's radial profile may be indistinguishable from one at the peak of a post-collapse bounce (see Section 1.2.2 and Heggie & Giersz 2009). Theoretical models are able to fit well the general slope of the profile, but are less good in the innermost and outermost extremes. Better models are required if radial profiles are to be used in investigating tidal stripping in the outer reaches of clusters, as well as furthering understanding of the observational characteristics of core-collapse. Debate even continues around whether density or luminosity profiles are best suited to this role. Stellar density methods are limited by the ability to resolve stars in the dense cluster core, but luminosity profiles are influenced strongly by the choice of wavelength (for example, the luminosity profile constructed using V-band images is predominantly made up of red giant stars). As in the use of radial profiles in searches for central black holes, accurately locating the centre position of a GC is key.

In Chapter 4, I present a new estimate for the centre position of NGC 6752, and then construct the cluster's radial density profile. NGC 6752's dynamical status is the topic of much debate, with evidence for both a collapsed and non-collapsed core (see, for example, Lugger et al. 1995; D'Amico et al. 2002; Ferraro et al. 2003a; Noyola & Gebhardt 2006). More accurate measurements of the central position and density profile are required to determine the true nature of the cluster's evolutionary status.

1.4.5 Binary Fraction

It has long been known that the fraction of stars in a GC that is contained in close binaries can greatly impact the evolution of the GC. As mentioned in Sections 1.1

and 1.3.3, GCs with only a few binary systems will tend to evolve through long term interactions, whereas the presence of a larger binary fraction can cause the GC to expand and evaporate quicker, while also delaying core-collapse. As well as primordial binaries, binary systems are created and destroyed in GCs because the high stellar density leads to frequent interactions. The ability to study potentially large numbers of binary systems involving stars which are at the same distance and (roughly) the same age makes GCs invaluable tools in the study of dense environments and stellar evolution. Thus, determining the binary fraction of globular clusters is of interest in a number of fields.

Measuring the binary fraction of an individual globular cluster is usually done using one of three methods: searching for variations in radial velocity (e.g. Hut et al. 1992); searching for stars which lie to the red side of the main-sequence on the CMD (e.g. Zhao & Bailyn 2005); searching for photometric variables (e.g. Dieball et al. 2007; Servillat et al. 2007). All three methods have associated difficulties: searches for radial velocity variations are only useful in investigating the very brightest GC stars, while searching for an excess of stars in the relevant part of the CMD requires very precise photometry. Searching for photometric variability tends to find binaries which have short periods and high orbital inclination binaries. Such searches are very useful in studying the different types of binary systems found in GCs and comparing them to field populations, but in order to build up a complete picture of the binary fraction of GCs, it is likely that a number of surveys of a number of clusters, using different methods will need to be completed and compiled. This thesis includes searches for photometric variability in two GCs, M 80 and NGC 6752.

In this chapter, I have introduced some aspects of GC astrophysics, describing the key characteristics that define a GC, and outlining its evolutionary stages. In the following chapter, attention shifts to the constituents of a GC; I will describe the stellar populations found within them, and how they can be studied.

Astronomy? Impossible to understand and madness to investigate.

SOPHOCLES (C. 497 – 406 BCE)

2

An Introduction to Stellar Populations Seen in Globular Clusters

In Chapter 1, I introduced globular clusters in the context of their large scale characteristics, as well as their formation and dynamical evolution. In this chapter, I focus instead on the stars that make up a cluster, and then outline some of the tools used to study them. In Section 2.1, I will describe in some detail the colour-magnitude diagram of a GC, and discuss the more exotic objects found in GCs and why they matter. In Section 2.4, I will explain why ultraviolet images are particularly useful in investigating these objects.

2.1 The Globular Cluster Colour-Magnitude Diagram

Much of what is known about the stars contained in globular clusters comes from studying the colour-magnitude diagram (CMD). Figure 2.1 shows the V - I CMD of NGC 6752, with the most important stellar populations highlighted.

In this section, I will discuss each of the marked star types, and introduce the current challenges in understanding their nature. The data and methods used in the creation of this CMD are described in Chapter 4.

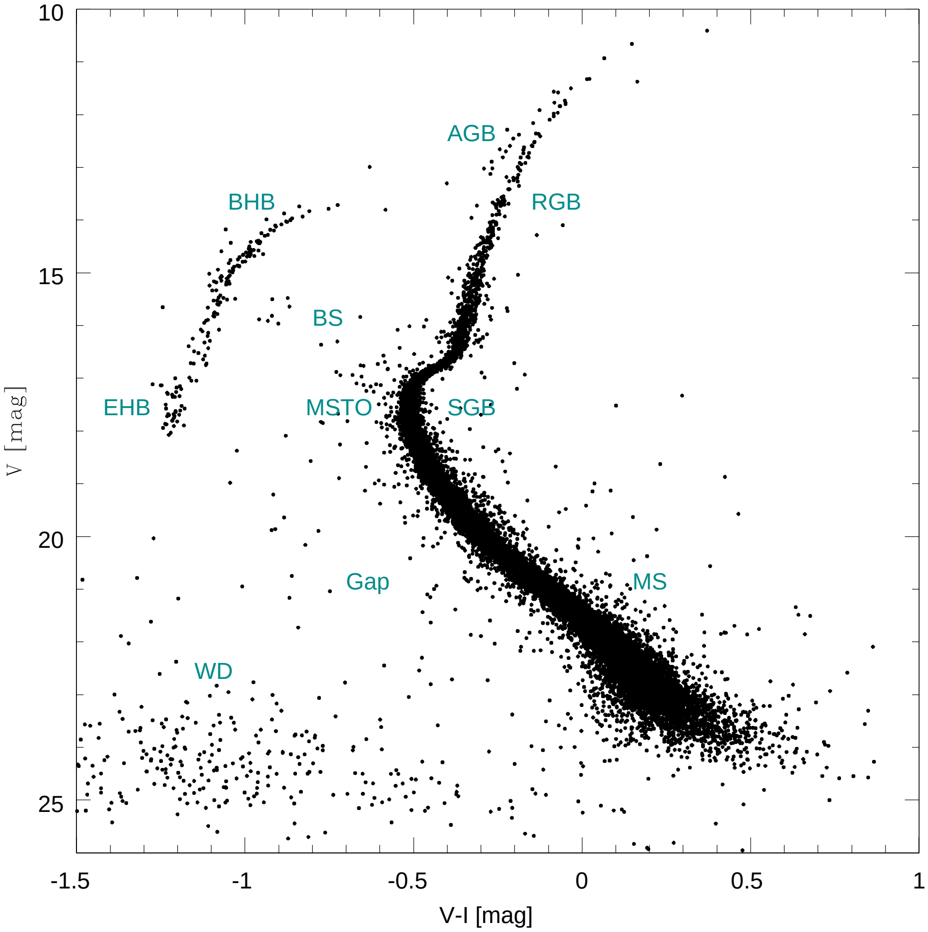

Figure 2.1: The colour-magnitude diagram of NGC 6752. Labelled are the main-sequence (MS), main-sequence turn-off (MSTO), sub-giant branch (SGB), red giant branch (RGB), asymptotic giant branch (AGB), white dwarfs (WDs), and blue stragglers (BS). The area between the WDs and MS is referred to throughout this thesis as the "gap" region, and is also labelled. The horizontal branch of NGC 6752 can be split into two regions: the blue horizontal branch (BHB) and extended (or extreme) horizontal branch (EHB). The construction of this CMD is described in Section 4.3.

2.1.1 The Main-Sequence

The vast majority of sources included in the V - I CMD are hydrogen burning, main-sequence (MS) stars. The MS extends from the main-sequence turn-off (MSTO) to fainter magnitudes and redder colours and ends at a limit dictated by the magnitude limit of the observations (in this case, $V \approx 24\,\mathrm{mag}$). If deep enough observations were available, the MS would end at the hydrogen burning limit, below which only brown dwarfs are found.

The luminosity of the MSTO is related to the age of the cluster; most studies yield approximate GC ages of $10 - 13\,\mathrm{Gyrs}$ (see, for example, Sarajedini 2008; Di Cecco et al. 2010; McNamara & McKeever 2011). The sharpness of the MSTO and the narrowness of the MS were thought to suggest the stars contained within a GC all formed at the same time and have the same chemical composition. As noted in Section 1.3.2, recent developments in instrumentation and photometry techniques have shown that the true picture might be more complicated.

2.1.2 The Sub-Giant and Red Giant Branch

Once the hydrogen in an MS star's core has been exhausted, the star moves onto the sub-giant branch (SGB) and then the red giant branch (RGB). Both of these are marked on Figure 2.1. Sources here have hydrogen burning shells, which move outwards as the star progresses up the RGB.

When the hydrogen shells reach the inner-most part of the convective shell, a chemical discontinuity is formed. This causes the rate of hydrogen burning to drop sharply. The star becomes slightly fainter and bluer, before continuing to progress up the RGB. This results in an over-abundance of stars at a certain part of the RGB, which is known as the red giant bump (Cho & Lee, 2002). Eventually, the degenerate helium core ignites at the tip of the RGB and the star progresses to the horizontal branch.

2.1.3 The Horizontal Branch

The horizontal branch (HB) is made up of stars with helium burning cores which have evolved off the RGB. HB stars are bluer than the RGB and brighter than the MS and are characterised by the fact that they have similar luminosities, but a range in colour.

On the whole, HBs extend blueward from a point close to the RGB, spanning the instability strip (which contains few stars in GCs; see Section 2.2). The HB can be split into a red horizontal branch (RHB) and blue horizontal branch (BHB), based on the position relative to the instability strip. At the blue end, they sometimes have a tail which extends towards fainter magnitudes. These sources have temperatures above $\approx 16,500\,\mathrm{K}$ (e.g. Momany et al. 2004; Brown et al. 2010). This is known as the extended or extreme horizontal branch (EHB).

The length and shape of the HB varies somewhat from cluster to cluster. In NGC 6752's CMD (see Figure 2.1), only one candidate HB source is seen to the red side of the instability strip, but the BHB and EHB are well populated. Other GCs, such as NGC 6637 (Sarajedini & Norris, 1994), exhibit a clear RHB, but have no sources blueward of the instability strip.

The main physical effect determining the morphology of the HB is the metallicity of the cluster. Higher metallicity leads to more opaque stellar envelopes, meaning the light that we see from a star comes from a shallower depth, so it appears red. Thus, higher metallicity GCs have redder HBs than low metallicity ones. Metallicity is known as the 'first parameter' in HB morphology.

It has long been known, however, that GC metallicity variations, alone, cannot explain all of the differences observed between HB morphologies (Sandage & Wildey, 1967). Some GCs have HBs which do not match the colours predicted from their metallicities, and HBs belonging to clusters with similar overall metallicity might appear quite different. Metallicity must not be the only factor influencing the appearance of the HB. This mystery is a topic of current research and is known as the 'second parameter problem'. It is strongly linked to the topic of multiple stellar populations, as discussed in Section 1.3.2.4.

There are a number of candidates for the role of second parameter (see, for example, Recio-Blanco et al. 2006; Fusi Pecci et al. 1993): (i) older GCs are thought to have bluer horizontal branches than younger ones, because the stars evolving onto the HB are less massive, so have less massive (and less opaque) envelopes; (ii) higher helium abundance (meaning lower hydrogen fraction) leads to a less opaque envelope, and a bluer HB; (iii) higher CNO abundance, on the other hand, makes the envelope more opaque, making the HB stars redder; (iv) finally, higher stellar core rotation rates affect the helium core mass and stellar mass loss, so might produce a bluer HB. There is also observational evidence to suggest that globular clusters with higher central densities tend to have bluer HBs. It is likely that some combination of these possible 'second parameters' is required in order to fully explain the differences in HB morphologies. The most likely candidates at present are age and central density (which is linked to mass; Dotter et al. 2010).

2.1.4 The Blue Hook

Some GCs are now known to host a population of objects located at the hottest (and optically faintest) end of the EHB. These stars have temperatures $> 31,500\,\mathrm{K}$ (Momany et al., 2004) and, following Whitney et al. (1998), are known as blue hook (BHk) stars.

Blue hook stars were first detected in ω Cen (Whitney et al., 1998) and NGC 2808 (Brown et al., 2001), but sizeable populations ($10-190+$) have since been found in a number of clusters, including M 54, NGC 6388 and NGC 2419. BHk candidates have also been found in M 80 (see Chapter 3 for discussion of the BHk population of this cluster), NGC 6441, M 70 and M 15 (see Dieball et al. (2009) and references therein). So far, BHk stars have only been found in the most massive clusters. Dieball et al. (2009) suggest that this might still be simply a selection effect; BHk stars are rare, so can only be found in clusters with sufficient numbers of stars. However, Brown et al. (2010) argue that, in fact, only the most massive clusters contain significant populations of BHks and that there is a lower mass limit.

2.1.5 The Asymptotic Giant Branch

A few asymptotic giant branch (AGB) stars can be seen in Figure 2.1. Once a star has exhausted its core helium, the core contracts and is surrounded by an inner shell of burning helium, and an outer shell of burning hydrogen. As the energy generation increases, the star ascends the giant branch for a second time, in a phase known as the asymptotic giant branch. Stars on the AGB are complex systems, and exhibit peculiar features such as He shell flashes, in which the star migrates briefly to the instability strip, as well as mass loss in the form of stellar winds.

2.1.6 White Dwarfs

Eventually, the hydrogen and helium shells of an AGB star become exhausted, and the source loses its envelope and becomes a white dwarf (WD).[1] As fusion is no longer taking place in the core, there is no heat source. Only electron degeneracy pressure prevents the star from collapsing. This makes WDs very dense; they have masses up to $\approx 1.4\,M_{\odot}$, with radii $< 0.02\,R_{\odot}$. The outer material radiates away, and the WD cools and becomes redder. Ultimately, a WD will become a black dwarf, in

---

[1] The ejected shell of plasma and gas might be observed at this point as a planetary nebula. A number of GC planetary nebulae have now been observed (see, for example, Pease 1928; Gillett et al. 1989; Jacoby et al. 1997).

thermal equilibrium with its surroundings. This is expected to take longer than the current age of the Universe, so no black dwarfs actually exist yet.

The WD cooling process takes a long time because the surface area from which the heat is radiated is very small, and the cooling rate follows Stefan's Law, $L = 4\pi R^2 \sigma T^4$, so the rate of cooling decreases as the temperature decreases. The age of the coolest WD in a region can, therefore, be used as a measure of the time since star forming began to take place in that region. In a GC, where the stars all formed at approximately the same time, the WDs form a sequence on the CMD, becoming fainter and redder. The age of the faintest star on that sequence corresponds to the age of the GC. As WDs are optically faint, this is difficult to ascertain and, for a long time, this measurement was beyond the reach of optical observations. Using the *Hubble Space Telescope*, it is now possible, at least in the outskirts of GCs, to detect significant WD populations in GCs. For example, Hansen et al. (2007) used V- and I-band observations of the outer part of NGC 6397 to measure the WD population. They found that it had a cut-off at V$=27.6$ mag, which corresponds to a GC age of 11.47 ± 0.47 Gyr. This is consistent with, but more precise than, previous measurements made using the main-sequence turn-off.

Measuring the complete luminosity function of WDs in the core of a GC is still not possible using optical observations, because they are very faint and optical images are too crowded; WDs can be seen at the very faint end of the V - I CMD in Figure 2.1. As (younger) WDs are blue, however, ultraviolet (UV) images can be useful tools in observing significant populations of them. UV observations are discussed in Section 2.4.

2.1.7 Helium White Dwarfs

Helium white dwarfs (He WDs) are WDs whose progenitors lost enough mass that they were unable to undergo helium ignition at the top of the RGB. They form a CMD sequence slightly to the red of the WD sequence and, as such, can be considered to reside in the "gap" region (see Section 2.1.9).

The most obvious method for the WD progenitor to lose mass before reaching the tip of the RGB is through mass loss or exchange in a binary system. He WDs can, therefore, be formed either in primordial binaries or through dynamical encounters. He WDs are usually associated with millisecond pulsars or ultra-compact X-ray binaries (see Section 2.3; Edmonds et al. 2001; Dieball et al. 2005a). In 47 Tuc, Knigge et al. (2008) discovered a He WD whose spectral energy distribution showed no sign of a companion, pointing to a dark companion such as a neutron star or white dwarf. Radial velocity studies would be needed to confirm or rule out this conclusion. Isolated He WDs may also be present in GCs, in cases where the He WD is ejected from a binary system through an exchange encounter. Studies of He WD populations in GCs can provide a unique insight into the dynamical processes involved in a host GC's evolution.

2.1.8 Blue Stragglers

The CMD in Figure 2.1 also exhibits blue stragglers (BSs). BSs lie along the line of the main-sequence but above the turn-off. They are abnormally massive, hydrogen burning stars that, under normal circumstances, should have evolved off the MS long ago. The formation mechanism (or mechanisms) responsible for BSs is a topic of debate. While many scenarios have been suggested, the two most likely mechanisms are direct stellar collisions (Hills & Day, 1976) and the coalescence of primordial binaries (McCrea, 1964).

A simple method to determine how a particular BS was formed from observations of that individual BS has not yet been found. Instead, research is focussing on attempting to determine the dominant formation mechanism for the BS population as a whole, by comparing the size of the BS population with the characteristics of the host GC.

Evidence for the presence of both formation mechanisms has been reported. Leigh et al. (2007) showed that the total number of BSs contained in a GC does not correlate with predicted collision rate, implying that collisions are not the dominant formation mechanism. On the other hand, Ferraro et al. (2004) and Mapelli et al. (2006) showed that the radial distribution of BSs has a central peak, followed by a decline in number, and then a rise at large radii. Simulations suggest that the central peak is larger than one would expect simply from mass segregation in a cluster containing primordial binaries, while an increase at large radii would not be expected for a collision dominated process. This has been interpreted as an indication that primordial binaries might be the dominant formation mechanism in the outer parts of a GC, but that in the core, BSs are formed from collisions.

In the core at least, if most BSs were formed in collisions between two single sources, the number of BSs should scale with collision rate, and the number in a cluster core should be $N_{BS,col} \approx \frac{\tau_{BS}}{\tau_{col}}$, where τ_{BS} is the typical BS lifetime, and τ_{col} is the time-scale on which collisions occur. Alternatively, if BSs form from binary systems, the number should scale as $N_{BS,bin} \propto f_{bin} M_{core}$, where f_{bin} is the GC core's binary fraction and M_{core} is the total stellar mass in the core. Knigge et al. (2009) studied a a sample of 56 GCs which were known to host BSs, to search for correlations between BS numbers and various cluster parameters. They found no correlation between the predicted number of single-single collisions and the number of BSs, across the whole sample. It should be noted that single-single collisions are considered in simple models, but it is recognised that collisions with binary systems are key in reality; the single-single situation is used to represent all such collisions. For the denser clusters (defined as $\rho_0 > 10^4 M_\odot pc^{-3}$) only, they found a weak correlation. In the search for a correlation between the number of BSs and core mass, however, they found a significant correlation. Even considering only the denser clusters, the correlation between number of BSs and cluster mass was stronger than that with collision rate, implying that core mass is the better predictor of BS population size, whether considering all clusters, or just the denser ones. They suggest, therefore, that binary coalescence is the dominant formation method for BSs, but note that the binaries themselves may have been subject to dynamical interactions.

Even more recently, Ferraro et al. (2009) reported the discovery of two distinct BS populations in M 30. Following comparisons with stellar isochrones, they suggested that the redder population arose from the evolution of close binaries which are probably still undergoing mass transfer, while the blue population arose from stellar collisions. Over time, the region between the BS populations will be filled due to stellar evolution, so the fact that the two populations can be distinguished is evidence that M 30 has undergone a short-lived, recent dynamical event. They suggest that the two populations are a consequence of core-collapse within the last $1-2$ Gyrs. The core-collapse process is known to enhance the gravitational interaction rate, increasing the number of stellar collisions and hardening existing binaries, causing mass-transfer to begin. This proposal can be tested in the future: if true, the red BS sequence should be populated by binaries with short orbital periods. It should be noted that M 30 is not thought to be unique in containing BSs formed through both collision and primordial binary channels; it is merely in an unusual evolutionary state in which the two types of BS can be distinguished.

Clearly, the BS formation mechanisms are strongly linked with the internal dynamics of their host cluster. The study of BSs is an ideal way to learn more about the impact of dynamics on stellar evolution.

2.1.9 “Gap Sources”

The final region highlighted on Figure 2.1 is the area between the white dwarfs and the main-sequence, which I refer to throughout this thesis as the “gap” region. This region contains He WDs, discussed in Section 2.1.7 and binary systems containing MS stars and compact objects.

Binary systems containing black holes or neutron stars emit predominantly at X-ray wavelengths. These systems are rare, and are a topic of current interest in their own right and in the context of differences between GC and field stars (Pooley, 2010; Knigge, 2012). X-ray binaries can be broadly divided into low mass or ultra compact X-ray binaries, depending on their X-ray luminosity and periods. A full discussion of ‘X-ray binaries’ can be found in Section 2.3.

The remaining gap sources are binary systems containing MS stars and WDs. The CMD alone does not allow for distinction between non-interacting and interacting MS-WD binary systems. Interacting MS-WD binaries are known as cataclysmic variables, and form the focus for this section. As these sources are quite faint in optical wavebands, it can be difficult to obtain reliable CMD positions for gap sources and WDs. Using ultraviolet observations can help, as discussed in Section 2.4.

Cataclysmic variables (CVs) are WD-MS binary systems in which the MS overflows its Roche lobe and mass from the MS is transferred to the WD, usually via an accretion disk (conservation of angular momentum means that material cannot fall directly onto the WD; instead, the material radiates away gravitational potential energy and loses angular momentum while spiralling through a disk; Warner 2003). This process leads to variability, UV excess and X-ray emission. There are many different sub-types of CVs, which are characterised by the shapes of their light curves.

In (classical) novae, the fusion of hydrogen accreted onto the WD is thermally unstable and leads to a runaway reaction, in which the accreted material is blown away from the WD surface. The process causes a brightness increase (or ‘outburst’) of $6 - 19$ magnitudes (Warner, 2003). Since the remaining WD is left to begin accreting material again, some novae are known to recur on time-scales of $10 - 80$ years.

Dwarf novae (DNe) have more frequent, smaller outbursts caused by instabilities in the accretion disk: gas in the accretion disk heats up due to friction, and when a critical temperature is reached, the rate of mass transfer through the disk changes rapidly, releasing gravitational energy. They typically exhibit outbursts of $2 - 5$ mag (with some up to 8 mag), and recur on time-scales from ≈ 10 days to several years

(Warner, 2003).

If the white dwarf in a CV has a strong magnetic field, the accretion flow can be affected and the light emitted can be polarised (Warner, 2003). In polars, or AM Her stars, the magnetic field prevents an accretion disk from forming. The flow of material from the companion star is controlled by the structure of the magnetic field, and falls onto the WD at the magnetic pole. As the material is, essentially, in free-fall until impact, it reaches high velocities and the collision generates a shock wave which releases X-rays. The magnetic field also causes the WD orientation to be locked to the companion, so the orbital and rotational periods match. In intermediate polars, also known as DQ Her stars, the inner extent of the accretion disk is truncated due to the magnetic field. Material migrates inwards through the disk until it reaches the point at which the magnetic field is strong enough to control the flow. It then flows from the inner edge of the disk onto the pole of the WD along magnetic field lines. As in the polar case, the shock which occurs as material reaches the magnetic pole is a source of X-rays. Intermediate polars are not necessarily tidally locked and have longer periods than AM Her stars, indicating that the ability to form a truncated disk is due to wider separation of the WD and companion (Patterson, 1994).

While it is now understood that CVs in GCs form predominantly through dynamical processes rather than as a result of the normal evolution of primordial binaries (Pooley & Hut, 2006), there are still a number of unresolved questions.

CVs are predicted to exist in GCs in their hundreds, but only a fraction of this number has been found. In 47 Tuc, for example, around 200 CVs are predicted, while around 30 have been found so far (Ivanova et al., 2006; Knigge et al., 2002; Edmonds et al., 2003a). This might be due to a genuine difference between theoretical predictions and the numbers of CVs in GCs, or it might simply reflect the difficulty in detecting the faintest CVs in GCs (Knigge, 2012).

Furthermore, there has been much discussion surrounding the apparent differences between CV populations in GCs and in the field. Galactic field CVs exhibit a well defined “period gap”; a dearth of CVs with orbital periods between 2 and 3 hours. They also have a minimum period of ≈ 80 minutes (e.g. Knigge 2012). These features have been key in the development of CV evolution theory (e.g. Knigge et al. 2011), but the period gap is not apparent in the (small) sample of CVs within GCs for which orbital periods are known. This may indicate a fundamental difference between the GC and field populations (since, for example, the majority of GC CVs are dynamically formed, whereas primordial binaries are more likely to survive and evolve in the field), but may still be due to selection effects

(Knigge, 2012).

In addition, the X-ray properties of field and GC CVs are known to differ (Edmonds et al., 2003b), leading some to suggest that GC CV populations are dominated by binaries containing magnetic WDs (which have truncated and, thus, more stable accretion disks; Dobrotka et al. 2006). Evolutionary theory might support this; in the field, magnetic WDs tend to be more massive than non-magnetic ones, and as the cross-section for dynamical encounters scales with mass, this means magnetic WDs might be more likely to form binaries dynamically (Ivanova et al., 2006), but it may also be put down to selection effects, as many CV detections in GCs depend on X-ray emission, and magnetic CVs are known to be X-ray bright (Edmonds et al., 2003b; Knigge, 2012).

Finally, dwarf novae are thought to be abnormally rare in GCs (Shara et al., 1996; Pietrukowicz et al., 2008), but predicting the number of observable DNe in GCs is difficult. Not enough is known about the intrinsic properties of DN outbursts (in particular, the duty cycle; the fraction of the time that a DN spends in outburst), and identifying DNe in GCs relies on observations which ‘catch’ the outburst and are deep enough to identify the system in quiescence (Knigge, 2012).

2.2 Pulsating Stars

The ability to study large numbers of stars within one telescope pointing makes GCs excellent sources for use in the study of intrinsically variable (‘pulsating’) stars. As well as providing insight into the nature of variable stars as a whole, and the intriguing differences between variables in GCs and the field, some types of variable stars are useful as standard candles, which allow the distances to GCs to be determined. This, in turn, is necessary for understanding the age, structure and formation of GCs and the Galaxy (Shapley, 1918; Smith, 1995). Detailed studies of variable stars are also of interest in the context of stellar structure and evolution.

Pulsating stars are found on the CMD in a near-vertical region known as the instability strip. The variability is well understood to be due to radial pulsations that result in radius and effective temperature changes. Beginning at the dimmest part of the cycle, the ionised gas in the outer shell of the star is opaque. It gets heated by the star’s radiation and expands. As a result, it cools and becomes more transparent, allowing radiation to escape and making the star appear brighter and bluer. Eventually, the expansion stops, and the star contracts again under gravity. This happens in the instability strip because stars in this region have effective temperatures in the required range. Stars to the blue of the instability strip ($\mathrm{T}_{eff} \gtrsim 7500\,\mathrm{K}$) have ionisation zones too close to the surface to allow pulsations to continue, whereas stars redder than those in the instability strip are too cool ($\mathrm{T}_{eff} \lesssim 5500\,\mathrm{K}$) and convection prevents the build up of heat pressure needed to drive pulsations (Smith, 1995).

The majority of variable stars in GCs are of the RR Lyrae type. Other GC variables found in significant numbers include SX Phoenicis and Cepheid variables (Clement et al., 2001).

2.2.1 RR Lyrae Stars

RR Lyrae stars are HB stars with T_{eff} of about $6000-7600\,\mathrm{K}$ and radii of $4-7\,R_{\odot}$ (e.g., Smith 1995; Lázaro 2006; Peña et al. 2008; Sódor et al. 2009), which exhibit periodic variability with amplitude $0.2-2$ mag at optical wavelengths (e.g. Wheatley et al. 2005). The vast majority of known RR Lyrae are in GCs.

There are two main, distinct groups of RR Lyrae: RR ab, which are fundamental mode pulsators, usually have periods of $\gtrsim 0.4$ days and are characterised by their asymmetric light curves, and RR c, which have first overtone pulsations, and have shorter periods and smaller amplitudes than RR ab, with more sinusoidal light curves. The ratio of RR ab:RR c is thought to be related to the metallicity of the cluster. Oosterhoff I (‘metal-rich’) clusters have $N_c/(N_{ab}+N_c) \sim 0.2$ while Oosterhoff II (‘metal-poor’) clusters have $N_c/(N_{ab}+N_c) \sim 0.5$ (Oosterhoff, 1939; Bono et al., 1994). Some RR Lyraes are thought to pulsate in both the fundamental and first overtone modes simultaneously (these are known as RR d; e.g. Nemec 1985), while a few are now suspected of having higher order, double-mode pulsations (Olech & Moskalik, 2009).

While many aspects of RR Lyrae stars are considered to be well understood, these stars are still a topic of current research and debate. At least 40% of RR ab stars exhibit a near-periodic modulation of their light curves, known as the Blazhko Effect (Kolenberg et al., 2010). The cause of this effect is not known and very different theoretical mechanisms have been suggested. The most prominent of these models are

1. the oblique pulsator model, which proposes that the modulation is caused by a difference between the magnetic and rotational axes of the star (Shibahashi, 2000),

2. the resonant pulsator model, in which energy transfer from radial to non-radial modes creates the modulations (Dziembowski & Mizierski, 2004), and

3. cyclical changes to the convection within the star, caused by a changing (turbulent or rotational) dynamo system which produces a transient magnetic field (Stothers, 2006).

Recent studies have shown that the Blazhko effect modulations might not even be periodic, and that more than one mechanism might be at work (Le Borgne et al., 2012).

2.2.2 Cepheid Variables

Cepheid variables, like RR Lyrae stars, inhabit the instability strip and vary in magnitude due to radial pulsations. They vary on longer time-scales than RR Lyraes, with typical periods of days to months. Cepheids can be split into two sub-groups, Type I and Type II, depending on whether they are Population I or II stars. Of course, only Type II Cepheids are found in GCs.

Sub-types of Cepheid variables include δ Scuti stars and SX Phoenicis stars. δ Scuti stars are fainter than classical Cepheids and vary with shorter periods ($0.01-0.2$ days). They often have superimposed periods, leading to complex light curves. SX Phoenicis stars are pulsating BS stars with periods of $\lesssim 2$ hours and optical amplitudes of ≈ 0.7 mag. They are, exclusively, Population II stars and are far more commonly found in GCs than in the field (Rodríguez et al., 2000; Jeon et al., 2001). They are located in the BS region or the lowest part of the instability strip on the CMD, in the region associated with (Population I) δ Scuti stars, so are thought to be their low metallicity counterparts. The physical characteristics of SX Phoenicis stars are not well explained by current theory (for example, Bruntt et al. (2001) suggest that more accurate effective temperature measurements are needed to further constrain the models), and the origin of BS stars is still a topic of discussion (see Section 2.1.8).

2.3 X-ray and Radio Sources

As previously mentioned, the high stellar densities found in the cores of GCs lead to frequent interactions between stars, and allow for the production of compact interacting binaries, many of which emit X-ray radiation.

As they tend to be more massive than ordinary stars, X-ray emitting systems tend to be found towards the cluster core, so high resolution X-ray telescopes are required to study them. The *Chandra X-Ray Observatory* (*Chandra*) has sub-arcsecond resolution, and has been used to identify X-ray sources in both Galactic and extragalactic GCs. *Chandra* surveys aimed at identifying faint X-ray sources in approximately 80 Galactic GCs have been completed to date (Pooley, 2010). Examples include 47 Tuc, where Heinke et al. (2005) detected 300 X-ray sources within the half-mass radius, NGC 2808, where Servillat et al. (2008) found an intriguingly small number of X-ray sources within the half-mass radius compared to 47 Tuc (just 16), which they attribute to differing metallicity and a more complex evolutionary history, and M 92, where Lu et al. (2011) identified the first optical counterparts to X-ray sources 16 years after the initial X-ray discovery (Johnston et al., 1994).

Radio telescopes are ideal tools for searching for the most compact objects in GCs. Timing of radio pulsations in compact objects allow for the determination of not just positions, but also velocity and acceleration measurements of radio sources.

X-ray emission in GCs is usually associated with interacting binary systems containing an MS star and a compact object. The majority of bright X-ray sources ($L_X \approx 10^{36} - 10^{39}\,\mathrm{erg\,s^{-1}}$; Webb 2006) in GCs are cataclysmic variables, in which the compact object is a white dwarf. Since CVs are optically faint and GC cores are very crowded, X-ray surveys are invaluable in hunting for CV populations in GCs. CVs have been found in many clusters in this way, including 47 Tuc, M 22, M 55, NGC 3201, and the two GCs studied in this thesis, M 80 and NGC 6752 (Grindlay et al., 2001; Webb et al., 2004a, 2006; Heinke et al., 2003; Pooley et al., 2002). A discussion of different types of CVs has already been presented (Section 2.1.9). In this section, I discuss some of the other main types of X-ray and radio sources that may exist in GCs.

2.3.1 Low-Mass X-ray Binaries

The first X-ray sources identified in GCs were low mass X-ray binaries (LMXBs), in which a neutron star (NS) or black hole (BH) accretes matter from a main sequence or giant companion. LMXBs can have bright X-ray emission ($L_X > 10^{36}\,\mathrm{erg\,s^{-1}}$), but are often very faint at optical wavelengths. The discovery that there are orders of magnitude more LMXBs per unit mass in GCs than elsewhere in the Galaxy (Katz, 1975; Clark, 1975) led to a key development in the theoretical understanding of LMXBs in GCs: they are dynamically formed there, rather than coming from primordial binaries. More recent observational evidence confirms this (Pooley et al., 2003). Several LMXB formation mechanisms have now been suggested, including the exchange of an NS into a primordial binary (Hills, 1976), tidal capture of another star by an NS (Fabian et al., 1975), and NS-giant collisions (Sutantyo, 1975). All of these formation mechanisms depend on the encounter rate of the GC, making distinguishing between the different processes very difficult (Ivanova et al., 2008).

Fifteen LMXBs are known in twelve GCs, and at least seven of these are transient, exhibiting outbursts and long, faint periods. Periods are known for ten of the LMXBs, including two in M 15 (Dieball et al., 2005a).

LMXBs with periods less than $60-80$ minutes are known as "ultra-compact" X-ray binaries (UCXBs) and are thought to have low mass ($< 0.1\,M_{\odot}$), degenerate companions. Five of the fifteen known LMXBs in GCs are known to be UCXBs. UCXBs are thought to form either when an existing WD-NS binary comes into contact through angular momentum losses via gravitational-wave radiation, or through the evolution of a star in a binary with an NS (Nelemans & Jonker, 2010). In GCs, these binary systems themselves are likely to form through dynamical interactions, such as capture of a passing star by an NS or exchange of an NS into a binary system. In order to reach the short periods observed, it is thought that the (new) companion star must be massive, and evolve into a giant before mass-transfer begins. Otherwise, the binary orbit will decrease until the donor star becomes degenerate, and then expand again. Such systems have minimum periods of $70-80$ minutes, so cannot account for UCXBs (Verbunt, 2005). Two UCXB systems in NGC 6440 (Altamirano et al., 2008, 2010) show millisecond X-ray pulsations during outburst, identifying the rotation period of the neutron star itself.

So called "faint X-ray transients" have been identified in the direction of the Galactic centre (not in GCs). These mysterious sources have peak luminosities of $10^{34} < L_{X,peak} < 10^{36}\mathrm{erg\,s^{-1}}$, and it is speculated that they require unusual formation mechanisms and very low mass companions. Searches for similar systems in GCs allow for follow-up observations in the optical and UV wavebands, which are not practical in the Galactic centre. One candidate system is M 15-X3, which has had X-ray peaks at 6×10^{33} and $< 10^{32}\mathrm{erg\,s^{-1}}$ (Heinke et al., 2009). This source has a likely optical counterpart with a mass of $\approx 0.65\,M_{\odot}$, which rules out the very low mass companion scenario.

Transient LMXBs in their quiescent state (qLMXBs) are around 10^4 times fainter than in outburst. The numbers of qLMXBs observed in GCs is in line with predictions from encounter rates and collision probability per unit volume (Webb et al., 2004b; Maccarone & Peacock, 2011). The correlation between collision rate and population size is actually important in the context of the blue stragglers discussed in Section 2.1.8. In the case of blue stragglers, confusion remains regarding the formation mechanisms, in part because the number of observed BSs does not scale with collision rate. The fact that the expected correlation is seen in the case of

LMXBs adds weight to the assertion that collision rate-number correlations should be expected in dynamically formed systems.

2.3.2 Millisecond Pulsars

Millisecond pulsars (MSPs) are the evolutionary products of (NS)LMXBs and emit in the radio as well as in X-rays. There is no evidence for substantial differences between the field and GC populations of MSPs, except that the dynamical formation makes them over-abundant in GCs. Spectral studies of MSPs in 47 Tuc indicate that most are well described by thermal emission from the poles of an NS (Bogdanov et al., 2006). Some show non-thermal emission, which may be due to magnetospheric emission (Rutledge et al., 2004) or confusion with other X-ray sources. A more interesting origin might be shocks between the pulsar wind and other material (Bogdanov et al., 2005). Some MSPs show radio eclipses, indicating the presence of gas escaping from a low mass ($\approx 0.1 - 0.2\,M_{\odot}$) MS companion. Some also show X-ray eclipses, with phases too wide to be due to eclipses of the NS by the companion. This suggests that the emission region is a shock between the pulsar wind and material flowing from the companion (Bogdanov et al., 2005). These objects are thought to belong to a particular phase in the transition between LMXB and MSP, in which the pulsar phase has begun, but the material has not yet ceased flowing from the companion.

The excellent positional accuracy that can be determined for radio sources makes it possible to obtain not just positions for radio sources in GCs, but also velocities and acceleration measurements. This can then tell us something about the host GC. For example, D’Amico et al. (2002) used the Parkes radio telescope to discover five MSPs in the GC NGC 6752, and obtain positions for them with ≈ 20 milliarcsecond (mas) accuracy. Using the accurate position and acceleration parameters measured in a subsequent survey, they suggested that the large radial distance from the GC of one MSP indicates the presence of a black hole-black hole binary. They also give a lower limit on the mass-to-light ratio of the GC of ≈ 10, which suggests that NGC 6752 hosts a high central density of unseen sources and demonstrates one of the ways in which studies of individual, exotic sources can lead to advances in the understanding of a GC as a whole.

2.3.3 Active Binaries

Isolated stars on the lower main-sequence are known to produce X-rays because of coronal activity. The luminosity is determined in part by their rotation rate, so as they age and spin down, the X-ray emission becomes too faint to be detected. Stars in close binaries, however, are tidally locked and forced to rotate quickly, leading to strong X-ray production. These systems are called active binaries (ABs), and they are thought to constitute the majority of faint ($L_X < 10^{31}\mathrm{erg\,s^{-1}}$) X-ray sources in GCs. ABs are difficult to pinpoint in GCs, because they appear to be normal MS stars, except that they are positionally coincident with an X-ray source. This leads to the risk that they might, instead, be chance coincidences. CMD positions in the binary region (just above the MS), the detection of Hα emission, or a lack of any UV excess can help to rule out mis-identification as cataclysmic variables (which are UV bright), foreground stars (which tend to be redder than the MS) or background active galactic nuclei (AGN; which tend to be bluer). Estimates of the number of false matches can also be used to rule out chance coincidences. Many active binaries have now been identified in globular clusters using these methods (Heinke, 2010). Most ABs in globular clusters are thought to be primordial in origin, as suggested by evidence that the number of ABs scales with mass, rather than collision rate (Bassa et al., 2004).

2.3.4 Black Holes

There has been much debate over the last few decades about the possible existence of black holes (BHs) in GCs. Theoretical predictions (Spitzer, 1969) initially suggested that substantial populations of black holes could not exist in globular clusters, because mass segregation would force the heavier stars to form a sub-cluster, which would then quickly evaporate. However, more recent theoretical studies (Mackey et al., 2007) show that some fraction of black holes could be retained. Initial detections of X-ray emission from GCs was interpreted as evidence of accretion onto a central black hole (Bahcall & Ostriker, 1975). This was quickly refuted following observations of an X-ray burst and shown to be due to accretion onto a neutron star (Grindlay et al., 1976; Woosley & Taam, 1976).

The debate was revisited following the first *Chandra* observations, which made it possible to resolve faint X-ray sources in the cores of GCs for the first time. A key problem at present is determining what signatures are required to provide indisputable proof that a source is, in fact, a black hole. X-ray luminosities higher than the Eddington luminosity for a $1.4\,M_{\odot}$ object could be caused by the superposition of a number of NSs; velocity dispersion profiles with sharp central peaks in mass-to-light ratios (indicating the presence of a dark mass in the centre) could be due to mass segregation, since the heaviest objects also have low mass-to-light ratios (NSs and WDs); even dynamical evidence can be disputed (e.g. Gerssen et al. (2003) found marginal evidence for a $\approx 200 M_{\odot}$ black hole in M15, but their data is also consistent with a population of NSs).

Five sources in extra-galactic globular clusters are now considered to be strong candidates for GC, stellar mass black holes, as they show more than one property supporting the BH scenario. Source NGC 4472 A is a very bright ($L_X = 4.5 \times 10^{39}\mathrm{erg\,s^{-1}}$) X-ray source, and shows variability, which rules out the possibility of multiple NSs (Maccarone et al., 2007). Spectral properties also rule out the possibility of a highly beamed NS, making a stellar mass BH the most likely scenario (Zepf et al., 2007, 2008). Brassington et al. (2010) and Shih et al. (2010) identified sources in NGC 3379 and NGC 1399 which emit strongly in X-ray and exhibit variability which exceeds the Eddington limit for an NS. Another source in NGC 1399 is thought to be a black hole based on its high X-ray luminosity ($L_X = 4 \times 10^{39}\mathrm{erg\,s^{-1}}$) and strong emission lines, although there is some debate about whether this a stellar mass or intermediate mass BH (Irwin et al., 2010; Maccarone et al., 2010a). Finally, Maccarone et al. (2010a) identified a second source in NGC 4472 which is a strong candidate black hole based on its peak luminosity ($L_{X,peak} \geqslant 2 \times 10^{39}\mathrm{erg\,s^{-1}}$), variability (by a factor of 4) and spectral properties.

In a recent study using the *Jansky Very Large Array* (*JVLA*), Strader et al. (2012a) identified two strong candidates for stellar mass BHs in a single globular cluster, M 22. As well as being the first strong candidates for stellar mass BHs in any Galactic GC, they are the first to be discovered through radio, rather than X-ray emission (Maccarone & Knigge, 2007). The sources were not found in archival *Chandra* observations, indicating an X-ray luminosity of $L_X < 2.2 \times 10^{30}\mathrm{erg\,s^{-1}}$ and a radio to X-ray luminosity ratio of $\log_{10}(\frac{L_R}{L_X}) \gtrsim -2.6$. The radio emission implies that the BHs are both accreting, but the lack of an observable, likely optical counterpart suggests that the two BHs are in binary systems with faint companions such as WDs. The possibility of two BHs residing in the same globular cluster is intriguing, since theories suggest that even if hundreds of BHs may form there, all but one will be ejected from the cluster (e.g. Kulkarni et al. 1993; Sigurdsson & Hernquist 1993).

The search for intermediate mass BHs (IMBHs; with masses of $10^2 - 10^4\,M_{\odot}$) is proving less fruitful. GCs might be expected to contain IMBHs formed in a manner analogous to the super-massive BHs now known to exist in the centre of massive galaxies (Volonteri & Perna, 2005). Such IMBHs may be identifiable from their effect on the radial density or brightness profile (see Section 1.4), velocity dispersion of stars in their vicinity or from X-ray or radio signatures of accretion onto them. As cusps in the radial profile and evidence of velocity dispersion can have other causes (e.g. mass segregation), Strader et al. (2012b) argue that searching for evidence of accretion onto an IMBH is a more robust method. They used ultra-deep *JVLA* radio continuum observations of the cores of three GCs (M 15, M 19 and M 22) to set an upper limit on the mass of IMBHs contained in those clusters of $360 - 980\,M_{\odot}$. This suggests either that more massive IMBHs are rare in GCs, or that any IMBHs with mass $\gtrsim 1000 M_{\odot}$ accrete very inefficiently, leading to very low luminosities.

Maccarone & Servillat (2008) compared the radio emission from twelve GCs (11 Galactic GCs plus G 1 in M 30, which may be a GC or may be a stripped dwarf galaxy) to set upper limits on the mass of any IMBH contained within them. They do this in two ways. First, they use a “most likely” value for the Bondi fraction (which measures the efficiency of the accretion of the interstellar medium onto the black hole) and an “optimistic” detection limit. Second, they make a more conservative estimate of the BH mass, using a lower accretion rate and higher detection limit. For the Galactic GCs, the mass estimates produced using the more conservative parameters are all less than $19000\,M_{\odot}$. Using the “more likely” parameters, one Galactic cluster (Pal 2) has an upper limit on the mass of a black hole of $3800\,M_{\odot}$, while the other Galactic GCs have BH mass limits of $\leq 2000\,M_{\odot}$. In the majority of cases, these limits are below the expected mass of a GC IMBH formed in a way analogous to the super-massive black holes found in galaxy centres.

Globular clusters are excellent laboratories for studying X-ray and radio populations, because of the high occurrence rate of such binaries in GCs. Studies of X-ray and radio populations in GCs, and comparisons with the global parameters characterising the host GCs, can also tell us something about the nature of the X-ray systems. For example, active binaries are primordial, so are found in GCs with high primordial binary fractions. LMXBs, on the other hand, are found in GCs with higher collision rates, because they are dynamically formed. Similarly, X-ray and radio observations can provide useful information about the host GC, such as the mass-to-light ratio.

The main problem with current X-ray instruments like *Chandra* is that, although the spatial resolution is good, the positional uncertainty is large in the context of a GC, which makes searching for optical counterparts to X-ray sources something of a

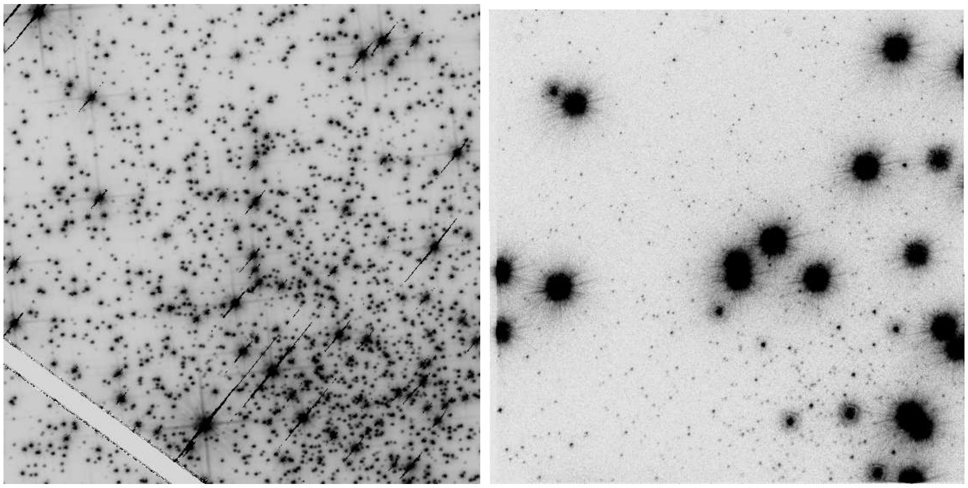

Figure 2.2: Left panel: portion of a V-band image of the core of NGC 6752. Right panel: far ultraviolet (FUV) image of the same field. The FUV image is far less crowded than the optical image.

challenge. In an optical image, the *Chandra* position's $3\,\sigma$ uncertainty region might contain many stars, so identifying the correct source can be difficult. An excellent way to overcome this problem is to use UV images, as discussed in Section 2.4.

2.4 Studying Globular Clusters in the Ultraviolet

As suggested throughout Section 2.1, the optical CMD provides an excellent resource for studying main-sequence and giant stars, as well as the cooler end of the horizontal branch, where the presence of the instability strip makes distinguishing between RHB and BHB stars straightforward. As one moves to (optically) fainter and bluer sources, however, the optical CMD becomes less useful. EHB and blue hook stars are difficult to discern on the optical CMD, because the EHB extends to very faint magnitudes. Furthermore, many gap sources and white dwarfs tend to be close to the detection limit of optical observations.

In the ultraviolet, the picture is very different. Main-sequence and giant stars emit strongly at optical wavelengths, but are very faint in far ultraviolet (FUV) and near ultraviolet (NUV) images because they are so cool. As shown in Figure 2.2, this means that UV images of the cores of GCs are far less crowded than optical images. Conversely, close binaries (such as gap sources) and other dynamically formed systems tend to have very blue spectral energy distributions (SEDs), making them appear as bright sources in UV images. Figure 2.3 shows the FUV - NUV CMDs of NGC 6752. The regions containing blue stragglers, white dwarfs and

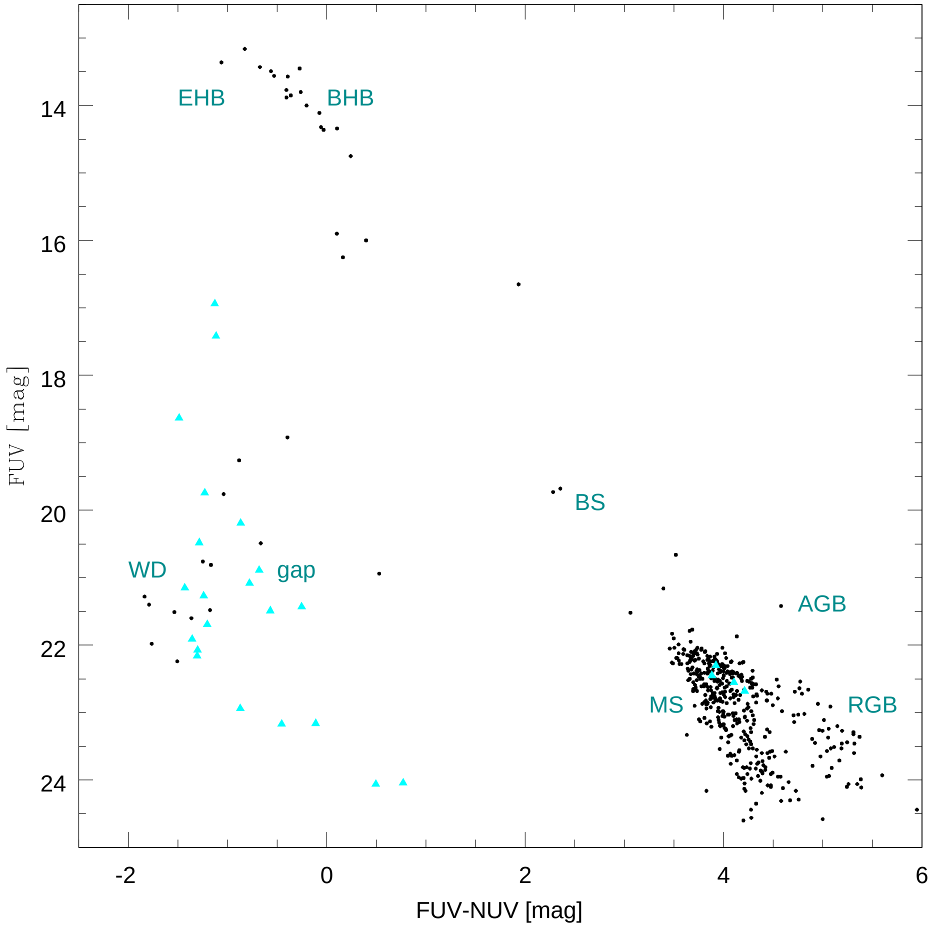

Figure 2.3: The FUV - NUV colour-magnitude diagram of NGC 6752. The BS region, WDs and gap sources are more obvious here than in the V - I CMD. The cyan triangles are very blue sources, which have no U-, V- or I-band counterpart. The construction of this CMD is described in Section 4.3.

gap sources are much easier to distinguish between than in the optical CMD in Figure 2.1. The cyan triangles indicate sources that were detected in the FUV and NUV, but had no detectable U-, V- or I-band counterpart.

As previously mentioned, understanding the nature of the binary population in globular clusters is important both in understanding GC evolution and in explaining dynamical binary formation and evolution. Prior to the start of my PhD, deep FUV surveys had been carried out for three GCs: 47 Tuc (Knigge et al., 2002), NGC 2808 (Brown et al., 2001; Dieball et al., 2005b) and M 15 (Dieball et al., 2007). In 47 Tuc, Knigge et al. (2002) confirmed the CV status of all the known *Chandra* CV candidates, suggested several further possible CVs, and also found a well populated blue straggler sequence, and a number of white dwarfs. In NGC 2808, Brown et al. (2001) discovered a population of EHB stars (the only previously known EHB had been in ω Cen), and Dieball et al. (2005b) then located a number of blue stragglers, CV candidates and young, hot white dwarfs. In M 15, Dieball et al. (2007) confirmed the UCXB status of M 15-X2, which had previously only been known to be an LMXB. There are now four known UCXBs in globular clusters (Maccarone et al., 2010b). Dieball et al. also identified populations of blue stragglers, CV and white dwarf candidates, a horizontal branch sequence, and 41 variable sources. This thesis includes two further FUV studies of globular clusters: M 80 and NGC 6752.

2.5 Open Questions in Globular Cluster Stellar Populations

In this chapter I have described the main characteristics of the stellar populations found in globular clusters, and indicated some of the aspects which are still not well understood. It is hoped that the work in this thesis will help to address these issues, by adding newer, deeper and more precise information about two particular clusters. In this section, I summarise the problems discussed throughout this chapter, for reference.

One of the most important questions in GC astronomy at present is the ‘second parameter problem’. It is known that GC metallicity is the dominant physical trait determining the shape and extent of the horizontal branch (more metal rich clusters tend to have redder HBs), but there is clearly another factor. Suggestions have included age and central density, but there is also a clear link between HB morphology and multiple populations. The ‘second parameter problem’ remains, and more precise CMDs are needed to further inform debate on this topic. In Chapters 3 and 4, I present CMDs of two clusters, and discuss the horizontal branch populations found in each.

Related to the horizontal branch morphology is the controversy surrounding blue hook stars. Blue hook populations have been found in the most massive clusters, but whether or not this indicates a lower cluster mass limit for blue hook production remains unclear. Again, this is most likely to be solved using new, deep CMDs, and the two in this thesis will contribute to investigations into this question.

An ongoing and far reaching question in GC astronomy is that of GC age. As GCs are thought to have formed around the same time as their host galaxies, determining their ages is important in terms of galaxy formation theory, as well as stellar evolution. Age estimates have been attempted using isochrone fitting and the luminosity of the main-sequence turn-off, but both methods are complicated by reddening and the need for precise distance measurements. As such, the colour difference between the MSTO and RGB is usually compared to give relative ages of clusters instead (Krauss & Chaboyer, 2003; Marin-Franch et al., 2009). A better method to determine the absolute age might be using the white dwarf cooling sequence. Deeper CMDs, particularly those making use of UV images, are needed to help construct and refine model white dwarf sequences. It is not yet possible to observe the faintest white dwarfs in GCs, but, as shown in Chapters 3 and 4, progress is being made, and I predict that white dwarf cooling sequences will soon be useful tools in estimating the ages of GCs.

An intriguing mystery in GC astronomy at present is the origin of blue stragglers. It is not yet understood whether blue stragglers form through direct stellar collisions or the coalescence of primordial binaries. Either way, BS formation is clearly closely linked to the internal dynamics of the host cluster. Research into this topic is ongoing and evidence for both proposed formation mechanisms has recently been presented. The blue straggler populations of M 80 and NGC 6752 are discussed in this thesis. Notably, the radial distribution of the redder and bluer BSs differs between the two clusters, indicating that different mechanisms might be at work.

In Section 2.1.9, I discussed the sources located in the “gap” region of the CMD, including non-interacting binary systems and cataclysmic variables. Globular clusters are excellent laboratories for studying close binaries, as the high stellar densities make stellar interactions common. As such, many hundreds of CVs are expected in GCs, but only a fraction of this number have been found. It is not known whether this is due to a genuine difference between theoretical predictions and reality, or the difficulty in detecting faint CVs in clusters. Secondly, further investigation is needed into the apparent differences between GC and field CVs. This includes the apparent lack of a ‘period gap’ in the CV population found in GCs so far. Similarly, it has been suggested (Pietrukowicz et al., 2008) that dwarf novae are abnormally rare in GCs compared to theoretical expectations, and it has been suggested that the low mass X-ray binaries in GCs are preferentially formed with magnetic white dwarfs. All of these findings might be demonstrating genuine differences between GC and field populations, but further work is needed to establish if the differences are real or simply due to selection effects. Efforts to clarify this are very much working on a ‘cluster by cluster’ basis at present, and this thesis includes the search for CVs in two GCs.

The ability to study large numbers of equidistant stars simultaneously makes

GCs excellent places to search for intrinsically variable stars, such as RR Lyrae stars and Cepheid variables. Research into such systems continues, in particular in terms of the Blazhko Effect seen in RR Lyrae stars. This thesis includes a search for such objects in M 80 and NGC 6752.

The ongoing search for black holes in GCs includes both stellar mass and intermediate mass black holes. This was discussed in terms of the effect on the radial profile in Section 1.4. Searches for X-ray sources can provide evidence of black holes, as well as neutron stars. There are now five candidates for stellar mass BHs, but no intermediate mass BHs have been confirmed. A key method in the search for such objects, and a way to distinguish between a single BH and multiple neutron stars, for example, is to search for variability in the optical counterpart. Developments in X-ray instrumentation have driven research into this topic forward, but the positional uncertainty in instruments like *Chandra* make searching for counterparts to X-ray sources using visible wavelengths difficult. UV observations can provide much needed insight, since the field is less crowded and positional coincidences are less likely. In Chapters 3 and 5, I discuss searches for counterparts to known X-ray sources in M 80 and NGC 6752, using both visible and UV observations.

Bright points in the sky or a blow on the head will equally
cause one to see stars.

P. LOWELL (1855 – 1916)

3

The Globular Cluster M 80

The Galactic globular cluster M 80 is fascinating because it appears to be a cluster of contradictions: it is one of the densest GCs in the Milky Way, but is not thought to be core-collapsed; it is famous for containing the classical nova T Scorpii, but despite the many observations that resulted from this discovery, only a few variable sources have been found.

This chapter focuses on an FUV survey of the core of M 80. In Section 3.1, I describe in some detail the creation of the FUV catalogue, and outline the results of the general survey. Although I was involved throughout this work, it should be noted that the data analysis described in this section was performed by Dr. Andrea Dieball, who led the investigation. This work has been published as Dieball et al. (2010) and is included here both because it sets the scene for what follows, introducing some key concepts and methods which are used throughout the rest of the thesis, and because I contributed to it and was involved in discussions throughout the work. In Section 3.2 I describe a variability study of the cluster, which I performed, and which has been published as Thomson et al. (2010).

3.1 A Far Ultraviolet Survey of M 80

M 80 has a metallicity of $[\mathrm{Fe/H}] = -1.7$ dex (Brocato et al. 1998, Alcaino et al. 1998, Cavallo et al. 2004), a distance of 10 kpc, and a reddening of $E_{B-V} = 0.18$ mag (Harris, 1996). It is a very dense cluster, with core radius $r_c = 9''$ (Harris 1996; corresponding to 0.44 pc at 10 kpc), and half-mass radius $r_h = 39''$ (corresponding to 1.89 pc), but it is not thought to be core-collapsed (Harris, 1996; 2010 edition). It has been suggested (Ferraro et al., 1999) that core-collapse is being delayed by stellar interactions, which, in turn, lead to the production of an extraordinarily large population of collisional BSs. Few variable sources are known in M 80 (Wehlau et al. 1990, Clement & Walker 1991, Clement et al. 2001). Based on the periods of its six known RR-Lyraes, M 80 is classified as Oosterhoff type II (Oosterhoff, 1939).

3.1.1 The Observations

The observations used in this survey cover the central ≈ 1.5 core radii (assuming a core radius of $r_c = 9''$) of M 80. The observations were carried out with the Advanced Camera for Surveys (ACS) on-board the *Hubble Space Telescope* (*HST*), using the FUV F165LP filter in the Solar Blind Channel (SBC) and the NUV F250W filter in the High Resolution Channel (HRC). The observations were made at a single pointing. The SBC has a field of view of $35'' \times 31''$, with a pixel size of $0\farcs034 \times 0\farcs030$, while the HRC field of view is slightly smaller, at $29'' \times 26''$, and has a plate scale of $0\farcs028 \times 0\farcs025$ per pixel.

The FUV data (data set j8y501) is made up of 32 individual exposures with durations ranging from 310 to 323 seconds, taken over 4 consecutive orbits in September 2004. The total exposure time was 10232 seconds. The NUV data (data set j8y504) comprised 8 individual exposures of 298 seconds, taken in a single orbit in October 2004, and resulted in a total exposure time of 2384 seconds. To simplify searches for time variability, dithers were not used.

3.1.2 Creating the Master Catalogue

3.1.2.1 Creating Master Images

The first step in creating the master catalogue was to combine all of the individual images into a master image for each filter. Master images were created using `multidrizzle` running under `PyRAF` and are shown in Figures 3.1 and 3.2. The `multidrizzle` routines correct field distortions present in the individual flat-

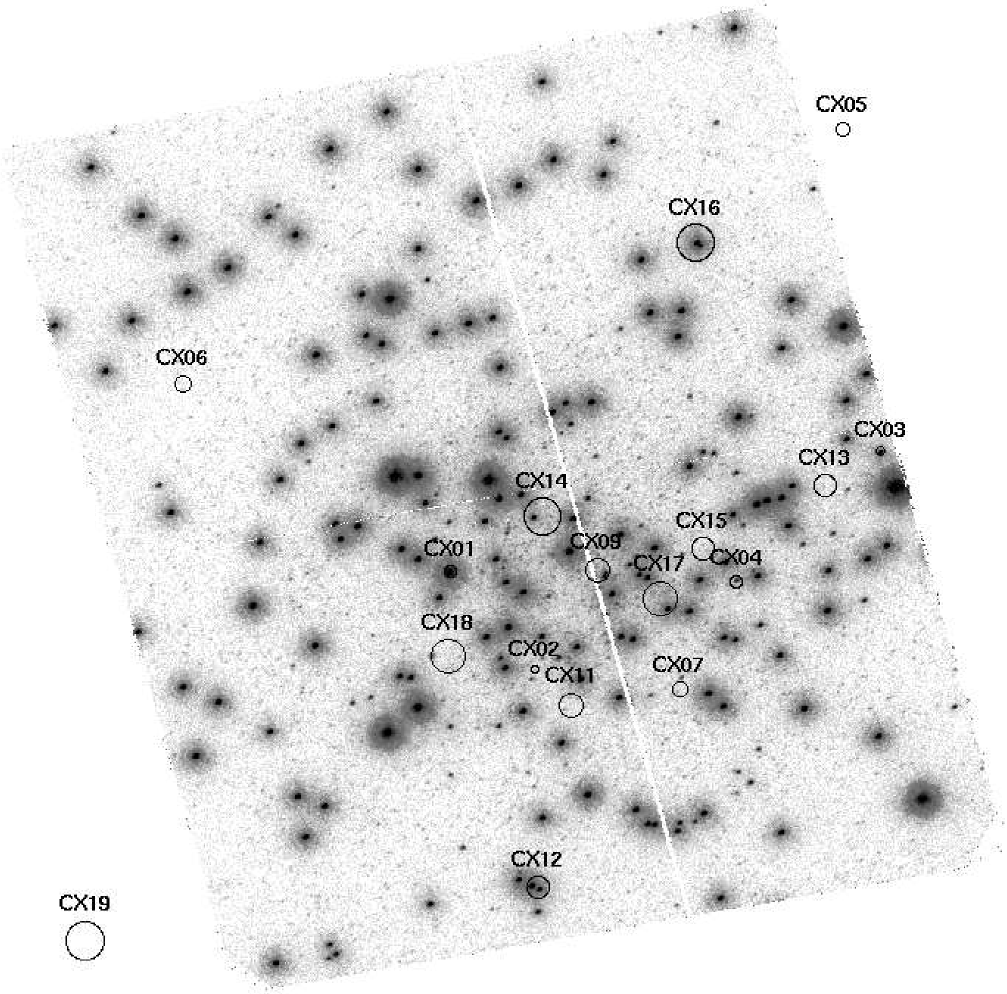

Figure 3.1: Combined and geometrically corrected master image of all FUV SBC/F165LP exposures taken from M 80's core region. North is up and east to the left. The field of view is $35'' \times 31''$. The image is displayed on a logarithmic intensity scale in order to bring out the fainter sources. The positions of the X-ray sources found by Heinke et al. (2003) are marked with their $3\,\sigma$ error circles. This is a reproduction of Figure 1 from Dieball et al. (2010).

fielded images and combine the individual frames to create a master image for each filter. The master images have a common pixel scale of $0.025''$ per pixel and are normalised to 1 second exposure time. In both images, the increase in concentration towards the core is apparent and, as expected, the FUV image (Figure 3.1) is considerably less crowded than the NUV one (Figure 3.2).

3.1.2.2 Source Detection

One of the main goals of the survey was to investigate fainter sources by constructing a deep, FUV - NUV CMD, so source detection was especially important. The

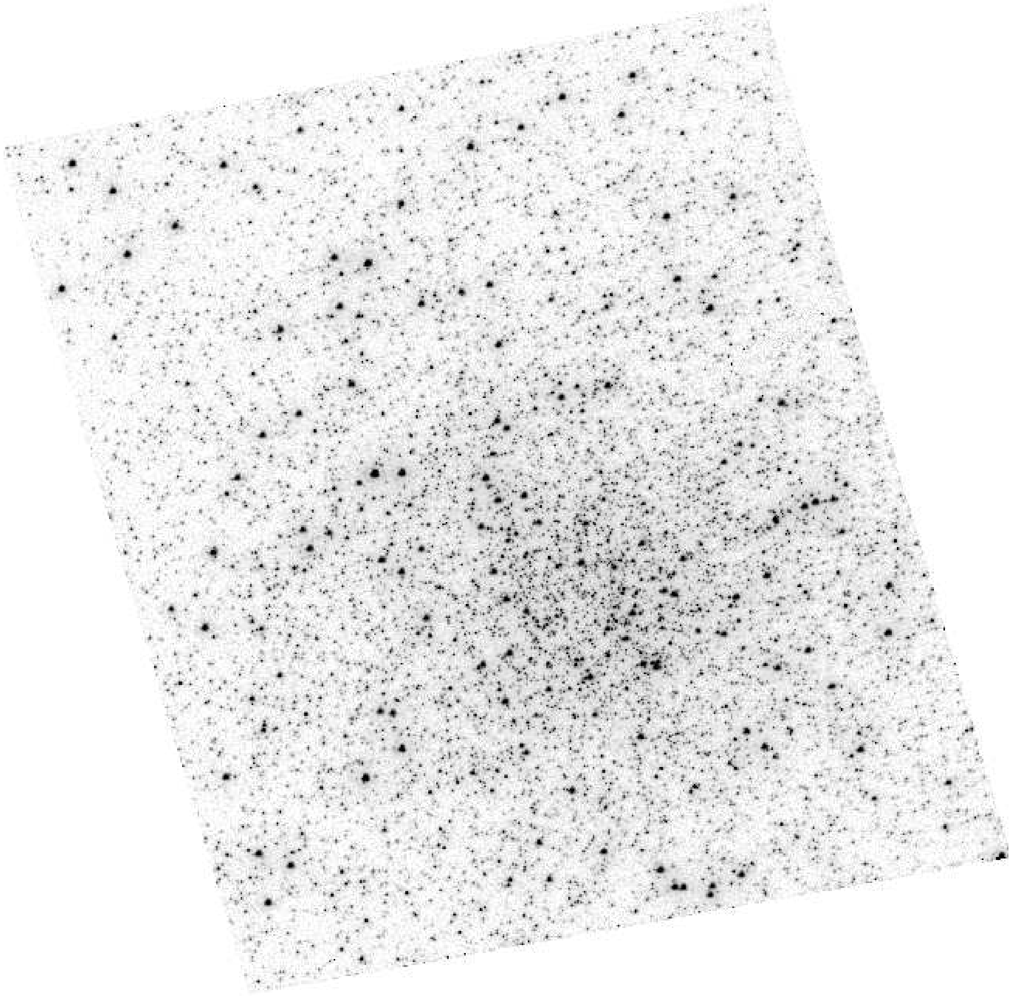

Figure 3.2: Same as Figure 3.1, but for the NUV HRC/F250W exposures. The HRC field of view is somewhat smaller than the SBC field of view with $29'' \times 25''$. This is a reproduction of Figure 2 from Dieball et al. (2010).

routine `daofind` (Stetson, 1991), running under `IRAF`,[1] was used to create initial source lists for the FUV and NUV images, and these images were then inspected by eye to add sources missed by `daofind` and remove false detections. The resulting source lists contained 3168 FUV and 9875 NUV sources.

3.1.2.3 Matching

The FUV and NUV source lists then had to be combined into one catalogue. A reference list containing the pixel coordinates of 92 sources that were clearly visible

---

[1] `IRAF` (Image Reduction and Analysis Facility) is distributed by the National Astronomy and Optical Observatories, which are operated by AURA, Inc., under cooperative agreement with the National Science Foundation.

in both images was created. The `geomap` and `geoxytran` tasks running under `IRAF` were used to determine the transformations required to align the coordinate systems. Shifts in the x and y directions, rotation of the field, and changes in scale were permitted in order to align the coordinate lists. The residual (RMS) errors in the transformation were less than 0.2 pixels (< 10 mas) for the 92 chosen sources.

As the FUV image contains fewer sources than the NUV, but the NUV field is smaller, the maximum number of matches that could, in principle, be found is the number of FUV sources that fell within the NUV field of view. There are 2574 such sources. After some experimentation, a maximum matching tolerance between FUV and NUV source positions of 2.5 pixels was chosen, in order to maximise the number of real matches, while limiting the number of spurious matches. 2345 matches were found, accounting for 91% of the possible FUV sources. Based on the number of sources and the areas of the fields, 45 of these matches ($\approx 1.9\%$) are expected to be false. More detail on this calculation can be found in Section 4.2.3.

In order to search for optical counterparts to the FUV sources, the FUV and NUV catalogue was matched to the optical catalogue from Piotto et al. (2002), who used WFPC2 data in which the PC chip was centred on the cluster core. Thirty-one HB sources that could be easily identified in the V-band F555W and FUV F165LP images were used to transform the FUV image to the optical catalogue's coordinate system. Using a matching tolerance of 1.1 PC pixels (≈ 2 FUV or NUV master image pixels), 1418 matches were found between optical and FUV sources, of which ≈ 40 are likely to be false matches.

3.1.2.4 Astrometry

As noted above, processing images with `multidrizzle` does correct for field distortion of images. It does not, however, improve their absolute astrometric accuracy. This is limited by the accuracy of the original guide star catalogue (GSC1), whose absolute positions are often only accurate to $1-2''$. The world coordinate system (WCS) of the images must, therefore, be improved before they can be matched to external catalogues. This is normally done by adjusting the WCS of the HST images to match an image whose positions are accurately known in a Tycho-based system. An example is the Second US Naval Observatory CCD Astrograph Catalog (UCAC2, Zacharias et al. 2004), which is tied to the Tycho system and has an absolute astrometric error of ≈ 70 mas for stars brighter than $\mathrm{R} = 16$ mag. Transforming the FUV and NUV catalogue directly to the UCAC2 system was not possible in this case, however, because the field of view is so small and the core is so crowded. No matching sources could be found. Instead, a bootstrapping approach was required. First, an ACS WFC image was chosen and obtained from the Hubble Legacy Archive to provide an intermediate-scale image. This image, taken with the F435W filter, has a field of view of $202'' \times 202''$, which includes the core, but also includes a region further out, where the stellar density is much lower. Using 16 sources which were easily identifiable in this image and had obvious matches in UCAC2, the WCS of the WFC image was transformed to match the UCAC2 system. The required shift was $\approx 1\farcs2$, and the resulting RMS residual error between the WFC and UCAC2 positions of these 16 sources was $0\farcs2$.

A further 16 sources were then chosen which were easily identified in the NUV HRC image and the WFC image. Allowing for shifts in the x and y directions, scale changes, and rotation, the WCS of the FUV and NUV images were updated. The positions in the final catalogue have a (conservative) error of $< 0\farcs2$.

Photometry could then be performed on the master images, which are not only combined and geometrically corrected images, but are also astrometrically tied to the Tycho system.

Aperture photometry was performed using `daophot` (Stetson, 1991) running under `IRAF`. More information on `daophot` can be found in Section 4.2.2. Due to the high stellar densities in the core of the cluster (particularly in the NUV image), a small aperture radius of 3 pixels and a small sky annulus of 5 to 7 pixels were used. Gaussian recentring of the input coordinates was also allowed at this stage.

Corrections were then applied to account for source flux missed due to the finite aperture size, and source flux included in the sky annulus. For both the FUV and NUV data sets, a few bright, isolated stars were measured with larger sky annuli, and the correction factor from small to large annuli was determined and applied to all sources. In the FUV, the finite aperture size was corrected for using empirical encircled energy curves. Isolated sources were photometered using a range of aperture radii, and the fraction of light enclosed at different distances was calculated and used to correct all sources. The aperture correction in the FUV was limited to a radius of 60 (SBC) pixels (to prevent nearby sources affecting the results), but the encircled energy curves suggest that the additional correction from 60 pixels to infinity is small. In the NUV case, aperture corrections were adopted from Sirianni et al. (2005). They give aperture corrections for the F250W filter in the HRC with a maximum radius of $0\farcs5$, and suggest that the correction from there to infinity is 0.132 mag. As this correction is applied to the NUV data, but a similar one is not available for the FUV, there may be a slight, systematic, red bias to the FUV - NUV colours.

Table 3.1: Correction and conversion factors used in converting measured fluxes into STMAGs.

Data set	PHOTFLAM $[\mathrm{erg\,cm^2\,\AA^{-1}counts^{-1}}]$	ee	skycorr	ZPT [mag]	addcorr [mag]
FUV	1.3596913E-16	0.47±0.02	1.029±0.005	21.1	...
NUV	4.7564122E-18	0.655±0.006	1.017±0.003	21.1	-0.132±0.002

Instrumental fluxes were converted to the STMAG system using

$$\mathrm{STMAG} = -2.5 \times \log_{10}(\text{count rate} \times \mathrm{PHOTFLAM} \times \text{apcorr} \times \text{skycorr}) + \mathrm{ZPT} + \text{addcorr},$$

where PHOTFLAM is the factor used to convert count rate into flux, apcorr is the aperture correction (apcorr $= 1/$encircled energy), skycorr is the correction from a $5-7$ pixel sky annulus to a $50-60$ pixel one, ZPT is the zero point, and addcorr is the additional magnitude needed to correct from a $0\farcs5$ aperture to infinity. The correction and conversion factors used are listed in Table 3.1.

The full, astrometrically corrected catalogue is available on-line (Dieball et al., 2010).

3.1.3 The Cluster Centre

Several estimates for the position of M 80's centre have been published and are listed in Table 3.2. Different methods were used to determine positions for the centre: Shawl & White (1986) used smooth scans of ESO/ERC photographic plates; Ferraro et al. (1999) used the average of the coordinates of stars in a WFPC2/PC image; Shara & Drissen (1995) used smoothed isophotes from a WFPC2/PC image. The Shawl & White (1986) estimate uses the SAO catalogue, while the latter two estimates are based on coordinates in the GSC1 system.

The centre position was redetermined using the NUV catalogue. The NUV data set is particularly suitable for this purpose, because it contains a sufficiently large number of stars, but is not too affected by crowding. Furthermore, the coordinate list is tied to the Tycho system, which is superior to both the SAO and GSC1 systems. The method used to estimate the central position is described in detail in Section 4.4.1. The result is shown in Table 3.2.

Table 3.2: Estimates of M 80’s centre position. Uncertainties in the position are included, where published.

RA [hh:mm:ss]	Uncertainty in RA	Dec [deg:mm:ss]	Uncertainty in Dec	Reference
16:17:02.432	0.″325	-22:58:34.62	0.″45	This Work
16:17:02.29	0.″23	-22:58:32.38	0.″23	Ferraro et al. (1999)
16:17:02.48	...	-22:58:33.80	...	Shara & Drissen (1995)
16:17:02.51	0.″5	-22:58:30.40	0.″5	Shawl & White (1986)

3.1.4 The Colour-Magnitude Diagram

Figure 3.3 shows the FUV - NUV CMD of the core region of M 80. Synthetic tracks for the zero-age main-sequence (ZAMS), zero-age horizontal branch (ZAHB), and WD and HeWD cooling sequences are included for orientation purposes. These were produced assuming a distance of 10 kpc, reddening of $E_{B-V} = 0.18$ mag and metallicity of $[\mathrm{Fe/H}] \simeq -1.7$ dex (Harris, 1996). Details of how tracks like these are created are given in Section 4.3. The dashed lines in Figure 3.3 show the theoretical ZAHB and ZAMS created using a distance and reddening of 11.5 kpc and $E_{B-V} = 0.17$ mag. These give a better fit to the data (in particular, the position of the ZAHB relative to the HB stars), but the absolute calibration of the UV data is not reliable enough to allow a thorough re-determination of the distance and reddening.

Various stellar populations can be seen in the CMDs, as introduced in Section 2.1. White dwarf candidates are plotted as violet points, blue stragglers are in blue, horizontal branch stars are in green and cyan, asymptotic giant branch stars are in red, and gap sources and (FUV bright) AGB manqué stars are in magenta. The divisions between these populations are judged by eye, using published CMDs as a reference. In most cases, the appropriate boundary between different stellar types is obvious. Discretion is needed most when distinguishing between white dwarf, gap and main-sequence stars. However, changing the positions of these boundaries by a reasonable amount (a few tenths of a magnitude, at most) would not significantly change the population sizes. A more formulaic approach might be useful in future studies, for example when comparing the CMDs of different clusters, but in this work the exact position of the dividing lines is not crucial. In the right-hand panel, optical sources with FUV - NUV counterparts are plotted in darker shades of the same colours (except for MS and RGB stars, which are black in both panels). In this subsection, I describe some interesting aspects of the CMDs in more detail.

The horizontal branch of the FUV - NUV CMD shows a number of features. Firstly, it can be split into two groups; HB sources with colours at least as blue as the ZAHB at $T_{eff} \approx 20,000$ K are defined to be EHB sources (e.g. Momany et al. 2004). Two gaps can be seen in the horizontal branch of both CMDs. The first is the large gap in the vertical part of the BHB/EHB tail in the optical CMD and was first noted by Ferraro et al. (1998). This gap is also visible in the FUV - NUV CMD, near the “corner” in the ZAMS at FUV – NUV ≈ -0.7 mag. The second gap is at fainter optical and bluer FUV - NUV magnitudes. This gap corresponds to $T_{eff} \approx 26,000$ K and is used to divide the EHB stars into two populations: EHB1 stars are redder than this gap, while EHB2 are bluer and are plotted as star shaped

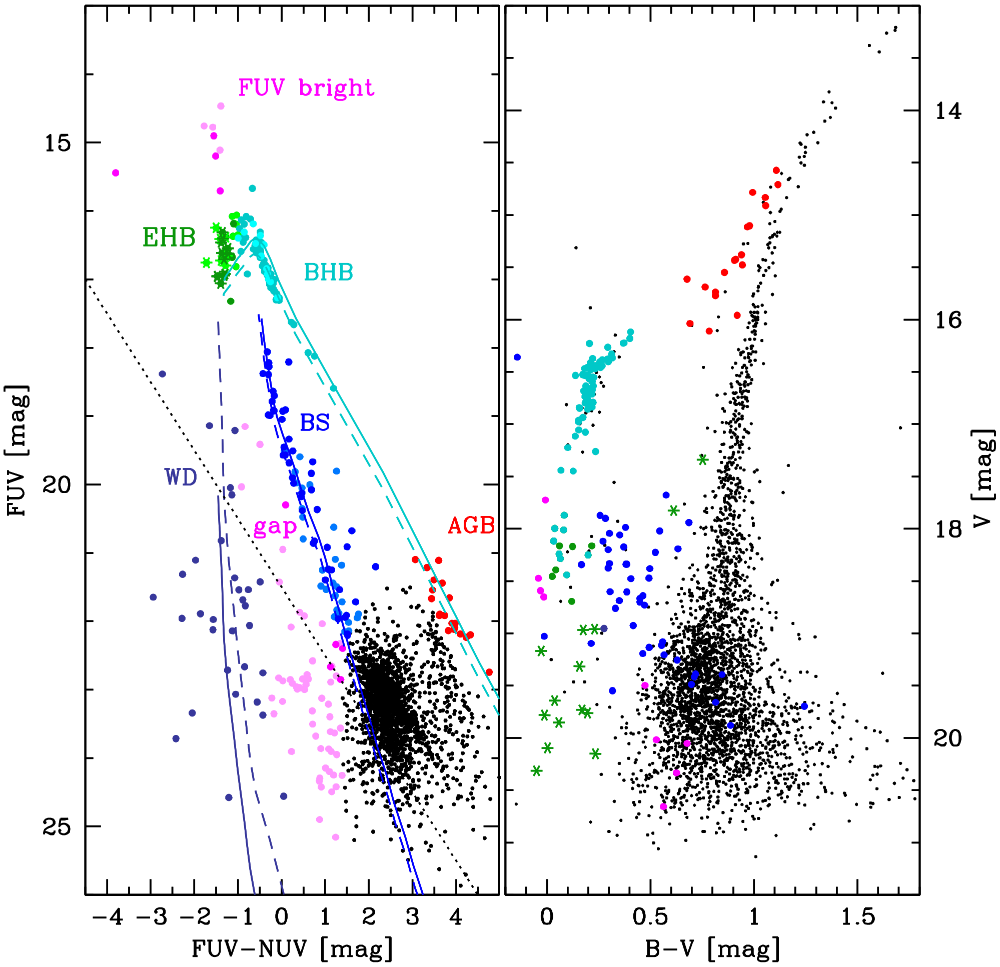

Figure 3.3: Left panel: FUV - NUV CMD of the core of M 80. For orientation purposes, theoretical tracks are included: WD and He WD cooling sequence (violet lines); ZAMS (blue line); ZAHB (cyan line). Different stellar populations are colour-coded: BHBs are plotted in cyan; EHB stars in green; BSs in blue; gap sources in magenta; WDs in violet; AGB stars in red. FUV bright sources which are likely to be AGB manqué stars are plotted in magenta. The remaining stars are MS and RGB stars. The FUV sources which have optical counterparts in plotted in a darker shade of the given colour (with the exception of MS and RGB stars). Right panel: optical CMD of M 80, plotted using the PC data from Piotto et al. (2002). Sources with FUV counterparts are coloured as per the left hand diagram. This is a reproduction of Figure 3 from Dieball et al. (2010).

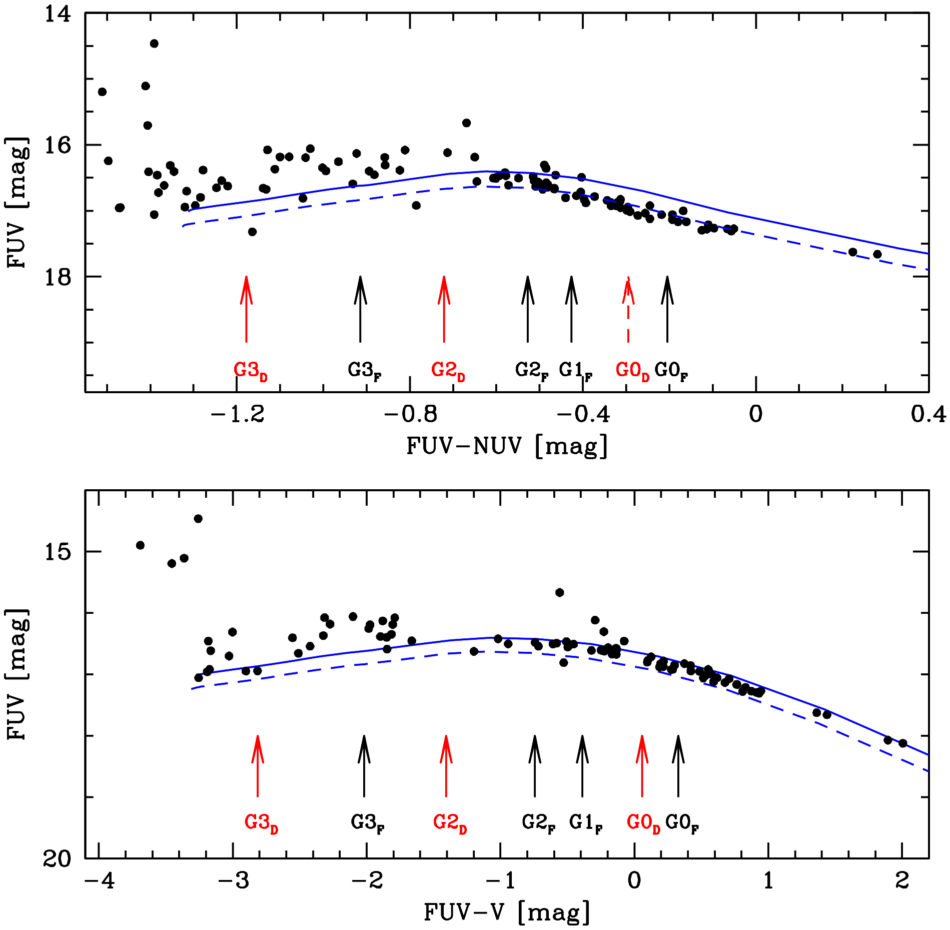

Figure 3.4: Top panel: FUV - NUV CMD of M 80, zoomed in on the HB. Bottom panel: HB of M 80 as in the FUV - V CMD. In both panels, black arrows indicate the gaps G_F suggested by Ferraro et al. (1998), while red arrows mark the locations of the gaps G_D, found in these CMDs. The locations appear to be shifted slightly. Gaps G_0 and G_2 match relatively well, but gap G_3 is more similar in temperature to the G3 gap in NGC 2808. This is a reproduction of Figure 5 from Dieball et al. (2010).

points on both CMDs.

Ferraro et al. (1998) discussed four gaps in the optical HB. Figure 3.4 shows the position of these gaps, along with the gaps visible in CMDs made using our ACS FUV data. None of gaps visible in these CMDs appear at the temperatures suggested by Ferraro et al. (1998); see Table 3.3. The apparent differences in temperatures are likely to be due to differences in the FUV filters (Ferraro et al. (1998) used WFPC2 F160BW images, while the CMDs shown here were created using the ACS SBC F165LP data), the HB models used (Ferraro et al. (1998) used the Dor-

Table 3.3: Gaps in the HB of the FUV - NUV and FUV - V CMDs. Columns 2 – 4 give the colours and temperatures of the gaps. Column 6 is the temperature given in Ferraro et al. (1998), and column 5 gives the colour associated with the temperatures in column 6.

	This Work			Ferraro et al. (1998)	
Gap	FUV−NUV [mag]	FUV-V [mag]	T_{eff} [K]	FUV-V [mag]	T_{eff} [K]
G0	...	0.059	10000	0.329	9500
G1	...	...	...	-0.389	11000
G2	-0.721	-1.405	14500	-0.743	12000
G3	-1.178	-2.814	25500	-2.019	18000

man et al. (1993) models, whereas the newer BaSTI models were used here), the parameters assumed for the HB model (distance, reddening), and the calibration of the data. This demonstrates the difficulty in obtaining reliable temperatures from comparison with stellar evolution models.

As described in Section 2.1, some globular clusters contain BHk stars, which are sources that are as blue as EHB stars, but FUV fainter. The FUV - NUV CMD shows only one source that is fainter than the hot end of the ZAHB. No optical counterpart was found for this source, which could be a BHk or just a faint EHB star. Momany et al. (2004) suggested, based on the data presented by Ferraro et al. (1998), that M 80 might contain a population of BHk stars. The CMD shown in Figure 3.3 demonstrates that the observations clearly extend to faint enough magnitudes that BHk stars, if present, should be detected. Since Momany et al. (2004) used WFPC2 observations with a larger field of view than the ACS observations used here, it is possible that a small population exists outside of the region covered by this survey. Nevertheless, if BHk stars do exist in M 80, these observations suggest that they are rare.

The FUV - NUV CMD (Figure 3.3) includes 75 likely blue stragglers, which are marked in blue and are clustered around the ZAMS, above the main-sequence turn-off. Forty-seven of the BS candidates have optical counterparts. The others might be outside the field of view of the optical images or might be undetectable in the optical images due to crowding.

Some of the optical counterparts are fainter than the optical MSTO. “Blue stragglers” (i.e. collision or coalescence products) fainter than the MSTO can exist (although they would be difficult to distinguish from normal MS stars); they are simply objects formed via the same channels as “normal” BSs, but with masses lower than

MSTO stars. In this case, however, the BSs are above the MSTO in one CMD, but below it in the other. This is probably due to photometric errors, which can cause a small apparent shift in the CMD positions. Some may also be false matches between the UV and optical catalogues. A more intriguing explanation is that the BS formation mechanism has left them FUV-enhanced. This is probably an overly complicated explanation, however, and false matches or photometric errors are more likely causes of the anomalous CMD positions.

Ferraro et al. (1999) used the F160BW (FUV), F255W (mid-UV), F336W (U-band) and F555W (V-band) filters with WFPC2 to study the BS population of M 80. They identified 305 BSs in their catalogue, and concluded that they formed a large, centrally populated population. They suggested that the BSs are formed through collisions (see Section 2.1 for a discussion of the formation mechanisms which may dominate in BS production) and also suggest that M 80 is in a transient dynamical state in which core-collapse is being delayed by dynamical interactions, which in turn produce a large BS population. In fact, Ferraro et al. (2003b) argued that M 80 has the largest and most concentrated BS population of the six GCs they compared (M 3, M 80, M 10, M 13, M 92, and NGC 288).

The CMD in Figure 3.3 shows 75 stars categorised as BSs; far fewer than Ferraro et al. found. The main reason for the different population sizes is, of course, the field of view of the surveys. Ferraro et al. used WFPC2 observations, and covered up to 100″ from the cluster centre, whereas the data used here is limited by the size of the NUV observations, which have a field of view of $29 \times 26''$. This explains why this survey found fewer BSs than the WFPC2 study, but does not establish whether or not the BS population found is still unexpectedly large. To do that, one must compare the observed population to expectations.

In a far ultraviolet study of M 15, 75 BSs were found (Dieball et al., 2007), the same number as in this M 80 study and in a similar field of view. The GCs differ, however, as M 15 is more massive, more concentrated, and more metal-poor than M 80. Scaling with the field size at the distance of the cluster, there are only slightly more BSs per square parsec in M 80 than M 15. The ratio comparing the number of BSs per square parsec in M 80 and M 15 is not significantly different from the ratio of white dwarf or gap sources. Compared to M 15, therefore, this suggests that the BS population in M 80 is not unusual. Another way to compare population sizes is using the BS specific frequency, defined by Ferraro et al. (1999) as $F^{BS}_{HB} = N_{BS}/N_{HB}$. The BS specific frequency for M 15 is 0.564, slightly lower than M 80's value of 0.641. This comparison agrees with the anticorrelation between GC mass and BS frequency found by Piotto et al. (2004). Allowing for Poisson errors on these numbers, however, the difference between the two clusters' BS frequencies is just 0.08 ± 0.12, which is not statistically significant. Thus, the BS population in M 80 is not unusual.

There are ≈ 30 white dwarf candidates in Figure 3.3. The expected number of WDs can be estimated from the number of HB stars (including EHB, BHB and AGB manqué stars) and their relative lifetimes. Only white dwarf candidates above the completeness limits in both the FUV and NUV filters can be considered, so the estimate is restricted to FUV$\lesssim 22$ mag (corresponding to $T_{eff} \approx 24,000$ K and a cooling age of 2×10^7 years). There are 24 white dwarf candidates in the CMD above this magnitude limit, which agrees well with the expected population size of 23 WDs. This suggests that most, if not all, of the WD candidates are real. One of the WD candidates has a surprisingly bright optical counterpart (marked in violet on the optical CMD, at $V \approx 19$ mag). This source is located near the rim of the repeller wire shadow in the NUV image, so might actually be NUV brighter. This would make the source redder, and shift it from the WD region of the FUV - NUV CMD to the BS region.

The sources marked in magenta in Figure 3.3 are fifty-nine so-called "gap" sources, which include CV candidates (see Section 2.1). Applying the same detection limits as before, only WDs with temperature $T_{eff} \gtrsim 24,000$ K are detectable, so the only CVs that can be found are relatively bright, long-period CVs. A number of detailed theoretical studies have been performed to estimate the expected number of CVs in 47 Tuc (Di Stefano & Rappaport, 1994; Shara & Hurley, 2006; Ivanova et al., 2006). As an example, Di Stefano & Rappaport (1994) predict 190 active CVs should exist in 47 Tuc, with half of the captures taking place in the core. Of these, about 20 will be long-period CVs. Ivanova et al. (2006) suggest a slightly larger population of $35 - 40$ detectable, long period CVs in the core of 47 Tuc. For the sake of simplicity, let's assume that this can be scaled with capture rate (e.g. Heinke et al. (2003); Pooley et al. (2003), but note that Pooley & Hut (2006) suggest that while most CVs are produced dynamically, in numbers scaling with encounter frequency, some are formed from primordial binaries, the numbers of which scale with mass). This leads to a predicted $10 - 20$ detectable CVs in the core of M 80. Noting that the field of view in M 80 covers ≈ 1.5 times the core radius, the population shown in Figure 3.3 is consistent with the number predicted. However, not all of the 59 gap sources are CVs; some will be non-interacting MS-WD binaries or He WDs. Five gap sources have optical counterparts, all of which are bluer than the MS and fainter than the MSTO ($V \approx 19$ mag). These sources could be CVs in which a relatively massive MS component dominates the optical colours. Alternatively, as these sources are all located near to the ZAMS in the FUV - NUV CMD, they could be BSs rather than CVs.

3.1.5 X-ray Sources

Using 50 ksec of observations taken using *Chandra*, Heinke et al. (2003) found 19 X-ray sources within the half-mass radius of M 80, down to a limiting $L_{0.5-2.5keV} \approx 7 \times 10^{30}$erg s^{-1}. They suggested that the brightest X-ray source might be the X-ray counterpart to the classical nova T Scorpii (T Sco) and that two more sources are likely quiescent LMXBs. Based on the hardness ratios, they also suggested that five sources are CVs. Fifteen of the X-ray sources are in the field of view of the FUV image.

Given the high stellar density in the core of M 80, it is important that the regions searched for matches to X-ray source positions are as small as possible. Heinke et al. (2003) used a bright star (HD146457) in the Tycho catalogue to register the X-ray source positions. This source is roughly 4$'$ from the core of M 80, and Heinke et al. allowed for an absolute error on their X-ray positions of 2$''$. HD146457 is not in the ACS catalogue used to correct the astrometry of the UV images (see Section 3.1.2). Instead, the positions of 52 X-ray sources identified by Heinke et al. (2003), outside the core were compared to the ACS WFC F435W image. Eight of the X-ray sources fell within the WCS field of view, of which two X-ray sources were near to bright F435W sources. The X-ray positions were corrected by the offset between the Heinke positions and these two stars ($\approx 0\overset{''}{.}13$ in α and $1\overset{''}{.}17$ in δ, well within the estimated X-ray position error).

Of the fifteen X-ray sources which fell in the FUV field of view, six were within 1$''$ of a bright FUV source with no optical counterpart. This included three of the four brightest X-ray sources (CX 01, CX 03 and CX 04; the other, CX 02 is thought to be a quiescent LMXB, so an FUV match is not expected). A final shift of $0\overset{''}{.}1$ was applied to the X-ray catalogue, to optimally match the positions of these three X-ray sources to their FUV counterparts. Figure 3.1 shows the positions of the X-ray sources, once these shifts have been applied. The circles represent the 3 σ statistical uncertainty in the position of the X-ray source, as determined by Heinke et al. (2003).

Table 3.4: X-ray sources and possible counterparts. Columns 1 – 3 give the X-ray source ID and revised positions. The 3 σ statistical uncertainty in position is in column 4, followed by the angular distance from the FUV object. Columns 6 to 14 contain details about the FUV source. The B and V magnitudes, where available, are from Piotto et al. (2002).

1	2	3	4	5	6	7	8	9	10	11	12	13
ID_X	RA [hh:mm:ss]	Decl. [deg:mm:ss]	3 σ [$''$]	Offset [$''$]	$\mathrm{ID}_{\mathrm{UV}}$	FUV [mag]	σFUV [mag]	NUV [mag]	σNUV [mag]	B [mag]	V [mag]	Comments
CX 01	16:17:02.817	-22:58:33.92	0.22	0.02	2129	15.444	0.005	19.247	0.008	*	*	FUVbright
CX 02	16:17:02.580	-22:58:37.73	0.13	0.08	1523	23.736	0.229	21.247	0.029	*	*	MS/RG
CX 03	16:17:01.600	-22:58:29.20	0.18	0.05	2818	17.614	0.011	*	*	*	*	outside HRC
CX 04	16:17:02.008	-22:58:34.28	0.23	0.04	2082	19.209	0.022	20.277	0.024	*	*	WD
				0.22	4790	22.589	0.134	18.748	0.007	16.289	15.198	RG
CX 05	16:17:01.711	-22:58:16.59	*	*	*	*	*	*	*	*	*	*
CX 06	16:17:03.573	-22:58:26.55	0.29	0.21	3221	23.656	0.181	21.152	0.031	*	*	MS/RG clump
			0.29	0.25	3181	23.448	0.162	21.210	0.024	*	*	MS/RG clump
CX 07	16:17:02.169	-22:58:38.52	0.27	0.12	1387	22.578	0.120	21.869	0.055	*	*	gap
				0.25	4850	22.926	0.159	20.666	0.020	*	*	MS/RG clump
CX 08	16:17:01.118	-22:58:30.58	*	*	*	*	*	*	*	*	*	*
CX 09	16:17:02.404	-22:58:33.85	0.44	0.40	2106	18.393	0.015	18.693	0.009	18.510	18.343	BS
CX 10	16:17:00.412	-22:58:30.12	*	*	*	*	*	*	*	*	*	*
CX 11	16:17:02.476	-22:58:39.11	0.43	0.28	1352	22.751	0.137	20.424	0.017	19.980	19.278	MS
				0.33	1341	22.424	0.112	20.209	0.015	19.821	19.296	MS

Table 3.4: (continued)

ID_X	RA [hh:mm:ss]	Decl. [deg:mm:ss]	3σ [$''$]	Offset [$''$]	ID_{UV}	FUV [mag]	σFUV [mag]	NUV [mag]	σNUV [mag]	B [mag]	V [mag]	Comments
				0.36	1283	23.065	0.158	20.560	0.033	*	*	MS/RG clump
CX 12	16:17:02.570	-22:58:46.25	0.43	0.10	214	17.965	0.014	*	*	*	*	outside HRC
				0.24	232	16.306	0.006	*	*	*	*	outside HRC
				0.33	251	21.981	0.112	*	*	*	*	outside HRC
CX 13	16:17:01.759	-22:58:30.54	0.42	0.11	2624	23.397	0.182	22.291	0.240	*	*	gap
				0.25	2605	24.091	0.264	22.384	0.078	*	*	MS/RG clump
CX 14	16:17:02.558	-22:58:31.75	0.70	0.30	2414	22.920	0.195	20.882	0.022	20.555	19.802	MS
				0.30	2453	22.237	0.108	19.372	0.009	18.991	18.185	RG
				0.32	2452	17.661	0.011	17.380	0.004	16.596	16.222	BHB
				0.38	2415	22.557	0.125	20.614	0.022	*	*	MS/RG clump
				0.42	2512	22.452	0.130	20.186	0.018	20.135	19.291	MS
				0.64	2428	22.337	0.144	20.313	0.015	19.602	18.618	MS
				0.67	2541	23.253	0.346	20.673	0.038	*	*	MS/RG clump
CX 15	16:17:02.104	-22:58:33.05	0.43	0.15	2269	23.664	0.232	*	*	*	*	no NUV
				0.17	2270	22.868	0.146	20.393	0.017	*	*	MS/RG clump
				0.17	2294	23.197	0.157	*	*	*	*	no NUV
CX 16	16:17:02.124	-22:58:21.05	0.70	0.05	3967	16.388	0.007	17.210	0.003	18.350	18.285	BHB
				0.23	4786	18.383	0.020	21.117	0.048	*	*	WD

Table 3.4: (continued)

ID_X	RA [hh:mm:ss]	Decl. [deg:mm:ss]	3σ [″]	Offset [″]	$\mathrm{ID}_{\mathrm{UV}}$	FUV [mag]	σFUV [mag]	NUV [mag]	σNUV [mag]	B [mag]	V [mag]	Comments
CX 17	16:17:02.224	-22:58:34.95	0.68	0.21	1944	22.971	0.235	22.555	0.158	*	*	gap
				0.33	2005	22.324	0.157	20.989	0.057	*	*	gap
				0.45	1952	23.262	0.221	21.275	0.045	*	*	MS/RG clump
				0.47	1911	23.045	0.224	20.214	0.021	*	*	MS/RG clump
				0.47	2022	21.579	0.093	18.727	0.007	15.046	13.441	RG
				0.51	1849	16.799	0.008	18.082	0.004	*	*	EHB
				0.52	2050	22.752	0.209	20.713	0.026	*	*	MS/RG clump
				0.53	4791	22.211	0.116	20.005	0.022	*	*	MS/RG clump
				0.61	1918	22.741	0.155	20.124	0.014	*	*	MS/RG clump
CX 18	16:17:02.824	-22:58:37.25	0.68	0.35	1559	23.374	0.221	20.390	0.027	*	*	MS/RG clump
				0.38	1659	23.318	0.178	20.465	0.016	20.127	19.329	MS
				0.45	1601	22.161	0.090	18.628	0.005	16.279	15.166	RG
				0.46	1531	22.672	0.122	20.249	0.020	19.973	19.245	MS
				0.64	1607	20.351	0.040	19.881	0.012	*	*	BS
CX 19	16:17:03.854	-22:58:48.35	*	*	*	*	*	*	*	*	*	*

Using the 3 σ statistical uncertainty, the positions of the X-ray sources were compared to the positions of sources in the UV catalogue. The results are summarised in Table 3.4. Where multiple sources were found within the X-ray error circle, possible counterparts are listed in increasing distance from the X-ray position. Four *Chandra* sources were outside the FUV field of view. These are included in the table in order to present their improved positions.

In the following subsections, I will discuss the individual X-ray sources and their possible counterparts.

3.1.5.1 CX 01: T Scorpii

The brightest X-ray source, CX 01, is located near to the site of the classical nova T Sco. Shara & Drissen (1995) compared the historical data to *HST* WFPC2 images, and obtained two estimates for the position of the nova. One was based on the offset from the cluster centre; the other used offsets from two nearby stars. The positions published by Shara & Drissen (1995) were updated to match the UV coordinate system using the difference in the positions of the two reference stars in the two coordinate systems. In the Tycho-based coordinate system, the nova's position is estimated using the offset from the cluster core as 16:17:02.80s, -22:58:32.21 (J2000), and from the two nearby stars as 16:17:02.84, -22:58:33.21.

Shara & Drissen (1995) identified a blue star as the most likely post-nova system, although they cautioned that at $B = 6.8$ mag, the source is about 10 times fainter than expected for an old nova. This star matches source 2422 in the UV catalogue, which has an FUV magnitude of 19.14 ± 0.02 and an FUV - NUV colour of -1.65 mag. This puts it slightly blue of the WD sequence and makes it a likely hot WD, and possibly a CV. As shown in Figure 3.5, source 2422 is close to both suggested positions for the nova, but is not consistent with the position of CX 01. As it is highly likely that the X-ray source is associated with the old nova system, this makes source 2422 unlikely to be associated with the nova remnant.

As shown in Table 3.4 and Figure 3.5, however, CX 01's position is consistent with that of source 2129 in the UV catalogue. Source 2129 has $\mathrm{FUV} - \mathrm{NUV} = -3.803$, which makes it not only the bluest source in the catalogue, but also bluer than an infinite temperature blackbody (which has $\mathrm{FUV} - \mathrm{NUV} = -1.8$). This suggests that the source decreased significantly in brightness between the FUV and NUV observations. Heinke et al. (2003) suggested that CX 01 is a CV, and the change in magnitude of source 2129 is consistent with this. Furthermore, source 2129 is ≈ 1.5 mag brighter in the NUV than the candidate put forward by Shara &

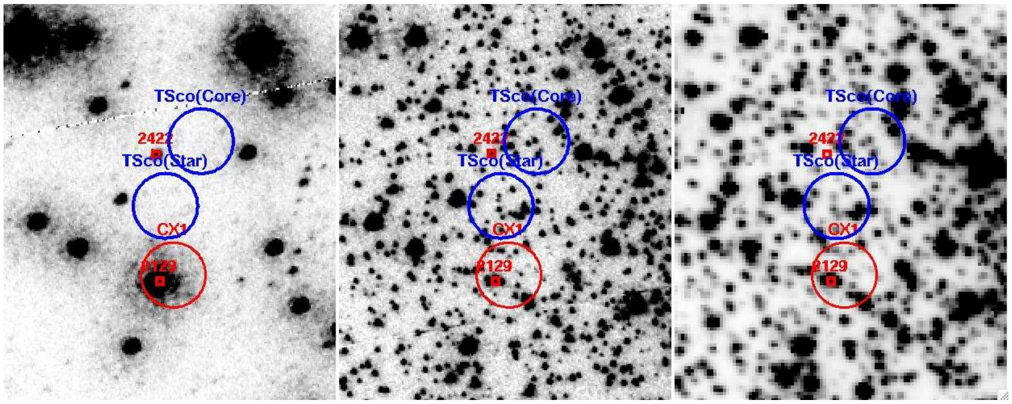

Figure 3.5: Portions of the FUV (left), NUV (middle) and ACS WFC F435W (right) images, showing estimates of the position of the classical nova T Sco. Labelled in blue are two estimates from Shara & Drissen (1995); one made using the offset from the cluster core, and one using the positions of two nearby stars. Also marked is source 2422, which Shara & Drissen (1995) suggested was likely to be the CV responsible for the nova. The red circle gives the position of the brightest X-ray source, and the source marked within it is source 2129, the most likely candidate for the nova remnant. This is a reproduction of Figure 6 from Dieball et al. (2010).

Drissen (1995), making it closer to the quiescent magnitude expected from other novae. Source 2129, therefore, is a much more likely counterpart to the quiescent nova T Sco.

This source is studied in more detail in Section 3.4.3.

3.1.5.2 CX 04, CX 07, CX 13, CX 16, CX 17: Cataclysmic Variables

As noted above and shown in Table 3.4, there are 15 X-ray sources in the FUV field of view, and all have at least one FUV source within their 3 σ statistical uncertainty matching radius. Clearly, positional coincidence is not enough to determine which, if any, are real matches. The most likely real counterparts to X-ray sources are those in the WD and gap region (which contains CVs) of the FUV - NUV CMD. Matches between X-ray sources and these sources can, therefore, be regarded as relatively ‘safe’. The error circles of CX 07, CX 13 and CX 17 contain gap sources, and the positions of CX 04 and CX 16 are consistent with the positions of WD candidates.

The 3 σ X-ray error circle of CX 07 contains two sources, numbers 1387 and 4850. Source 4850 is in the red giant (RG)/MS clump, so there is no reason to suspect that this is the real counterpart. Source 1387, however, is closer to the X-ray position, and is a gap source. It was also identified by Shara et al. (2005a) as a CV which underwent a DN outburst in their observations. They suggested that this source, which they called DN 1, was associated with CX 17. Using the more accurate positions, it is now clear that DN 1 is associated with CX 07. Source 1387 is included in the variability study described in Section 3.4.3.

3.1.5.3 Other X-ray Sources

The other seven X-ray sources that fall within the FUV and NUV fields of view (CX 02, CX 06, CX 09, CX 11, CX 14, CX 15 and CX 18) each have at least one source within the 3σ error circle, but none of these positional coincidences form obvious counterparts on the basis of CMD position. Heinke et al. (2003) identified CX 02 and CX 06 as qLMXBs based on their luminosities and hardness ratios. The only possible counterparts to these objects, which are greater than 1σ from the X-ray source position, are MS/RG sources, so are unlikely to be real counterparts. As the X-ray flux of a qLMXB is much higher than the optical flux, this non-detection is consistent with the suggestion that these sources are quiescent LMXBs.

Sources CX 03 and CX 12 have bright FUV sources within their 3σ error circles, but, as they are located in regions with no NUV coverage, the objects cannot be placed on the CMD, so cannot be classified.

The other four X-ray sources which are within the half-mass radius (CX 05, CX 08, CX 10 and CX 19) were outside the FUV field of view.

3.1.6 The Radial Distributions of the Stellar Populations

Figure 3.6 shows the radial distributions of various stellar populations. White dwarfs and main-sequence stars are not included here due to incompleteness in the FUV, particularly in the core where nearby bright sources may prevent the detection of faint white dwarfs and main-sequence stars. The first panel shows that the blue stragglers are the most centrally concentrated population, as already noted by Ferraro et al. (1999).

Kolmogorov-Smirnov (KS) tests were used to assess how statistically significant the differences in the radial distributions were. The KS test measures the probability that a difference as large as the one observed can be found between two populations that are drawn from the same underlying distribution. Therefore, the higher the percentage given by a KS test, the more likely it is that the two populations come from the same parent distribution, whereas a low percentage means that the two populations are significantly different. Tables 3.5 and 3.6 show the numbers of sources included in each sample and the results of KS test performed on various pairs of populations.

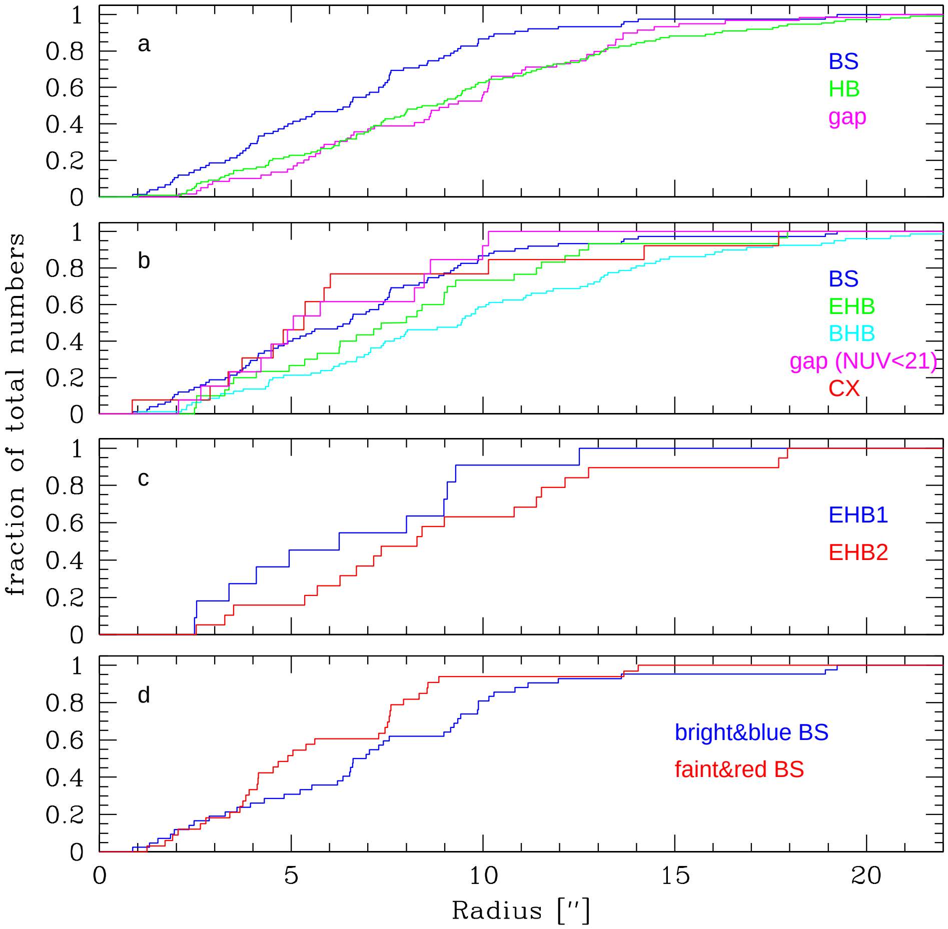

Figure 3.6: Cumulative radial distributions of various stellar populations. Panel (a): the main stellar populations - HB, gap and X-ray sources - are shown. WDs and MS stars are not included due to completeness issues. Panel (b): the main populations again, but the HB is split into EHB and BHB stars. Only gap sources brighter than NUV = 21.5 mag are included. Panel (c): the two sub-populations of EHB stars are compared. Panel (d): the BSs are split into bright/blue and faint/red. This is a reproduction of Figure 8 from Dieball et al. (2010).

Table 3.5: Number of sources associated with various stellar populations.

Population	$N_{sources}$	
	All	NUV $<$ 21.5 mag
BS	75	75
BHB	80	80
EHB	30	30
EHB1	11	11
EHB2	19	19
gap	59	13

Table 3.6: Results of KS tests on the radial distributions of various pairs of stellar populations, showing the probability that the two populations are drawn from the same underlying distribution. The most significant KS test results (i.e. KS probability $<$ 5 %) are highlighted in bold.

Populations	KS Test Result	
	All	NUV $<$ 21.5 mag
BS vs. gap	**0.06**	95.1
BS vs. HB	**0.2**	**0.2**
BS vs. BHB	**0.02**	**0.02**
BS vs. EHB	28.5	28.5
BS vs. X-ray	21.7	21.7
gap vs. HB	79.9	7.0
gap vs. BHB	77.5	**4.0**
gap vs. EHB	23.4	40.2
gap vs. X-ray	**0.9**	82.8
HB vs. X-ray	**0.3**	**0.3**
BHB vs. EHB	9.1	9.1
BHB vs. X-ray	**0.2**	**0.2**
EHB vs. X-ray	**4.4**	**4.4**
EHB1 vs. EHB2	49.5	49.5
bBS vs. fBS	**3.5**	**3.5**

As the CMD depth is limited by the NUV data, the second panel of Figure 3.6 shows radial distributions only for sources brighter than $\mathrm{NUV} = 21.5\,\mathrm{mag}$. This criterion only makes a difference to the gap sources. X-ray sources are also included here. The BSs, X-ray sources and gap sources are more centrally concentrated than the HB stars, as expected from their relative masses and different formation methods (see Section 4.5 for more details). The KS test results confirm that these differences are significant, but that BS, X-ray and gap sources' distributions are not significantly different from one another.

In the third panel, the two sub-populations of EHB stars (see Section 3.1.4) are presented. There is no significant difference between the distributions of EHB1 and EHB2 stars.

The fourth panel of Figure 3.6 compares two sub-populations of BS stars, defined using a division at $\mathrm{FUV} - \mathrm{NUV} = 0.9\,\mathrm{mag}$ on the CMD. Nearly all of the FUV bright (and blue) BSs were also optically bright; of the 33 'blue' BSs which had optical counterparts, 28 had $V < 19\,\mathrm{mag}$. Similarly, 11 of the 14 'red' BSs with optical counterparts had $V > 19\,\mathrm{mag}$. This is shown in Figure 3.7, in which BS stars are marked as red or blue, depending on their colour relative to the $\mathrm{FUV} - \mathrm{NUV} = 0.9\,\mathrm{mag}$ distinction.

It was expected that bright, blue BSs, which are thought to be more massive and younger than their faint, red counterparts, should be more centrally concentrated. However, surprisingly, the radial distributions in panel (d) of Figure 3.6 show that the faint, red BSs are the more centrally concentrated group. The KS test indicates that the probability that the bright and faint BSs are drawn from the same distribution is just 3.5%. To check how sensitive this result was to the exact position of the adopted cluster centre, Monte Carlo simulations were carried out, in which the centre position was shifted at random in accordance with the error derived in Section 3.1.3. The KS test was then re-run with distances based on each new centre. In 100,000 iterations, 63% of tests gave KS results suggesting that the populations are different at better than $2\,\sigma$ confidence. The exact location of the cluster centre does not, therefore, have a strong impact on this marginally significant, but unusual result. If we assume that the observed difference between the distributions is real, a possible explanation might be that the BSs get a 'kick' during their formation, and then sink back towards the centre. If they are pushed out to a region from which the relaxation time-scale is longer than the typical age of a bright BS, the bright BSs would not have had time to move back to the core. The faint BSs, which have longer lifespans, last long enough to settle back to the expected distribution, and are thus more centrally concentrated. In Section 4.5, the radial distribution of BSs

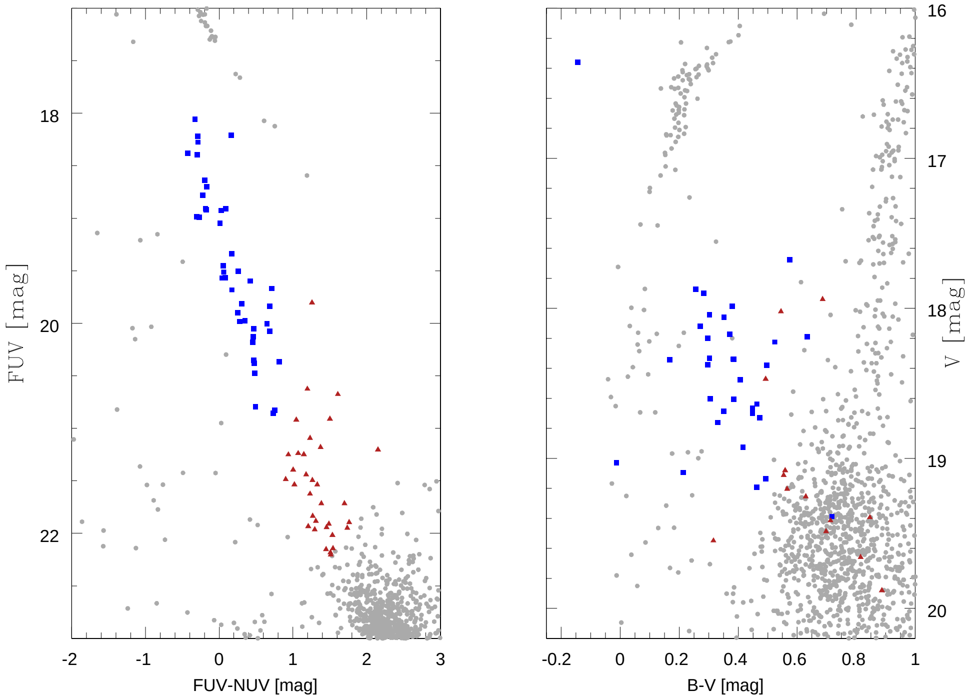

Figure 3.7: CMDs of the core of M 80 with sub-populations of BS stars indicated. Blue squares: brighter, bluer BSs (FUV – NUV ≤ 0.9 mag). Red triangles: fainter, redder BS stars (FUV – NUV > 0.9 mag). Nearly all of the FUV bright (and blue) BSs were also optically bright.

in NGC 6752 is investigated, for comparison with this interesting and unexpected result.

3.1.7 The Typical Masses of the Stellar Populations

The typical masses of stars belonging to a given stellar population can be estimated by comparing the populations' radial distribution to that of theoretical distributions of stars of a given mass. Using the method described in Heinke et al. (2003), we assume that the cluster can be well described by a classic King (1966) model and compare the radial distributions of the sources to those of generalised theoretical King models described by

$$S(r) = \int (1 + (\frac{r}{r_{c\star}})^2)^{\frac{1-3q}{2}} dr,$$

where $r_{c\star}$ is the core radius and the parameter $q = M_X/M_\star$ is the ratio of the mass of the stellar population used to determine $r_{c\star}$ to the mass of the stellar population being considered. We take an MSTO star with mass $0.8\,M_\odot$ to be a typical star

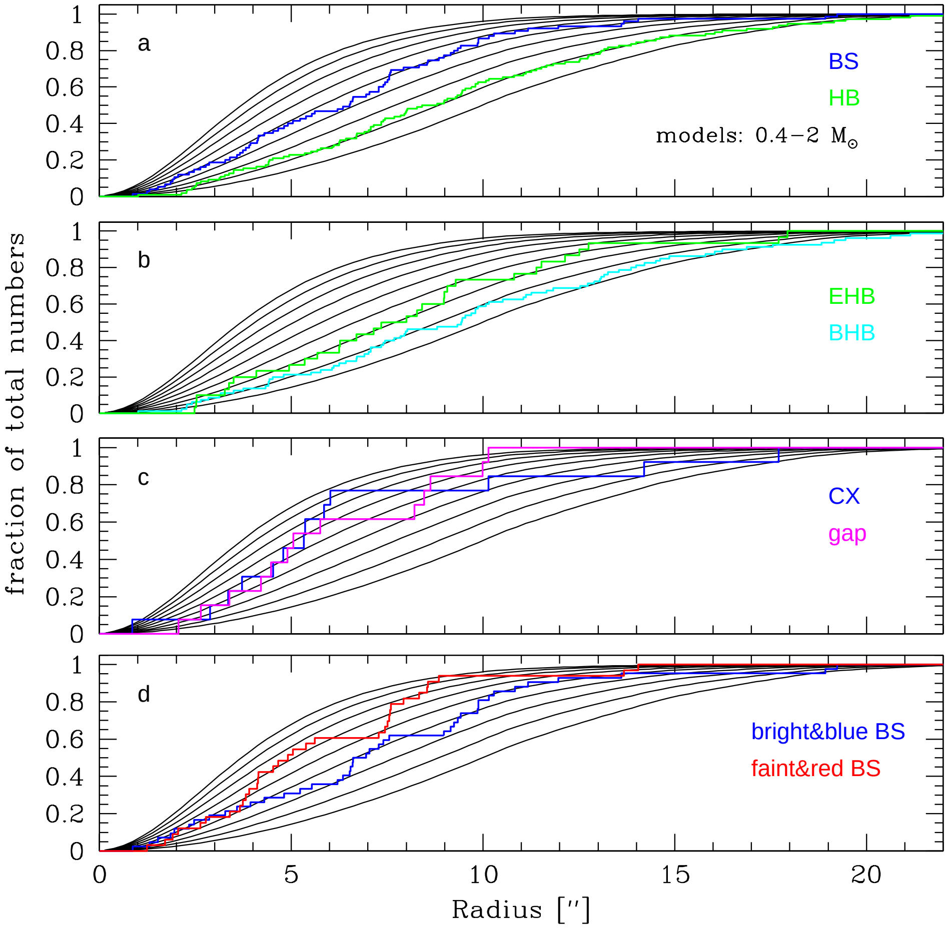

Figure 3.8: Cumulative radial distributions of various stellar populations, plotted along with theoretical King models of different average masses. The model masses range from $0.4 M_\odot$ (bottom black line in each panel) to $2 M_\odot$ (top black line), in steps of $0.2 M_\odot$. Panel (a): BS and HB populations. Panel (b): EHB and BHB stars. Panel (c): X-ray sources and gap sources brighter than NUV = 21.5 mag. Panel (d): bright and faint BSs. This is a reproduction of Figure 8 from Dieball et al. (2010).

that defines the core radius and adopt the core radius determined by Ferraro et al. (1999) of $r_{c\star} = 6\overset{''}{.}5$. The models were adapted to cover the actual field of view of the instruments, in order to maximise the radial coverage of the models.

Figure 3.8 shows the models, with the radial distributions of various populations over-plotted. The BS and HB stars' distributions agree well with models with typical masses of $1.2 M_\odot$ and $0.6 M_\odot$, which, in turn, agree reasonably well with the average masses expected from the location of the stars along the ZAMS and ZAHB. From panel (b), the EHB stars appear to be more massive than the BHB stars ($0.8 M_\odot$ compared to $0.6 M_\odot$). This is contrary to the expected average masses from the positions along the ZAHB, from which the BHB stars are estimated to have average mass of $0.58 M_\odot$, while the EHB stars should have masses $\lesssim 0.51 M_\odot$. Note that the KS test showed that the radial distributions of these two populations are not statistically significant, however. Panel (c) shows the X-ray sources and brighter gap sources. Both populations have characteristic dynamical masses $> 1 M_\odot$, but a more accurate estimate is not possible from these models. This mass estimate is consistent with Heinke et al. (2003), who found an average X-ray source mass of $1.2 \pm 0.2 M_\odot$. Finally, panel (d) shows the two groups of BSs, as described above. From the mass distribution along the ZAMS, the bright BSs are expected to be more massive than the fainter ones, with average masses of $1.34 M_\odot$ for the bright, blue BSs and $1.04 M_\odot$ for the fainter, redder sources. By contrast, panel (d) of Figure 3.8 indicates that the fainter BSs have masses $\approx 1.4 M_\odot$, while the brighter ones are less massive at $\approx 1 M_\odot$. In order to use radial distributions to estimate masses, however, one has to assume that the populations are in thermal equilibrium. This is not the case for the bright BSs if the “kick” scenario described above is true.

3.1.8 Conclusions

In this section I have described an FUV and NUV study of the GC M 80. The analysis was led by Dr. Andrea Dieball, although I was involved, and the resulting catalogue formed the basis of the variability study described in the next section.

The catalogue was created using FUV and NUV images, which were astrometrically tied to the Tycho-based system. The Tycho-based WCS used here is more accurate than the systems used in previous attempts to estimate the position of the cluster centre, so a new estimate was determined from the NUV catalogue.

The CMDs show a variety of stellar populations. The horizontal branch can be split into BHB and EHB stars, and both the FUV - NUV and V - I CMD reveal gaps in the horizontal branch. Only one candidate blue hook star was found. The numbers of gap and white dwarf sources are in line with theoretical predictions.

A previous study by Ferraro et al. (1999) suggested that M 80 contains a large, centrally concentrated BS population. Seventy-five BSs were found in our study, which is not remarkable when compared to the catalogue for M 15, which covers a similar field of view. Overall, the BSs were among the most centrally concentrated populations, but, surprisingly, the fainter and redder BSs were found to be more centrally concentrated than the brighter and bluer ones (with marginal statistical confidence). This is unexpected, since bright, blue BSs are thought to be the younger and more massive group. One possible explanation is that BSs get a kick during formation and move outwards to regions where the relaxation time-scale is longer than the typical age of a bright BS, but shorter than that of faint BSs. In that case, bright BSs would not have had time to settle (back) towards the cluster core. In Section 4.5.1, I investigate the blue straggler population of NGC 6752, for comparison with this result.

Source positions were compared to the *Chandra* X-ray source catalogue from Heinke et al. (2003), to search for counterparts to X-ray sources. Once the X-ray positions were corrected to match the Tycho-based WCS, it became clear that the position of the famous nova, T Sco, which was discovered in 1860, matches with that of the brightest X-ray sources in the cluster, CX 01. Furthermore, the object responsible for the nova was recovered in the FUV - NUV catalogue. It was found to be a dwarf nova, and one of the brightest and bluest FUV sources in the cluster. Another one of the X-ray sources, CX 07, was already known to be associated with a DN (Shara & Drissen, 1995); the FUV counterpart to this source was also recovered. Both of these sources are studied in more detail in Section 3.4.3 as part of the variability study. Five further X-ray sources were found to be associated with WD or gap sources in the FUV - NUV catalogue and are classified as likely CVs.

3.2 A Far Ultraviolet Variability Survey

In Section 3.1, I discussed a far ultraviolet study of M 80. In the rest of this chapter, I discuss a variability study based on this survey. Three stars were discovered which exhibit significant variability, the most interesting of which is an RR Lyrae star in the core of the cluster. This star, which I call TDK 1, was observed around the peak of the light curve in the FUV observations, manifesting a high-amplitude (> 3 mag), luminous ($L_{\rm UV} \simeq 6 \times 10^{34}$erg s^{-1}), short-duration ($t \lesssim 5$ hours) FUV brightening. Further investigation using archive data shows that it is also variable in optical wavebands, but the data coverage is not sufficient to determine the period of the variation. The other two new variables discovered in this survey are another possible RR Lyrae and an SX Phoenicis star. I also discuss in more detail the FUV counterparts to two known variables: the famous nova T Scorpii (T Sco) and the known dwarf nova DN 1 (Shara & Drissen, 1995).

Table 3.7: UV and optical data used to study the variable source TDK 1. The first column gives the camera used, followed by the filter (column 2), the number of images taken (column 3), the date of observation (column 4) and the individual exposure time (column 5).

Camera	Filter	N_{images}	Obs. Date	Exp. Time [sec]
ACS/SBC	F165LP	8	2004 September 11	310
ACS/SBC	F165LP	24	2004 September 12	323
ACS/SBC	F150LP	8	2004 September 20	310
ACS/SBC	F140LP	8	2004 September 26	310
ACS/HRC	F250W	8	2004 October 07	298
WFPC2	F439W	4	1994 October 05	300
WFPC2	F439W	2	1996 April 05	30
WFPC2	F555W	4	1996 April 05	23
WFPC2	F656N	3	1997 August 29	1300
WFPC2	F675W	3	1997 August 29	260

3.3 The Observations and Data Analysis

3.3.1 The Ultraviolet Data

The UV survey described in Dieball et al. (2010) and Section 3.1 required a single, deep image for each filter, so individual images taken using each filter were combined to give master images. By contrast, the individual images were needed to search for variability. For the variability study, a total of 48 FUV images were used, all obtained using the ACS in the Solar Blind Channel (SBC). These consisted of 32 images taken with the F165LP filter in four consecutive orbits, and one orbit (eight images) with each of the F150LP and F140LP filters. A further eight images were taken in one orbit using the F250W filter with the ACS/HRC. The images were all taken at the same pointing. Table 3.7 gives an overview of the UV data.

The 32 F165LP images, obtained within a 5.5 hour period, were used in the search for variable sources. Any source that was detected in enough images to be reliably investigated for variability should have been detected in the master image, meaning that source detection was not necessary; I was able to simply use the catalogue created using the master images, as described in Section 3.1.2. I used the FUV source catalogue as input to `daophot` (Stetson, 1991) running under `IRAF` in order to perform photometry on each individual F165LP image. The same parameters as described in Section 3.1.2 were used, but I kept the position of the input coordinates fixed (rather than using recentring routines).

For each source I derived a reduced χ^2 value relative to a constant brightness model. The χ^2 value evaluates how well set of measurements matches the expected values. It is given by

$$\chi^2 = \frac{1}{n}\sum_{i=1}^{n}\frac{(O_i-\mu)^2}{\sigma_i^2},$$

where O_i is an observed value, μ is the expected or model value, σ_i is the error on the measured value and n is the number of degrees of freedom. In this case, μ is the weighted mean of the source's magnitude measurements, σ_i is the error given in the `daophot` output, and $n = (\text{number of measurements} - 1)$.

In principle, this value reflects the likelihood that a source's magnitude does not change over the 32 measurements. However, the photometric errors produced by `daophot` (σ in the equation above) tend to be overestimated for faint sources and underestimated for bright sources. As shown in Figure 3.9, this causes the reduced χ^2 value to decrease monotonically towards fainter (mean) magnitudes, as the photometric error increases. One cannot, therefore, simply assume that any source with a reduced χ^2 value above a certain limit must be varying.

Instead, I compared the reduced χ^2 value for each source to its mean FUV magnitude (see right panel of Figure 3.9) and looked for sources whose χ^2 was significantly larger than that of other sources of comparable brightness. The red line in the right panel of Figure 3.9 indicates the χ^2 values above which I expect to find 0.1% of sources (for simplicity, this selection line was produced by assuming that the χ^2 value at a given magnitude is Gaussian distributed), equating to 2 expected outliers in the catalogue of 2345 sources. There were three sources which had χ^2 values higher than this line, and these sources are highlighted in Figure 3.9. As shown in the left panel of Figure 3.9, the photometric errors of these sources (red points) give no indication that they are remarkable compared to other sources of similar brightness. The χ^2 value, at least for sources 2234 and 2324, are not exceptional compared to the catalogue as a whole; it is only when one plots the χ^2 value against magnitude that they begin to stand out. The three outlying sources were investigated in further detail, along with two previously known variable sources, T Sco (see Section 3.1.5.1) and DN 1 (Section 3.1.5.2). Table 3.8 gives their positions and magnitudes, and, in Figure 3.10, the parts of the master FUV and NUV images that include the five sources investigated in this section are shown.

One of the outlier sources, TDK 1, showed the strongest evidence of brightness variations. Figure 3.11 shows the FUV image of TDK 1 when it is brightest (left) and faintest (right).

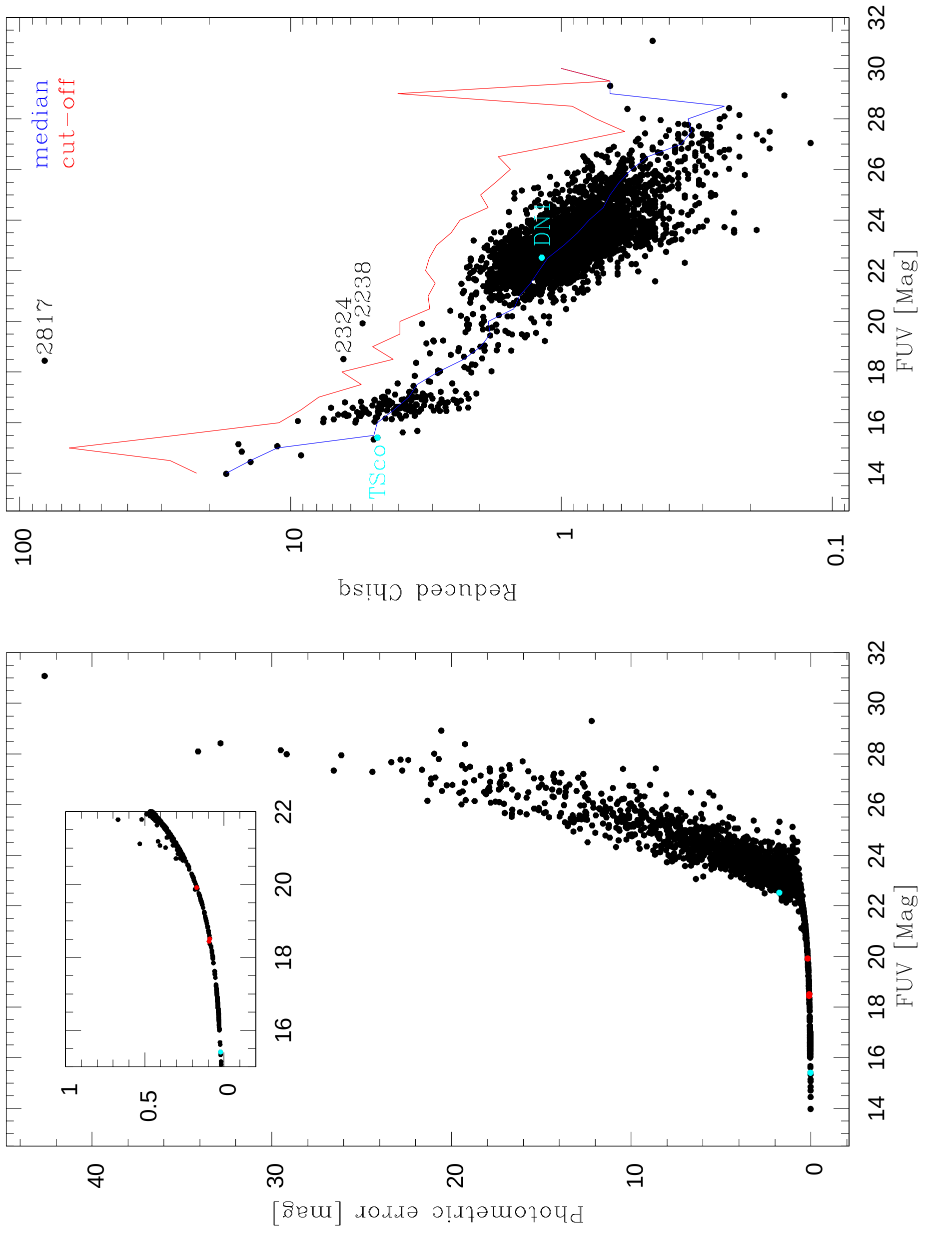

Figure 3.9: Left: the photometric error increases towards fainter magnitudes. Inset: the three variable sources (red points) do not appear to be remarkable in the plot of magnitude versus photometric error. Right: reduced χ^2 value for each source in the FUV catalogue, compared to its mean magnitude. The most significantly variable sources are highlighted. Note that χ^2 was determined using the actual magnitudes (in STMAG), but they are plotted on a log scale. The blue line shows the median χ^2 in the magnitude bins of width 0.5 magnitude. The red line indicates the cut-off; sources above this line were investigated for variability. Also marked (cyan points) are the two known variable sources, T Sco and DN 1.

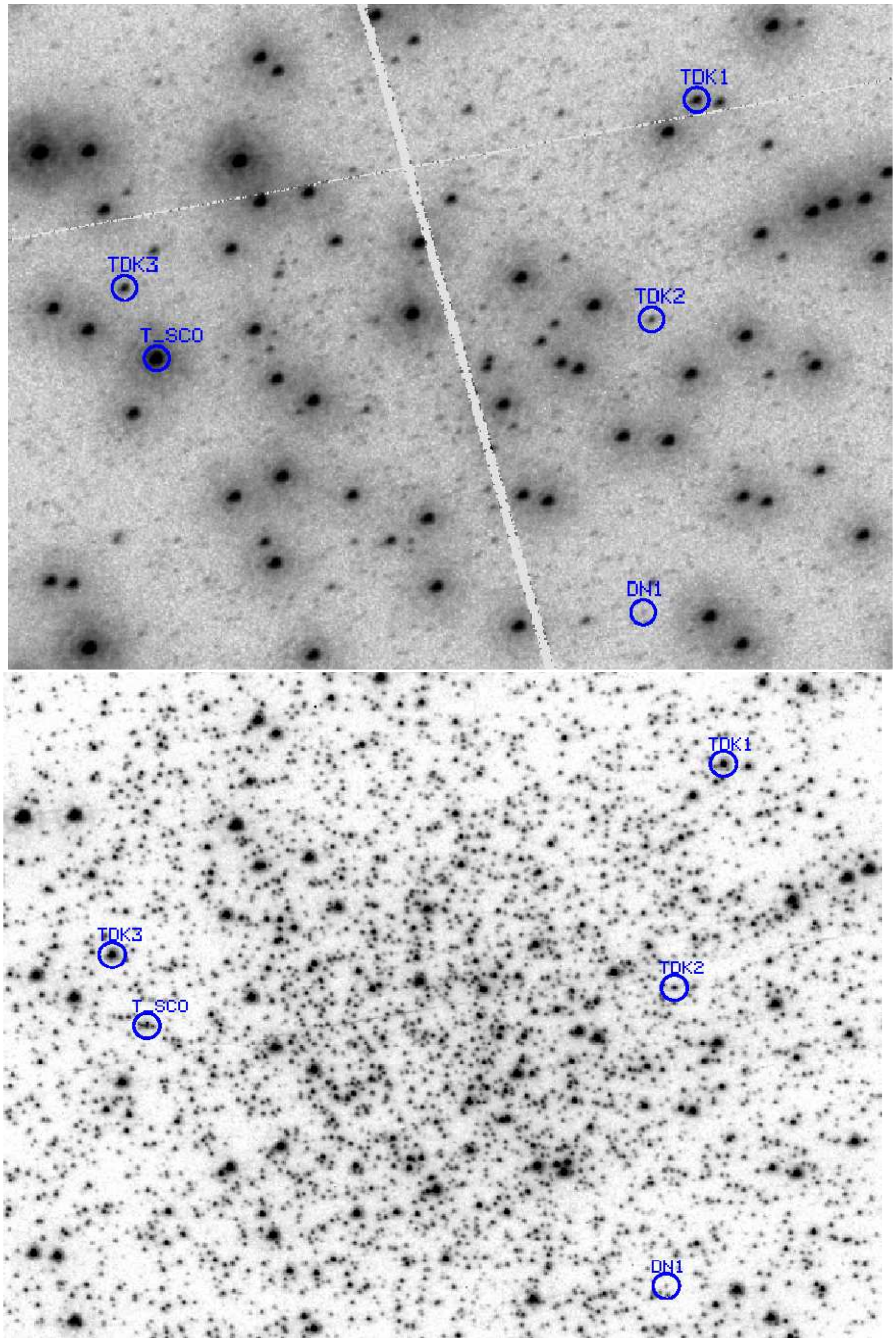

Figure 3.10: Portion of the combined FUV (top) and NUV (bottom) image showing the five variable sources discussed in this section. North is up and East is to the left.

Table 3.8: Positions of the variable sources TDK 1, 2 and 3, as well as DN 1 and T Sco. The first column is the source name, followed by the FUV ID number. Columns 3 and 4 give the source position in RA and DEC coordinates. Columns 5 to 8 give the FUV and NUV magnitudes and corresponding photometric errors as derived from `daophot`. Column 9 gives the ID number of the optical counterpart taken from Piotto et al. (2002), followed by the optical magnitudes (as reported by Piotto et al. 2002) in columns 10 and 11. Note that the magnitudes given are calculated from the master image in each filter and are thus subject to variability intrinsic to the source.

1 ID	2 ID_{FUV}	3 RA [hh:mm:ss]	4 DEC [deg:mm:ss]	5 FUV [mag]	6 σFUV [mag]	7 NUV [mag]	8 σNUV [mag]	9 ID_{piotto}	10 B_{piotto} [mag]	11 V_{piotto} [mag]
1	2817	16:17:02.104	-22:58:29.23	18.209	0.014	18.045	0.005	2710	16.217	16.360
2	2238	16:17:02.164	-22:58:33.24	19.981	0.032	19.703	0.011	2172	19.015	19.028
3	2324	16:17:02.861	-22:58:32.65	18.593	0.016	17.403	0.003	1450	16.594	16.226
DN 1	1387	16:17:02.176	-22:58:38.59	22.578	0.120	21.869	0.055	*	*	*
T Sco	2129	16:17:02.818	-22:58:33.94	15.444	0.005	19.247	0.008	*	*	*

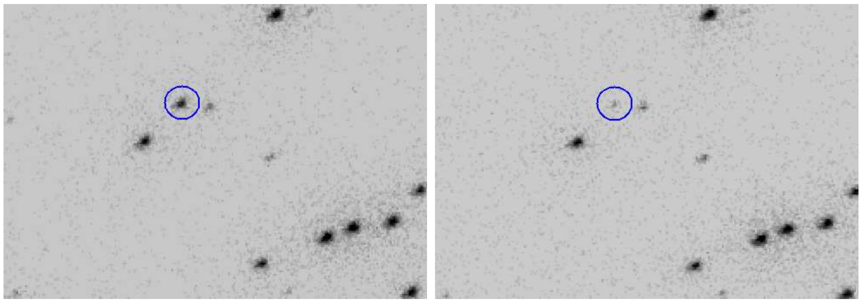

Figure 3.11: The variable source, TDK 1, at the brightest (left) and the faintest (right) that was seen in the FUV observations. North is up and East is to the left. Note that the difference in brightness shown between the left and right images is an underestimate of the actual variation: the high state magnitude is an underestimate of the peak brightness, due to a gap in the data at this point; the low state magnitude is not the true low state, as the source was still growing fainter when this observation occurred.

3.3.2 The Optical Observations of TDK 1

As mentioned above, TDK 1 is highly variable, brightening by more than 3 magnitudes during the FUV observations. In order to gather more information about this source, I analysed additional data of the core region of M 80. Table 3.7 gives an overview of all the data used to study TDK 1, including the filters used, and the observation dates and exposure times. The additional data, from the *HST* archive, was taken with the WFPC2 and included six images taken with the F439W filter, four images taken in F555W, three images in the narrow-band Hα filter F656N, and three images in the broad-band Hα filter F675W. Figure 3.12 shows TDK 1 as it appears in individual images taken with each of these other filters.

Photometric measurements of all stars in the field were not required for the variability study. In fact, in order to determine whether TDK 1 is variable in other wavebands, absolute photometry of TDK 1 was not needed. Instead, I performed relative photometry using nine non-varying stars of similar magnitude for comparison. In each data set, the sources were identified and photometry was performed on the individual images. In each case, a 3 pixel aperture and a small sky annulus of 5 – 7 pixels was used. Although the core of M 80 is very crowded (particularly in the optical images), TDK 1 and the nine stars chosen for comparison are bright and relatively isolated, so an aperture of 3 pixels was a good compromise between trying to include most of the light from the source and avoiding flux from neighbouring stars. The same photometry procedure was followed as for the FUV images, but published aperture corrections from Holtzman et al. (1995) were used. For the narrow-band Hα data, the aperture correction is not included in the list published by Holtzman

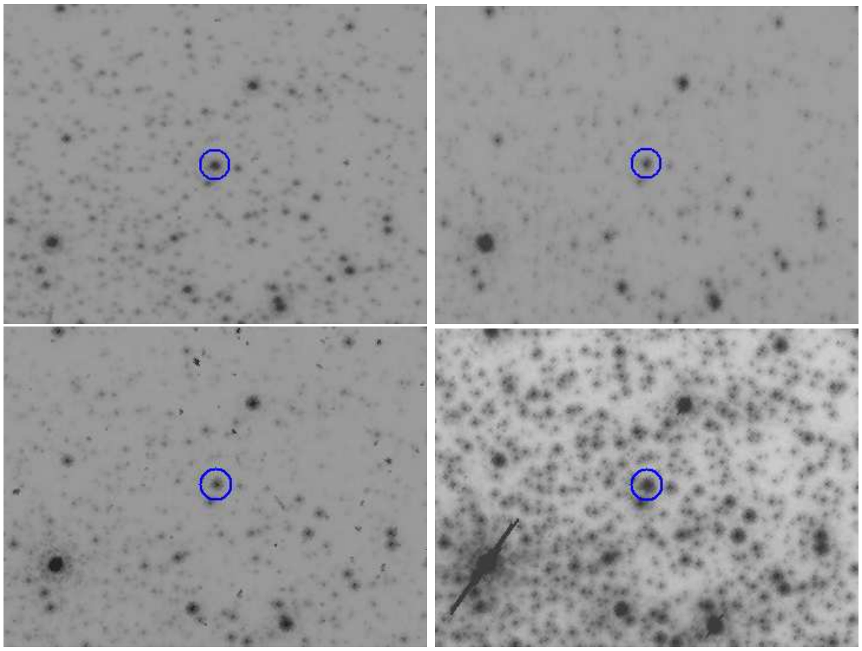

Figure 3.12: The variable source, TDK 1, as seen in the F439W (top left), F555W (top right), F656N (bottom left) and F675W (bottom right) filters. North is up and East is to the left.

et al. (1995), so I estimated the correction using the values given for the bracketing filters (in wavelength space). Henceforth, the STMAG system is used, except for the optical magnitudes in Table 3.8 and Figure 3.15, which are taken from Piotto et al. (2002) and are Johnson magnitudes.

3.4 FUV Variable Sources in the Core of M 80

The three objects highlighted in Figure 3.9 exhibited significant, short-term variability in the FUV survey of M 80. This is interesting, considering the fact that I defined outliers based on the reduced χ^2 above which I expect to find two outliers. Two other known variable sources, T Sco and DN 1, were found to have counterparts in the FUV catalogue. In this section, I discuss the light curves of these sources, as well as the spectral energy distribution (SED) of the most interesting source, TDK 1.

During the course of this investigation, I found that the brightest sources exhibit trends on the time-scale of *HST*'s orbit, possibly due to telescope breathing leading to changes in the point-spread function (PSF). Figure 3.13 shows the light curves of three examples of bright sources which demonstrate this trend. To quantify the systematic effect, I found the best-fitting gradient to each orbit of each of these light curves and then used the average gradient for each orbit in order to detrend all of

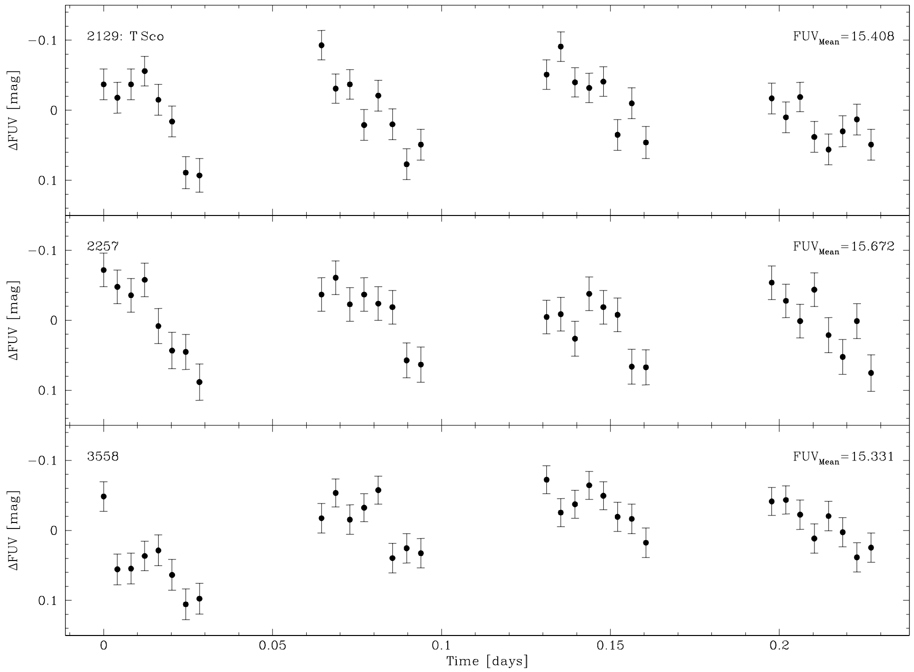

Figure 3.13: Light curves for three of the brightest FUV sources in the catalogue. All three show a periodic effect on a time-scale which matches the orbital period of *HST*. I used the best-fit lines to each orbit of these light curves to detrend all other light curves shown in this chapter.

the light curves shown throughout this chapter.

3.4.1 TDK 1

In this section I will discuss the results of the investigation into TDK 1 and present evidence that this source is an RR Lyrae star. As described in Chapter 2, RR Lyrae stars are pulsating HB stars which exhibit periodic variability with amplitude 0.2 – 2 mag at optical wavelengths. Although many of these stars have been observed in near-infrared and optical wavelengths and the form of the light curve in these ranges is well-established, very few have been well observed at wavelengths shorter than $\sim$ 3000 Å. Among the examples of short wavelength observations of RR Lyraes, Bonnell & Bell (1985) and Fernley et al. (1990) observed a selection of RR Lyrae stars using the *International Ultra-Violet Explorer* in the range 2000 – 3000 Å, and Downes et al. (2004) discovered 11 RR Lyrae stars in the core of the GC NGC 1851 using FUV observations taken with STIS, on-board *HST*. Wheatley et al. (2005) presented the first observation of an RR Lyrae star in which an entire cycle was covered simultaneously with FUV, NUV and optical instruments. The variation in apparent magnitude is much more extreme at shorter wavelengths (Wheatley et al. (2005) predict FUV amplitudes of up to ~ 8 magnitudes). This makes FUV observations a potentially useful tool for identifying new RR Lyrae (or similar) stars, so the lack of UV observations of RR Lyrae stars is surprising. One should note, however, that the FUV magnitudes of RR Lyrae stars away from maximum brightness are very faint compared with optical and near-infrared values, so observations long enough to include an entire period or fortuitous observations of maxima would be required to allow such variables to be recognised in FUV data sets.

The number and type of RR Lyraes present in a GC is related to the metallicity (and Oosterhoff classification) of the cluster (see Chapter 2). Previous studies of variable sources in M 80 have attempted to classify the cluster according to Oosterhoff's criteria, but small number statistics have meant that it has never been convincingly determined. Until recently, only six RR Lyrae were known in M 80, of which 4 were RR ab, making M 80 a borderline Oosterhoff II cluster. Kopacki (2009) raised the totals to 7 RR ab and 8 RR c, with an RR c fraction of 53%, confirming the Oosterhoff II classification. This is consistent with other classification methods. For example, Alcaino et al. (1998) and Cavallo et al. (2004) found an iron abundance of $[\mathrm{Fe/H}] \simeq -1.7$ dex for M 80.

3.4.1.1 Variability

The FUV light curve for TDK 1 is displayed in Figure 3.14. The left, middle and right panels show the data obtained with the F165LP, F150LP and F140LP filters, respectively. The star increased in brightness from 18.3 mag to 17.2 mag within the first orbit (≈ 40 min) and then faded over the next three orbits (≈ 4.5 hours) to ≈ 20 mag. Due to the gap in the data between the consecutive orbits, the peak in the light curve was not observed. Simple linear fits to the light curve on either side of the peak (shown in Figure 3.14) suggest that TDK 1 might have reached FUV $\simeq 16.7$ at its peak. The F150LP and F140LP data sets suggest that the low brightness state of the source corresponds to around FUV ≈ 21 mag, giving a difference between the minimum (F150LP data) and maximum brightness (F165LP data) of about 4 magnitudes. This is consistent with the FUV amplitudes of RR Lyraes, as demonstrated by Downes et al. (2004) and Wheatley et al. (2005). Furthermore, the shape of the F165LP light curve is asymmetric - the rise to maximum brightness is considerably steeper than the decline that follows - indicating that TDK 1 is an RR Lyrae star of type ab. Comparing TDK 1's light curve with a phase-folded light

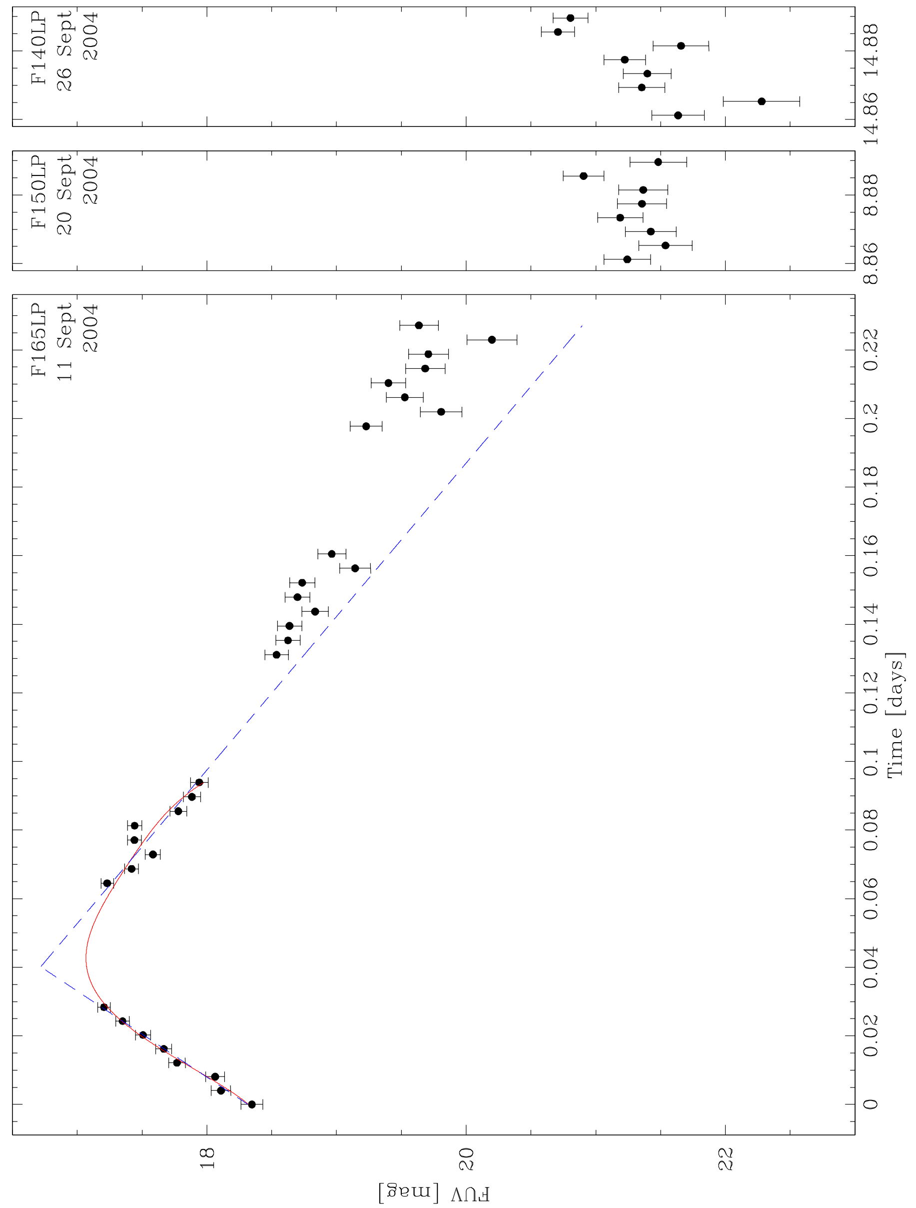

Figure 3.14: Light curve for the variable source TDK 1, including all FUV data. The lines show simple polynomial fits to the first two orbits of data, illustrating the range of possible peak magnitudes of the outburst. The blue dashed line shows straight line fits to each of the first two orbits' points, while the solid red line shows a 5th order polynomial fit to the data. Left panel: a set of 32 images taken using the F165LP filter. Middle panel: eight images taken approximately 9 days later using the F150LP filter. Right panel: a set of eight F140LP images taken around 15 days after the first image.

Table 3.9: Magnitude variations in TDK 1 compared to the average values for a collection of nine comparison stars.
[a] Note that in the F555W filter image, only eight comparison stars were used as the ninth was outside the field of view.

Filter	RMS Variation [mag]		Peak to Peak Variation [mag]	
	TDK 1	Comparison	TDK 1	Comparison
F439W	0.24	0.02	0.62	0.07
F555W[a]	0.07	0.03	0.18	0.07
F656N	0.11	0.01	0.26	0.02
F675W	0.04	< 0.01	0.10	0.01

curve based on the data given by Wheatley et al. (2005), and adjusting the period of the folded light curve until the slopes around the peak were aligned, I estimate that TDK 1's period is ≈ 0.84 days. This is consistent with the conclusion that TDK 1 is a type ab RR Lyrae.

Photometric measurements based on the available *HST* optical imagery (see Section 3.3.2) show, as might be expected, that TDK 1 is variable in all wavebands. Table 3.9 shows the RMS and peak-to-peak magnitude variation for TDK 1, and the average values for the nine comparison stars. TDK 1 exhibits more variability than the comparison stars in all bands.

The variability in all wavebands makes placing TDK 1 on a CMD something of a challenge. Figure 3.15 shows the CMD of M 80, with the variable sources highlighted. For TDK 1, the UV magnitudes are the averages from the orbits in which it was faintest in order to minimise the effect of variability on the CMD position. In the UV CMD, TDK 1 is located close to the BHB/BS region, as might be expected for an RR Lyrae star, although its position is still subject to error due to variability even when the data taken during the peak of the light curve is excluded. The optical CMD was created using data from Piotto et al. (2002), in which the average magnitudes from two F439W and four F555W observations were used (observations taken in 1996; see Table 3.7); Piotto's location for TDK 1 is indicated with subscript P. To minimise the effect of variability in these two wavebands, I also plot the 'low-state' position of TDK 1, marked TDK 1_{L}. To do this I used the faintest data point in each band and converted them to Johnson magnitudes using the `IRAF/STSDAS` package `synphot` (as mentioned previously, Piotto et al. (2002) uses Johnson magnitudes). This brings TDK 1 much closer to the BHB. As explained in more detail in Section 3.4.1.2, TDK 1 was not exactly at minimum brightness in these observations, so this is still not the true low state; furthermore, the F555W data was taken at a

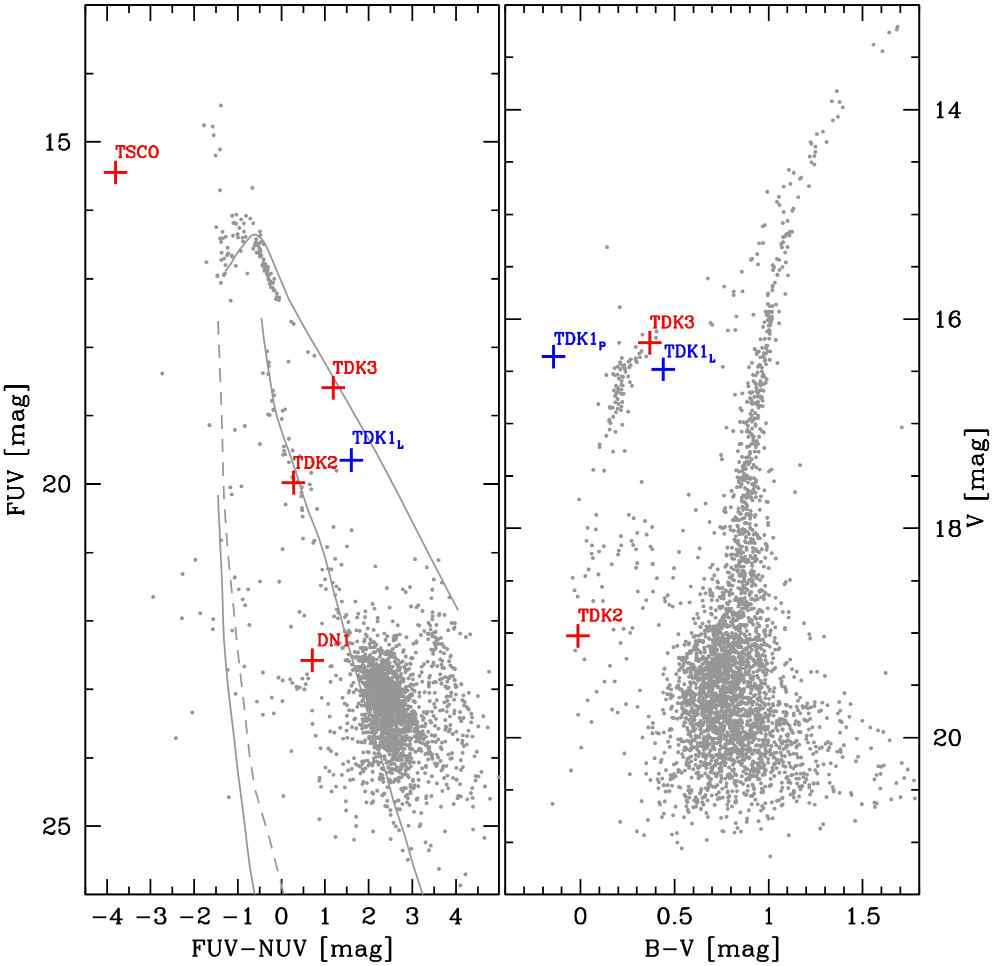

Figure 3.15: Left: FUV - NUV CMD of the core of M 80, with the variable sources marked in red, except for TDK 1 which exhibited large variation in FUV magnitude and is highlighted in blue. Note that the FUV magnitude for TDK 1 is the average value from the last eight data points of the F165LP data only, to indicate the minimum brightness location. Note that this is still an overestimate of the FUV brightness since the system was still declining from its outburst during the last F165LP orbit. All other magnitudes are derived from the master image of the given filter (F165LP and F250W). For reference, a theoretical WD and He WD cooling sequence (dashed and solid line towards the blue), a zero-age main-sequence (middle), and a zero-age HB track (reddest/brightest) are included (see Section 3.1.4 for details). Right: optical CMD of M 80 with the optical counterparts of the variable sources marked, as in the Piotto et al. (2002) catalogue. Piotto et al. used master images created from two F439W and four F555W observations. For TDK 1 I also include the position obtained using only the faintest data point in each band, which gives, as close as possible with this data, the 'low-state' position (see text for details). This point is marked TDK 1_L, whereas Piotto et al.'s position is TDK 1_P.

brighter point in the cycle than the F439W data, making the source appear redder than if they were taken simultaneously. I conclude that, subject to errors due to variability, TDK 1's position on both CMDs is consistent with it being an RR Lyrae.

3.4.1.2 The Spectral Energy Distribution

In order to confirm that TDK 1 is an RR Lyrae star, as suggested by the variability in the FUV and optical wavebands, I constructed the spectral energy distribution (SED) of TDK 1. In doing so I tried to use observations taken when the star was close to minimum brightness ('low state'), but one should be aware that lack of truly low-state observations mean the SED produced is still not actually that of minimum brightness. For the FUV and NUV, I used the average magnitude from the faintest orbits; for F165LP only the average magnitude from the last eight data points is included, in order to minimise the effect of the large magnitude variation in the FUV light curve. The F165LP data could have been excluded entirely, but tests of this showed that it did not significantly change the results. As shown in Table 3.9, there was some variability present in each of the optical data sets. In fact, TDK 1 is undergoing brightening in the 1996 observations (the last two F439W images, followed by the four F555W images; see Table 3.7) and again in the 1997 observations (three F675W observations followed by three F656N observations). To minimise the effect of this variability I simply used the faintest magnitude measurement for each filter, to give the best possible approximation of a low-state SED. While I expect that this will introduce errors of a few tenths of a magnitude in each waveband, it is sufficiently accurate to get an idea of the shape of the SED and to estimate parameters such as temperature and radius.

TDK 1's SED is shown in Figure 3.16 (black data points). Due to the complex combinations of variability and intrinsic measurement errors, error bars are not shown on the plot. Each point is plotted at the pivot wavelength for the corresponding filter. The SED is consistent with a single star. Figure 3.16 also shows that the source appears brighter in the narrow-band F656N filter than in the bracketing optical broadband data points in the SED, suggesting an Hα excess.

Synthetic photometry was carried out for models in the Kurucz (1993) grid using the `IRAF/STSDAS` package `synphot` and assuming a distance of 10 kpc, a reddening of $E_{B-V} = 0.18$ mag and a metallicity of $[\mathrm{Fe/H}] = -1.75$ dex. The synthetic SEDs were then fit to the data using a least squares fitting method, in which each point was given equal weight. I found that TDK 1's SED can be reasonably described by a star with $T_{eff} \simeq 6700$ K, $R \simeq 4.2\,R_{\odot}$, and $\log g \simeq 3.0$, giving a mass of $M \simeq 0.6\,M_{\odot}$.

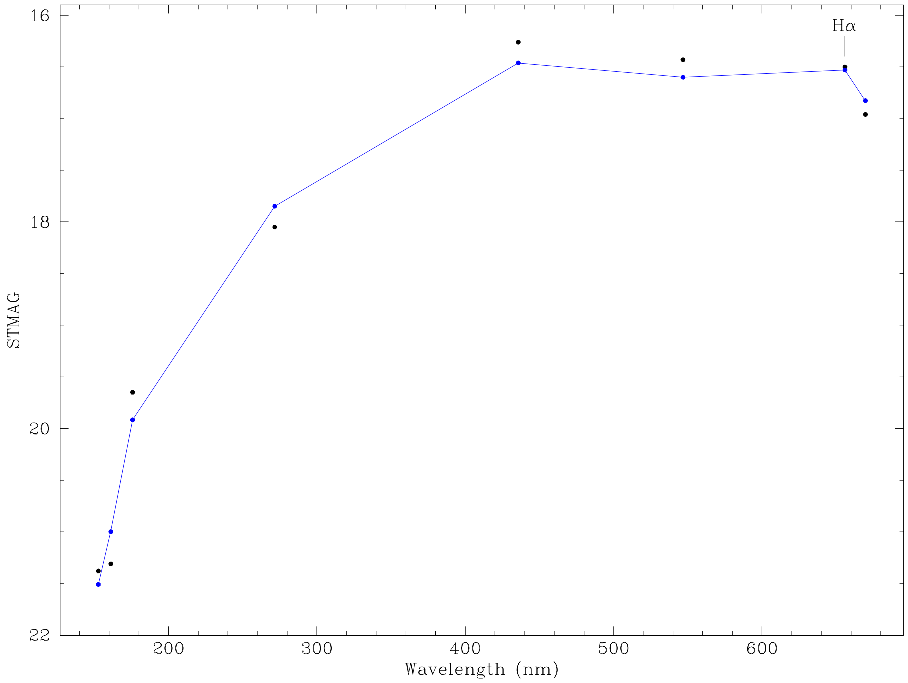

Figure 3.16: Spectral energy distribution (SED) for TDK 1 (black points), along with the best model fit to the data (blue line), which has $T_{eff} \simeq 6700$ K, $R \simeq 4.2 R_{\odot}$, and $\log g \simeq 3.0$, leading to a mass estimate of $M \simeq 0.6 M_{\odot}$. Error estimates are not shown, due to the complex combinations of variability and intrinsic measurement errors involved.

These values are all within the acceptable range for RR Lyrae stars.

In order to estimate the contribution of the Hα line to the underlying stellar spectrum, I repeated the synthetic photometry including an Hα line of varying equivalent width (EW). The best fit model suggests a marginally significant ($\approx 2\sigma$) Hα line with EW$\simeq$ 20 Å, without significantly affecting the other fit parameters. The best fit SED, including an Hα line with EW$\simeq$ 20 Å, is plotted as a blue line in Figure 3.16. The presence of an Hα line can be explained by the fact that TDK 1 is undergoing a brightening phase during the F656N and F675W observations; type ab RR Lyrae are known to exhibit Hα emission during rising light (Smith, 1995). This adds further evidence that TDK 1 is a type ab RR Lyrae.

As shown in Figure 3.16, the models do not fit well to the observed slope in the optical data; the data in this region shows a much steeper slope (i.e. bluer colour) than the models. As the pivot wavelengths for the optical filters are quite similar, the colours indicated by comparisons between these filters are sensitive to, and can be easily distorted by, variability. The variability observed in the optical filters (a few tenths of a magnitude) is, therefore, sufficient to account for the very blue optical colour of TDK 1. A key feature of the data's SED is that the maximum brightness (the 'turnover') occurs at $\lambda = 439$ nm; the luminosity decreases as one moves to shorter wavelengths. Models with $T_{eff} \geq 7500$ K continue to increase in luminosity to wavelengths shorter than $\lambda = 439$ nm. Fitting the slope of the optical data alone gives a far higher T_{eff} than my best-fit model. In fact, such a model over predicts the brightness in the UV by such a large amount that it becomes impossible to account for the observed UV magnitudes. Furthermore, it is the data taken using the F140LP and F150LP filters that best represent the brightness in the low-state. Thus, T_{eff} can be well determined by ensuring that the model is a good match to the magnitudes obtained using the F140LP and F150LP filters.

The radius of the best-fitting model is determined by the flux normalisation required to the distance to M 80: decreasing the model's radius makes the model fainter at all wavelengths, and increasing it makes the model brighter. As previously mentioned, the least-squares fitting method indicated that the data was best fit using a model with $R \simeq 4.2 R_{\odot}$. This is quite well constrained. For example, changing the model radius by $\Delta R = 0.2 R_{\odot}$ changes the model brightness by ≈ 0.1 mag at all wavelengths, while a change of $\Delta R = 0.5 R_{\odot}$ leads to changes in magnitude of ≈ 0.3 mag. Thus, small changes in R lead to quite large shifts in the model.

It is worth noting that while T_{eff} is well constrained by the turnover in the SED, and the radius by the flux normalisation to M 80's distance, the global shape of the SED can be reasonably well described using a range of $\log g$ values. I experimented with models using $\log g$ values from 2.5 to 5, and while $\log g = 3.0$ gave the best fit based on the least-squares fitting method described above, the best-fitting model created with each of the other tested values for $\log g$ corresponded to a reasonable (i.e. physically plausible) estimate for T_{eff} and R. Thus, a slight change in input T_{eff} or R has a huge impact on the model SED, whereas large changes in $\log g$ only have relatively small effects. RR Lyrae stars have been noted to have a wide range of $\log g$ values (see Peña et al. 2009 for examples of RR Lyraes with $\log g$ values of 1.3 to 2.2 at minimum brightness, and 2.5 to 3.5 at maximum), so while the best-fit value of $\log g \simeq 3$ found here is reasonable, I caution that variability in the data limits the ability to make a reliable determination of $\log g$ and, consequently, the mass. By contrast, the temperature and radius estimates should be fairly reliable.

I conclude, based on the radius and temperature obtained from the SED and the suggestion of Hα excess during the brightening phase, that TDK 1 is indeed an RR Lyrae star of type ab. The $\log g$ and mass values obtained are also consistent with this explanation, but are less reliable as they are affected more significantly by slight variations in magnitude.

3.4.2 Other FUV Variable Sources: TDK 2 and 3

In this section, I briefly discuss the nature of two other sources in the FUV catalogue that showed strong signs of variability.

3.4.2.1 TDK 2

The light curve of TDK 2 (source 2238; see Figure 3.17) shows short-term variability with a peak to peak variation of ≈ 1 mag. I used the Lomb-Scargle (LS) method to determine the period of the magnitude variations. The Lomb-Scargle method calculates the spectral power as a function of angular frequency (i.e. the power of fitting the data as a function of period of oscillation). A distinct advantage of the Lomb-Scargle method over other least-square fitting techniques is that it can be used on data with differing sampling intervals, and is weighted by data point, rather than time interval (Lomb, 1976; Scargle, 1982; Press et al., 2007). Figure 3.18 presents the Lomb-Scargle periodogram, which suggests a period of 55.42 ± 0.66 minutes.

The horizontal lines on Figure 3.18 indicate various confidence levels. These were calculated using a Monte Carlo simulation in which 20,000 fake data sets were created by shuffling the magnitude measurements, keeping the time intervals the same. This method assumes that peaks in the data are uncorrelated, so shuffling the measurements in this way creates a white-noise time series. Periodograms were created for each of these fake data sets, and the confidence levels determined based on how many fake data sets had Lomb-Scargle power higher than a given value. The 90% confidence level, for example, is defined to be the level above which Lomb-Scargle power peaks were found in 10% of fake data sets. The 55.42 ± 0.66 minute period indicated for TDK 2 is significant at $> 3\,\sigma$.

Figure 3.19 displays the light curve of TDK 2, folded on this period. The solid line shows a sinusoidal fit created using a least-squares fitting method, which suggests a semi-amplitude of 0.45 mag. The position of TDK 2 is in the BS region in both the UV and optical CMDs (Figure 3.15). This, together with the period of ≈ 1 hour, suggests that TDK 2 is an SX Phoenicis star.

Further observations would be needed to determine additional information about TDK 2. The short time span over which the observations were taken in this survey limit the ability to determine the period to a high level of accuracy, or detect the presence of multiple pulsation modes. If a pulsation spectrum could be obtained, parameters such as mass and metallicity may be found and could lead to

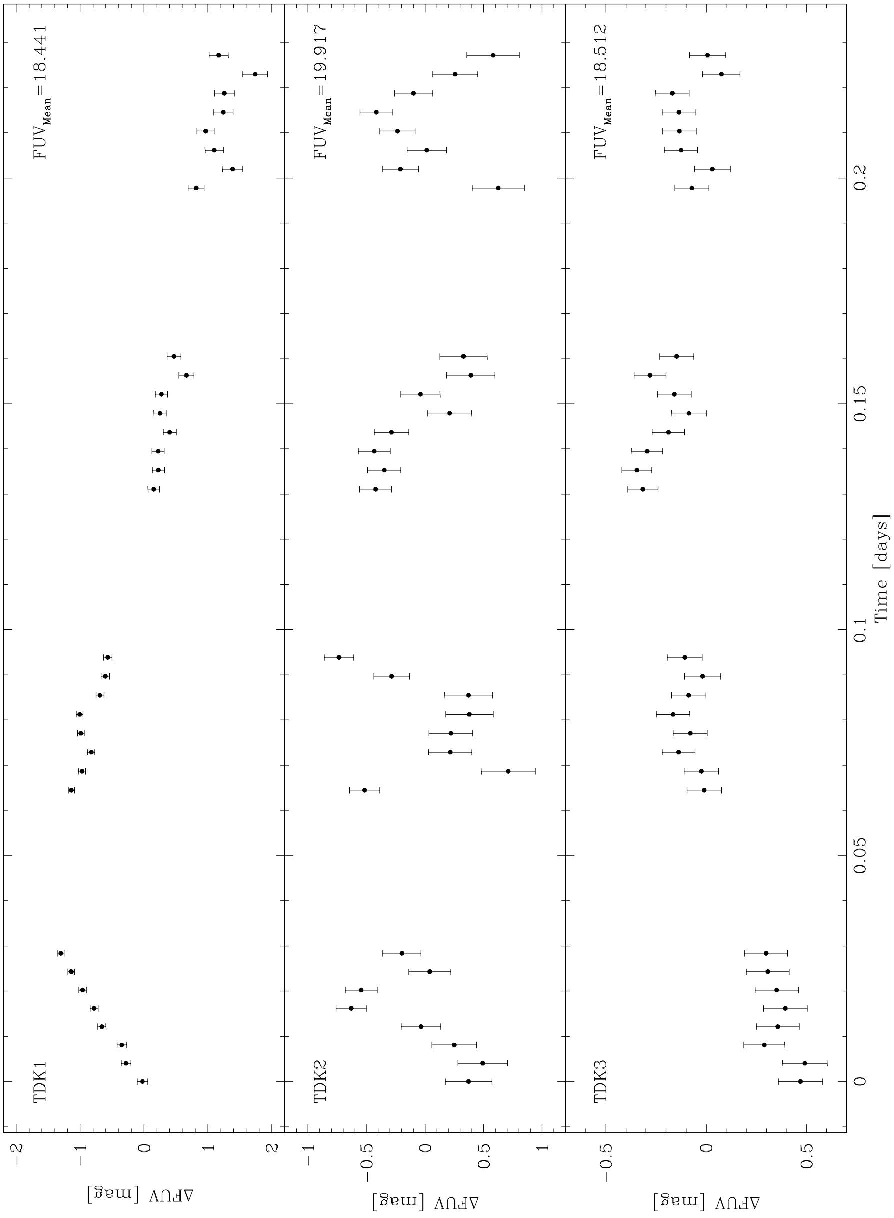

Figure 3.17: Light curves for the variable sources identified in M 80, showing the variation from the mean magnitude ($\Delta\mathrm{FUV} = \mathrm{FUV} - \mathrm{FUV}_{Mean}$). All light curves are detrended to remove trends due to the period of *HST*'s orbit which are visible in the light curves of the brightest sources.

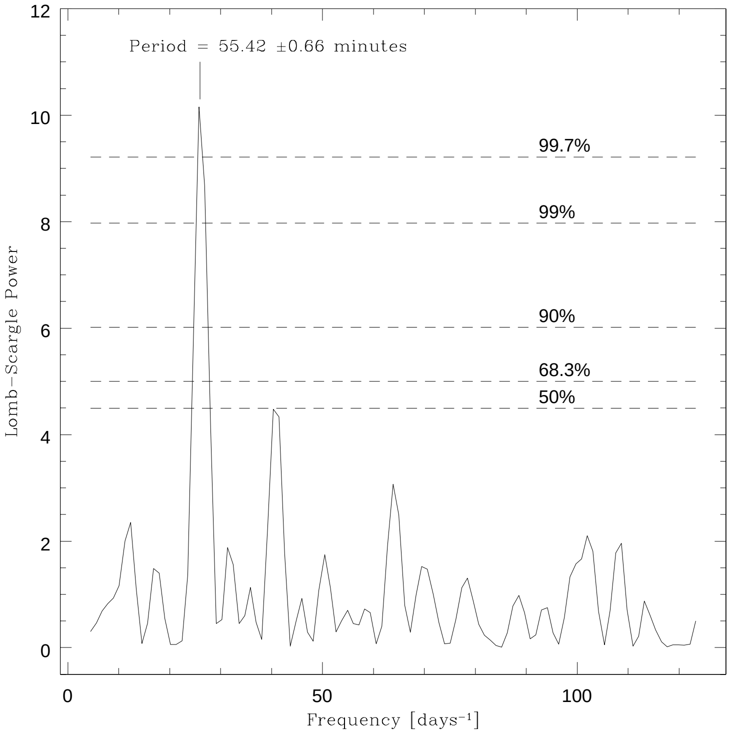

Figure 3.18: Lomb-Scargle periodogram of TDK 2. The strongest peak is significant at a level $> 3\,\sigma$ and corresponds to the period of 55.42 minutes.

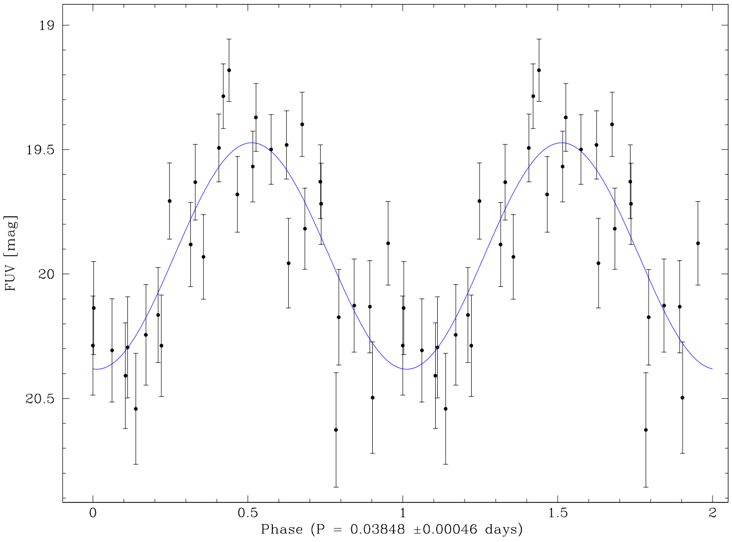

Figure 3.19: Light curve of variable source TDK 2, folded with a period of 0.03848 days, or 55.42 minutes. Two complete cycles are shown. The blue line is a sinusoidal fit with the same period and an amplitude of 0.45 mag.

new insights into the formation and evolution of SX Phoenicis stars and BS stars in general.

3.4.2.2 TDK 3

The light curve of source TDK 3 (source 2324), shown in Figure 3.17, displays variability with $\gtrsim 0.5$ mag semi-amplitude, with a period significantly longer than the timespan of the FUV observations. The data coverage is not good enough to attempt a period determination for such long-term trends. Based on its position in the CMDs (Figure 3.15), however, TDK 3 is likely to be another RR Lyrae star or a Cepheid variable. The shallow rise in brightness makes a type ab RR Lyrae scenario unlikely, but TDK 3 could be a type c RR Lyrae star. RR c stars have shorter periods than RR ab ($\lesssim 0.5$ days) and FUV amplitudes of 1.3 – 3.3 mag (Downes et al., 2004), while Cepheid variables have periods on the order of days, with FUV amplitudes of around 1 magnitude (Smith 2005; Moffett et al. 1998). Both of these are plausible explanations for the light curve of TDK 3; the data does not allow us to constrain the parameters of TDK 3 well enough to determine which is the most likely option.

3.4.3 Previously Known Variable Sources

In addition to the sources described above, which were identified in the variability search of the FUV data described in Section 3.3.1, the FUV counterparts to two well-known variable sources, the classical nova T Sco and the dwarf nova DN 1 were also investigated.

3.4.3.1 T Scorpii

Source number 2129 in the FUV catalogue was identified (see Section 3.1.5.1) as the counterpart to the classical nova T Scorpii (T Sco). T Sco is one of only two novae known to have occurred along the line of sight to a GC. Source 2129 was not strongly variable in the FUV observations. In fact, after subtracting trends due to PSF changes over *HST*'s orbital period that were present in the light curves of the brightest sources (see Figure 3.13), T Sco exhibits only very little evidence for real variability in the FUV data, with amplitude < 0.1 magnitudes. The (detrended) light curve is shown in the top panel of Figure 3.20. Bruch (1992) suggests typical nova flickering amplitudes of a few tenths of a magnitude, and one would expect more variation in the bluer wavebands, but this was not detected. The Lomb-Scargle

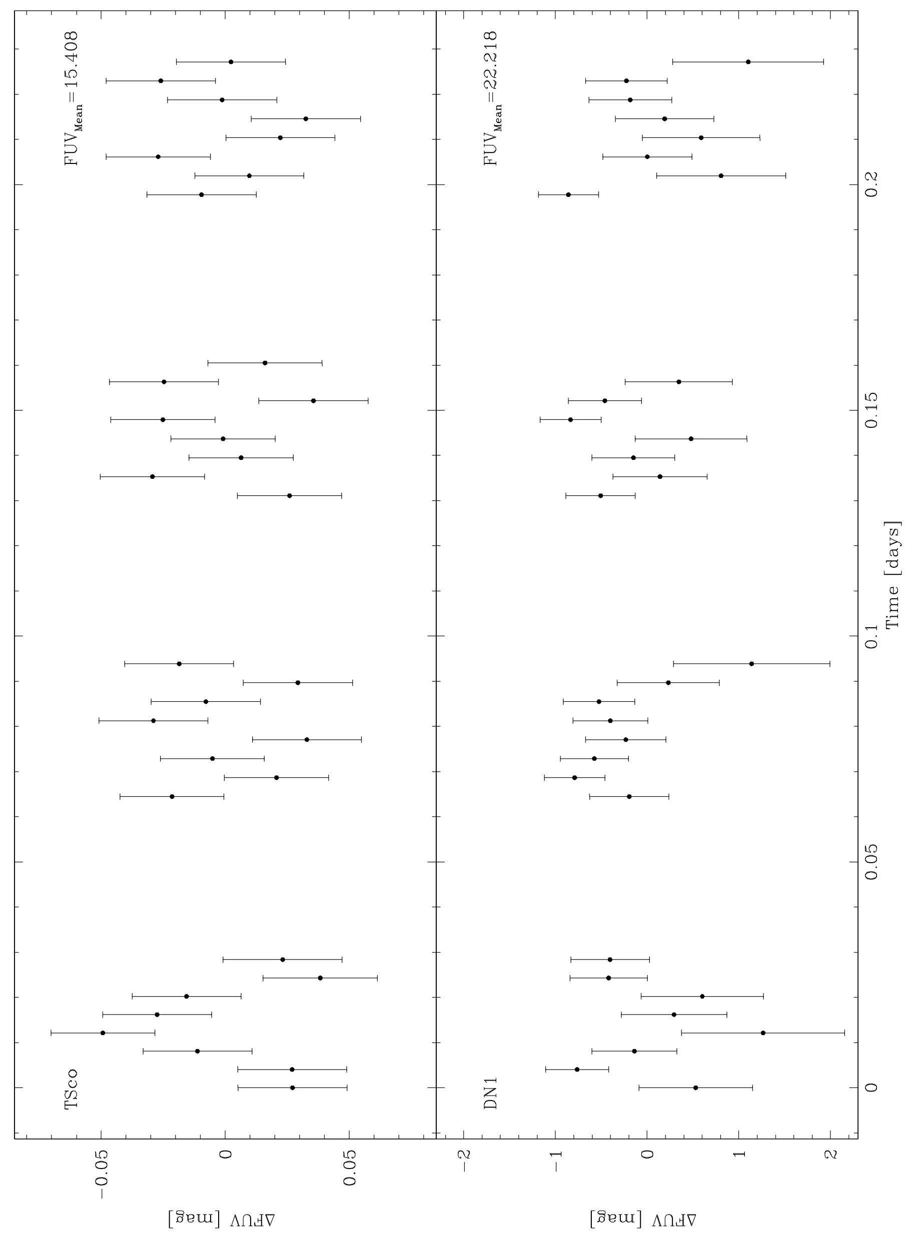

Figure 3.20: Light curves for the previously known variable sources, T Sco (top panel) and DN 1 (bottom), showing the variation from the mean magnitude (ΔFUV = FUV − FUV$_{Mean}$). All light curves are detrended to remove trends due to the period of *HST*'s orbit which are visible in the light curves of the brightest sources.

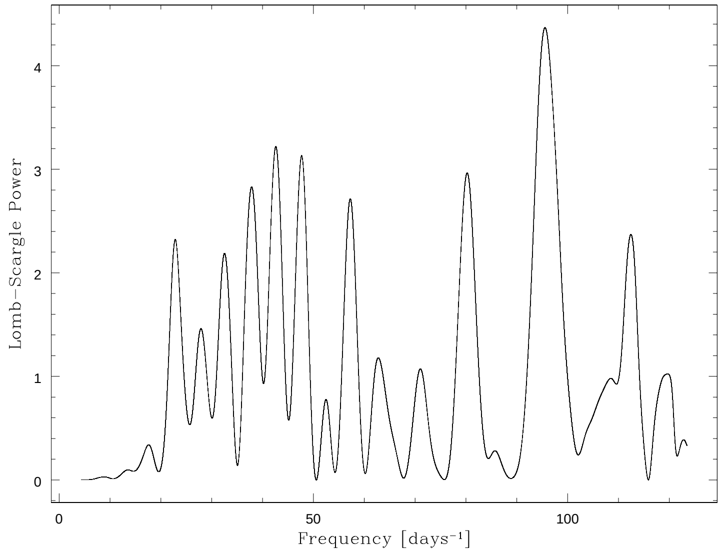

Figure 3.21: Lomb-Scargle periodogram of T Sco, after the light curve has been detrended to remove small changes in magnitude due to PSF changes over the course of *HST*'s orbit. No significant peaks are found (simulations show that the 50% confidence level is at LS power = 4.36).

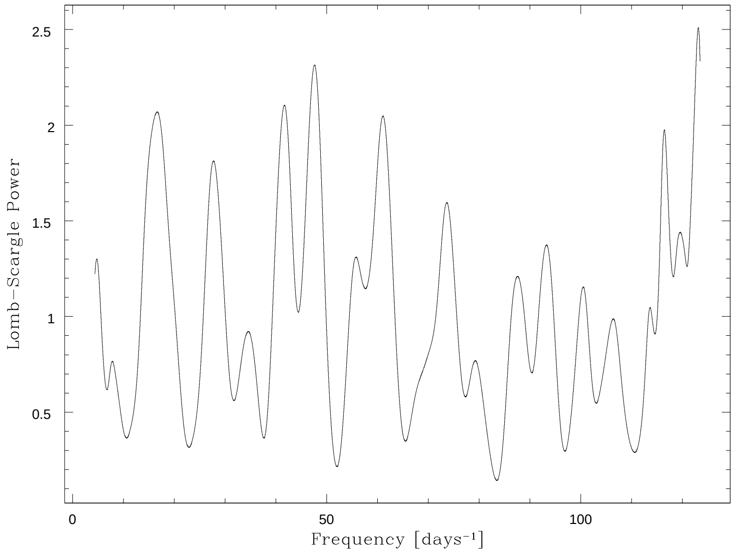

Figure 3.22: Lomb-Scargle periodogram of DN 1. No significant peaks are found (simulations show that the 50% confidence level is at LS power = 4.26, far higher than any peaks shown here), indicating that the source does not exhibit detectable periodic variability in our FUV data.

power spectrum for the detrended light curve is shown in Figure 3.21 and demonstrates that no strong indication of periodic variability is apparent in the light curve. Simulations show that the highest peak in T Sco's power spectrum is significant at a level of only $\approx 50\%$ (50% of simulations created using the method described in Section 3.4.2.1 exhibited peaks higher than LS power $= 4.36$). I note, however, that T Sco, as one of the brightest sources in the catalogue, was used in the determination of the trend based on *HST*'s orbit, which was later subtracted from all light curves. Some intrinsic variability might, therefore, have been removed during this process (see Figure 3.13).[2]

As described in Section 3.1.5.1, T Sco was among the brightest objects in the FUV catalogue ($\mathrm{FUV} = 15.44 \pm 0.01$ mag). It was also the bluest object in the catalogue; in fact, it was found to be unphysically blue ($\mathrm{FUV} - \mathrm{NUV} = -3.81$ mag, while an infinite temperature blackbody would have $\mathrm{FUV} - \mathrm{NUV} = -1.8$ mag), so must have decreased in brightness in the month between the FUV and NUV observations. This implies that T Sco was in a high state during the FUV observations. I suggest, therefore, that the flickering normally observed in the light curves of classical novae might be suppressed because the source was caught in a high state. Suppressed flickering in high states has been observed in DNe (Warner, 2003). Bruch (1992) also shows that lower amplitude flickering is seen in novae with lower inclinations, so the lack of observed flickering seen here suggests that the system has a very low inclination. The faint FUV magnitudes when at its faintest makes searching for flickering away from the outburst difficult; if it were achievable, measurements of flickering elsewhere in the light curve would allow for more certain conclusions to be drawn. The implied FUV outburst is interesting, as one cannot rule out the possibility that T Sco is, in fact, a recurrent nova. However, this is probably a far-fetched explanation for the inferred FUV brightening; a DN eruption, for example, is a much more likely scenario.

3.4.3.2 DN 1

Source number 1387 in the catalogue is the relatively faint FUV counterpart to X-ray source CX 07 identified by Heinke et al. (2003). This source is also DN 1, one of the DNe found by Shara & Drissen (1995). As shown in the bottom panel of Figure 3.20 and in Figure 3.22, this source did not exhibit detectable variability in the

---

[2] Note that although T Sco is expected to show flickering, the magnitude variation shown in Figure 3.13 demonstrates that any such variability is very small. Intrinsic T Sco variability included in the 'detrending' step will not, therefore, have a detrimental effect on the conclusions drawn regarding variability in other sources.

FUV data. The LS-power indicated in Figure 3.22 is far smaller than even the 50% confidence level (which has LS power $= 4.26$). However, DN 1 is a relatively faint FUV source (FUV $= 22.578$), so instrumental errors are large (up to 0.9 mag) and limit the ability to draw any conclusions about the presence or absence of flickering or orbital variations.

3.5 Summary

I used 32 individual FUV images from the UV survey of the core region of M 80 (Dieball et al., 2010) to search for variable sources in the FUV catalogue. Three sources exhibit strong evidence for variability.

TDK 1 (source 2817) is an RR Lyrae in the core of the cluster. The FUV light curve shows that it was observed from around 40 minutes before to 4.5 hours after maximum brightness, and further investigation using archival WFPC2 optical data showed that it is clearly variable in all wavebands. Its SED is reasonably well described by a star of temperature $T_{eff} \approx 6700\,\mathrm{K}$ and radius $R \approx 4.2\,R_{\odot}$, consistent with expected parameters for an RR Lyrae star. More specifically, I show that TDK 1 is a type ab RR Lyrae, based on the asymmetry in the FUV light curve. This is the eighth RR ab found in M 80, and brings the fraction of c type RR Lyrae in the cluster to 50%, exactly in line with the expected fraction for an Oosterhoff II ('metal-poor') cluster (see Section 2.2).

This is only the third cluster in which an RR Lyrae star has been identified based on UV observations (others were found in NGC 1851 by Downes et al. (2004) and M 15 by Dieball et al. (2007)). UV surveys can be useful tools in identifying RR Lyraes and similar objects, particularly in the cores of (dense) GCs where optical surveys are seriously hampered by crowding.

TDK 2 (source 2238) is likely an SX Phoenicis star with a period of 55.42 ± 0.66 minutes and amplitude of ≈ 1 mag. TDK 3 (source 2324) might be another RR Lyrae or a Cepheid.

Finally, I discussed two well known variable sources, T Sco and DN 1, the FUV counterparts of which were recovered in the FUV survey. T Sco exhibited surprisingly little flickering in the FUV data, possibly because it was caught in a high state compared with the NUV observations a month later. DN 1 is a very faint UV source, so photometric errors dominate over any possible intrinsic flickering or other variations.

After this paper was completed, I found that TDK 1 and TDK 3 are included in

Kopacki's variability survey of M 80 (Kopacki, private communication). Kopacki agrees with my classification of these two sources as RR Lyrae stars. A preliminary summary of his results, including periods but not including coordinates or finder charts for the sources, is given in Kopacki (2009).

Now my own suspicion is that the Universe is not only queerer that we suppose, but queerer than we can suppose.

J. B. S. HALDANE (1892 – 1964)

4

The Globular Cluster NGC 6752: The Colour-Magnitude Diagram and Radial Profile

NGC 6752 is a nearby cluster with a very dense core. Despite being relatively close and frequently studied, the dynamical status of NGC 6752 remains a subject of debate.

In the next three chapters, I present an in-depth, multi-wavelength study of NGC 6752, performed using NUV, U- and V-band data taken with the Wide Field Camera 3 (WFC3) on-board (*HST*), as well as FUV observations using the Space Telescope Imaging Spectrograph (STIS), and the V- and I-band catalogue from the ACS Survey of Galactic Globular Clusters (Sarajedini et al., 2007).

This chapter introduces the study, explaining the creation of the catalogue, the CMD and the different types of stars found within the cluster. I will also investigate the puzzling dynamical status of the cluster by constructing a radial density profile and comparing this to King (1966) models. The work in this chapter has been published, forming part of Thomson et al. (2012).

Table 4.1: Summary of observations used in this survey. The individual images from the FUV and NUV wavebands are listed, as these were used to search for variability. In all other cases, total exposure times are listed.

Instrument/ Detector	Field of View	Plate Scale [″/pixel]	Waveband	Filter	Exposures	Date
STIS	25.″1 × 25.″3	0.025	FUV	F25QTZ	10 × 650 s	2001 March 30
					3 × 900 s	2001 March 30
WFC3/UVIS	162″ × 162″	0.04	NUV	F225W	6 × 120 s	2010 July 31
					6 × 120 s	2010 August 7
					6 × 120 s	2010 August 21
WFC3/UVIS	162″ × 162″	0.04	U	F390W	1590 s	2010 May 1 - 5
WFC3/UVIS	162″ × 162″	0.04	B	F410M	1800 s	2010 May 1 - 5
ACS/WFC	202″ × 202″	0.05	V	F606W	142 s	2006 June 24
ACS/WFC	202″ × 202″	0.05	I	F814W	162 s	2006 June 24

4.1 The Globular Cluster NGC 6752

The globular cluster NGC 6752 lies at a distance of 4 kpc, has a reddening of $E_{B-V} = 0.04$ mag, and a metallicity of $[\mathrm{Fe/H}] = -1.54$ dex (Harris, 1996; 2010 edition).

Despite the fact that NGC 6752 is a relatively close GC, there is no consensus on its dynamical status. NGC 6752 has an unusually high mass-to-light ratio, suggesting an excess of low-luminosity stars in the core (D'Amico et al., 2002), which might be evidence of a central BH. Further evidence for the existence of BHs in GCs might be found in the stellar radial distributions. A central BH is likely to produce a central cusp in the surface brightness profile, which can be distinguished from a core-collapsed profile by its slope (Baumgardt et al., 2005).

There has been much discussion in previous studies regarding whether or not NGC 6752 should be classified as core-collapsed. Ferraro et al. (2003a) found that the radial profile can only be modelled using a combination of two King (1966) profiles, which they interpret as an indication that it has undergone core collapse. However, other studies (e.g. Lugger et al. 1995) argued that the surface brightness profile is not inconsistent with a single King model. Noyola & Gebhardt (2006) produced surface brightness profiles for 38 GCs and found that NGC 6752 was the only GC previously reported as core-collapsed that did not show a central cusp. Like Lugger et al. (1995), they found that the central part of the surface brightness profile was flat.

The rest of this chapter is structured as follows. In Section 4.2, I describe the observations and data reduction. In Section 4.3, an analysis of the CMD is presented. In Section 4.4, I present a new estimate for the position of the cluster centre and investigate the dynamical status of the cluster as a whole. In Section 4.5, I examine the distributions of various stellar populations and estimate their characteristic mass. My conclusions are summarised in Section 4.6.

4.2 The Observations and Creation of the Catalogue

4.2.1 Observations

The data used in this survey come from three sources, summarised in Table 4.1. The instruments used in this survey are described in Appendix B.

First, the majority of this investigation deals with observations carried out using the UVIS detector on the WFC3 on-board *HST*, together with the F225W (NUV) and F390W (U-band) filters. The NUV data consist of 18 individual images of 120 s exposure time, which are used in the search for time variability (see Chapter 5). The U-band data set is comprised of 6 images with exposure times between 2 s and 880 s each, giving a total exposure time of 1590 s. I also include 3 exposures with the F410M filter with exposure times of 40 s and 880 s. These data are included in the discussion of optical counterparts to X-ray sources in Chapter 5, for completeness. The WFC3/UVIS has a field of view of $162'' \times 162''$ and a plate scale of $0\farcs04$/pixel.

Second, I used images taken with the Advanced Camera for Surveys (ACS) in the Wide Field Channel (WFC), which have total exposure times of 142 s with the F606W (V-band) filter and 162 s with the F814W (I-band) filter (PI. Sarajedini). The ACS has a larger field of view than the WFC3, at $202'' \times 202''$, but a slightly coarser plate scale of $0\farcs05$/pixel.

Finally, I also used FUV observations consisting of 13 individual exposures of 650 s or 900 s taken on 2001 March 30 with STIS on-board *HST* using the F25QTZ filter. This has a wavelength range of 1475 – 1900 Å. The STIS observations have a field of view of $25\farcs1 \times 25\farcs3$ and a plate scale of $0\farcs025$/pixel. This data set was used to perform time variability studies of sources in the core of the cluster, the results of which are discussed in Chapter 5.

4.2.2 Photometry

Astrometry and photometry were performed on the WFC3 data (NUV, U- and B-band) using the WFC3 module of `DOLPHOT` (Dolphin, 2000). `DOLPHOT` is a modified version of `HSTPhot` (Dolphin, 2000). It is a point-spread function (PSF) fitting package specifically designed for stellar photometry on *HST* images. The package identifies sources above a given threshold and performs photometry on individual (flat-fielded, dark subtracted) frames, giving the output in a pixel coordinate system derived from a reference image. `DOLPHOT` applies charge-transfer efficiency corrections and reports final magnitudes for each source in each individual image, as well as an overall measurement, in VEGAMAG.

The VEGAMAG magnitude system is one defined such that Vega has magnitude 0 at all wavelengths. The magnitude of a star in VEGAMAG is calculated using

$$\mathrm{VEGAMAG} = -2.5 \times \log_{10}\left(\frac{\mathrm{F}_{star}}{\mathrm{F}_{Vega}}\right),$$

where F_{Vega} is the current flux of Vega.

First, master images to be used as reference images for the World Coordinate

System (WCS) were made for each of the WFC3 data sets (one per filter), by combining the individual frames using `multidrizzle` running under `PyRAF`[1].

The `DOLPHOT` procedure *wfc3mask* was used to mask the pixels identified as saturated or bad by the *HST* pipeline. The `DOLPHOT` tasks *splitgroups* and *calcsky* were used to divide the exposures into their component chips (so they can be aligned to the master image), and to create a sky image for each frame. To correct for changes in alignment between individual frames, a few reference stars were found in each individual image and the reference image, and *wfc3fitdistort* was used to determine how each individual frame related to the reference image. `DOLPHOT` was then used to perform photometry on each individual image, giving a catalogue in the coordinate system of the reference frame. I cleaned the resulting catalogues by removing sources which were deemed too sharp or too extended, as these are likely to be cosmic rays or background galaxies, or which were badly affected by the presence of nearby neighbours so that PSF-fitting could not be completed adequately. The resulting catalogues contained 14511 NUV, 27099 U-band, and 32780 B-band sources. The magnitudes of these sources were transformed from VEGAMAG to STMAG using the difference between the measured zeropoints (Kalirai et al., 2009).

The V- and I-band ACS data were taken from the ACS Survey of Galactic Globular Clusters (Sarajedini et al. 2007, Anderson et al. 2008; henceforth ‘the ACS Survey Catalogue’). This catalogue contains 52818 stars that were found in both the V- and I-bands.

As previously described, the FUV observations were performed using STIS. `DOLPHOT` does not work on STIS data because pixel area maps are not available. A consistent photometric process across all of the images was, therefore, not possible; a different approach to photometry had to be used when dealing with the FUV images. While PSF fitting is the better method in the crowded optical images, sources in the FUV are sparsely populated enough that aperture photometry is adequate.

The individual FUV exposures were aligned using the `IRAF` routine `imalign`, as image distortion coefficients are not available for these images (meaning that this step could not be performed using `multidrizzle`), and then combined using the `IRAF` routine `imcombine`. I used `daofind` (Stetson, 1991) running under `IRAF` to create an initial source list for the FUV master image. When using `daofind`, the user can specify values for the FWHM of the point-spread function (PSF), as well

---

[1] Note that this procedure is limited to combining a maximum of 15 frames by the capabilities of the *wfc3mask* routine of `DOLPHOT`, but this only affects the NUV data set as the U- and B-band data are made up of fewer individual exposures; this limit will not affect the outcome of the photometry.

as a search threshold. The FWHM is not necessarily the true FWHM of the detector, but rather a value chosen to minimise the number of false detections that are made, particularly at the edges of the image. The threshold is also a compromise: a higher threshold reduces the number of false detections (caused by noise at the image edges, multiple detections of bright stars, and false detections around saturation spikes), while a lower threshold means that more faint (real) sources are detected. While the automatic process gives a good initial source list, inspecting the image by eye allows the user to delete false detections and add missing, faint sources. This left 503 sources in the FUV catalogue.

I performed aperture photometry on the master FUV image using the `IRAF` routine `daophot` (Stetson, 1991). In using `daophot`, the user chooses two key parameters; the aperture radius and sky annulus. The aperture radius determines the size of the aperture considered for any given star. Too small a radius will result in some of the light being lost, particularly from brighter stars, but too large an aperture may include light from other stars, or background flux. The sky annulus, on the other hand, is used to measure the background flux which is later subtracted from the source's flux. Again, this must be carefully chosen. If the sky annulus is too small, light from the target star will be included with the background measurement, but if it is too large, it is likely to be affected by nearby stars. To avoid introducing errors caused by the high stellar density in the core, I chose a small aperture of 3 pixels and a sky annulus of $5-7$ pixels. To account for the small aperture and sky annulus, a few reference stars were used to determine correction factors. The reference stars were bright, isolated, and far enough from the edge of the chip that photometry could be performed using a larger radius and sky annulus. I performed photometry on these stars using a larger sky annulus of $50-60$ pixels and found the factor by which the flux changed in going from small to large annuli. I also used a range of aperture radii, and calculated the fraction of light enclosed at different distances. In using this method, I assumed that 100% of the source's light is enclosed in the largest annulus (60 pixel radius), but plots of encircled energy against radius indicate that this is reasonable. These correction factors were applied to all sources.

Once they had been corrected, the instrumental fluxes were converted to the STMAG system using

$$\mathrm{STMAG} = -2.5 \times \log_{10}(\mathrm{count\ rate} \times \mathrm{PHOTFLAM} \times \mathrm{apcorr} \times \mathrm{skycorr}) + \mathrm{ZPT},$$

where PHOTFLAM is the factor used to convert count rate into flux, apcorr is the aperture correction ($\mathrm{apcorr} = 1/\mathrm{encircled\ energy}$), skycorr is the correction from a

$5-7$ pixel sky annulus to a $50-60$ pixel one, ZPT is the zero point. In this case, PHOTFLAM is the average of the individual images used as input to `imcombine`, weighted according to their exposure time. The parameters used here are[2]

- PHOTFLAM $= 1.132155 \times 10^{-16} erg\, cm^{2} \text{Å}^{-1} counts^{-1}$,
- encircled energy $= 0.4759451113$,
- skycorr $= 0.953132393$,
- ZPT $= 21.1$.

4.2.3 Matching the Catalogues

In order to match the catalogues from the different wavebands, I first transformed all of the catalogues to the world coordinate system (WCS) of the master WFC3/NUV image. This has one of the largest fields of view of the images, but is not so crowded that locating matching sources becomes problematic. For each catalogue, I created a reference list of up to 16 sources (not all sources were visible in all images), which are easily visible in the image to be transformed and also in the NUV reference image. I then used the `IRAF` tasks `geomap` and `geoxytran` to determine the transformations required to shift the catalogues to the NUV WCS, allowing for shifts in the x and y directions, scale changes, and rotation. This gave a reasonable fit to the new WCS. I repeated the process using up to 48 reference sources to refine the transformations. The (RMS) residual errors in the transformations were small: 0.28 pixels (7 milli-arcsecond, mas) error in the FUV transformation, and a maximum of 0.11 pixels (4.4 mas) in the WFC3 and ACS catalogue transformations.

I searched for matches between all of the catalogues (noting that the ACS catalogue from Sarajedini et al. (2007) contains only sources that are visible in both

---

[2] After publication of this paper, it was discovered that one of the ten sources used to measure skycorr had an erroneous value. The actual result should be skycorr $= 1.03977603$. This error means that all FUV magnitudes should be very slightly lower (brighter). The effect is small; at $\mathrm{FUV}_{STMAG} \approx 20$ mag, $\Delta\mathrm{FUV}_{STMAG} \approx 0.03$ mag. In this chapter, this change would alter only the CMD in Figure 4.2 and the catalogue shown in Table 4.3. This does not impact any of the conclusions of this thesis or the published paper. At the time of writing, the paper is published with the erroneous measurement included; a decision on whether or not to publish an erratum has not yet been made. If an erratum is issued, the catalogue online will reflect the change and the erratum will include this note.

the V- and I-band), allowing for a 2 STIS pixel ($0\farcs05$) difference in the STIS and WFC3 positions, and a 1 WFC3 pixel ($0\farcs04$) difference between the various WFC3 catalogues and between WFC3 and ACS positions. Table 4.2 gives the number of matches found in each case. Note that only V- and I-band sources with a match in at least one of the WFC3 data sets are included. This gives a total catalogue of 39411 sources. The full catalogue is available in the on-line version of Thomson et al. (2012), and a portion of it is shown in Table 4.3.

Table 4.2 also gives the percentage and number of these matches that I expect to be spurious matches, found using the method from Knigge et al. (2002). The number of false matches expected when matching two catalogues depends on the number of matches found (n_{match}), the matching tolerance (i.e. the area of the image 'taken up' by a single source, πR_s^2), the area of the overlapping images ($A_{overlap}$, in pixels) and the number of sources in each catalogue (n_{s1} and n_{s2}). The number of expected false matches is then given by

$$n_{spurious} = P \times f \times n_{s2}$$

where

$$P = \frac{n_{s1} \times \pi R_s^2}{A_{overlap}}$$

is the upper limit on the probability of chance coincidences occurring (since some sources will overlap, the total area taken up by sources is actually less than $n_{s1} \times \pi R_s^2$), and

$$f = \frac{n_{s2} - (n_{matches} - n_{spurious})}{n_{s2}}$$

is the fraction of sources in image 2 without a real counterpart (so the equation given for $n_{spurious}$, above, is actually a quadratic equation).

When matching the FUV and NUV images, I calculated this value for the entire FUV field of view; for all other matches I used a circle centred on the cluster core (see Section 4.4.1) to represent the overlapping region. As the area used includes the core, where I expect to find the most spurious matches, the numbers quoted in Table 4.2 can be considered as upper limits on the expected percentage and number of false matches, since the outer regions will not contain as many spurious matches as these calculations predict. I note that the method used does not take into account the increase in stellar density towards the cluster centre.

Table 4.2: Number of matches between catalogues. The first two columns indicate the data sets being matched. The third column gives the number of matches found. The last two columns give the expected percentage of false matches and the number of expected false matches that this equates to.

Catalogues		N_{match}	$\%_{false}$	N_{false}
STIS/FUV	WFC3/NUV	492	3.84	19
WFC3/NUV	WFC3/U	12020	0.05	6
WFC3/NUV	WFC3/B	11883	0.06	7
WFC3/NUV	ACS/V&I	13494	0.03	4
WFC3/U	WFC3/B	22910	0.08	18
WFC3/U	ACS/V&I	24258	0.03	7
WFC3/B	ACS/V&I	23045	0.16	37

Table 4.3: Catalogue of all sources in the WFC3 field of view. The first column is the source ID number. Columns 2-5 give the source position in RA and decl. and image pixel coordinates (using the F225 'master' image). Column 6 is the FUV magnitude measured using `daophot`. Columns 7 and 9 give estimates of the FUV and NUV variability amplitude, defined to be the standard deviation of the source relative to its mean magnitude. Columns 8, 10 and 11 give the NUV, U- and B-band magnitudes derived using `DOLPHOT`. Columns 12 and 13 give the corresponding V- and I-band magnitudes from the ACS Survey Catalogue. The final column shows the source type found using the NUV - U or V - I CMDs and any further comments. Only 15 entries are listed here to demonstrate the catalogue's form and content. A machine-readable version of the full table is available in the on-line version of Thomson et al. (2012).

1	2	3	4	5	6	7	8	9	10	11	12	13	14
ID	RA [hh:mm:ss]	Decl. [deg:mm:ss]	x_{NUV} [pixels]	y_{NUV} [pixels]	FUV [mag]	σFUV [mag]	NUV [mag]	σNUV [mag]	U [mag]	B [mag]	V [mag]	I [mag]	Comments
8001	19:10:52.440	-59:59:05.81	2439.584	2354.241	...	...	18.929	0.060	16.642	16.503	16.451	16.804	RGB
8002	19:10:52.296	-59:59:05.88	2439.486	2381.566	...	...	20.366	0.101	18.751	18.594	18.742	19.153	MS
8003	19:10:57.678	-59:59:03.12	2439.706	1360.024	...	...	22.662	0.310	19.868	19.706	19.567	19.916	MS
8004	19:10:52.072	-59:59:06.01	2439.866	2424.109	24.014	1.002	19.639	0.051	18.256	18.267	18.376	18.855	MS
8005	19:10:52.136	-59:59:06.01	2440.693	2412.017	...	...	19.458	0.093	18.006	17.886	18.050	18.515	MS
8006	19:10:49.722	-59:59:07.26	2441.015	2870.224	...	...	20.386	0.061	18.746	18.655	18.770	19.229	MS
8007	19:10:51.289	-59:59:06.46	2441.085	2572.808	...	...	20.191	0.077	18.632	18.526	18.694	19.105	MS
8008	19:10:52.862	-59:59:05.66	2441.262	2274.257	...	...	18.476	0.043	17.156	17.062	17.308	17.802	MS
8009	19:10:47.418	-59:59:08.47	2441.816	3307.576	...	...	18.532	0.037	17.385	17.266	17.513	18.039	MS
8010	19:10:51.232	-59:59:06.53	2442.112	2583.698	...	...	19.567	0.044	18.265	18.126	18.323	18.812	MS
8011	19:10:49.680	-59:59:07.34	2442.489	2878.296	...	...	19.871	0.061	18.441	18.323	18.490	18.974	MS
8012	19:10:53.602	-59:59:05.33	2442.524	2133.886	...	...	17.912	0.026	14.248	14.036	13.648	13.881	RGB
8013	19:10:52.486	-59:59:05.91	2442.698	2345.726	21.428	0.174	21.685	0.187	...	...	...	...	MS
8014	19:11:00.147	-59:59:01.97	2442.849	891.5843	...	...	18.327	0.031	16.869	16.726	16.889	17.347	SGB
8015	19:10:51.167	-59:59:06.59	2442.784	2596.081	...	...	18.238	0.042	16.872	...	16.961	17.424	SGB

4.2.4 Improving the Astrometry

The standard world coordinate system (WCS) provided with *HST* data is based on the original guide star catalogue (GSC 1), with absolute position accuracy of $1-2''$. In order to compare my astrometric results to those in the literature (e.g. the position of the centre), it was necessary to improve the accuracy of the absolute astrometry. To do this, I used the third U.S. Naval Observatory CCD Astrograph Catalog (UCAC3; Zacharias et al. 2009). The astrometry provided in UCAC3 is on the Hipparcos (or Tycho) system and has astrometric errors of $15-20$ mas for stars in the $10-14$ mag range in V- and R-band.

I located 23 stars from the UCAC3 catalogue that could also be identified in the catalogue, and updated the astrometric solution for the WCS for each of the images. As in Section 4.2.3, I repeated this process using a further 70 sources, to get a more precise transformation. The RMS error between positions in the catalogue and the UCAC3 sample was $\approx 0\overset{''}{.}15$.

4.3 The Colour-Magnitude Diagram

The NUV - U and V - I CMDs for NGC 6752 are shown in Figure 4.1. Different stellar populations are highlighted: white dwarf (WD) candidates are shown in grey; blue stragglers (BSs) in purple; asymptotic giant branch (AGB) stars in dark red and ‘gap’ sources as orange crosses. As in the M 80 study (see Section 3.1.4), the CMD boundaries between the populations were judged by eye. Again, moving the borders by a reasonable amount would only result in very minor changes to the numbers of stars assigned to each stellar population and would not fundamentally alter the conclusions of the study. See Chapter 2 for a discussion of the different stellar types found on the CMD.

The sources marked in black are main-sequence (MS), sub-giant branch (SGB) or red giant branch (RGB) stars. Where a source can be clearly identified as belonging to a certain stellar population in the NUV - U CMD, it is also marked as belonging to that population in the V - I CMD. The location of sources on the V - I CMD agrees well with the expected position based on the NUV - U CMD. Sources that are not in the NUV - U CMD are then classified according to their position in the V - I CMD. This method results in a handful of sources that appear to lie on the MS in the V - I CMD, but are marked as gap or WD sources; they clearly belong to that category in the NUV - U CMD. The spurious CMD positions of these sources mean that they may be false matches, or may be binary systems in which

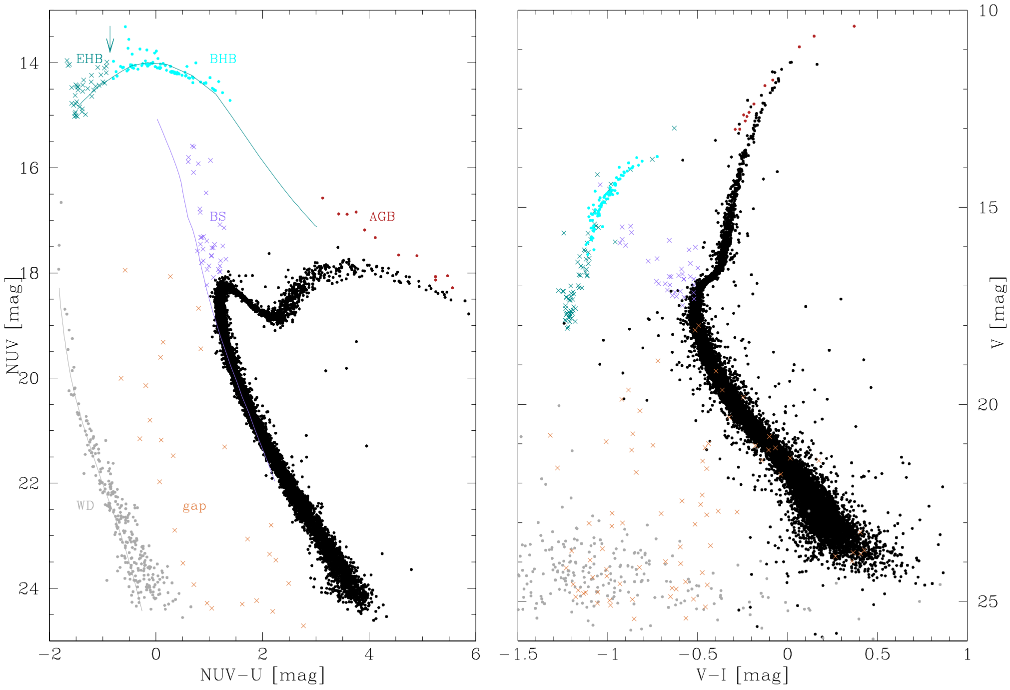

Figure 4.1: Left panel: NUV - U CMD of NGC 6752. EHB stars are plotted as dark green crosses, BHB stars are plotted in cyan, BSs in purple, AGB stars in red, WDs in grey, and gap sources (including CV candidates) are orange crosses. The remaining (black) sources are MS, SGB and RGB stars. For reference, I also include a theoretical zero-age horizontal branch (ZAHB, dark green line) and zero-age main-sequence (ZAMS, purple line), and a WD cooling sequence (grey line). Right panel: optical CMD of NGC 6752, using data from the ACS Survey Catalogue. Counterparts to NUV/U sources are plotted with the same colours and symbols as in the left panel. Optical sources with no NUV - U counterpart are categorised according to their V - I CMD position and coloured accordingly.

the redder source dominates at redder wavelengths, while the blue source dominates in the bluest bands. There are also some sources that appear to be AGB stars in the V - I CMD, but were categorised as RGB stars in the NUV - U catalogue. For consistency, I retain the NUV - U classification where one exists.

The horizontal branch (HB) is divided into blue horizontal branch (BHB) stars (light cyan), and extended or extreme horizontal branch (EHB) stars (dark green crosses). I define EHB stars to be HB stars which are bluer than an apparent gap in the NUV - U HB corresponding to around 16,500 K (marked with an arrow in Figure 4.1). This is consistent with the usual definitions for EHB stars (e.g. Momany et al. 2004; Brown et al. 2010).

Figure 4.1 also shows a theoretical zero-age horizontal branch (ZAHB, dark

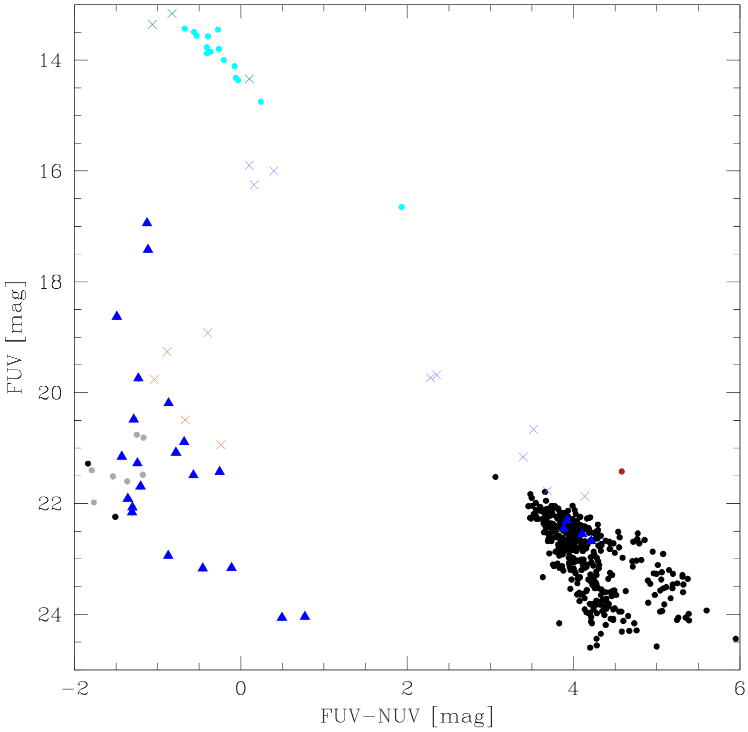

Figure 4.2: FUV - NUV CMD of NGC 6752. Sources are coloured according to their position in the NUV - U CMD (see Figure 4.1 and text). EHB stars are plotted in dark green, BHB stars in cyan, BSs in purple, AGB stars in red, WDs in grey, and gap sources (including CV candidates) are in orange. Blue triangles indicate sources that have no counterpart in the U-, B-, V- or I-bands. The remaining (black) sources are MS, SGB and RGB stars.

green line), zero-age main-sequence (ZAMS, purple line), and a WD cooling sequence (grey line). These were created using a distance of 4.0 kpc, reddening of $E(B-V) = 0.04$ mag (Harris, 1996; 2010 edition) and metallicity of $[\mathrm{Fe/H}] \simeq -1.5$ dex (Gratton et al., 2005). The ZAHB is based on the α-enhanced BaSTI ZAHB model. Following Dieball et al. (2005a), I used `synphot` within `IRAF` to translate the BaSTI output into NUV, U, V and I-band magnitudes. The ZAMS was constructed using the fitting formulae of Tout et al. (1996) to estimate the appropriate stellar parameters. The magnitudes in the various wavebands were estimated using the Kurucz grid of model stellar atmospheres within `synphot`. To generate the WD sequence, the Wood (1995) grid of theoretical WD cooling curves was interpolated, using a mean WD mass of $0.55\,M_{\odot}$. Again, the required magnitudes were calculated from the result by carrying out synthetic photometry using `synphot`.

The FUV - NUV CMD is shown in Figure 4.2. The colours are as per Figure 4.1. The blue triangles indicate sources for which there is no U-, V- or I-band counterpart. The FUV - NUV CMD is not populated enough to clearly distinguish between WD and gap sources.

4.4 The Dynamical Status

As discussed in Chapter 1, the dynamical status of a GC can be described in terms of its concentration parameter, which gives an indication as to whether the cluster is core-collapsed. Although NGC 6752 is one of the closest GCs, its dynamical status is still a topic of debate. Djorgovski & King (1986) and Auriere & Ortolani (1989) suggested that NGC 6752 has undergone core-collapse and might be in a post-core-collapse bounce phase. Lugger et al. (1995), however, claimed that the radial profile is not inconsistent with a single King profile, implying that core-collapse models need not be invoked to describe its profile. Later, Ferraro et al. (2003a) argued that two King profiles were needed to fit the radial distribution based on star counts and that a post-core-collapse bounce is the most likely scenario. In a study of 38 GCs, Noyola & Gebhardt (2006) found that NGC 6752 was the only likely core-collapsed cluster to exhibit a flat core in the surface brightness profile. In this section, I construct radial profiles based on the new WFC3 and ACS data in order to shed new light on the dynamical status of this GC.

4.4.1 Finding the Cluster Centre

In order to construct radial profiles of the cluster, I first had to determine the location of the cluster centre. This is important, because mis-placing the cluster centre will lead to a flattening of the radial density profile, hiding possible core structure. There are two distinct, basic ways to define the centre: using luminosity, C_{lum}, or using mass, C_{grav}. As stellar luminosity varies differently with stellar mass for different types of stars, these two centres are not necessarily at the same location. Furthermore, different types of stars dominate the cluster's luminosity in different observational wavebands, so C_{lum} measured in one band may differ from that measured in another. It has been shown that C_{grav} is the better measure of the 'true' centre, in terms of consistency between colour bands (e.g. Montegriffo et al. 1995), and radial symmetry (e.g. Calzetti et al. 1993). In this study, therefore, I will use C_{grav}.[3]

---

[3] It is important to note, however, that the estimate of the centre that I refer to as centre of gravity, C_{grav}, is determined using the distribution of all stars, regardless of their mass or evolutionary status, so is not, strictly speaking, the gravitational centre. It is actually the geometrical centre.

Table 4.4: Estimates of the cluster centre position.

R.A [hh:mm:ss]	Decl. [deg:mm:ss]	Uncertainty [″]	Offset [″]	Reference
19:10:52.128	-59:59:04.56	0.5	...	This paper
19:10:52.040	-59:59:04.64	0.5	0.67	Ferraro et al. (2003a)
19:10:52.240	-59:59:03.81	1.5	1.13	Noyola & Gebhardt (2006)
19:10:52.110	-59:59:04.40	0.1	0.21	Goldsbury et al. (2010)

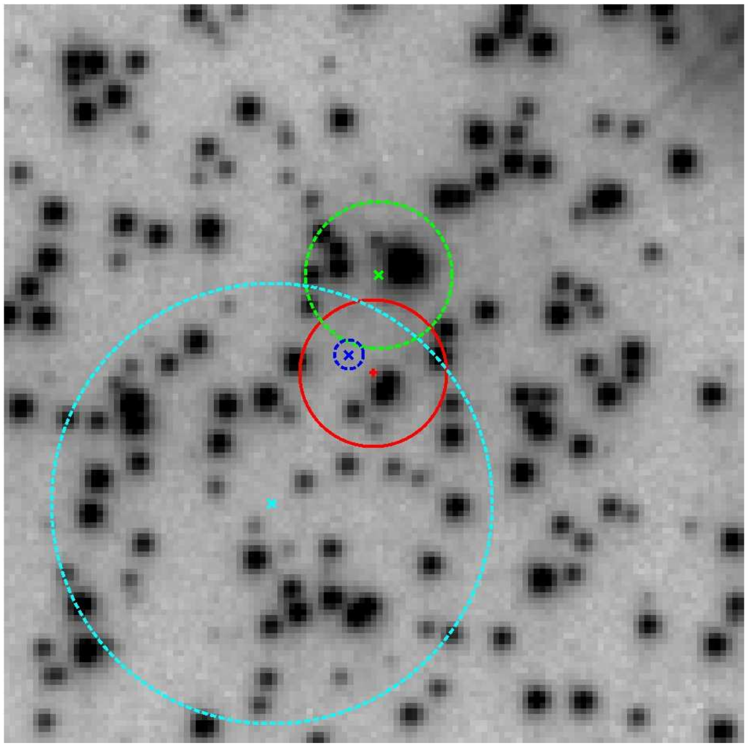

Figure 4.3: Combined and geometrically corrected ‘master’ image of 15 NUV images, with estimates of the cluster centre position. North is up and East is to the left. The field of view is 5″ × 5″ and the pixel scale is 0.″04/pixel. The red + is the new measurement determined in this paper. The green × is the estimate from Ferraro et al. (2003a), the cyan × is the estimate from Noyola & Gebhardt (2006), and the blue × is the estimate from Goldsbury et al. (2010). The circles indicate the uncertainty in position (see Table 4.4).

Following Dieball et al. (2010), I estimate the location of the cluster centre by finding the position at which the number of sources contained within a circular region of given radius, r_{lim}, is a maximum. This was carried out using sources in the U-band catalogue, down to limiting magnitude of $U_{STMAG} = 19\,\mathrm{mag}$. The U-band catalogue is particularly good for this purpose, as it contains a sufficiently large number of sources (8546 sources have $U_{STMAG} < 19\,\mathrm{mag}$), but is not seriously affected by crowding. The adopted magnitude limit ensures that faint stars in the wings of bright sources are not missed, which would create a discrepancy between the centres found using only bright or only faint sources. For the final result, I used $r_{lim} = 300\,\mathrm{pixels}\ (= 12'')$, but other reasonable choices gave results consistent with this. To estimate the uncertainties in the measurements, I used a simple bootstrapping method which involved sampling with replacement from the catalogue to create 1000 fake catalogues and estimating the centre of each one. The standard deviation of these 'fake' centres gives the error on the real measurement.

As a result, I find the cluster centre to be at $x = 2404 \pm 12\,\mathrm{pixels}$, $y = 2411 \pm 13\,\mathrm{pixels}$ in the local (WFC3) coordinate system. For comparison, I also used the V- and I-band source positions from the ACS Survey Catalogue. Using the same method I estimated the centre to be at $x = 2404 \pm 13$, $y = 2411 \pm 15\,\mathrm{pixels}$ in the local (WFC3) coordinate system, in excellent agreement with the U-band based estimate. This corresponds to $\alpha = 19^h10^m52.128^s$, $\delta = -59^\circ59'04''\!.56$ in the Tycho-based system, with an estimated uncertainty of $0''\!.5$.

Table 4.4 lists estimates of the centre position from the literature. Ferraro et al. (2003a) found the average α and δ coordinates of all stars in the PC chip of their WFPC2 image. Using WFPC2, PC images, Noyola & Gebhardt (2006) estimated the location of the centre by dividing the area surrounding each assumed centre position into eight regions. They define the centre to be the point for which the standard deviation in the number of sources in the surrounding regions is lowest. This can be described as the point around which sources are most symmetrically distributed. Goldsbury et al. (2010) used the same ACS catalogue as is used here and fitted ellipses to contours of constant number density. The average centre of these ellipses was interpreted as the centre. My estimate is consistent with these previous results. In Figure 4.3, the positions of these estimates are marked on the combined NUV image.

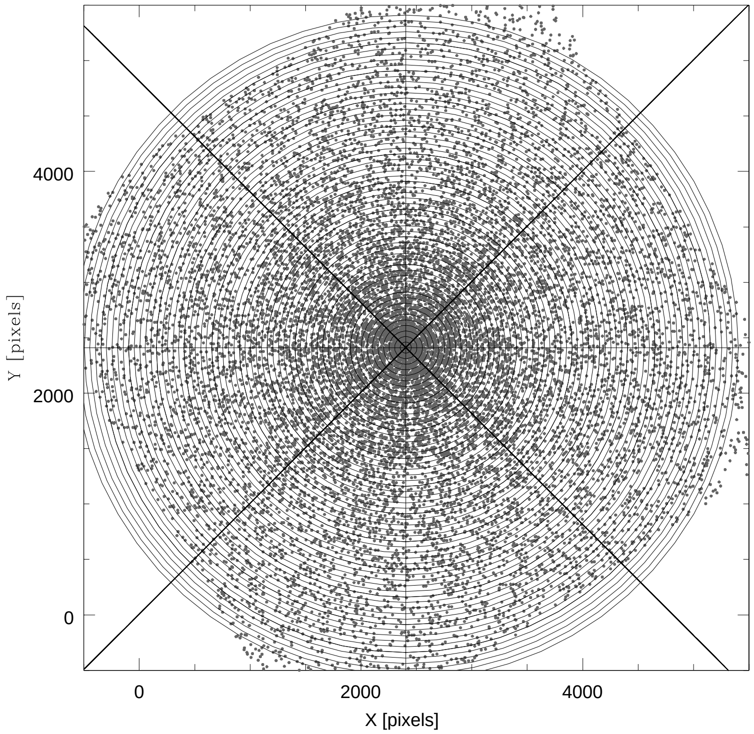

Figure 4.4: Illustration of the procedure used to determine the stellar density. The grey points are the positions of the stars in the V- and I-band catalogue, in pixel coordinates. The catalogue is divided into concentric circles, centred on the cluster centre. The concentric circles' radii increase in steps of 50 pixels ($2''$). Each annulus is split into eight equal sectors. The number of sources falling within a segment is divided by the area of the segment to give the stellar density.

4.4.2 Constructing the Stellar Density Profile

For the purposes of determining radial profiles for NGC 6752, I rely on the V- and I-band data from the ACS Survey Catalogue, as this is the deepest available data set. Repeating the process using the WFC3/NUV catalogue gave the same overall shape, with a simple shift in density that was consistent at all radii. This indicates that depth is the dominant difference between the observed distributions.

The procedure I used is similar to that described by Djorgovski (1988). As shown in Figure 4.4, the catalogue is divided into concentric circles, centred on the cluster centre, increasing in radius by 50 pixels ($2''$) each step. Each annulus is split into eight equal sectors. Due to the off-centre location of the cluster centre on the chip, the number of segments which fell entirely on the chip in V- and I-band data ranges from 35 to 52, depending on the sector considered, while sectors in the NUV data contained 35 to 46 complete segments. The number of sources falling within a

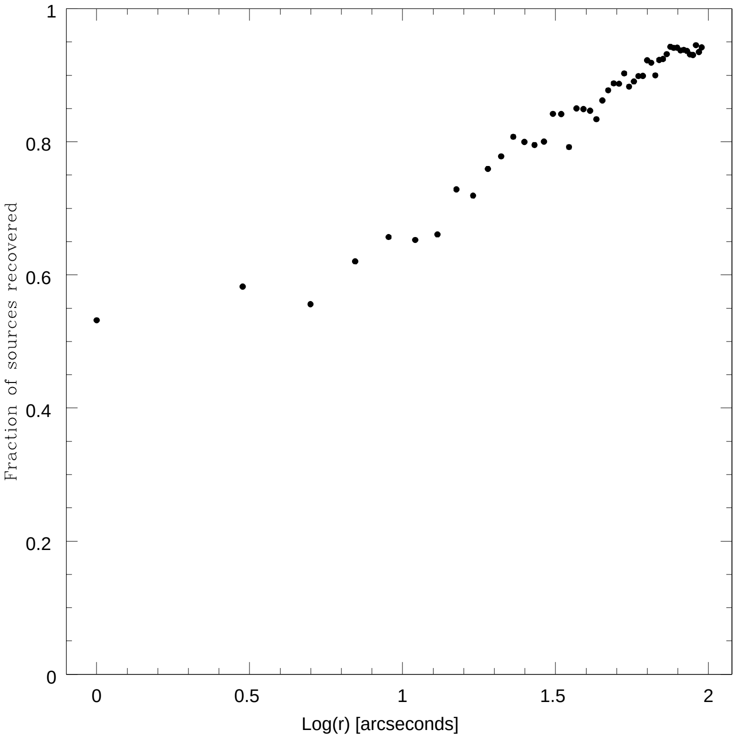

Figure 4.5: Completeness at different radii, for sources brighter than $V_{STMAG} = 19.7$ mag, determined using the artificial star catalogue from the ACS Survey.

segment is divided by the area of the segment to give the stellar density.

The overall density for a given annulus is then computed as the average of the densities of the segments corresponding to that annulus. The error on the overall density of an annulus is the standard deviation of the densities in the annulus' segments. This is justified by the fact that the dominant error source is the discrete nature of the distribution; if there is an unusually dense region of stars in one segment, that segment will contribute an artificially high number to the annulus, but the corresponding dispersion will also be larger.

In constructing the radial density profiles, I include all of the sources listed in the ACS Survey Catalogue (unlike in previous sections, in which only V- and I-band sources with a match in the WFC3 catalogues are included). This has a plate scale of $0.''05$/pixel out to radius $\simeq 101''$. I limit the data to sources brighter than ≈ 2 mags below the MSTO, corresponding to to $V_{STMAG} = 19.7$ mag, to reduce the likelihood of incompleteness impacting the results. I further correct for completeness using the artificial star catalogue for NGC 6752 that was created by Anderson et al. (2008) as part of the ACS Survey. Following their method, I consider a star to be recovered if the input and output fluxes agree to within 0.75 mag and the posi-

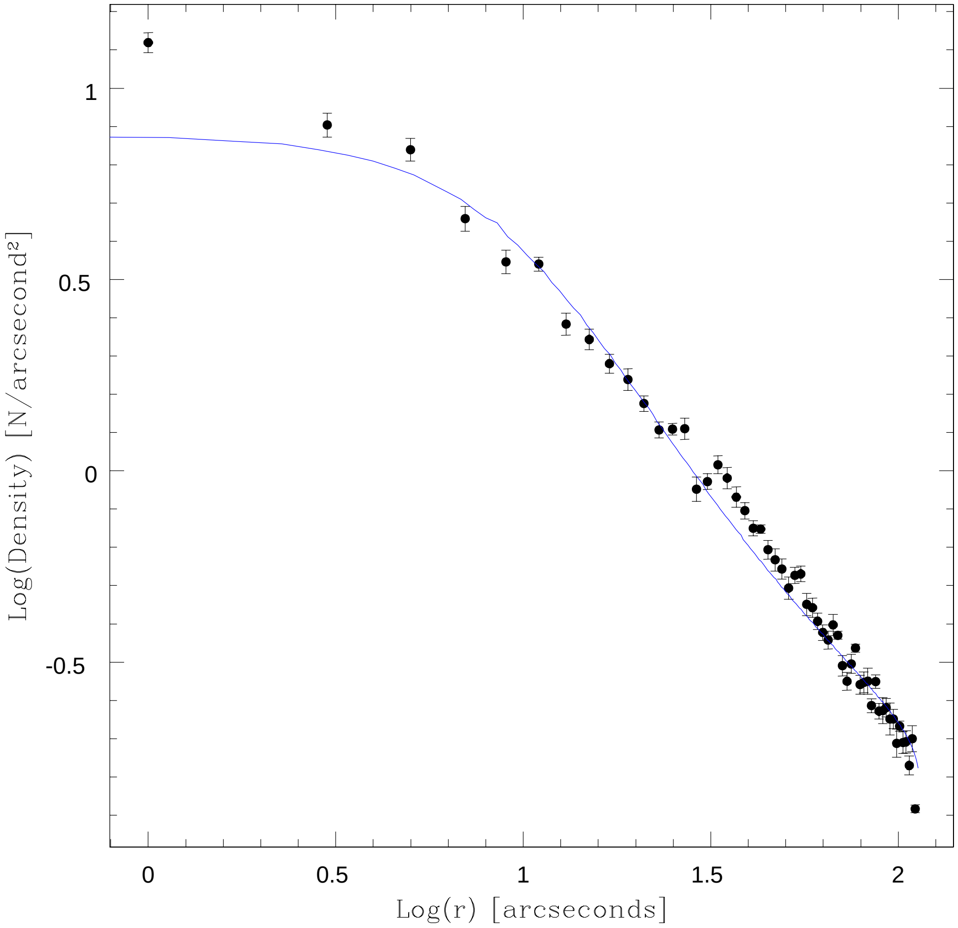

Figure 4.6: Observed radial density profile using V- and I-band data from the ACS Survey Catalogue, based on the centre determined in Section 4.4.1. Blue, solid line: best-fit King model to the data for the overall observed density profile, with $W_0 = 11$, $r_c = 9''$, $c = 2.547$. The poor fit to the data indicates that the profile of NGC 6752 cannot be well modelled with a single King profile.

tions agree to within 0.5 pixels. Using the centre determined in Section 4.4.1 I test for completeness as a function of radius, for stars brighter than $V_{STMAG} = 19.7$ mag. As shown in Figure 4.5, I find that completeness is almost 100% at the edges of the images, and is over 50% even in the core. I correct the stellar densities using the fractions of artificial sources recovered at each radius.

The radial profile obtained using this method is plotted in Figure 4.6. The profile shows a continuing rise in density towards the centre of the cluster. This agrees with the findings of Ferraro et al. (2003a), and is contrary to the findings of Noyola & Gebhardt (2006), whose surface brightness profile showed a flat core within $log(r) \approx 0\farcs5$. As shown in Table 4.4 and Figure 4.3, the centre used by Noyola &

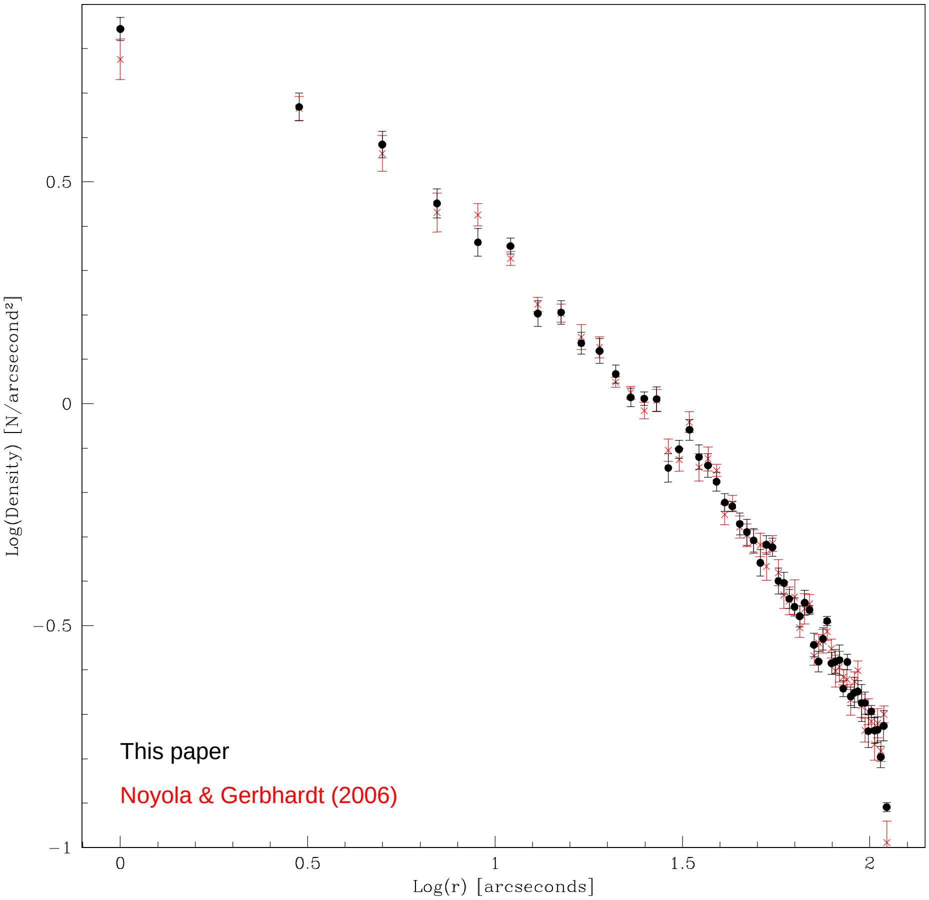

Figure 4.7: Radial density profile using different estimates of the centre position. Black points: observed radial density profile using V- and I-band data from the ACS Survey Catalogue, based on the centre determined in Section 4.4.1. Red crosses: observed radial density profile using the same data, but using the centre estimate from Noyola & Gebhardt (2006). Note that the data in this figure are raw data, not corrected for completeness.

Gebhardt differed from ours by nearly $1''$. Figure 4.7 shows the result of creating a radial density profile using this data but the centre given by Noyola & Gebhardt. The majority of the profile is unchanged, but the density at the innermost measurement point is slightly lower, giving the impression of a flatter core. The difference between the radial profile found here and that of Noyola & Gebhardt could, therefore, be partly due to the difference in the assumed centre positions. An alternative explanation is that there is a fundamental difference between the stellar density profile and surface brightness profile. D'Amico et al. (2002) showed that NGC 6752 has an usually high mass-to-light ratio ($\gtrsim 10$), leading to a high proportion of optically faint sources in the core, which may contribute to the stellar density, but not the surface brightness.

4.4.3 Modelling the Stellar Density Profile

In order to find the model which best describes the radial stellar density profile of NGC 6752, I used single-mass King (1966) models, which I then projected to create 2-dimensional stellar density profiles. King (1966) models begin by assuming that the GC can be modelled using an isothermal sphere, of known central potential, with a constant velocity dispersion. Once projected onto a 2-dimensional plane, they can be described in terms of three parameters: W_0 is a dimensionless quantity proportional to the value of the potential at the cluster centre; r_c is the core radius; $\sigma(0)$ is the central density.

As I suspected that a plausible, single King model may not provide a good representation of the profile, I searched for the model that gave the best best fit to the data, without constraining the parameters to plausible physical ranges. Instead, I allowed the parameters (W_0, r_c, and $\sigma(0)$) to vary as required. The model that best described the data over the entire radius range had $W_0 = 11$, $r_c = 9''$, $c = 2.547$, and is plotted as a solid, blue line on Figure 4.6. While this r_c value is comparable to that of $10\rlap{.}''2$ given by Harris (1996; 2010 edition), a concentration parameter of $c \gtrsim 2 - 2.5$ is usually considered to indicate a core-collapsed cluster, which should not be modelled using a single King profile. It is immediately apparent from the plot that the model does not give a good fit, demonstrating the difficulty in modelling the radial distribution of NGC 6752 with a single King model, as previously found by Ferraro et al. (2003a).

As noted above, Ferraro et al. (2003a) presented a radial profile of NGC 6752 based on WFPC2 and ground-based data, and also concluded that two King models were required to adequately fit the data. In their investigation, the PC chip of the WFPC2 was roughly centred on the core of the GC, so the spatial resolution available was $0\rlap{.}''046/\text{pixel}$ for the central region, out to $\approx 18\rlap{.}''5$ radius. Outside this radius, the WFPC2/WF chips and ground-based data were used, with pixel scale, at best, of $0\rlap{.}''1/\text{pixel}$. In the central region, the resolution of the images used by Ferraro et al. is comparable to that of the ACS/WFC and WFC3, but beyond a radial distance of $\approx 18\rlap{.}''5$, the data set used in the present investigation has considerably better resolution.

In Figure 4.8, I compare the data to the radial profiles from Ferraro et al. (2003a), including the two King models they used to fit the data. The result shows that the

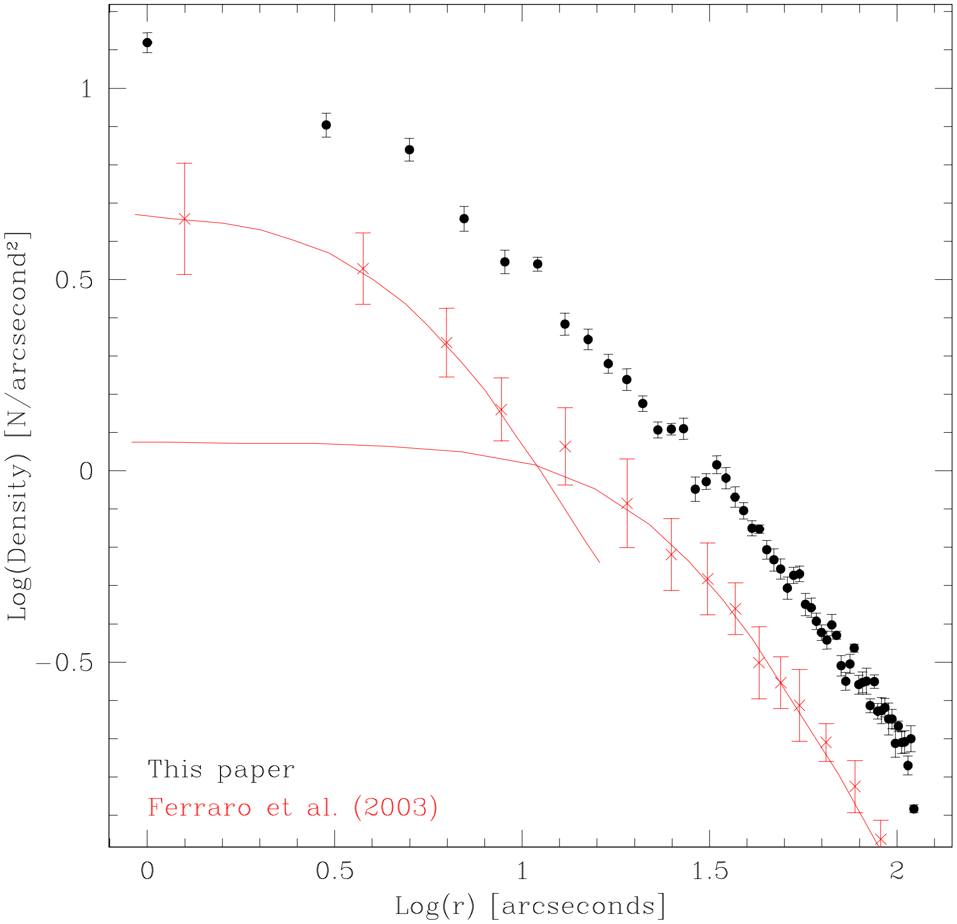

Figure 4.8: Black points: observed radial density profile using V- and I-band data from the ACS Survey Catalogue, based on the centre determined in Section 4.4.1. Red crosses/lines: Figure 5 of Ferraro et al. (2003a), showing the two King models that they use to fit the data.

measured V- and I-band stellar density is higher than theirs at all radii, because of the different brightness limits used (Ferraro et al. cut off at $V_{STMAG} = 18.5$ mag, while I include stars down to $V_{STMAG} = 19.7$ mag), but the shapes are quite similar.

As modelling the radial profile of NGC 6752 with a single King model gave such a bad fit, I also split the data, following Ferraro et al. (2003a), and used separate King profiles to fit the inner and outer parts of the cluster. I note that a double King model is a purely phenomenological structure, and has no actual physical basis. Furthermore, I treat the two parts of the cluster independently, neglecting any contribution to one regime from the other (for example, there should be a contribution to the inner part of the cluster's density profile from the underlying King model used in the outer part, which I have ignored). As before, I do not restrict the model

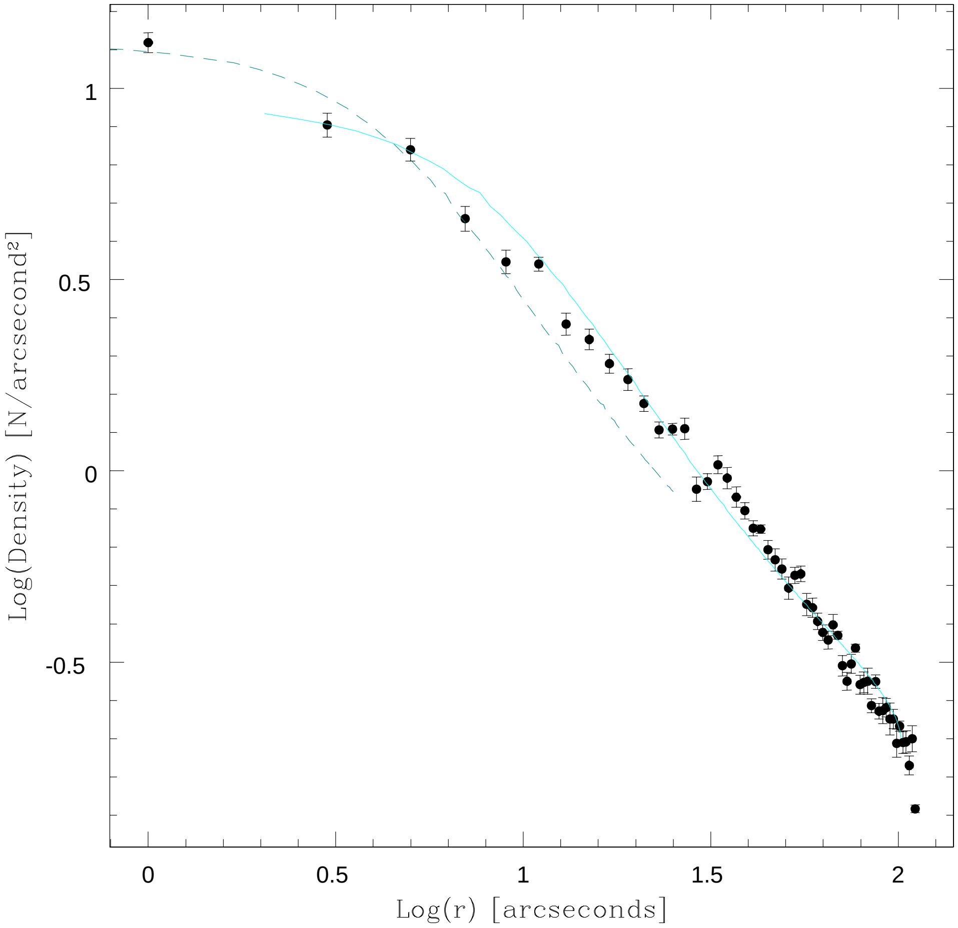

Figure 4.9: Black points: observed radial density profile using V- and I-band data from the ACS Survey Catalogue, based on the centre determined in Section 4.4.1. Dark green, dashed line: best-fit King model to the innermost part of the cluster ($\log_{10}(r) < 0.9$). Cyan, solid line: best-fit King model to the outer part of the cluster ($\log_{10}(r) > 1.2$).

parameters to physically reasonable ranges; instead I simply found the best fits to the data. I define the inner part of the cluster to have $\log_{10}(r) < 0.9$, and the outer part to have $\log_{10}(r) > 1.2$.

Figure 4.9 shows the resulting fits. The inner part of the cluster (dark green, dashed line) is best described by a King model with $W_0 = 13$, $r_c = 5''$, $c = 2.944$, while the outer part (cyan, solid line) has $W_0 = 11$, $r_c = 9''$, $c = 2.547$. The core radius for the inner part is not dissimilar from that found by Ferraro et al. (2003a). The core radius for the outer part is not a good match, but at $\log_{10}(r) > 1.2$ there is little difference in the shapes of models with different core radii. The values of W_0 and c that I found are considerably higher than expected, but a large change in W_0

leads to a very small change in the shape of the profile, particularly near the core, and c comes directly from the best-fit W_0 value. Models with lower values of W_0 (and, therefore, c) fit the data almost as well, especially at small radial distances.

Comparing Figure 4.6 and Figure 4.9, it is clear that NGC 6752's radial density profile is better fit using a combination of two King profiles than a single one, suggesting that the cluster is undergoing, or has undergone, a core-collapse phase.

4.5 The Radial Distributions and Masses of Stellar Populations

4.5.1 Radial Distributions

The cumulative radial profiles of various stellar populations identified in the CMDs are shown in Figure 4.10. Also shown is the radial profile of the X-ray sources identified by Pooley et al. (2002).[4] In order to prevent completeness affecting the results, I use V- and I-band data to consider the horizontal branch stars and blue stragglers, while the positions of gap sources are determined using measurements taken with NUV and U-band filters. I only consider sources brighter than $NUV_{STMAG} = 22.5$ mag to make sure that completeness does not affect the results. In this way, I can be confident that the sources have been categorised correctly and that the radial distributions are not biased by 'missing' faint sources towards the core. I limit the distributions to a radial distance of $68''$ in the ACS (V- and I-band) data and $72''$ in the WFC3 (NUV and U-band) data, in order to avoid bias due to the edges of the detectors. Only 13 of the 19 known X-ray sources are included, because the others are more than $72''$ from the core. Table 4.5 lists the number of sources considered from each stellar population.

Kolmogorov-Smirnov (KS) tests were carried out on various pairs of populations. As explained in Section 3.1.6, the KS test calculates the probability that a difference in distribution as large as that observed can occur amongst sources drawn from the same underlying distribution. I caution that some of the samples used are relatively small, so care should be taken when interpreting the KS test results. Table 4.6 shows the results of the KS tests.

Figure 4.10 shows that X-ray sources are the most centrally concentrated population, with BSs and gap sources also being centrally concentrated. This is to be expected, since all of these types of sources may be formed through dynamical

---

[4] The positions listed in the Pooley et al. (2002) were first registered to my WCS; see Chapter 5.

Table 4.5: Number of sources from each stellar population considered in computing radial profiles.

Population	$N_{sources}$
HB (overall)	119
BHB	78
EHB	41
BS (overall)	32
bBS	16
fBS	16
gap	14
X-ray	13

Table 4.6: Result of KS tests, which give the probability (shown here in %) that a single population can exhibit differences in radial distributions as large as those observed. This gives an indication of the likelihood that the two populations are from the same distribution. The most significant KS test results (i.e. KS probability $< 5\,\%$) are highlighted in bold.

Populations	KS test result [%]
BHB vs. EHB	73.15
bBS vs. fBS	23.83
BS vs. HB	**4.13**
BS vs. BHB	7.94
BS vs. EHB	5.21
BS vs. gap	91.69
BS vs. X-ray	10.48
gap vs. HB	9.21
gap vs. BHB	9.30
gap vs. EHB	18.49
gap vs. X-ray	30.34
X-ray vs. HB	**0.08**
X-ray vs. BHB	**0.12**
X-ray vs. EHB	**0.14**

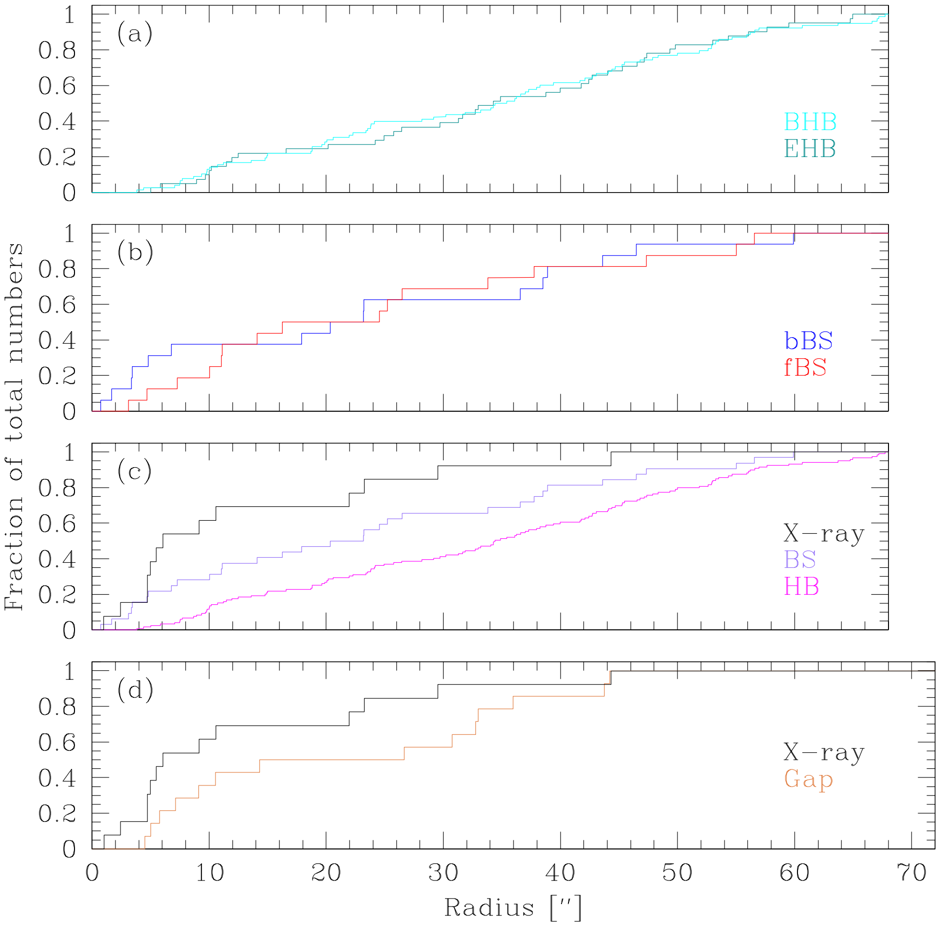

Figure 4.10: Cumulative radial distributions for various stellar populations identified in the CMDs and of the X-ray sources within the field of view. Panels (a) and (b) compare the radial distributions of the EHB and BHB sources, and those of bright (blue) BSs and faint (red) BSs. Panel (c) shows the radial distributions of the X-ray sources, along with the (overall) BS and HB populations. Panel (d) compares the distribution of X-ray sources with that of the gap sources, down to a limiting magnitude of $NUV_{STMAG} = 22.5$ mag.

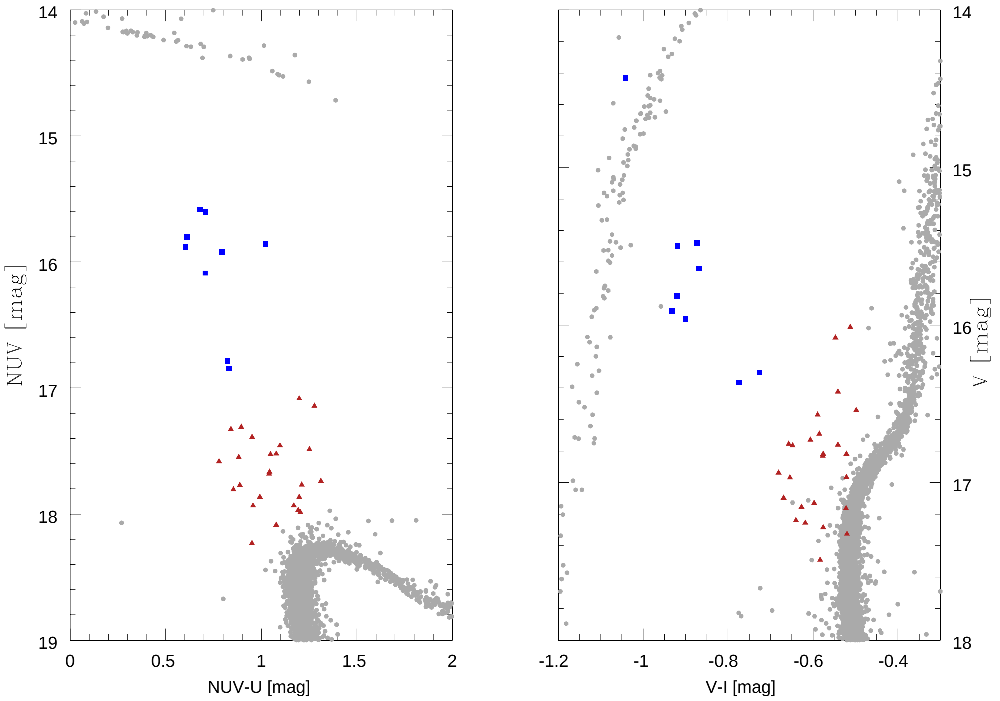

Figure 4.11: CMDs of the core of NGC 6752 with sub-populations of BS stars indicated. BS stars are categorised as bright and blue (blue squares), or faint and red (red triangles) according to their CMD position relative to $NUV_{STMAG} < 17$ mag. All sources with $NUV_{STMAG} < 17$ mag also have $M_{V-I} < -0.7$ mag, while just 2 out of 25 with $NUV_{STMAG} > 17$ mag and $M_{V-I} < -0.7$ mag.

interactions, which are far more likely in the dense cluster core. Furthermore, X-ray binaries, most gap sources (e.g. CVs and non-interacting MS-WD binaries) and BSs (see Section 2.1.8) are expected to be more massive than ordinary cluster members, so will sink towards the core due to mass segregation. As shown in Table 4.6, there is no significant difference between the distributions of X-ray sources and gap sources or blue stragglers (KS test results of 30.34% and 10.48%, respectively), but the X-ray sources have a significantly different radial distribution from the horizontal branch stars (the KS test shows that the likelihood of the X-ray and HB sources resulting from the same underlying distribution is 0.08%). The distribution of gap sources (brighter than $NUV_{STMAG} = 22.5$ mag) is much closer to that of BSs than HBs, but the KS test does not give statistically significant results for either comparison. There is no evidence to suggest that the EHB and BHB sources (see panel (a) of Figure 4.10) are formed from different underlying populations.

Bright blue straggler stars (bBSs) are thought to be younger (Ferraro et al., 2003b) and more massive (Sills et al., 2000) than faint BSs (fBSs), so should be more centrally concentrated (assuming that all BSs are older than the GC's relaxation time). However, as shown in Dieball et al. (2010) and Section 3.1.6, the fainter, redder BSs in M 80 were found to be more centrally concentrated than the brighter, bluer ones. To see how this compares to NGC 6752, I also compare brighter and fainter BSs here. Like in M 80, I found that UV-bright BSs were also bluer in V-band (7 out of 7 sources with $NUV_{STMAG} < 17$ mag also have $M_{V-I} < -0.7$ mag, compared to just 2 out of 25 with $NUV_{STMAG} > 17$ mag and $M_{V-I} < -0.7$ mag). As shown in panel (b) of Figure 4.10, the distribution in BSs in NGC 6752 does not follow that of M 80, but is more in line with the conventional model. There is no significant difference between the radial profiles of bright and faint BSs, and the KS test gives a probability of 23.83% that differences as large as those observed could be found in populations drawn from the same underlying distribution; there is no substantial evidence that they come from different initial distributions.

4.5.2 Masses of Populations

The typical masses of the different stellar populations were estimated using the method described in Heinke et al. (2003), which is discussed in more detail in Section 3.1.7. Adopting a core radius of $r_c = 10\farcs47$, as determined by Trager et al. (1993) using stars at or brighter than the main-sequence turn-off, and assuming that the core radius is defined by MSTO stars with $M_{\star} = 0.8\,M_{\odot}$, the radial distributions found above were compared with generalised theoretical King models at different masses (although, as discussed in Section 4.4.2, the assumption that the cluster can be well described by a classic King (1966) model may be over-simplified).

As in Section 4.5.1, I use V- and I-band data to compare the HB stars and BSs, and NUV and U-band detections for the gap sources. Again, I only consider NUV sources brighter than $NUV_{STMAG} = 22.5$ mag. This ensures a uniform completeness limit. In order to avoid inconsistencies due to the edge of the field of view, I limit the area considered to a circle centred on the cluster core with radius $68''$ for the ACS data and $72''$ for the WFC3 data. I consider all of the X-ray sources that are within $72''$ of the cluster core.

Figure 4.12 shows models for sources of mass $0.4 - 2\,M_{\odot}$, along with the radial distributions of the BSs, HBs, X-ray sources and gap sources. Panel (a) gives a mass estimate of $\approx 0.9\,M_{\odot}$ for the blue stragglers and $\approx 0.6\,M_{\odot}$ for the overall horizontal branch population (BHB and EHB). These results are consistent with theoretical expectations. Comparison with the theoretical ZAMS (see Section 4.3) suggests BS masses of $0.95 - 1.65\,M_{\odot}$ and comparison with the ZAHB suggests an HB mass

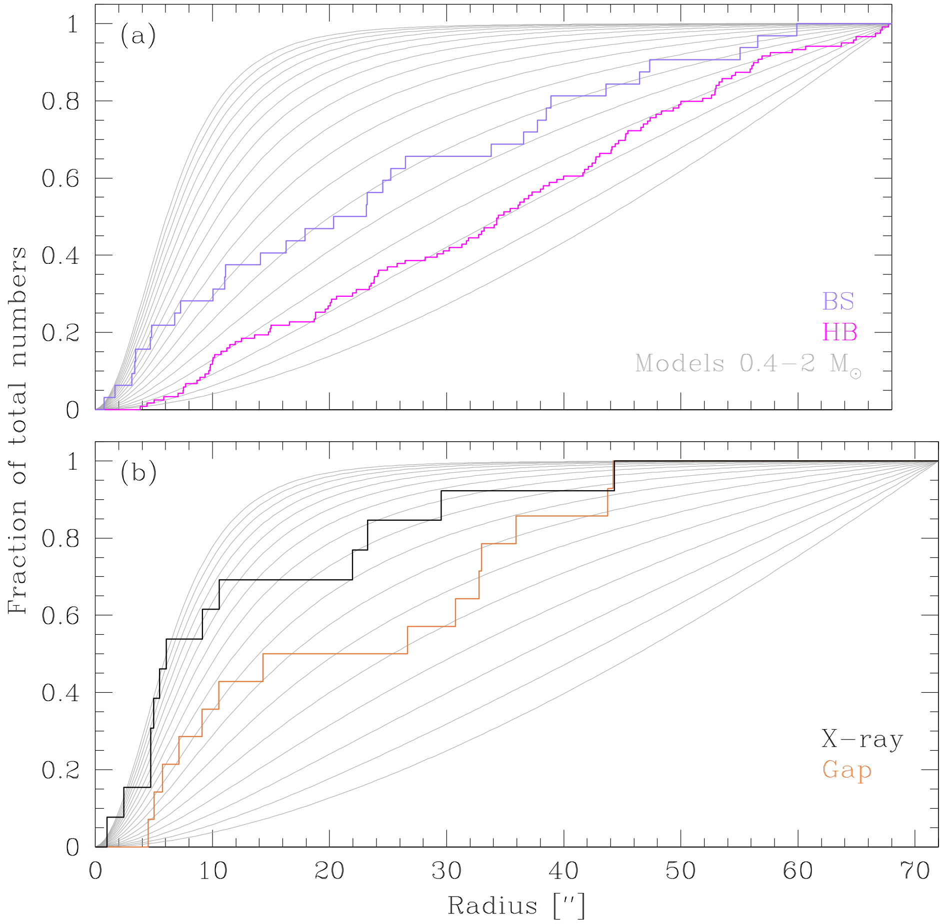

Figure 4.12: Comparison of the radial distributions of various stellar populations with theoretical King models with average masses of $0.4M_\odot$ (lowest grey line in each panel) to $2M_\odot$ (top grey line), in steps of $0.1M_\odot$. Panel (a) shows that the BS distribution agrees well with a mass of $0.9M_\odot$, while the HB population is consistent with a mass of $0.6M_\odot$. Panel (b) shows the radial distribution of X-ray sources and gap sources. The X-ray sources have masses larger than $1.1M_\odot$, while the gap sources have masses greater than $0.8M_\odot$.

range of $0.49 - 0.66\,M_{\odot}$. In both cases, the majority of sources lie towards the lower mass (fainter) end of the sequence. Panel (b) shows that the X-ray sources have characteristic dynamical mass larger than $1.1\,M_{\odot}$, while the gap sources have characteristic dynamical masses of at least $0.8\,M_{\odot}$, consistent with expectations for dynamically formed systems.

4.6 Conclusions

I have analysed FUV images taken with STIS, and NUV, U- and B-band images taken with the WFC3 on-board *HST* of the nearby, dense GC NGC 6752. I matched the catalogues to the V- and I-band data from the ACS Survey Catalogue, to produce a catalogue with a total of 39411 sources. The NUV - U CMD shows plentiful blue straggler and horizontal branch populations, along with a number of 'gap' sources in the region where I expect to find CVs and non-interacting WD-MS binaries. The images are also deep enough to reveal 360 white dwarfs.

Using the U-band and V-band catalogue, I estimated the position of the geometrical centre of the GC and used this centre to produce stellar density profiles of the cluster. Contrary to the surface brightness profile created by Noyola & Gebhardt (2006), I do not find a flat core; this may be because of the different centre position used or because the stellar density profile and surface brightness profile of NGC 6752 are physically different. I conclude that the radial profile cannot be well modelled using a single King model, indicating that the cluster is undergoing, or has undergone, core-collapse.

In the next chapter, I will search the catalogue for counterparts to known X-ray and radio sources, and for sources exhibiting signs of variability.

It is reasonable to hope that in the not too distant future we shall be competent to understand so simple a thing as a star.

A. EDDINGTON (1882 – 1944)

5

The Globular Cluster NGC 6752: X-ray Counterparts and New Dwarf Novae

In the previous chapter, I discussed a multi-wavelength survey of the globular cluster NGC 6752. Here, I focus on the search for counterparts to its known X-ray and radio sources and the search for previously unknown interacting binaries.

Pooley et al. (2002) used *Chandra* observations to identify 19 X-ray sources in NGC 6752 and found 12 optical counterparts, including 10 CV candidates. D'Amico et al. (2002) then identified 5 millisecond pulsars (MSPs), four of which have no known optical counterparts. The other (PSR A) has a white dwarf counterpart (Bassa et al., 2003), but this MSP is located ≈ 74 core radii from the centre, and it is not clear whether this source is a cluster member (Bassa et al. 2006; Cocozza et al. 2006). If it is, one possible explanation for its offset position is that it was propelled there by an interaction with a BH-BH binary system (Colpi et al., 2002).

In Section 5.1, I discuss the results of the search for counterparts to known X-ray sources. In Sections 5.2, and 5.3, I describe the search for counterparts to known radio sources and the search for brightness variations amongst sources in my stellar catalogue. The work in this chapter has been published, forming part of Thomson et al. (2012).

5.1 Identification of the X-ray Counterparts

Based on *Chandra* observations, Pooley et al. (2002) identified 19 X-ray sources within the 115$''$ half-mass radius of NGC 6752, including six within the 10$.\!''$5 core radius, down to a limiting luminosity of $L_X \approx 10^{30}$erg s^{-1}. Using archival *HST* data, Pooley et al. suggested 12 optical counterparts. These include 10 CV candidates, one to three RS Canum Venaticorum (RS CVn) or BY Draconis (BY Dra) sources (based on their X-ray-to-optical flux ratio limits), and one or two that are background objects. Seven of the X-ray sources had no detectable optical counterparts. One of the CVs, CX 4, is now known to be a dwarf nova (Kaluzny & Thompson, 2009).

Sixteen of the *Chandra* X-ray sources are in the field of view of the WFC3 observations, and 7 are also in the field of the FUV image. Using the most obvious known matches (the DN and other bright CVs), I made a first attempt to register the X-ray source positions to the (Tycho-based) WCS. Comparing the positions of all X-ray sources to the catalogue revealed more matches that could be considered 'safe', including two further DNe (see Section 5.1.1). I used the (now three) DN counterparts to refine the correction. I found that the *Chandra* positions quoted by Pooley et al. (2002) should be shifted by 0$.\!''$540 in right ascension and $-0.\!''055$ in declination in order to best match the positions of the DNe, giving an RMS offset between the X-ray and optical positions of the DNe of 0$.\!''$012 in right ascension and 0$.\!''$003 in declination.

Pooley et al. (2002) do not provide estimates of the errors on the positions given in their paper, so the errors had to be determined from the number of source counts that they listed. Kim et al. (2007) derived empirical equations for the positional uncertainty of *Chandra* X-ray sources. The equation derived for the 90% confidence level is

$$\log_{10} PU = 0.1142OAA - 0.4839\log_{10}C + 0.0499, 0.0000 < \log_{10}C \leq 2.1336$$
$$\log_{10} PU = 0.0989OAA - 0.2027\log_{10}C + 0.5500, 2.1336 < \log_{10}C \leq 3.3000$$

where positional uncertainty, PU, is in arcseconds, off-axis angle, OAA, is in arcminutes, and C is source counts.

Using this equation, and ignoring the off-axis angle in the *Chandra* observations (which is likely to be negligible given the relatively small field of view of the data considered here), I reconstructed the 90% confidence level uncertainty of the X-ray source positions. This was the dominant source of error in the X-ray positions; for

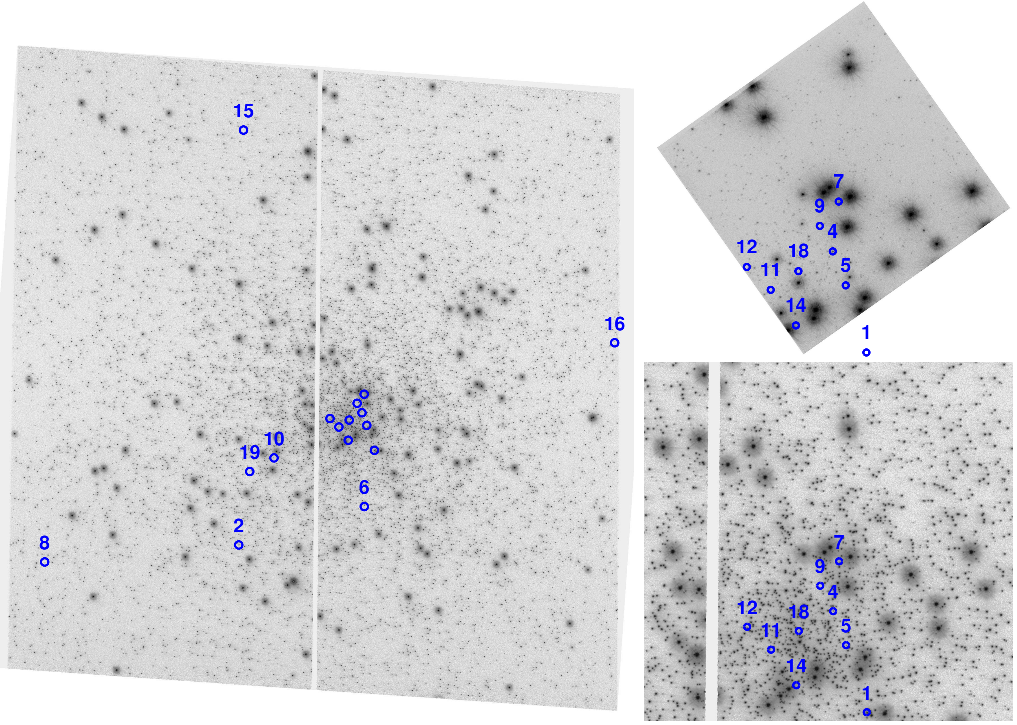

Figure 5.1: Left panel: combined and geometrically corrected 'master' image of 15 NUV images. North is up and East is to the left. The field of view is 162″ × 162″ and the pixel scale is 0.″04/pixel. X-ray source positions are marked in blue circles and labelled with their CX number (except those in the core). Top right panel: combined 'master' image of 13 FUV images, with X-ray positions marked. Again, North is up and East is to the left. The STIS field of view is 25.″1 × 25.″3 and the pixel scale is 0.″025/pixel. Lower right panel: zoomed in version of the central region of the master NUV image, with the central X-ray sources marked and labelled with their CX number. The field shown is ≈ 40″ wide and 38″ high and the position and scale corresponds to that of the FUV image shown above.

all but the very brightest sources, the *Chandra* uncertainty was several times larger than the estimated error on the boresight correction.

I compared the positions of all X-ray sources to the catalogue to search for matches, using the 90% confidence level uncertainty in X-ray position as the maximum matching radius. Figure 5.1 shows the FUV and NUV images with the X-ray source positions over-plotted, and Figure 5.2 presents finder charts of all counterparts.

Using the method described in Section 4.2.3, I calculate that I expect to find two spurious matches to the sixteen X-ray sources in the field of view. As outlined in the following sections, I find twelve sources within the regions searched, at least seven of which are likely to be the real optical counterpart, based on their CMD positions or light curves. For one X-ray source (with a likely 'real' counterpart), there are two

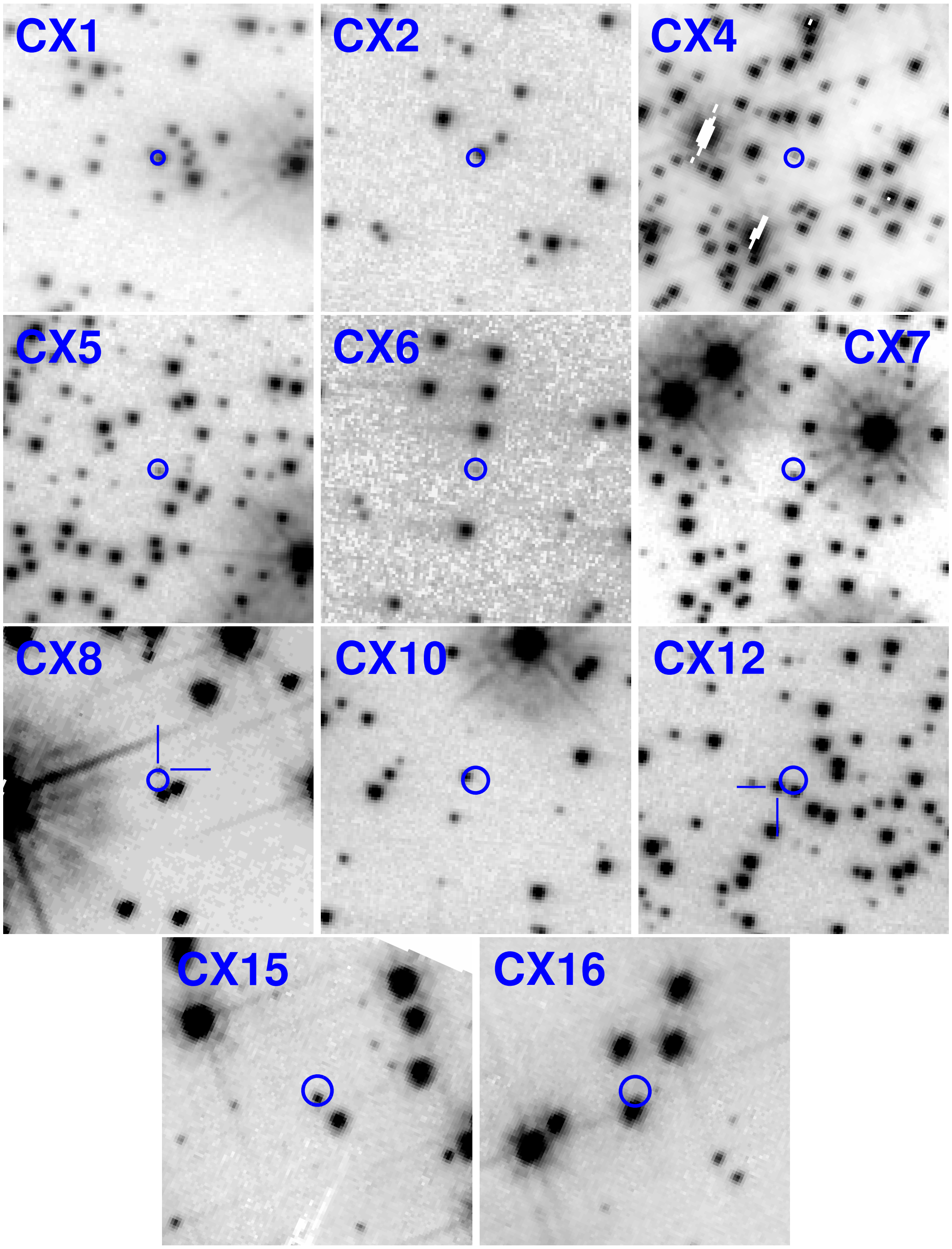

Figure 5.2: Finder charts showing possible counterparts to X-ray sources. In each case, the field covers $4'' \times 4''$ and North is up and East is to the left. The circles show the 90% confidence level uncertainty in X-ray position that I searched for counterparts. For sources CX 1, 2, 5, 6, 7, 10 and 12, the image is the NUV 'master' image created by combining 15 individual F225W exposures. For sources CX 4, 8, 15 and 16, the image is a combination of 6 U-band images taken with the F390W filter. The grey-scale is varied to enhance the visibility of the counterparts. Sources CX 3, 9, 13, 17 and 19 are outside the WFC3 field of view. No sources were detected within the 90% confidence error circle of CX 11, 14 or 18.

sources within the maximum matching radius; clearly, at least one of these matches is spurious. Of the remaining five matches, which are MSs or were only detected in one waveband, the calculation suggests that one is likely to be a spurious match, while the other four may be real counterparts. I caution that Poisson errors on these numbers mean that they are approximations only.

I searched for hints of periodic variability in the light curves of every potential X-ray counterpart. This was done using the FUV and NUV data. The FUV data was used because, as discussed in Section 2.4, variable sources are often easier to detect, or have larger amplitude variations at shorter wavelengths. The NUV data was chosen because it had the largest number of individual exposures (18), and is a good compromise between short wavelength and large field of view.

Following the method described in Section 3.3, I performed photometry on the individual FUV exposures, using the overall FUV catalogue as input to `daophot` (Stetson (1991); see Section 4.2.2). As described in Section 4.2.2, photometry was carried out on the NUV data using `DOLPHOT`, which gives individual magnitudes for each source in each of the 18 individual images as part of its output. I produced FUV and NUV light curves for each of the candidate counterparts and inspected them to search for signs of variability. I also produced a power spectrum for each of the sources to search for hints of periodic variability and used a randomisation test to estimate a false alarm probability (FAP); this is the probability that a higher peak could be produced at any frequency if the associations between times and fluxes are shuffled randomly, creating a white-noise time series with the same sampling and overall variance as the original data. Tables 5.1 and 5.2 summarise the results. Figure 5.3 shows the light curves of the four most interesting counterparts.

The main result is that two of the X-ray sources that Pooley identified as CV candidates are, in fact, dwarf novae (DNe). This confirms the CV nature of these sources and determines their sub-class. For two other X-ray sources I identified previously unknown optical counterpart candidates, including one which is a variable source.

The CMD positions of all of the counterparts discussed (where CMD information is available) are shown in Figure 5.4. The most likely counterpart in each case is marked with a dark coloured cross. The two DNe, which showed strong magnitude variations, are placed on the CMD using the NUV magnitudes of their fainter states, as indicated with a subscript ‘F’. Two interesting objects found just outside the error circles for X-ray sources CX 12 and CX 16 are marked using cyan triangles.

In the following subsections, I provide details on all of the potential counterparts to each of the X-ray sources in the field of view.

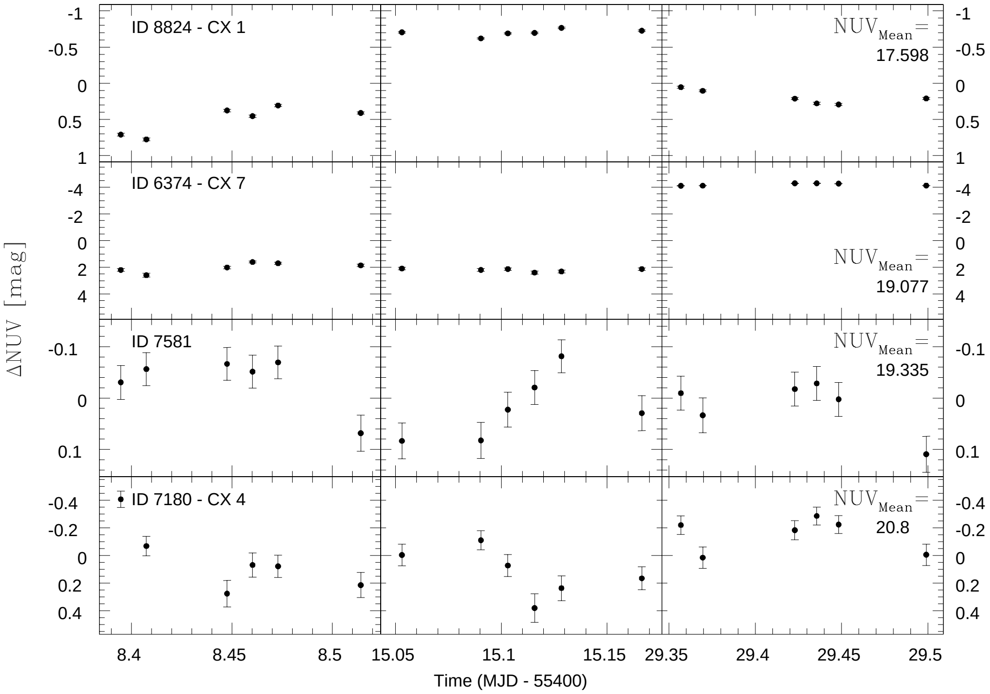

Figure 5.3: Light curves of four likely optical counterparts to X-ray sources. The NUV variation from the mean NUV magnitude is shown ($\Delta NUV = NUV - NUV_{Mean}$). This value does not necessarily match the magnitude stated in the catalogue, which is an overall (weighted average) magnitude, as opposed to a simple mean value. Top panel: source 8824, the optical counterpart to CX 1, which shows a brightening in the middle epoch and is a likely DN. Second panel: source 6374, the counterpart to CX 7. This source is ≈ 6 mag brighter in the third epoch than the first two. I conclude that this source is a DN. Third panel: source 7581, which may be the previously unidentified counterpart to CX 12 and is an SX Phoenicis star. Bottom panel: source 7180, which corresponds to X-ray source CX 4 which is a known DN.

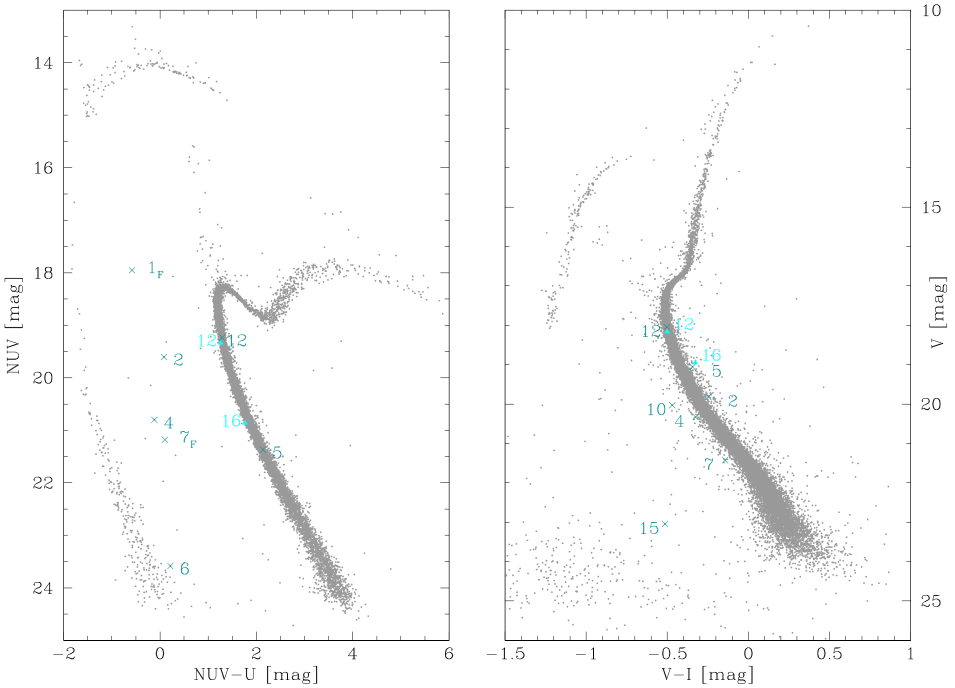

Figure 5.4: NUV - U (left panel) and V - I (right panel) CMD of NGC 6752. The most likely counterpart to the X-ray sources are shown as dark crosses and labelled with their X-ray source ID. The most likely counterparts to CX 1 and CX 7 exhibit strong variation in their light curves (see Section 5.1.1). The NUV magnitude plotted is the average magnitude of the source when in its 'fainter state' and is marked with a subscript 'F'. Interesting optical sources that lie just outside the *Chandra* error circle of CV 12 and CX 16 are marked with cyan triangles and the X-ray source ID. See Section 5.1 for details of X-ray matching.

Table 5.1: Properties of potential counterparts to *Chandra* X-ray sources. The first column is the *Chandra* ID number from Pooley et al. (2002), followed by my catalogue ID number in Column 2. Columns 3-4 give the source position in R.A. and decl. (shifted to match the Tycho-based WCS). Column 5 gives the $0.5-2.5$ keV X-ray luminosity from Pooley et al. (2002). Columns 6-7 and 9-10 give the magnitudes in STMAG, and Column 8 gives an estimate of the variability amplitude, defined to be the standard deviation of the source from its mean magnitude. Columns 11 and 12 give the magnitudes in STMAG from the ACS Survey Catalogue.

1	2	3	4	5	6	7	8	9	10	11	12
ID_X	ID_{cat}	R.A. [hh:mm:ss]	Decl. [deg:mm:ss]	$L_{X,0.5-2.5}$ [erg s^{-1}]	FUV [mag]	NUV [mag]	ΔNUV [mag]	U [mag]	B [mag]	V [mag]	I [mag]
CX 1	8824	19:10:51.134	-59:59:11.83	2.1×10^{32}	...	17.700	0.539	18.528	...	...	...
CX 2	12078	19:10:56.009	-59:59:37.38	6.0×10^{31}	...	19.604	0.423	19.520	19.728	19.818	20.064
CX 3	...	19:10:40.354	-59:58:41.34	5.3×10^{31}	...	...	...	...	...	...	...
CX 4	7180	19:10:51.583	-59:59:01.76	4.0×10^{31}	19.756	20.800	0.212	20.914	21.002	20.328	20.653
CX 5	7796	19:10:51.410	-59:59:05.16	3.6×10^{31}	...	21.371	0.140	19.234	19.089	19.057	19.402
CX 6	10808	19:10:51.499	-59:59:27.05	2.2×10^{31}	...	23.583	0.652	23.367	...	...	...
	34433				...	...	...	...	23.102	...	...
CX 7	6374	19:10:51.504	-59:58:56.77	1.9×10^{31}	20.941	20.412	3.067	21.084	21.650	21.424	21.567
CX 8	24678	19:11:02.981	-59:59:41.94	2.1×10^{31}	...	...	...	24.011	23.648	...	...
CX 9	...	19:10:51.756	-59:58:59.21	1.3×10^{31}	...	...	...	...	...	...	...
CX 10	9343	19:10:54.742	-59:59:13.92	6.0×10^{30}	...	20.288	0.098	...	...	20.029	20.499
CX 11	...	19:10:52.411	-59:59:05.61	6.2×10^{30}	...	...	...	...	...	...	...

Table 5.1: (continued)

1	2	3	4	5	6	7	8	9	10	11	12
ID$_X$	ID$_{cat}$	R.A. [hh:mm:ss]	Decl. [deg:mm:ss]	L$_{X,0.5-2.5}$ [erg s^{-1}]	FUV [mag]	NUV [mag]	ΔNUV [mag]	U [mag]	B [mag]	V [mag]	I [mag]
CX 12	7592	19:10:52.730	-59:59:03.33	5.6×10^{30}	23.199	19.235	0.045	17.946	17.840	18.044	18.547
	7581^E				...	19.336	0.058	18.073	17.954	18.169	18.669
CX 13	...	19:10:40.601	-60:00:06.12	4.6×10^{30}	...	...	...	...	...	...	...
CX 14	...	19:10:52.075	-59:59:09.18	4.2×10^{30}	...	...	...	...	...	...	...
CX 15	14708	19:10:55.834	-59:57:45.58	3.2×10^{30}	...	...	...	22.583	23.295	23.044	23.558
CX 16	31669	19:10:42.509	-59:58:42.88	3.0×10^{30}	...	...	...	...	23.484	...	...
	4190^E				...	20.861	0.135	19.090	18.935	18.949	19.278
CX 17	...	19:11:05.316	-59:59:04.08	2.7×10^{30}	...	...	...	...	...	...	...
CX 18	...	19:10:52.042	-59:59:03.74	2.7×10^{30}	...	...	...	...	...	...	...
CX 19	...	19:10:55.613	-59:59:17.60	2.2×10^{30}	...	...	...	...	...	...	...

[E] Source 7581 is outside the error circle of CX 12, but is included because it shows variability.

Source 4190 is outside the error circle of CX 16. I include it in the table because Pooley et al. (2002) concluded that this source is a BY Dra or RS CVn source based on its CMD position and Hα emission.

Table 5.2: Properties of potential counterparts to *Chandra* X-ray sources, continued. Columns 1 – 5 are as per Table 5.1. Column 6 gives previous suggestions of source type, and Column 7 gives the CMD position and categorisation of each source. Where a source is marked '(CV)', I detected the counterpart suggested by Pooley et al. (2002), but the data were not sufficient to allow me to draw any further conclusions regarding its nature. The final two columns give the best-fitting period for the NUV light curve, where a period could be found, and the false alarm probability (FAP).

1	2	3	4	5	6	7	8	9
ID_X	ID_{cat}	R.A. [hh:mm:ss]	Decl. [deg:mm:ss]	$\mathrm{L}_{X,0.5-2.5}$ [erg s^{-1}]	Previous Status	CMD position, Comments	Period [hours]	FAP
CX 1	8824	19:10:51.134	-59:59:11.83	2.1×10^{32}	CV^P	gap, DN	4.1	0.04
CX 2	12078	19:10:56.009	-59:59:37.38	6.0×10^{31}	CV^P	gap, (CV)	...	...
CX 3	...	19:10:40.354	-59:58:41.34	5.3×10^{31}	CV^P	...	...	...
CX 4	7180	19:10:51.583	-59:59:01.76	4.0×10^{31}	CV^P, DN^K	gap, CV	6.9	0.20
CX 5	7796	19:10:51.410	-59:59:05.16	3.6×10^{31}	CV/BY Dra^P	MS, (CV)	...	...
CX 6	10808	19:10:51.499	-59:59:27.05	2.2×10^{31}	CV^P	WD, (CV)	...	...
	34433					...	...	...
CX 7	6374	19:10:51.504	-59:58:56.77	1.9×10^{31}	CV^P	gap, DN	3.5	0.06
CX 8	24678	19:11:02.981	-59:59:41.94	2.1×10^{31}	...	gap	...	...
CX 9	...	19:10:51.756	-59:58:59.21	1.3×10^{31}	...	...	...	...
CX 10	9343	19:10:54.742	-59:59:13.92	6.0×10^{30}	CV^P	gap, (CV)	...	...
CX 11	...	19:10:52.411	-59:59:05.61	6.2×10^{30}	MSP^D, CV/Gal^P	...	...	...
CX 12	7592	19:10:52.730	-59:59:03.33	5.6×10^{30}	...	MS	...	...

Table 5.2: (continued)

1	2	3	4	5	6	7	8	9
ID$_X$	ID$_{cat}$	R.A. [hh:mm:ss]	Decl. [deg:mm:ss]	L$_{X,0.5-2.5}$ [erg s^{-1}]	Previous Status	CMD position, Comments	Period [hours]	FAP
	7581					MS, Variable^E	4.0	0.35
CX 13	...	19:10:40.601	-60:00:06.12	4.6×10^{30}	CV^P	...	...	...
CX 14	...	19:10:52.075	-59:59:09.18	4.2×10^{30}	...	...	...	...
CX 15	14708	19:10:55.834	-59:57:45.58	3.2×10^{30}	CV/Gal.^{P}	gap/WD, (CV)	...	...
CX 16	31669	19:10:42.509	-59:58:42.88	3.0×10^{30}		...	...	...
	4190				BY Dra^P	MS^E	...	...
CX 17	...	19:11:05.316	-59:59:04.08	2.7×10^{30}	MSP/Gal.^{P}	...	...	...
CX 18	...	19:10:52.042	-59:59:03.74	2.7×10^{30}	...	...	...	...
CX 19	...	19:10:55.613	-59:59:17.60	2.2×10^{30}	Close binary^K	...	...	...

[P] Counterpart type suggested by Pooley et al. (2002). ‘Gal.’ indicates that the source may be a galaxy.

[K] Kaluzny & Thompson (2009) found that CX 4 (their V 25) is a DN, and suggest that CX 19 is a close binary hosting an NS or a BH.

[D] The position of CX 11 is consistent with the MSP PSR D from D’Amico et al. (2002).

[E] Source 7581 is outside the error circle of CX 12, but is included because it shows variability.

Source 4190 is outside the error circle of CX 16. I include it in the table because Pooley et al. (2002) concluded that this source is a BY Dra or RS CVn source based on its CMD position and Hα emission.

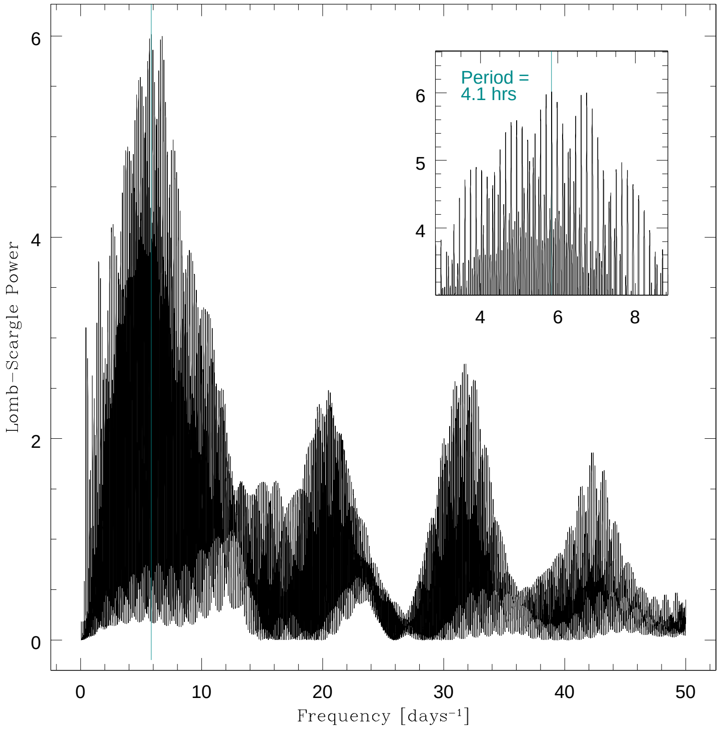

Figure 5.5: Lomb-Scargle power spectrum for source number 8824, after the mean magnitude in each observing epoch has been removed from the light curve. This source is the counterpart to X-ray source CX 1, and is a DN. The power spectrum's highest peak is at 4.1 hours. Monte Carlo simulations (see Section 3.4.2.1) suggest that this peak is ≈ 95% significant.

5.1.1 CX 1 and CX 7: Two Dwarf Novae

Very few dwarf novae have been found in GCs (Pietrukowicz et al., 2008), although to what extent this is due to selection effects remains unclear (Knigge, 2012). Prior to this study, only one DN was known in NGC 6752 (Kaluzny & Thompson, 2009). Two X-ray sources which were previously known to be CVs, CX 1 and CX 7, show DN-like outbursts in my data. This takes the number of known DNe in NGC 6752 up to three, more than any other cluster.

Pooley et al. (2002) identified source CX 1 as a CV. This source matches with star number 8824 in my catalogue, which was outside the FUV field of view but was detected in the NUV and U-band images. The light curve obtained from the NUV images, shown in Figure 5.3, shows that the source is ≈ 1.5 mag brighter in the second observing epoch than in epochs one and three. Subtracting the mean

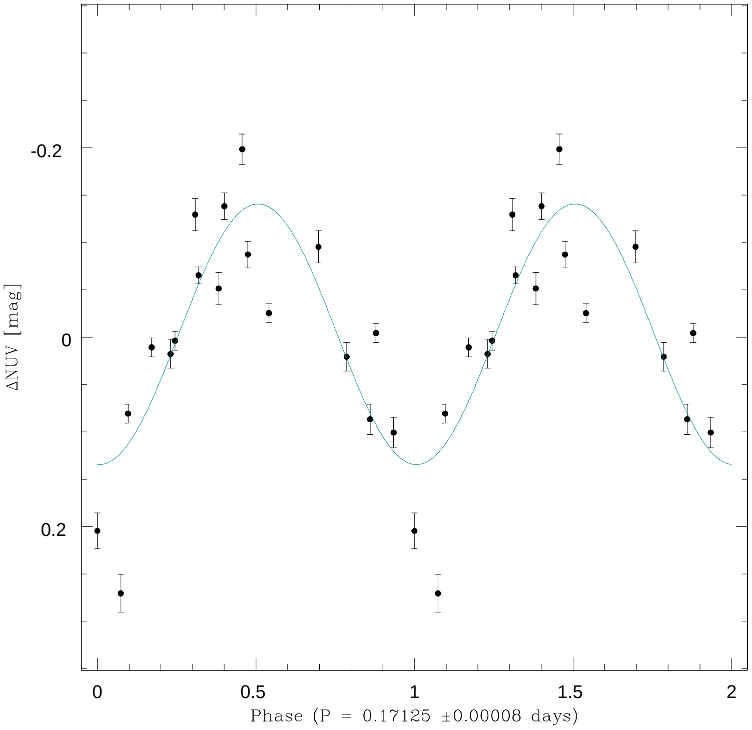

Figure 5.6: Light curve for source number 8824, folded using the period found using the Lomb-Scargle power spectrum.

magnitude from each epoch, a Lomb-Scargle power spectrum (Figure 5.5) shows that the small scale NUV variability could be fit with a period of 4.1 hours, but the peak in the power spectrum is only marginally significant ($\lesssim 2\sigma$). Figure 5.3 also shows that the amplitude of the variation is suppressed somewhat during the outburst. Figure 5.6 shows the light curve, folded on the best-fitting period. It is confused somewhat by the smaller amplitude variation during the outburst. This source exhibits X-ray emission, has short time-scale variability, as well as an outburst, and is situated in the gap between WD and MS on the CMD. I therefore argue that this source should be considered to be a confirmed CV of the DN sub-class.

CX 7 was first identified as a CV candidate by Bailyn et al. (1996), who found a period of 3.7 hours. This source corresponds to source 6374 in my catalogue and was identified in all of the wavebands used. The second panel of Figure 5.3 presents the light curve from the NUV data, which clearly shows a 6 magnitude outburst in the final observing epoch. This indicates that this source is also a DN. Subtracting the mean magnitude measured in each observing epoch from the NUV data, I used the Lomb-Scargle method described in Section 3.4.2 and found a tentative best-fit period of 3.5 hours (see the power spectrum in Figure 5.7). Using the Monte Carlo

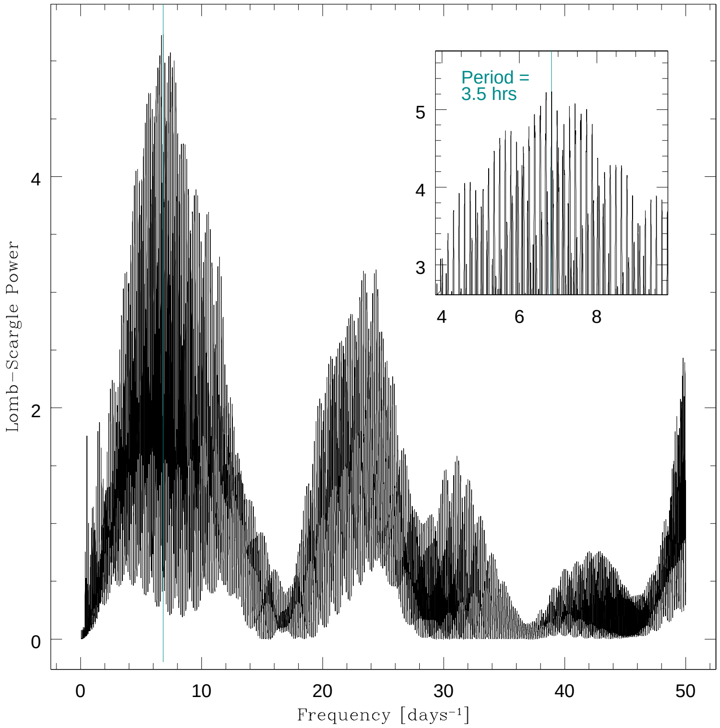

Figure 5.7: As Figure 5.5, for source number 6374, which is the counterpart to CX 7. The power spectrum indicates a marginally ($\approx 90\%$) significant peak at 3.5 hours.

simulation method described in Section 3.4.2.1, I found that the peak at 3.5 hours is higher than any in $\approx 90\%$ of simulated data sets.

Figure 5.8 shows the light curve when folded on the best-fitting period and the period found by Bailyn et al. (1996). Visual inspection of the folded light curves suggests (as expected from the power spectra) that a period of 3.5 hours gives a better fit to the shape of the light curve, but again, the data are not sufficient to draw strong conclusions regarding the period.

5.1.2 CX 8, CX 12 and CX 16: New Optical Counterpart Candidates

Two of the X-ray sources without optical counterparts in Pooley et al. (2002), CX 8 and CX 12, have new potential optical counterparts in my data. For a further source, for which Pooley et al. (2002) did suggest a counterpart, I have found a source that may be a better match.

CX 8's error circle contains source ID 24678. CX 8 is outside the FUV field of

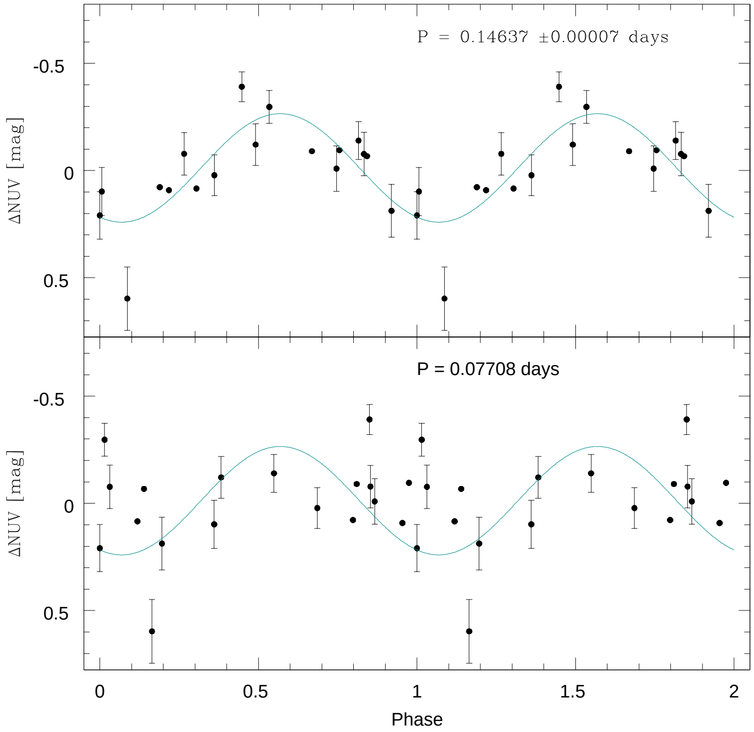

Figure 5.8: Phase-folded light curve for source number 6374. Top panel: folded using the marginally significant, best-fitting period found using the Lomb-Scargle power spectrum. Bottom panel: folded using the best-fitting period found by Bailyn et al. (1996).

view, but 24678 was detected in the U- and B-band images. The light curve does not exhibit variability, but the CMD positions indicate that it is a faint gap source. I suggest that this source may be a CV.

The main-sequence source 7592 is within the *Chandra* error circle of CX 12, but the FUV and NUV light curves showed no hint of variability. Interestingly, source 7581, which is just outside CX 12's error circle, does appear to vary, with a possible period of 4 hours ($>$ 95% confidence; see third panel of Figure 5.3 and Figure 5.9). The phase-folded light curve is shown in Figure 5.10. This source is also on the MS. It was not detected in the FUV data, despite being in the field of view. Based on the variability, possible period and the fact that the CMD position makes a faint BS classification possible, I suggest that this is an SX Phoenicis star. SX Phoenicis stars are a Population II subset of Cepheid variables. Recently, X-ray emission has been detected from Cepheid variables (Engle et al., 2009), possibly due to magnetic activity associated with pulsations, or the presence of an active binary companion. Knigge et al. (2008) found a source in 47 Tuc (their Star 2),

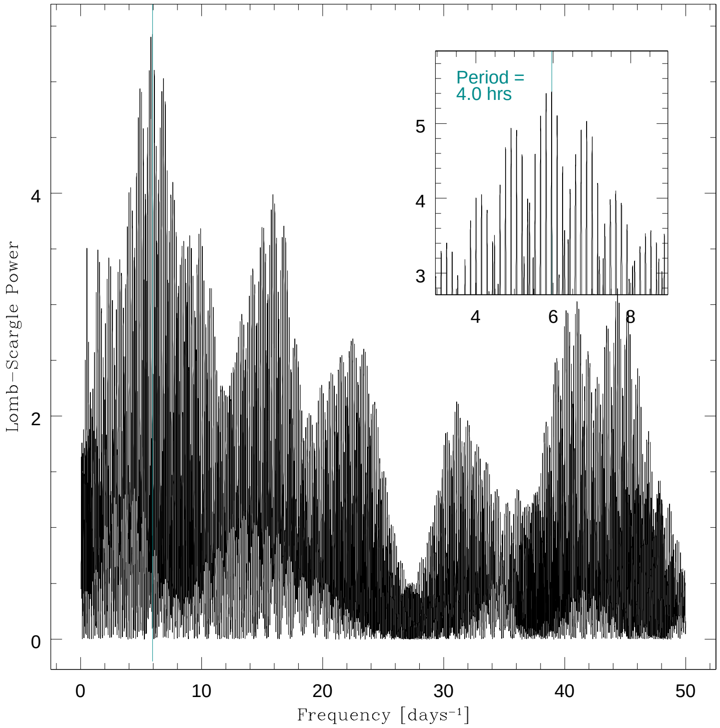

Figure 5.9: Lomb-Scargle power spectrum for source number 7581. This source is the most likely counterpart to X-ray source CX 12, and is an SX Phoenicis star. The power spectrum indicates a marginally ($>$ 95%) significant peak at 4 hours.

which they suggest is a BS star in a binary system with a massive, hot WD. A similar configuration could be invoked here: BSs are not expected to be X-ray bright, but the presence of a faint WD companion could explain the X-ray detection (CX 12 has $L_X = 5.6 \times 10^{30}$erg s^{-1}), without significantly affecting the measured colours. Source 7581 is marked on the finder chart (Figure 5.2).

Source CX 16 was identified as a BY Draconis (BY Dra) star by Pooley et al. (2002). BY Dra stars are a subset of RS Canum Venaticorum (RS CVn) stars. They are late type MS stars, which exhibit variability due to chromospheric activity. I detected the optical counterpart they suggested and agree with the CMD position that they found (on or slightly above the MS), but this source was slightly outside the 90% confidence error circle of the X-ray position. The data are not sufficient to allow further conclusions regarding this source. Another source, 31669, was found to be closer to the position of the X-ray source than the counterpart suggested by Pooley et al. This source was only detected in the B-band images, so the data are not sufficient to draw any conclusions about its nature. However, based on the proximity to the X-ray source, I suggest that this may be the true counterpart.

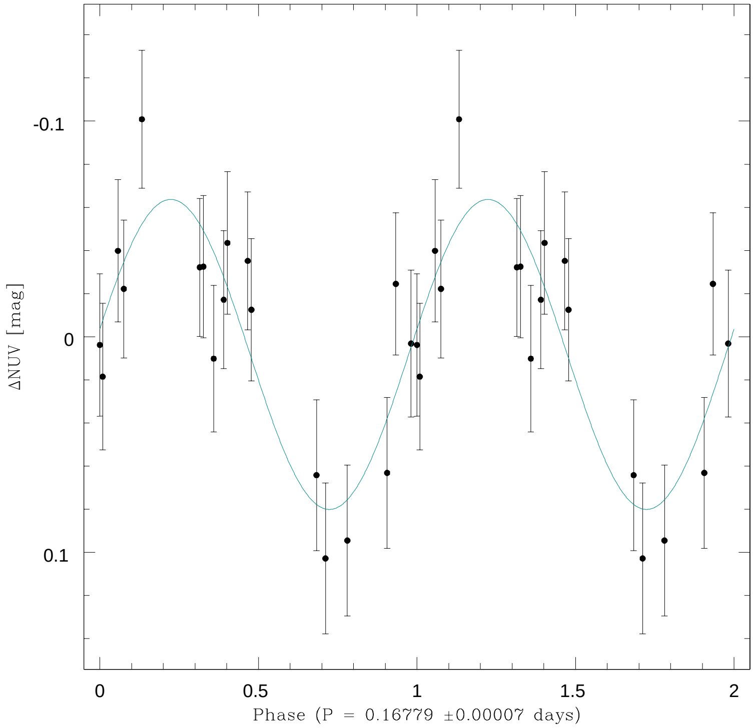

Figure 5.10: Light curve for source number 7581, folded using the marginally significant, best-fitting period found using the Lomb-Scargle power spectrum.

5.1.3 Other X-ray Sources

5.1.3.1 CX 4: A Known Dwarf Nova

CX 4 was shown to be variable by Bailyn et al. (1996), who determined a period of 5.1 hours. It was identified as a U Gem type DN by Kaluzny & Thompson (2009). This source, number 7180 in the catalogue, was identified in every waveband in this data set. Analysis of the NUV data suggests a best-fitting period of 6.9 hours, but the strength of the Lomb-Scargle peak is marginal, with simulations suggesting $\approx 90\%$ confidence. The complete NUV light curve is shown in Figure 5.3, while the Lomb-Scargle power spectrum is in Figure 5.11. Figure 5.12 shows the light curve folded on both the period suggested by Bailyn et al. (1996) and by the Lomb-Scargle power spectrum. Upon visual inspection, it is difficult to judge which is the better fit; neither appear to be particularly convincing. The folded light curves demonstrate that the data is not sufficient to draw strong conclusions regarding source 7180's nature.

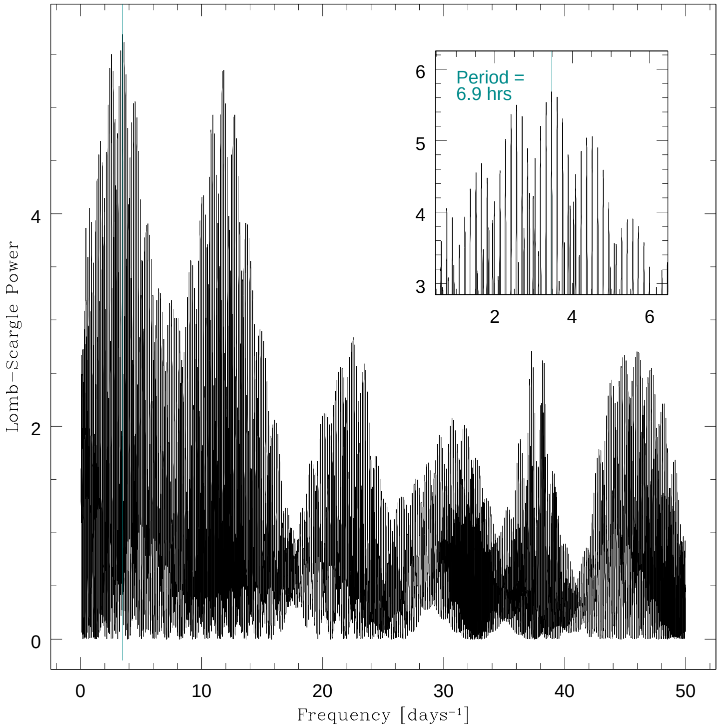

Figure 5.11: Lomb-Scargle power spectrum for source number 7180, the counterpart to CX 4 which was previously identified as a U Gem type DN. The power spectrum indicates a marginally ($\approx 90\%$) significant peak at 6.9 hours.

5.1.3.2 CX 2, CX 3, CX 5, CX 6, CX 10, CX 13, CX 15: Cataclysmic Variables

Of the remaining X-ray sources, CX 3 and CX 13 were outside the WFC3 field of view. For CV candidate sources CX 2, CX 5, CX 6, CX 10, and CX 15, I was able to detect the sources that Pooley et al. suggest are the optical counterparts, but the data are not sufficient to draw any further conclusions regarding their characteristics. For CX 6, I found a second source within the *Chandra* error circle. This is source 34433, which was identified in the B-band image only and is included in Tables 5.1 and 5.2 for completeness.

5.1.3.3 CX 11 and CX 17: The Others

I did not detect the counterpart to CX 11 that Pooley et al. found. They suggest that this source is a CV or a background galaxy, neither of which are ruled out by the lack of detection. Inspection of the image and completeness in the surrounding region suggests that any counterpart must be fainter than $NUV_{STMAG} \approx 22.5$ mag.

Source CX 17, which is thought to be an MSP or a background galaxy (Pooley

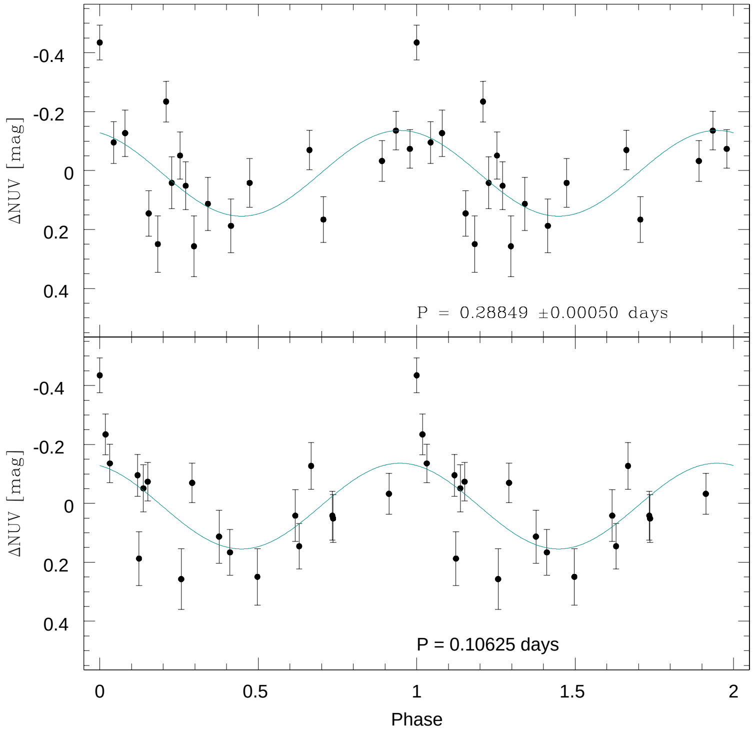

Figure 5.12: Phase-folded light curve for source number 7180. Top: folded using the period found using the Lomb-Scargle power spectrum. Bottom: folded using the period found by Bailyn et al. (1996).

et al., 2002) is outside the WFC3 field of view.

5.1.3.4 CX 9, CX 14, CX 18 and CX 19: No Optical Counterpart

Pooley et al. were unable to locate an optical counterpart for sources CX 9, CX 14, CX 18 or CX 19, and I was also unable to identify a counterpart.

Kaluzny & Thompson (2009) claim a match to CX 19, which is also visible in the observations, but this source is outside the $0\farcs2$ *Chandra* error circle in my catalogue. Kaluzny & Thompson do not state the size of the area they searched for counterparts. However, the source they found is $\approx 0\farcs5$ from the *Chandra* position and corresponds to my source 9889. While Kaluzny & Thompson suggest a period of 0.11 days, I found no such period in the NUV light curve. I believe that this source is unlikely to be a real counterpart to CX 19, and conclude that the search for a counterpart to this source should be considered unresolved.

5.2 A Search for Millisecond Pulsar Counterparts

There are five known millisecond pulsars (MSPs) in NGC 6752 (D'Amico et al., 2002), of which 3 (PSR B, D and E) are inside the field of view of the WFC3 and STIS observations. All three of these are known to be isolated (D'Amico et al., 2002), and optical emission from the pulsars themselves has not yet been detected. I used the ($\leq 0\overset{\prime\prime}{.}01$) uncertainty in the radio positions from D'Amico et al. (2002) to compare the MSP positions to the positions of sources in my catalogue, and found no optical counterparts. I note that the position of X-ray source CX 11 is consistent with that of PSR D, but I did not detect any optical sources within the search region for this source. Based on nearby sources that were detected in the study, I set an upper brightness limit on the MSP counterparts of $NUV_{STMAG} \approx 22.5$ mag.

5.3 A Search for Variable Sources

In addition to searching for variability among optical counterparts to X-ray sources, I also carried out a general search for variability using sources detected in the FUV and NUV images. This was done in two ways. First, I compared the standard deviation relative to the mean magnitude (ΔFUV or ΔNUV; see Table 5.1) for each source to that of sources of similar brightness, and searched for outliers, noting that the ΔFUV and ΔNUV values increase as brightness decreases because the larger photometric errors create more scatter. Second, for each source, I calculated a reduced χ^2 value by comparing each magnitude measurement to the mean magnitude for the source and identified sources where the reduced χ^2 value for the FUV or NUV magnitudes was significantly higher than that of other sources of similar brightness. Outliers found in either of these way are likely to be variable, and are highlighted as such in the catalogue (Table 4.3).

I then produced power spectra for the outliers and, as in Section 5.1, used a randomisation test to estimate the probability that shuffling the positions of the data could produce a higher peak (the false alarm probability, FAP). Based on the number of outliers I investigated, I expect ≈ 1 source with an FAP value < 0.015. It should be noted that the presence of excess power implies that a source varies on a particular time-scale, but this variability does not necessarily have to be periodic. For example, red noise produces excess power over a range of frequencies, but the variability is not periodic. Aside from the DNe, I found three sources with FAP < 0.015 and three more sources with FAP $\leqslant 0.005$. However, periodograms of these sources tend to have peaks at frequencies close to zero, suggesting that the

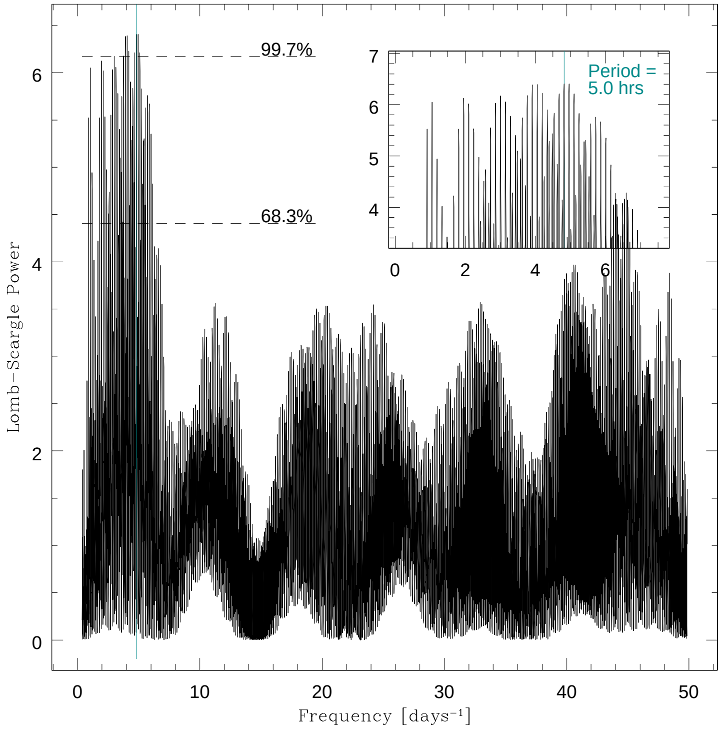

Figure 5.13: Lomb-Scargle power spectrum for source number 596. This periodogram has FAP = 0.01, but there are a number of peaks of similar significance close to zero, indicating that the power spectra is dominated by long-term trends.

power spectra in these cases are affected by long-term trends so the period detection is marginal, at best.

As an example, one of the periodograms with a low FAP is shown in Figure 5.13. This source's power spectrum has a number of peaks of similar power. Figure 5.14 shows the light curve fitting on the 'best-fitting' period of 5 hours (frequency = 4.81 days^{-1}), as well as two other periods which had strong LS periodogram peaks. This demonstrates that the light curve can be fit almost as well whether a period of 5, 8 or 11.2 hours is chosen. Clearly, the variation cannot be well modelled with a simple sine wave, and a low false alarm probability in the Lomb-Scargle test is not sufficient evidence to suggest that the true period of variation has been found. A combination of Lomb-Scargle result, FAP, and careful inspection of the light curve is necessary to ensure that the resulting period is real.

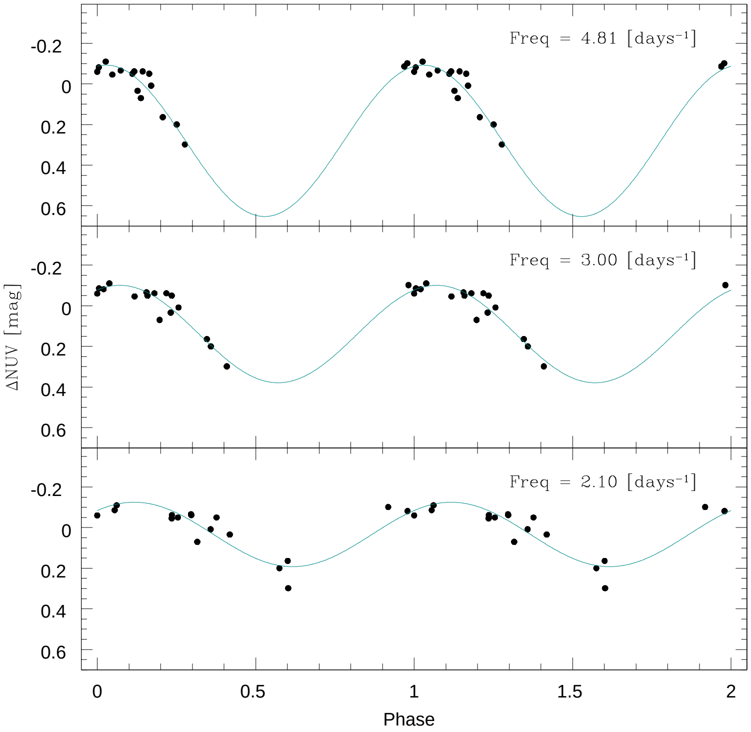

Figure 5.14: Light curve for source number 596 folded on various periods. Top panel: folded on the best-fitting period (5 hours) as determined from the LS power spectrum. Middle panel: folded on a period of 8 hours. Bottom panel: folded on a period of 11.24 hours. In all cases, the error bars are too small to be apparent. The poor fit to the data indicates that the variability exhibited by this source cannot be well modelled using a simple sine-wave.

5.4 Conclusions

By comparing the positions of sources in the catalogue with those of known X-ray sources, I have found that two X-ray sources, CX 1 and CX 7 which were previously thought to be CV candidates are actually dwarf novae. Prior to this study only one DN was known to exist in NGC 6752. With a total of three known dwarf novae, NGC 6752 now harbours more known DNe than any other GC. Shara et al. (1996) and Pietrukowicz et al. (2008) suggest that dwarf novae appear to be abnormally rare in globular clusters compared to the field, but Knigge (2012) suggests that this may be due to selection effects. This survey shows that NGC 6752 might be a good place to study known dwarf novae in a globular cluster environment, since all three can be observed in one telescope pointing. It also demonstrates how useful UV observations can be in general in searching for DNe.

I have identified previously unknown optical counterparts to two X-ray sources, and suggest that one is a CV and the other is an SX Phoenicis star. Another source, number 7582 in the catalogue, which is just outside the X-ray position uncertainty of CX 12, shows variability with a period of 4.1 hours. One X-ray source, CX 16, was thought to be a BY Dra binary. I suggest an alternative optical source as the true counterpart. A search for variability revealed a number of potentially variable sources, which are indicated in the catalogue.

The work described in this chapter demonstrates the importance of using multi-wavelength, and particularly UV wavelength studies of GCs as tools for investigating the X-ray populations. Using a combination of X-ray, UV and optical observations, sources can be classified more securely than using just one type of survey. Secure classifications of X-ray sources and other close binaries are essential for further investigations of the dynamical history and status of the GC and comparisons between such populations in globular clusters and the field.

The most exciting phrase to hear in science, the one that heralds new discoveries, is not ‘Eureka!’ but ‘That’s funny...’

I. ASIMOV (1920 – 1992)

6

The Globular Cluster NGC 6752: The Search for Broadening in the Main-Sequence

Globular clusters were once thought to be made up of stars that formed at the same time and from the same material, making them reliable examples of simple single stellar populations. Recent observations have, however, provided overwhelming evidence that GCs are much more complex than traditionally believed. Evidence from spectroscopy and, more recently, photometry has revealed differing chemical abundances and multiple CMD sequences, indicating that multiple generations of stars are contained within individual clusters.

In this chapter, I search for hints of multiple stellar populations in the NUV - U and V - I CMDs of NGC 6752.

6.1 The Possibility of Multiple Stellar Populations in NGC 6752

A summary of the development of knowledge of multiple populations of stars in GCs is included in Chapter 1. In this chapter, I focus on the possibility of multiple MS populations residing within NGC 6752. Throughout this chapter, as before, I assume that the phrase ‘multiple populations’ is synonymous with ‘multiple generations of stars’.

The Galactic globular cluster NGC 6752 is one of the closest and most frequently observed GCs and is a known contender for harbouring multiple populations. Strong evidence of abundance anomalies has been found (for example, Pasquini et al. 2008 found a difference in nitrogen abundance between two MSTO stars of more than an order of magnitude), and it has been suggested (Kravtsov et al., 2011) that bluer and redder RGB sources on the U - B CMD are radially segregated.

Milone et al. (2010) analysed the MS and SGB of NGC 6752 (excluding the central $1'$ due to crowding) and found evidence for a broadened MS, and some indication of a split in the MS. In this chapter, I follow closely the analysis method used by Milone et al. (2010), and search for further evidence of MS broadening, including, for the first time, the core of the cluster. Searching for signs of broadening in the core is important because radial segregation of multiple populations is expected from their formation mechanisms. As described in Section 1.3.2.6, the leading theories on the origin of the material which forms the second generation stars involve ejecta from massive stars, suggesting that the second generation forms close to the core of the cluster. Finding evidence of broadening in the core is, therefore, vital if we are to understand the origin of the multiple populations. In this search, I use data taken with the ACS and WFC3 on-board *HST* to study broadening in the MS of the V - I and NUV - U CMDs. I also include a search for a radial trend in the broadening.

The structure of this chapter is as follows. In Sections 6.2 and 6.3, I outline the observations and data reduction method, including routines required to correct for position-dependent instrumental effects on measured colours. Sections 6.4 and 6.5 contain a description of the search for broadening of the MS in the NUV - U and V - I CMDs. In Section 6.6, I describe the simulations I used to assess the validity of the claimed levels of broadening within each CMD, and investigate the validity of the approximations used in the simulations created throughout this investigation. In Section 6.7, I take advantage of the fact that I have two independent CMDs

(NUV - U and V - I) and compare the colours of stars in both CMDs; this allows me to assess the strength of the conclusions drawn from the apparent broadening. In Section 6.8, I search for radial trends in the amount of broadening. I briefly discuss the intriguing signs of multiple populations in the SGB and RGB in Section 6.9, and in Section 6.10, I summarise the conclusions of this work.

6.2 The Observations

For this study, I used data from two instruments on-board *HST*, as summarised in Table 6.1. First, I used data taken with the WFC3/UVIS filters F225W (NUV) and F390W (U-band). Second, I used data taken using the ACS/WFC, with the F606W (V-band) filter and the F814W (I-band) filter.

The ACS has a large field of view, at $202'' \times 202''$, and a plate scale of $0\farcs05$/pixel, while the WFC3 has a slightly smaller field of view of $162'' \times 162''$, but a finer plate scale of $0\farcs04$/pixel (see Appendix B for details of *HST* instruments). The improved resolution afforded by the WFC3 meant that crowding in the core is less of a problem, particularly at these bluer wavelengths, while it is possible to observe a reasonable portion of the cluster in one exposure, allowing significant numbers of stars to be observed simultaneously. In Chapter 4, I showed that the expected completeness in the V- and I-band data is over 50% in the core of the cluster, and almost 100% in the outer region, down to a limiting magnitude of $V_{STMAG} = 19.7\,$mag, which, for MS sources, corresponds to $I_{STMAG} = 20\,$mag. While I caution that completeness will affect the number of faint sources detected in the core, this should not impact the conclusions drawn regarding the measured broadening.

In order to ensure that any broadening I observed in the CMD was not merely due to photometric errors, I chose data sets that are easily divided into two groups, so that photometry could be carried out on two comparable, but independent, subsets of the data. The images were split into groups such that one group contains the images taken earliest, and the other group contains the later images; in this way, any time-dependent problems with the images will be exaggerated, rather than hidden. For the sake of clarity, I refer to Group 1 or Group 2 throughout; note that for the F390W images, each ‘group’ actually contains only one image (see Table 6.1).

Table 6.1: Summary of observations used in this investigation.

Instrument/ Detector	Field of View	Plate Scale [″/pixel]	Waveband	Filter	Date	Number × Exptime Overall	Per Group
WFC3/UVIS	162″ × 162″	0.04	NUV	F225W	2010 July 31, August 7, 21	18 × 120 s	9 × 120 s
WFC3/UVIS	162″ × 162″	0.04	U	F390W	2010 January 5	2 × 348 s	1 × 348 s
ACS/WFC	202″ × 202″	0.05	V	F606W	2006 May 24	4 × 35 s	2 × 35 s
ACS/WFC	202″ × 202″	0.05	I	F814W	2006 May 24	4 × 40 s	2 × 40 s

6.3 Data Reduction

Photometry was performed on each group of images individually, as well as on the overall data sets, which were used to create a reference catalogue for each filter with the smallest possible photometric errors.

Photometry of the ACS and WFC3 images was carried out using the ACS and WFC3 module of `DOLPHOT`, respectively. As described in Section 4.2.2, `DOLPHOT` performs photometry on individual images, giving the output in the WCS of a reference image. In this case, I used `multidrizzle` running under `PyRAF` to combine all of the F225W images into a drizzled, distortion-corrected, master image, which I used as the reference image for the photometry of the F225W and F390W images. Similarly, I created a reference image for the F606W and F814W photometry by combining all of the F606W images. `DOLPHOT` is capable of performing photometry simultaneously on images from different filters, as long as sources can be found in each individual image that can also be found in the reference image. The `DOLPHOT` output contains the result for each source in each individual frame, as well as the combined result for each filter used.[1] Photometry was then performed on the following sets of images, following the method described in Section 4.2.2:

- ‘Overall’ NUV and U-band – All 18 of the 120 s F225W images and both of the 348 s F390W images,
- ‘Group 1’ NUV and U-band – The first 9 F225W images and the first of the F390W images,
- ‘Group 2’ NUV and U-band – The remaining 9 F225W images and the other F390W image,
- ‘Overall’ V- and I-band – All 4 of the 35 s F606W images and all 4 of the 40 s F814W images,
- ‘Group 1’ V- and I-band – The first 2 F606W images and the first 2 F814W images,
- ‘Group 2’ V- and I-band – The remaining 2 F606W images and the latter 2 F814W images.

---

[1] This feature was not used in the full survey of NGC 6752 described in Chapter 4; `DOLPHOT` was only used to photometer data from two of the five filters in that investigation, so the work involved in preparing the images for combined photometry would have been comparable to that in simply matching the catalogues afterwards.

Using the parameters recommended in the `DOLPHOT` manual, I removed sources which had extreme sharpness estimates, which `DOLPHOT` suggested were not stars (cosmic rays etc.) and extreme crowding measurements. This minimised contamination of the catalogue from non-stellar objects, or stars who were poorly measured.

6.3.1 A Position-Dependent Error Correction

Determining the level of broadening in the CMD requires accurate photometry, so it is important to account for any position-dependent instrumental effects that might lead to errors in the measured colours. These might be caused by differential reddening, inadequacies in the PSFs, telescope breathing, or inadequacies in the charge-transfer efficiency correction built into the *HST* pipeline and `DOLPHOT`.

Charge transfer efficiency (CTE) is a measure of how well the CCD is able to move charge from one pixel to the next during the chip readout phase. A perfect device would transfer all of the charge and would have CTE of 100%. In reality, defects in the silicon cause charge to be trapped momentarily in certain pixels and released some time (microseconds to seconds) later. Some defects may be introduced during the manufacturing of the device, but more develop over time as a result of radiation damage. *HST* CCDs are particularly susceptible to CTE degradation, because *HST*'s low-Earth orbit frequently crosses through parts of the Earth's Van Allen radiation belt. Moreover, the CTE degradation in *HST*'s newest instrument, WFC3, is considerably worse than anticipated. This may be as a result of the last few years' increase in solar activity, resulting in an increase in solar wind strength and more charged particles in the magnetosphere.

CTE problems manifest themselves in two ways. Firstly, they cause a loss in source flux, so sources falling on affected pixels appear fainter. Secondly, the delayed release of charge gives erroneously high flux readings for pixels further from the CCD chip amplifiers, making sources appear to have tails. Figure 6.1 shows an example of the visual effect of CTE problems.

The amount of source flux lost due to CTE inefficiencies depends on three major factors: pixels further from the amplifiers are more prone to problems than those near to the amplifiers, because the charge must transfer via more pixels, so is more likely to encounter a trap; fainter sources are affected more than bright sources, because they lose proportionally more of their flux; images with lower background flux suffer more than those with high background, because a higher background flux is more likely to fill some of the charge traps, reducing the loss of source flux during readout.

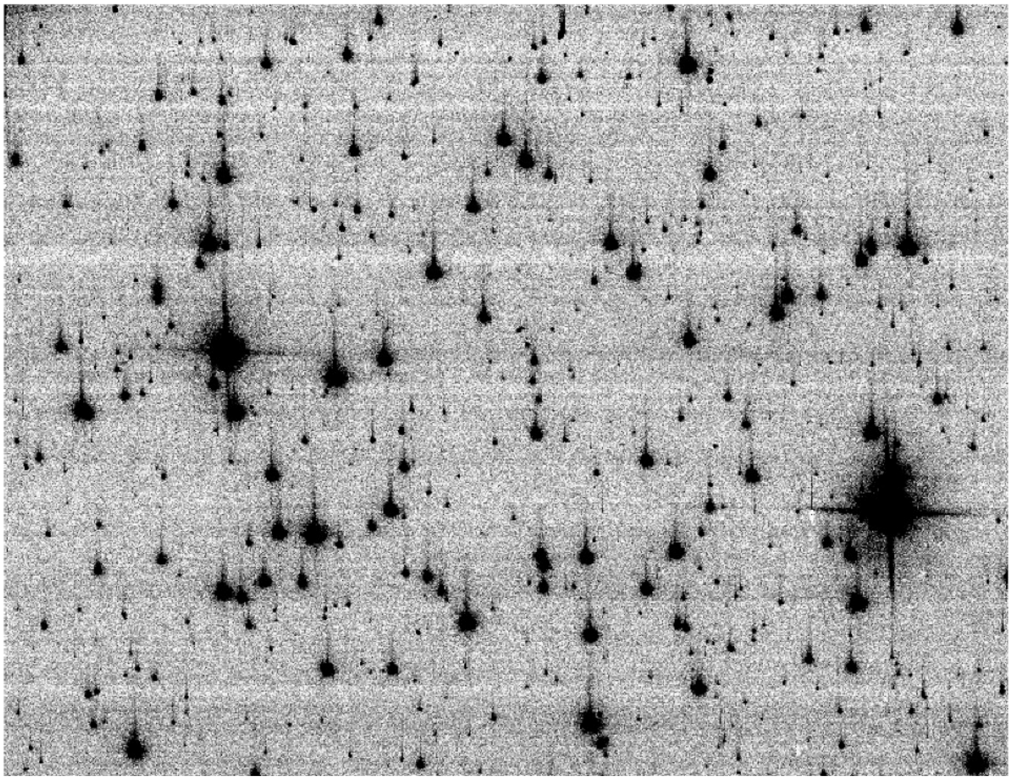

Figure 6.1: The effect of CTE inefficiencies. This is part of a 30 s, *HST*/ACS/WFC exposure of the GC 47 Tuc (image ja9bw2ykq_flt.fits). The trails extending upward from the stars are due to imperfect CTE (Anderson & Bedin, 2010).

In this investigation, CTE problems are far more obvious in the NUV and U-band images than in the V- and I-band ones. Moreover, the V- and I-band images are taken with the ACS, for which the level of CTE is well understood and well-established corrections are available.[2] Furthermore, the V- and I-band images were taken at almost the same alignment, so sources positioned farthest from the amplifier (which are, therefore, most prone to flux loss) in V-band images are also farthest from the amplifier in the I-band images[3]. The NUV and U-band images, on the other hand, were taken with the WFC3, for which CTE problems are less well understood and are poorly accounted for by current correction algorithms. The images taken with the U-band filter are aligned almost perpendicular to the NUV images. This means that, unlike in the V- and I-band case, sources are affected differently in the two data sets.

---

[2] Note that a new version of the CTE correction for the ACS/WFC has been released since this investigation was completed. The new version is based on work by Anderson & Bedin (2010) and Ubeda & Anderson (2012), and includes a correction algorithm which takes into account pixel-based CTE, and time and temperature dependent CTE losses.

[3] I note that there is no reason to assume that the flux loss in the two filters is the same; merely that there is likely to be a spatial trend in the proportion of flux lost in two filters at the same alignment.

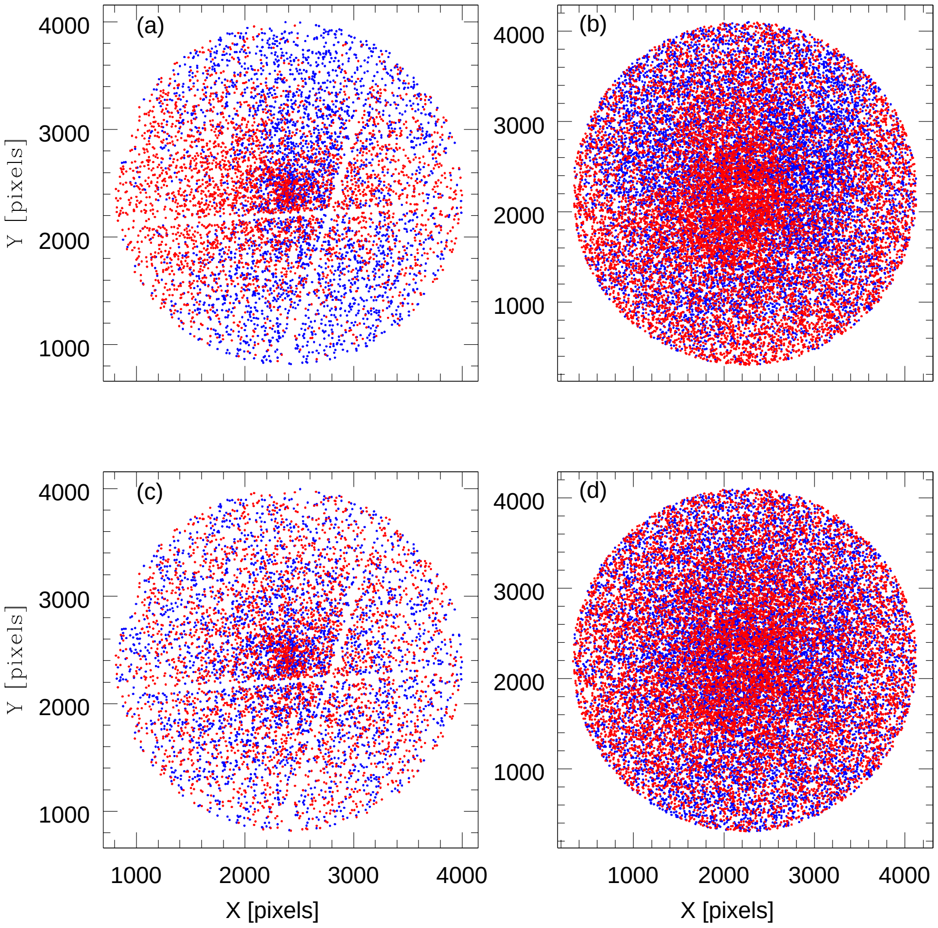

Figure 6.2: Before and after the catalogues are corrected for position-dependent instrumental colour effects. Panel (a) shows the X, Y positions of MS sources from the NUV - U CMD, before the correction algorithm is applied. Sources are coloured red and blue depending on their CMD positions relative to an MSRL. The red and blue sources are not distributed isotropically; areas of almost entirely red or blue can be seen. Panel (b) shows the same thing, for the V- and I-band MS sources. Panels (c) and (d) show the positions of the red/blue NUV and U-band, and V- and I-band sources, respectively, after the colour correction algorithm has been applied. The red and blue sources are much more evenly distributed.

Consider, for example, a source positioned far from the amplifier in the NUV images. This source will appear fainter than it should in the NUV measurements. It is not necessarily among the most affected sources in the U-band images, however, so may lose less flux in U-band, and appear red in the CMD. Sources most prone to flux loss in the U-band images, on the other hand, appear fainter in the U-band, but not necessarily in the NUV, so appear blue. Furthermore, the NUV exposures are fairly short (120 s each; see Table 6.1), so there is a low background ($\lesssim 10$ counts), and the MS sources considered in this investigation are relatively faint ($\lesssim 700$ counts), making these images susceptible to CTE effects. The U-band images are longer (348 s each), with higher background and source flux ($8 - 30$ and $5000 - 60000$ counts, respectively), so CTE problems have less impact than in the NUV case, but the effect is still not negligible.

In the top panels of Figure 6.2, sources are coloured red or blue depending on their position relative to a main-sequence ridge-line, to demonstrate the different ways that CTE and other position-dependent problems manifest in the two CMDs. In the NUV and U-band case (panel (a)), there is an excess of red sources along the near-horizontal axis (the gap along this axis is the chip gap in the NUV images), and a large population of blue coloured sources along the near-vertical, U-band chip gap. In the V- and I-band case (panel (b)), the pattern is not so obvious, but it is still clear that something is affecting the colours and creating excessively red and blue areas.

Regardless of the reason for the position-dependent colour variations shown in Figure 6.2, an empirical, star-by-star correction can be applied to improve the measured colours. The procedure, which follows Milone et al. (2010), is as follows. The steps are illustrated in Figure 6.3.

1. Refer to panel (a) of Figure 6.3.
   Use the overall V - I CMD to plot a main-sequence ridge-line (MSRL) by finding the median colour in successive, narrow magnitude bins. Refine the result using sigma-clipping, performed using the perpendicular distance from the ridge-line to each source. This ensures that the whole MSRL is treated equally, regardless of the direction of the MSRL at a given magnitude, to give as precise a ridge-line as possible.

2. Refer to panel (b) of Figure 6.3.
   Select a ‘target’ source to be corrected. Calculate the distance (defined as difference in colour, rather than perpendicular distance) from this source in the (overall) CMD to this ridge-line.

3. Refer to panel (c) and (d) of Figure 6.3.
   From the ‘target’ source, find the nearest 50 – 100 MS stars (on the image) that are

   - ‘well-behaved’ (i.e. the `DOLPHOT` output shows a high signal to noise, very small photometric error, and good values for the χ, sharpness, crowding and roundness parameters),
   - within ± 2 I-band magnitudes of the ‘target’ source,
   - within 250 pixels (10″) of the target source. This leads to some ‘target’ sources having $<$ 100 ‘calibration’ sources (but all ‘target’ sources have at least 50 ‘calibration’ sources).

4. Refer to panel (d) and (e) of Figure 6.3.
   Find the mean distance in colour from these sources to the MSRL.

5. Refer to panel (f) of Figure 6.3.
   Correct the ‘target’ source’s colour by this amount.

6. Choose the next source to be used as a ‘target’ source and repeat steps 2 – 5.

A similar process is carried out for sources in the NUV - U CMD, with two changes:

- Due to the more exaggerated change in the width of the MS spread with magnitude (see Figures 4.1 and 6.4), I limit the sources to those within ± 0.7 U-band magnitudes of the chosen source.

- The lower stellar density in the NUV and U-band mean that I use the nearest 10 – 50 MS stars to calculate the correction factor in these wavebands.

Experiments with different, reasonable, magnitude limits gave consistent results, as did using the median distance for the colour correction instead of the mean. As the groups of images are taken at almost identical pointings, creating separate MSRLs for the Group 1 and Group 2 images, and running the correction algorithm on each group independently of the overall image, made little difference.

The lower panels of Figure 6.2 show the position of red and blue sources after the colour correction algorithm has been applied. The distributions of red and blue coloured sources are much more even in these panels, indicating that the position-dependent colour gradients have been reduced.

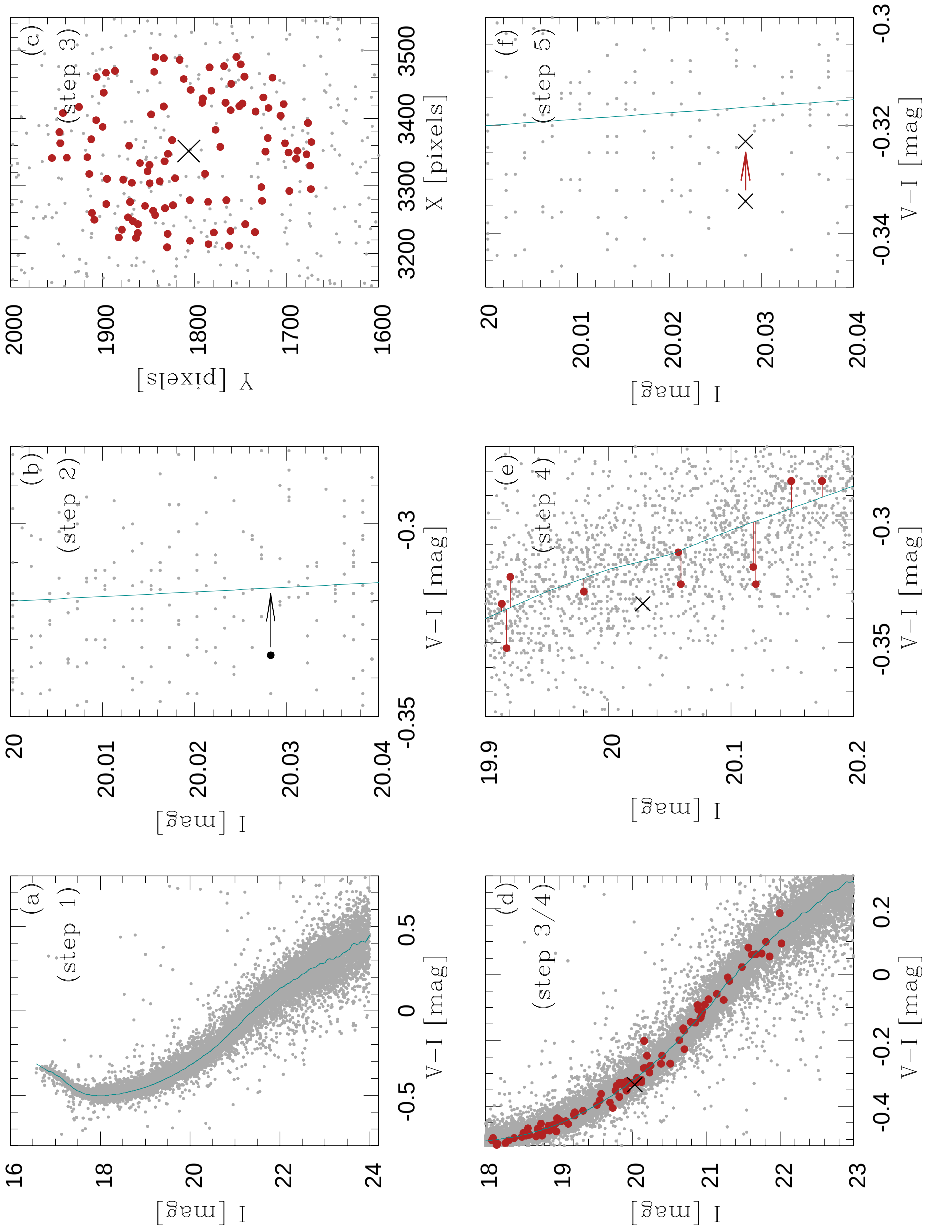

Figure 6.3: Illustration of the key steps in the algorithm used to correct for position-dependent instrumental colour effects. See text for details.

6.4 The Search for MS Broadening in the NUV - U CMD

In this section, I investigate broadening in the MS of the NUV - U CMD. Anderson et al. (2009) showed that using independent data sets is a reliable way to distinguish between photometric errors and real broadening. If the broadening is real, then a source that is measured to be towards the red side of a sequence in one half of the data should be measurably redder than average in the other half. If it is due to photometric errors, however, the colour in one half of the data will not be the same in the other half of the data. Milone et al. (2010) used this technique to study the MS of NGC 6752 using B- to I-band data, excluding the innermost $1'$. Here, I follow this process, but extend it by using UV images and including the cluster core.

First, I create an MSRL for the NUV and U-band Group 1 images, using the process described in Section 6.3.1, and find the distance from each source to this line. In panel (a) of Figure 6.4, the distance from the MSRL to each source is plotted against U-band magnitude, and the sources are coloured red or blue depending on their position relative to the MSRL. I note that the distance from the ridge-line is a simple difference in colour, rather than the distance perpendicular to the MSRL.

I then create an MSRL for the Group 2 images and find the sources' distance from this MSRL on the Group 2 CMD. This is plotted in panel (b). Each star has the colour that was assigned to it in panel (a). The colours are reasonably well maintained between the two panels.

Panel (c) emphasises the relationship between the source positions in panels (a) and (b), by displaying the correlation between the colours of each star in Group 1 and Group 2. I have split this panel into separate magnitude bins to avoid confusion due to the increase in photometric errors at fainter magnitudes. In each magnitude bin I include a diagonal line with a gradient of 1, indicating the expected result if there was a perfect correlation and no photometric errors. I also show the best-fit line to the data. Table 6.6 lists the gradient of the best-fit lines to the data in each magnitude bin, as well as Spearman's rank test results. A Spearman's rank test is a non-parametric measure of statistical correlation between two data sets. Without being affected by the relative spreads of the data, it simply assesses how well the relationship between the data sets can be described with a monotonic function. A positive Spearman's rank correlation coefficient means that, in general, as one variable increases, so does the other. A perfectly monotonic function would give a Spearman coefficient of $+1$. The gradients shown in Table 6.6 are close to 1,

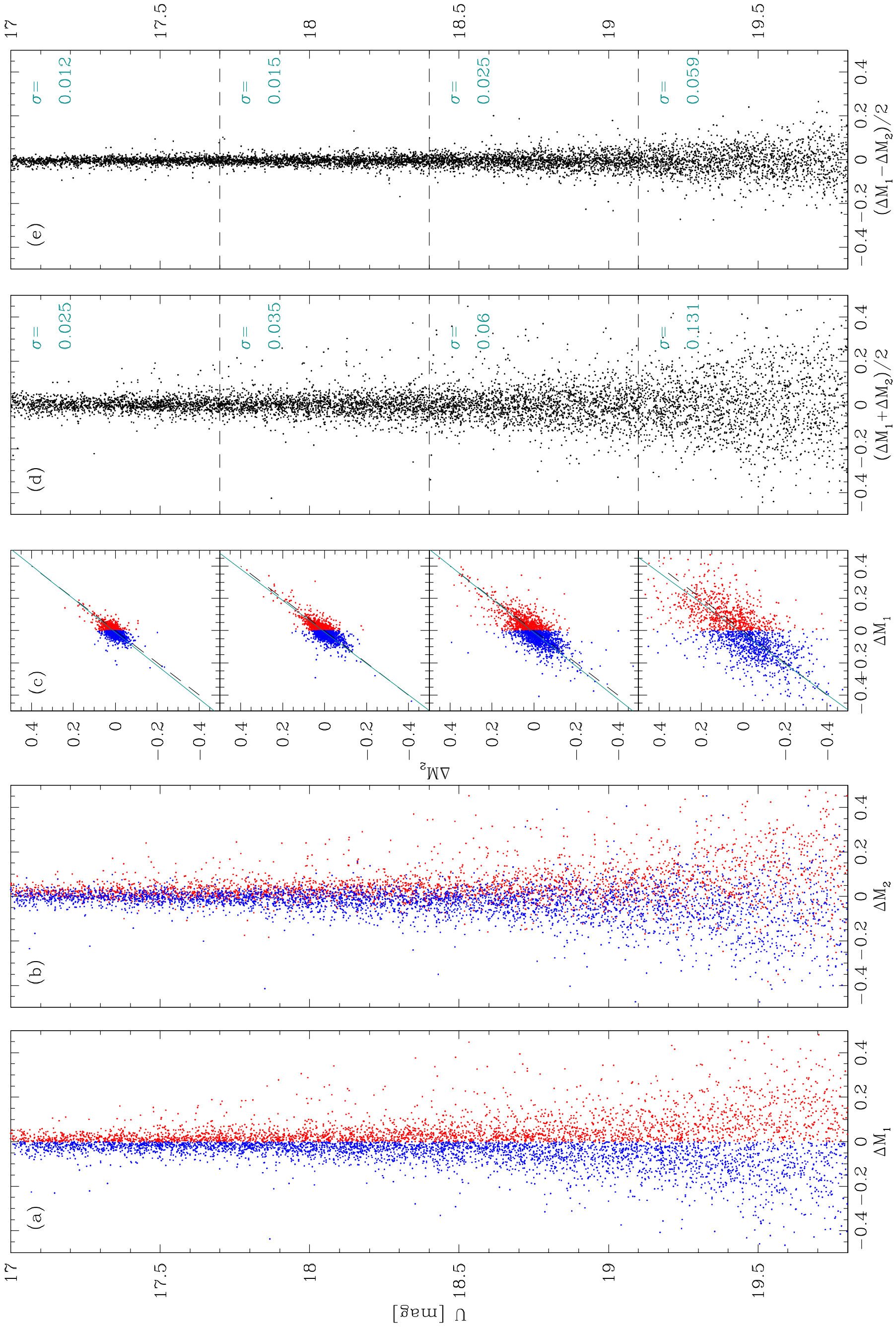

Figure 6.4: Evidence for broadening in NUV - U data. Panel (a): straightened MS for Group 1 data. Stars are coloured blue or red depending on their colour relative to the MSRL. Panel (b): straightened MS for Group 2 data. Each source is plotted with the colour assigned to it in panel (a). Panel (c): correlations between the two measurements, in U-band magnitude bins. The black, dashed line has a gradient of 1 and is the expected result if there was a perfect correlation between the measurements, with no photometric errors. The dark green, solid line shows the actual best-fit line to the data. Panel (d): the mean distance of each source from the MSRLs. Panel (e): estimates of errors in the mean colour.

demonstrating that the colours measured in Group 1 and 2 are consistent, and the Spearman's rank correlation coefficients are all positive, showing that there is a correlation. The Spearman's rank values indicate that the correlations are strongly statistically significant.

In panel (d) of Figure 6.4, I calculate the mean distance of each source from the MSRL. Combining Group 1 and Group 2 data in this way means that the errors in this panel are smaller than in either of the individual panels ((a) or (b)) by a factor of $\sqrt{2}$. Panel (e) shows estimates of the colour errors, found by calculating half of the difference between the independent colour measurements. In each section of panels (d) and (e), I give the standard deviation of the spread, as determined from the interquartile range. It is immediately apparent that the colour errors seen in panel (e) cannot account for all of the MS spread seen in panel (d).

An estimate of the intrinsic broadening in each magnitude bin can be calculated using

$$\text{broadening} = \sqrt{\sigma^2_{Mean} - \sigma^2_{Error}}.$$

Table 6.2 lists the intrinsic broadening measured in each magnitude bin.

The amount of helium enhancement required to reproduce the amount of MS broadening seen here can be determined using comparisons to BasTI models (see Section 4.3). In Table 6.3, I list the amount of broadening produced at various magnitudes when different helium enhancement levels are invoked in the models. I show the colour difference between a helium abundance of $\mathrm{Y}=0.249$ and three other values: $\mathrm{Y}=0.3$, 0.35, 0.4. These correspond to relative helium enhancements of 20, 40 and 60%. In each U-band magnitude bin considered, a helium abundance of $\mathrm{Y}=0.3$ (so $\Delta\mathrm{Y}=0.05$; an enhancement of or 20%) is sufficient to reproduce the MS broadening seen in the data. The models do not allow for a more precise measurement of the helium abundance required, but interpolating on the grid of available models, I suggest that the actual helium abundance required is $\mathrm{Y}=0.27\pm0.01$ ($\Delta\mathrm{Y}=0.02\pm0.01$), which corresponds to an enhancement of 8%.

Table 6.2: Estimates of the level of broadening of the MS in the NUV - U CMD, at different U-band magnitudes. The first two columns give the U-band magnitude bin considered and the number of sources included. Columns 3 and 4 give the results of the comparison between Group 1 and Group 2 measurements (see panel (c) of Figure 6.4); Column 3 gives the gradient of the best-fit line, and Column 4 lists the Spearman's rank correlation coefficient (SRCC). Columns 5 and 6 give the standard deviation of the mean distance from the MSRL and the standard deviation of the error on this distance. In both cases, the standard deviation is determined from the interquartile range, and is also shown on panel (d) and (e) of Figure 6.4. The final column lists the estimated upper limit on the intrinsic broadening, given by $\sqrt{\sigma_{Mean}^2 - \sigma_{Error}^2}$.

U	$N_{sources}$	Group 1 vs Group 2		σ_{Mean}	σ_{Error}	Intrinsic Broadening
[mag]		Gradient	SRCC	[mag]	[mag]	[mag]
17.0 – 17.7	1475	0.966 ± 0.041	0.549	0.0245	0.0122	0.0213
17.7 – 18.4	1831	1.024 ± 0.028	0.627	0.0355	0.0154	0.0320
18.4 – 19.1	1887	0.967 ± 0.030	0.621	0.0603	0.0254	0.0547
19.1 – 20.0	1618	1.058 ± 0.036	0.627	0.1310	0.0587	0.1171

Table 6.3: The level of helium enhancement required to reproduce the measured MS broadening in the NUV - U CMD. The first column gives the U-band magnitude bin considered. In the data, the sources are split according to these magnitude bins; in the models, the median magnitude in each bin is used. The second column gives the intrinsic broadening measured in the data. Columns 3 – 5 give the level of broadening expected from BasTI models if different helium enhancements are used. Starting with the (canonical) helium abundance of Y= 0.249, I list the values obtained comparing the Y= 0.249 colours to helium abundances of Y= 0.3, 0.35, and 0.4, corresponding to enhancements of 20, 40 and 60%.

U	Measured Broadening	Model Broadening: Y= 0.249 and		
[mag]		Y= 0.30	Y= 0.35	Y= 0.40
17.0 – 17.7	0.0213	0.0384	0.0853	0.1310
17.7 – 18.4	0.0320	0.0874	0.1448	0.2099
18.4 – 19.1	0.0547	0.1204	0.2113	0.2908
19.1 – 20.0	0.1171	0.1538	0.2691	0.3668

6.5 The Search for MS Broadening in the V - I CMD

The search for broadening was repeated for the V- and I-band CMD, and the result is shown in Figure 6.5 and Table 6.7. The broadening is less obvious here than in the NUV and U-band data; the difference between the distributions in panel (d) and (e) of Figure 6.5 is less pronounced than in Figure 6.4, and the maximum intrinsic broadening in the V- and I-band, listed in Table 6.7, is considerably smaller than that shown in the NUV and U-band data. This is in line with findings in other clusters, which suggest the colour spread due to metal enhancement has more effect in blue wavebands than in V- and I-band (see, for example, Milone et al. 2012a, their Figures 7 – 9).

Comparison between the broadening seen in the data and that seen in BasTI models of different helium abundances (see Table 6.5) shows, as in the NUV - U case, that the helium enhancement required to reproduce the observed broadening is $< 20\%$. As before, I interpolated the models to provide broadening estimates for a finer grid of helium abundances. As the correlation between helium abundance and broadening is not always linear, I restricted the calculation to magnitude bins in which the change in the level of broadening with helium enhancement could be well approximated by a straight line, to allow for a more straightforward interpolation (I used only those bins with a product moment correlation coefficient, $r > 0.995$; this included only magnitude bins for which $19.2 < \mathrm{I} < 21.6$). I suggest that the helium abundance required to reproduce the observed broadening is $\mathrm{Y} = 0.265 \pm 0.01$ (so $\Delta\mathrm{Y} = 0.015 \pm 0.01$; helium enhancement of 6%), which is consistent with the result found in the NUV - U case.

Panel (c) of Figure 6.5 shows the correlation between the colour measurements in the Group 1 and 2 images. Although the Group 1 and Group 2 colours' correlation appears to be worse than that of the NUV and U-band measurements, the best-fit line has a positive slope in every magnitude bin, indicating that there is a positive correlation, and Spearman's rank tests show that the correlation is significant at all I-band magnitudes.

Panel (d) shows the mean spread of the data. As this is the combined data set, the colour error on any point here is a factor of $\sqrt{2}$ smaller than in either panel (a) or (b), making this the most accurate demonstration of the true colour, and the most likely place to be able to distinguish features in the MS. I see no suggestion of the split in the MS of the V - I CMD suggested by Milone et al. (2010), however.

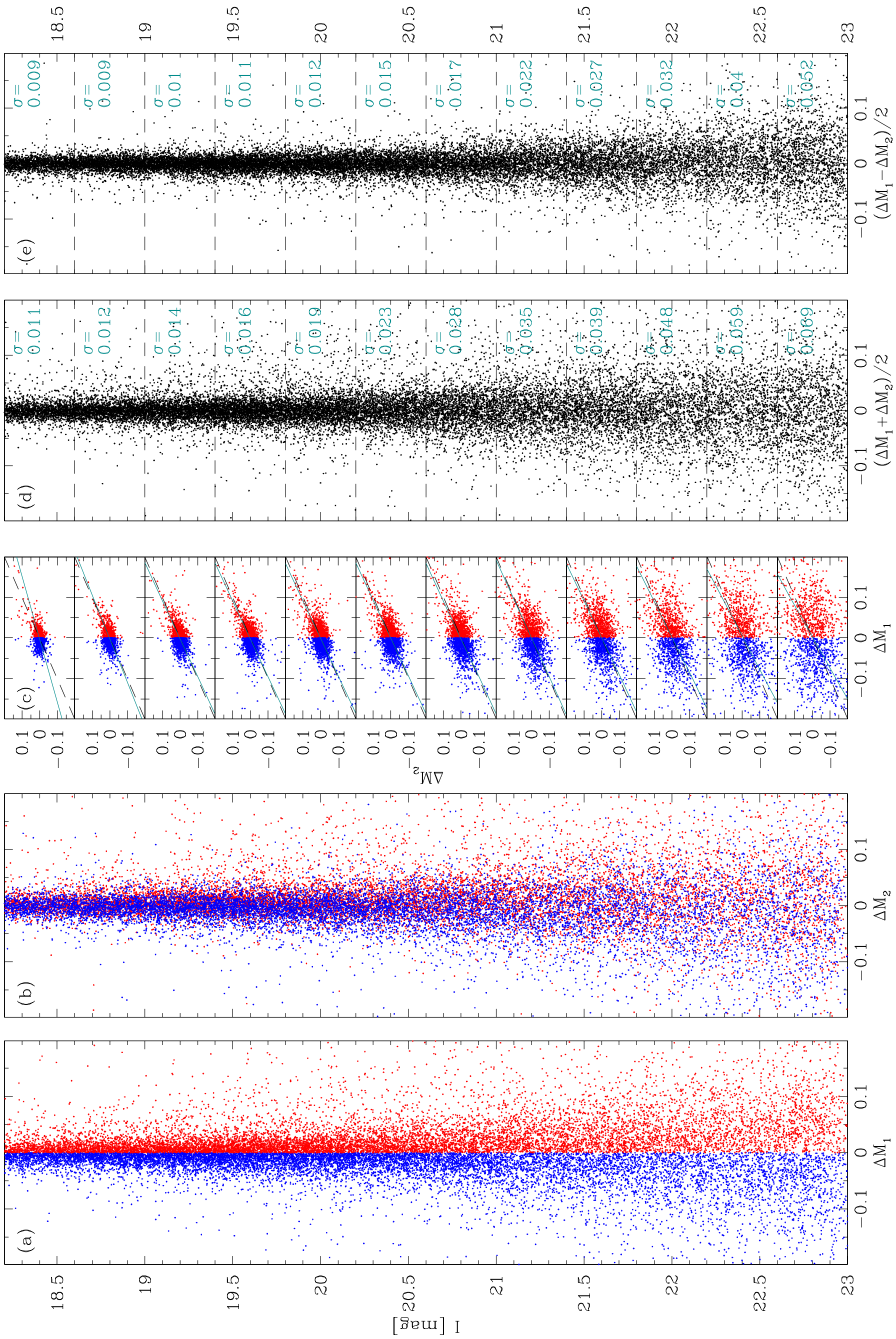

Figure 6.5: Same as Figure 6.4, but for the V- and I-band data, as a function of I-band magnitude.

Table 6.4: As Table 6.2, but for V- and I-band data.

I	$N_{sources}$	Group 1 vs Group 2		σ_{Mean}	σ_{Error}	Intrinsic Broadening
[mag]		Gradient	SRCC	[mag]	[mag]	[mag]
18.2 – 18.6	1619	0.646 ± 0.079	0.200	0.0108	0.0085	0.0066
18.6 – 19.0	2060	0.923 ± 0.069	0.262	0.0116	0.0087	0.0077
19.0 – 19.4	2308	1.070 ± 0.071	0.312	0.0142	0.0100	0.0101
19.4 – 19.8	2509	1.072 ± 0.062	0.329	0.0162	0.0108	0.0122
19.8 – 20.2	2349	1.083 ± 0.061	0.333	0.0188	0.0125	0.0140
20.2 – 20.6	2055	1.072 ± 0.065	0.351	0.0230	0.0149	0.0176
20.6 – 21.0	1952	1.074 ± 0.065	0.368	0.0278	0.0172	0.0219
21.0 – 21.4	1729	1.048 ± 0.057	0.386	0.0353	0.0222	0.0275
21.4 – 21.8	1706	1.091 ± 0.070	0.346	0.0385	0.0273	0.0272
21.8 – 22.2	1479	1.140 ± 0.078	0.348	0.0478	0.0323	0.0353
22.2 – 22.6	1396	1.208 ± 0.104	0.288	0.0588	0.0400	0.0431
22.6 – 23.0	1438	1.296 ± 0.117	0.259	0.0693	0.0523	0.0454

Table 6.5: Same as Table 6.3, but for V- and I-band data. Model broadening values are not available fainter than I= 22.2 mag, as the model isochrones do not extend this far.

I	Measured Broadening	Model Broadening: Y= 0.249 and		
[mag]		Y= 0.30	Y= 0.35	Y= 0.40
18.2 – 18.6	0.0066	0.0225	0.0328	0.0528
18.6 – 19.0	0.0077	0.0271	0.0428	0.0653
19.0 – 19.4	0.0101	0.0289	0.0492	0.0707
19.4 – 19.8	0.0122	0.0349	0.0585	0.0810
19.8 – 20.2	0.0140	0.0348	0.0673	0.0936
20.2 – 20.6	0.0176	0.0358	0.0685	0.0985
20.6 – 21.0	0.0219	0.0420	0.0744	0.1093
21.0 – 21.4	0.0275	0.0448	0.0738	0.1137
21.4 – 21.8	0.0272	0.0876	0.1199	0.1408
21.8 – 22.2	0.0353	0.1811	0.2032	0.1908
22.2 – 22.6	0.0431	...	...	...
22.6 – 23.0	0.0454	...	...	...

6.6 A Comparison to Simulations

The results described above depend on a good correlation between the colours measured in the two independent groups of images. To assess the reliability of these results, I constructed simulated data sets and compared the simulations' correlations to those from the data. The simulations are performed assuming that the spread of the colours measured in each group of images (panel (a) and (b) of Figure 6.4 and 6.5), and the mean spread and error distributions (shown in panel (d) and (e) of Figure 6.4 and 6.5) are well approximated by Gaussian distributions. The distance from the MSRL in the simulated data set is then a combination of two Gaussian distributions; one representing the intrinsic broadening, and another due to the the error on the colour measurement.

The assumption that the intrinsic broadening, mean distance from the MSRL and measured errors can be well approximated by a Gaussian distribution should be reasonable. I begin this section by investigating the validity of this assumption, however, as the distances from the MSRL considered in this investigation are so small that I suspect that subtle deviations from this model must be considered.

In the left panels of Figures 6.6 and 6.7 I replicate panel (d) from Figures 6.4 and 6.5, respectively. These show the mean distance of a source from the MSRL in the NUV - U and V - I CMDs. In the right panels, I plot the results as a histogram for each magnitude bin, and over-plot a Gaussian distribution with width σ_{Mean}, where σ_{Mean} was determined from the interquartile range of the data. At small distances from the MSRL, the data is well fit by the Gaussian approximation. At larger distances, however, the shape of the histograms diverge from the Gaussian distribution.

In Figures 6.8 and 6.9, I repeat the process for the errors on the mean distance (see panel (e) of Figures 6.4 and 6.5). I over-plot a Gaussian distribution with width σ_{Error}, to see how well the model fits to the data. Again, the data moves away from the Gaussian distribution as the errors increase. This is more apparent in the V - I case than the NUV - U, although the error distribution is wider in the V - I, and there are more sources, making differences more obvious.

These investigations show that the Gaussian approximations used in the simulations are reasonable for small mean distances and errors, but that the distributions of the data are strongly influenced by sources farther from the MSRLs which are not well modelled. This could contribute to differences between the data and simulations seen in Sections 6.6 and 6.7.

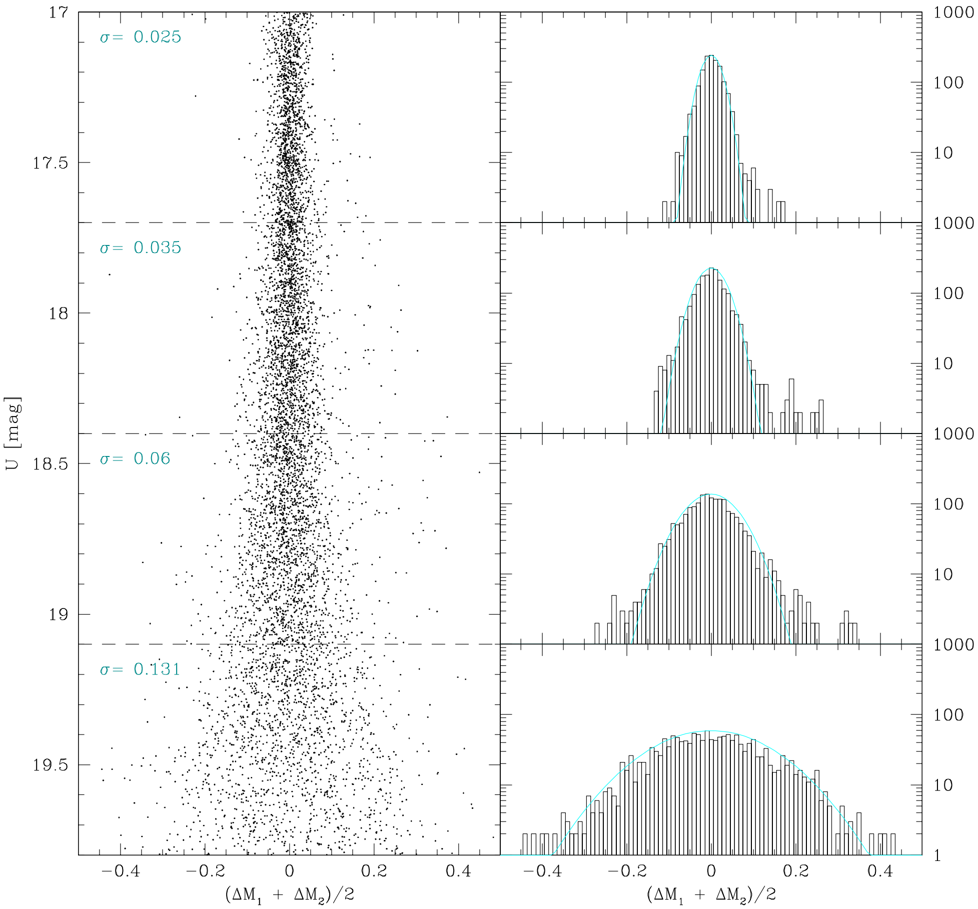

Figure 6.6: Left panel: reproduction of panel (d) from 6.4. Right panel: mean distance from MSRL in the NUV - U CMD, plotted as a histogram. The cyan line shows a Gaussian with width σ_{Mean} (determined from the interquartile range of the data).

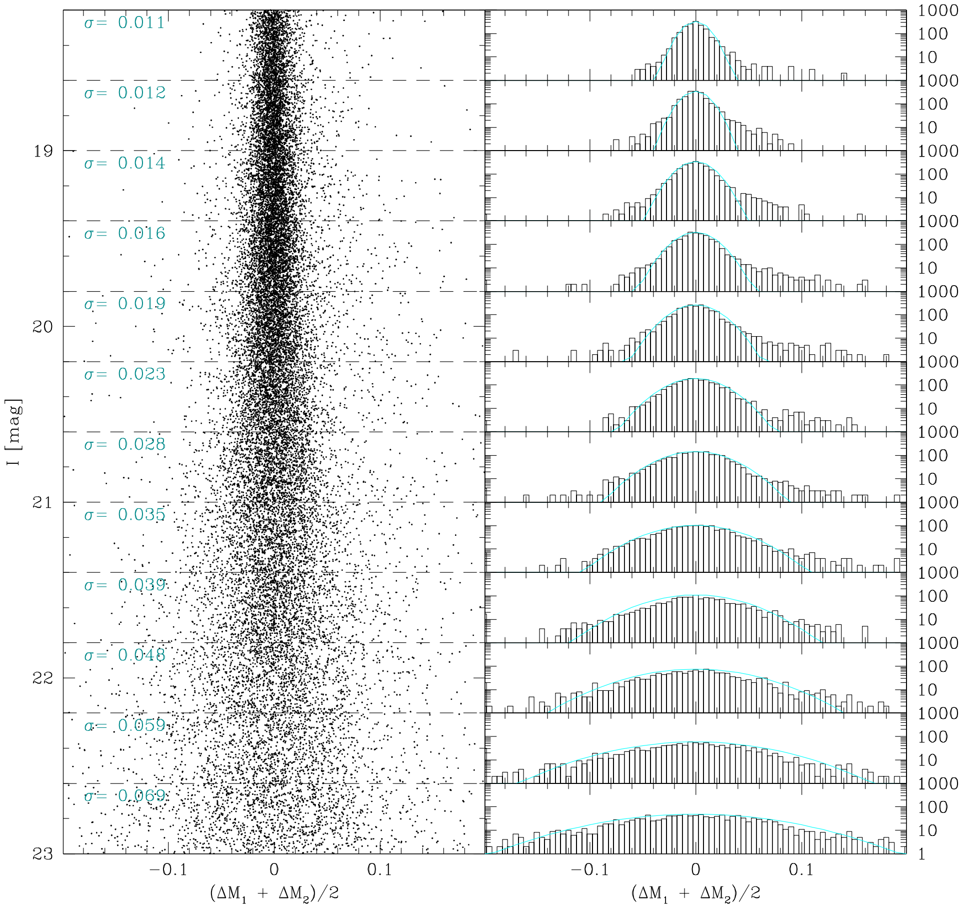

Figure 6.7: As Figure 6.6, but for the V - I case.

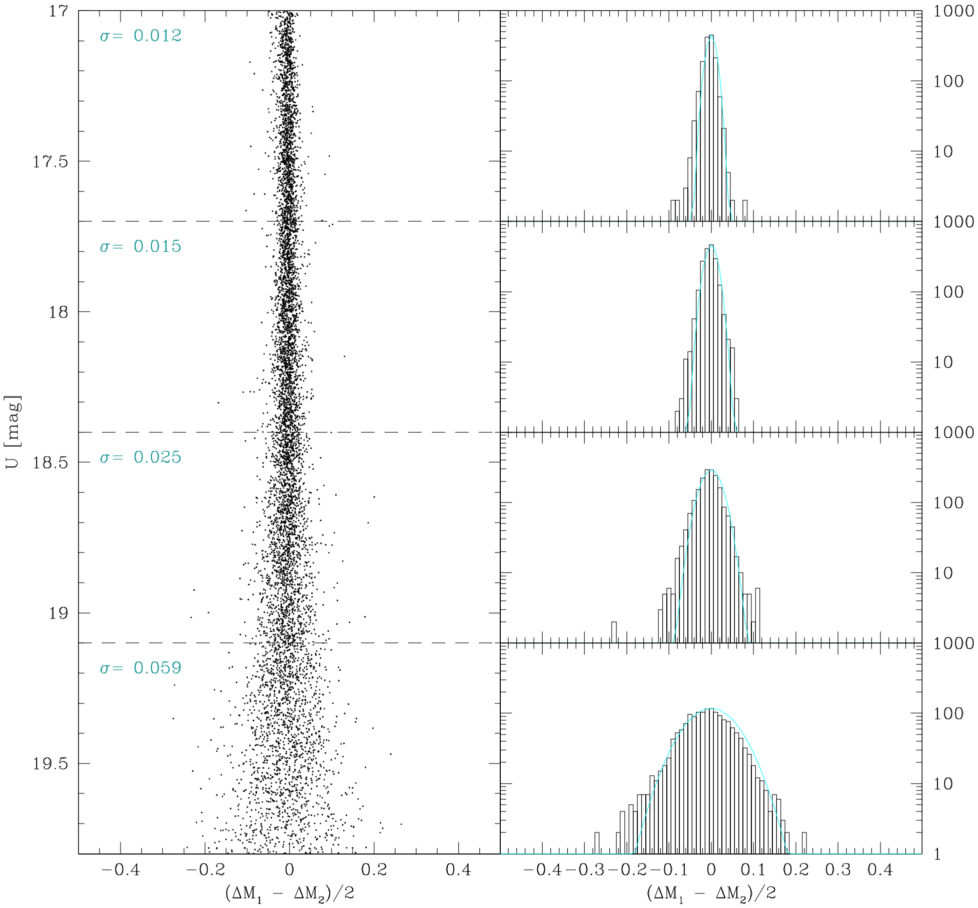

Figure 6.8: Left panel: reproduction of panel (e) from 6.4. Right panel: error on the mean distance from the MSRL in the NUV - U CMD, plotted as a histogram. The cyan line shows a Gaussian with width σ_{Error} (determined from the interquartile range of the data).

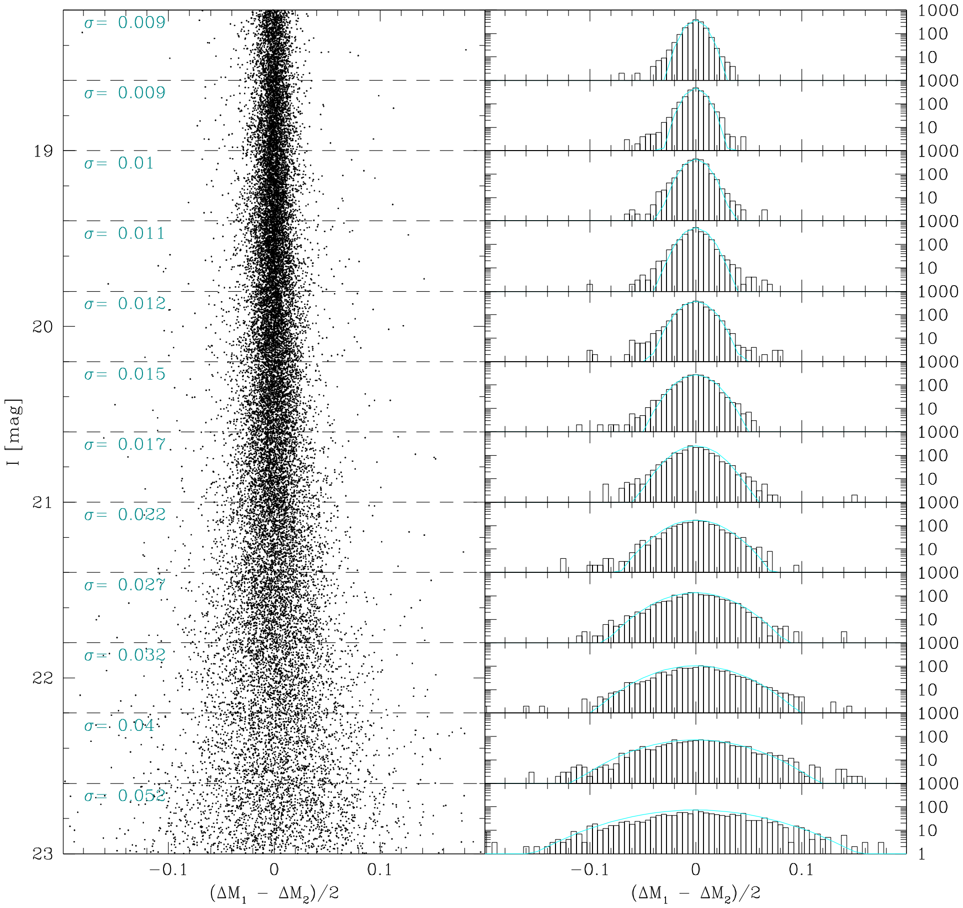

Figure 6.9: As Figure 6.8, but for the V - I case.

Starting with the NUV and U-band data set, I created mock data sets in two ways. First, I created a ‘Group 1’ data set for each magnitude bin, containing the same number of sources as the real data, by adding a colour drawn from a Gaussian distribution with width equal to the intrinsic broadening to an error value drawn from a second Gaussian distribution with width equal to the error (see Table 6.2). A simulated ‘Group 2’ data set was then created by assigning each source the same intrinsic colour as in Group 1, and adding another Gaussian-distributed error value. Plots of simulated Group 1 colour against simulated Group 2 colour are shown in the middle panels of Figure 6.10, while the results from the real data (panel (c) of Figure 6.4) are replicated in the left hand panels.

The simulated data exhibits narrower distributions than the real data. Columns 5 and 6 of Table 6.6 give the gradient and Spearman’s rank correlation coefficient found when comparing these two fake data sets. They show, as expected, that comparisons between simulations in which the only difference between the colour measurements in the two groups is caused by photometric errors show strong correlations between measured colours. They also show that the results from the real data (Columns 3 and 4) are reasonable.

If the photometric errors were different in the Group 1 and Group 2 images (due to, for example, telescope breathing), there would be a difference between the widths of the distributions shown in panels (a) and (b) of Figure 6.4, which would alter the shape of the distributions shown in panel (c). To see what effect I should expect this to have on the data, I created simulated data sets in which the Gaussian distribution representing the overall intrinsic broadening was replaced by Gaussian distributions reflecting the spread of the colour measurements in each independent group of images. Group 1’s fake data set was made up of sources with colours drawn from a Gaussian distribution with width equivalent to the (measured) intrinsic broadening of the Group 1 colours (defined as $\sqrt{\sigma_1^2 - \sigma_{Error,1}^2}$, where σ_1 is the standard deviation of the Group 1 data, determined from the interquartile range, and $\sigma_{Error,1} = \sqrt{2} \times \sigma_{Error}$ is the error on either of the data sets), and a Gaussian representing the error on the Group 1 colours, which is $\sqrt{2} \times \sigma_{Error}$. Assuming that any difference in the errors would create a systematic change in measured broadening, the ratio of the measured widths should be the same as the ratio of the errors on each group. To create Group 2 data, I multiplied the Group 1 colour measurement by the ratio of the spreads in the Group 1 and Group 2 colours, and added an error drawn from an independent Gaussian distribution. The resulting colours are plotted in the right-hand panels of Figure 6.10. The last two columns in Table 6.6 show the gradient and Spearman’s rank correlation coefficient obtained when these two

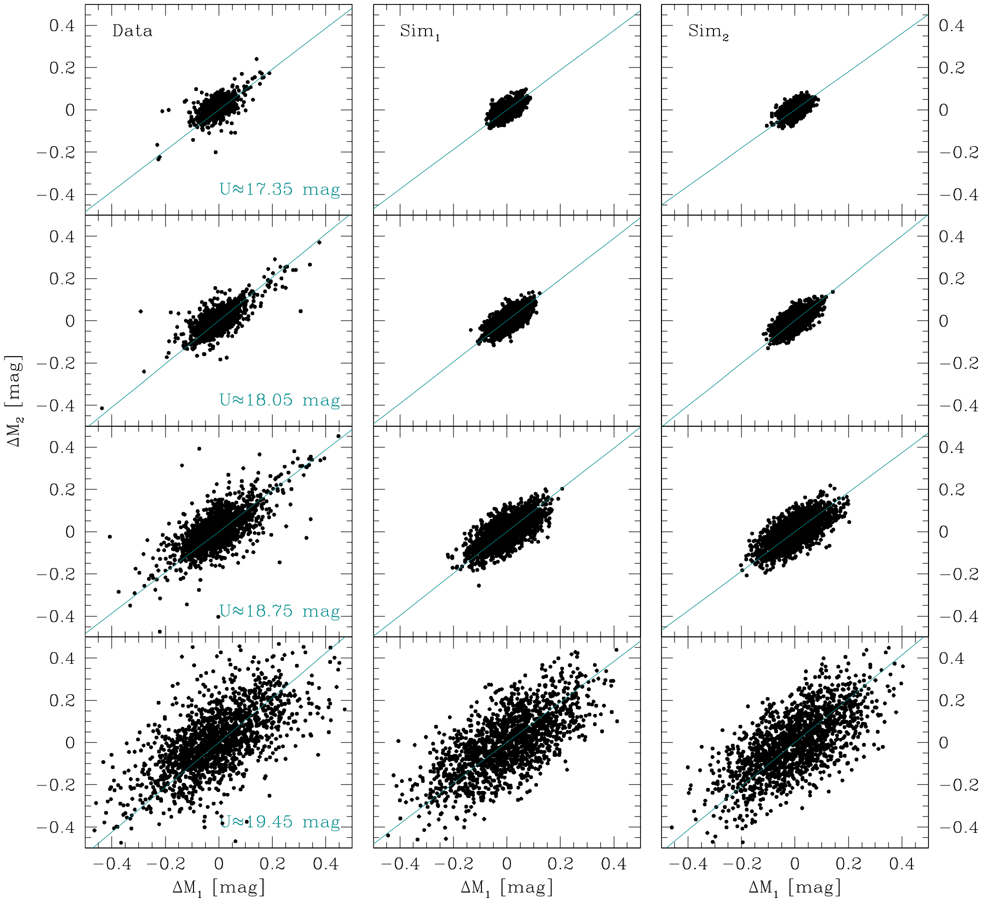

Figure 6.10: Comparison of Group 1 and Group 2 colours in NUV and U-band images. Left: real data. Middle: simulation assuming that the broadening seen in either group of images is the same as the overall intrinsic broadening. Right: simulation allowing for different intrinsic broadening measurements in the two groups of images. This might happen because of, for example, telescope breathing resulting in larger errors and wider spread in one group's colours.

simulated data sets are compared.

In the NUV and U-band case, there is little difference between the results based on real data and the simulated data, regardless of which simulation method is used. This shows that the data is consistent with the simulations and that the spread measured separately in Group 1 and Group 2 is consistent with the overall measurements.

The process was repeated using numbers appropriate to the V- and I-band data set. Plots of Group 1 colour against Group 2 colour using the real data (see Figure 6.11) exhibit more spread than those of the simulations. This is expected, since

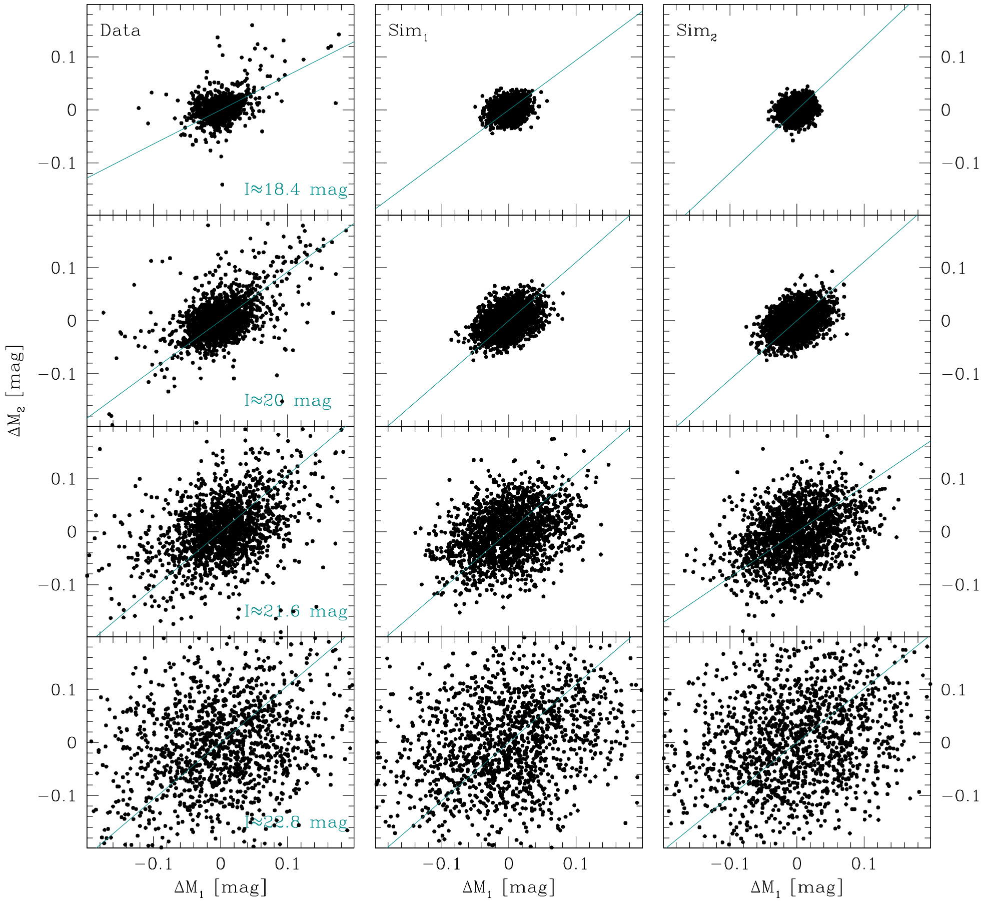

Figure 6.11: As Figure 6.10, for V- and I-band images. Four of the twelve magnitude bins are shown.

the photometric errors (panel (e) of Figure 6.5) are comparable to the colour spread (panel (d)). The gradients and Spearman's rank tests listed in Table 6.7 show, however, that the data were consistent with the simulations in most magnitude bins. The obvious exception to this is in the brightest magnitude bin ($18.2 < I < 18.6$), in which the real data has a gradient of 0.646 ± 0.079, and the simulations have gradients of 0.913 ± 0.083 or 1.613 ± 0.190, depending on the simulation method used. This magnitude bin has the smallest intrinsic broadening (0.00657 mag; see Table 6.4), so is most affected by photometric errors, which may explain the poor match in this instance.

Table 6.6: Results of the investigation into consistency between the Group 1 and Group 2 measurements of MS sources in the NUV - U CMD. The first two columns give the U-band magnitude bin and the number of sources included. Columns 3 and 4 give the gradient of the best-fit line to the plot shown in panel (c) of Figure 6.4 and the corresponding Spearman's rank correlation coefficient (SRCC). Columns 5 to 8 give the gradient and SRCC of similar plots created using simulated data. In Columns 5 and 6, I have assumed that the spread of the data in Group 1 and Group 2 measurements are equal; in Columns 7 and 8, I have allowed for differences between the measurements. See Section 6.6 for more details of these simulations.

U	$N_{sources}$	Data		Simulation Method 1		Simulation Method 2	
[mag]		Gradient	SRCC	Gradient	SRCC	Gradient	SRCC
17.0 – 17.7	1475	0.966 ± 0.041	0.549	0.980 ± 0.034	0.589	1.039 ± 0.035	0.592
17.7 – 18.4	1831	1.024 ± 0.028	0.627	0.978 ± 0.025	0.650	1.003 ± 0.024	0.668
18.4 – 19.1	1887	0.967 ± 0.030	0.621	0.986 ± 0.022	0.696	0.974 ± 0.022	0.706
19.1 – 20.0	1618	1.058 ± 0.036	0.627	0.974 ± 0.029	0.634	1.103 ± 0.038	0.601

Table 6.7: As Table 6.6, but for V- and I-band data.

I	$N_{sources}$	Data		Simulation Method 1		Simulation Method 2	
[mag]		Gradient	SRCC	Gradient	SRCC	Gradient	SRCC
18.2 – 18.6	1619	0.646 ± 0.079	0.200	0.913 ± 0.083	0.246	1.613 ± 0.180	0.196
18.6 – 19.0	2060	0.923 ± 0.069	0.262	1.078 ± 0.091	0.246	1.153 ± 0.079	0.293
19.0 – 19.4	2308	1.070 ± 0.071	0.312	0.981 ± 0.055	0.322	1.459 ± 0.099	0.279
19.4 – 19.8	2509	1.072 ± 0.062	0.329	0.920 ± 0.040	0.387	0.958 ± 0.044	0.374
19.8 – 20.2	2349	1.083 ± 0.061	0.333	0.976 ± 0.050	0.354	1.025 ± 0.051	0.353
20.2 – 20.6	2055	1.072 ± 0.065	0.351	1.019 ± 0.055	0.350	0.969 ± 0.046	0.411
20.6 – 21.0	1952	1.074 ± 0.065	0.368	0.999 ± 0.045	0.417	1.221 ± 0.052	0.431
21.0 – 21.4	1729	1.048 ± 0.057	0.386	0.908 ± 0.037	0.475	1.167 ± 0.055	0.408
21.4 – 21.8	1706	1.091 ± 0.070	0.346	0.975 ± 0.063	0.338	0.984 ± 0.053	0.387
21.8 – 22.2	1479	1.140 ± 0.078	0.348	1.042 ± 0.070	0.353	1.246 ± 0.077	0.361
22.2 – 22.6	1396	1.208 ± 0.104	0.288	0.909 ± 0.065	0.332	1.276 ± 0.081	0.388
22.6 – 23.0	1438	1.296 ± 0.117	0.259	1.053 ± 0.085	0.308	0.890 ± 0.081	0.264

Comparisons between the Group 1 and Group 2 measurements, and comparisons between real and simulated data, indicate that there appears to be clear evidence of broadening on the MS in both the NUV - U and V - I CMDs. In the following section, I will take advantage of the fact that I have two completely independent data sets (NUV and U-band, and V- and I-band), in order to assess the extent to which this measured broadening can be trusted.

6.7 Comparing the NUV - U and V - I Results

If the broadening seen in both of the CMDs is real, I expect to see a correlation between the colours measured in NUV - U and V - I; a source located to the blue side of the MS in the NUV - U CMD should, ordinarily, also lie to the blue side of the MS on the V - I CMD. If the positions in the two CMDs are not consistent, this would indicate that at least one of the measured broadenings cannot be trusted. In this investigation I use the overall measurements for each waveband, which have smaller intrinsic photometric errors than those of either group (see Table 6.1).

6.7.1 The Overall Results

The two catalogues were transformed to match the Tycho-based WCS, using the method described in Section 4.2.3 and 4.2.4, and matches between the two catalogues were identified. Approximately 90% of the possible matches were recovered.

Figure 6.12 shows the distribution of sources in ΔM_{NUV-U}, with sources coloured red and blue depending on a source's position relative to the MSRL in the V - I CMD. The data is split into bins based on I-band magnitude, to avoid confusion due to the increase in photometric error at fainter magnitudes. The histograms show that there is a weak correlation; the blue histograms peak slightly to the left of the red histograms.

The grey points in Figure 6.13 show ΔM_{NUV-U} against ΔM_{V-I} for all (individual) sources, and show a weak but positive gradient, indicating that there is a weak correlation between the sources' positions in the two CMDs. I note that one should not expect a 1:1 correlation between the two colours as in panel (c) of Figures 6.4 and 6.5. Instead, I expect the best-fit line to have a gradient equal to the ratios of the intrinsic broadening in the two CMDs. This will then be complicated by the fact that the intrinsic broadening of each MS changes differently with magnitude, so the ratio will be different for brighter and fainter sources. The expected result

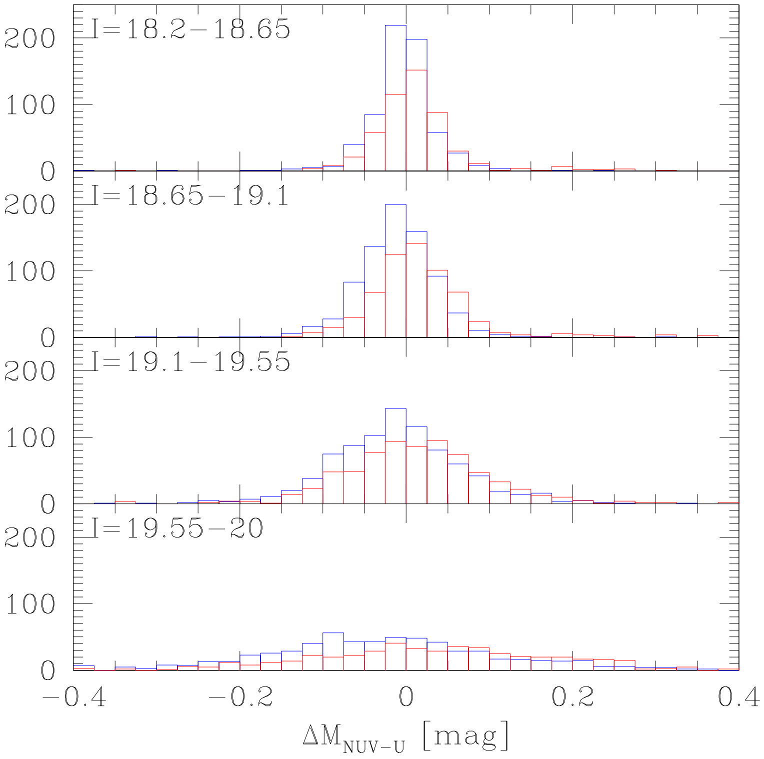

Figure 6.12: Distribution of sources about the MSRL in the NUV - U CMD, with sources coloured red and blue depending on a source's position relative to the MSRL in the V - I CMD, in I-band magnitude bins.

is further complicated by photometric errors, which are different in each waveband and introduce different levels of scatter at different magnitudes.

The red triangles in Figure 6.13 show the median ΔM_{V-I} value for ΔM_{NUV-U} bins. The correlation between the two colour measurements is more apparent, as is the changing gradient of the slope with ΔM_{NUV-U}. The black bars give the standard deviation of the data in each bin, while the red bars indicate the error on the median value (given by $\frac{\sigma}{\sqrt{N}}$).

The positive correlation between the NUV - U and V - I colours indicates that the colours obtained for sources in the two independent CMDs are consistent, suggesting that the broadening seen in each of the CMDs (Figures 6.4 and 6.5) is real.

6.7.2 A Comparison to Simulations

Simulated data can be used to establish how well the data shown in Figure 6.13 fits with expectation. The first method used to create fake data sets assumes that the intrinsic broadening and photometric errors are both Gaussian distributed. First, I

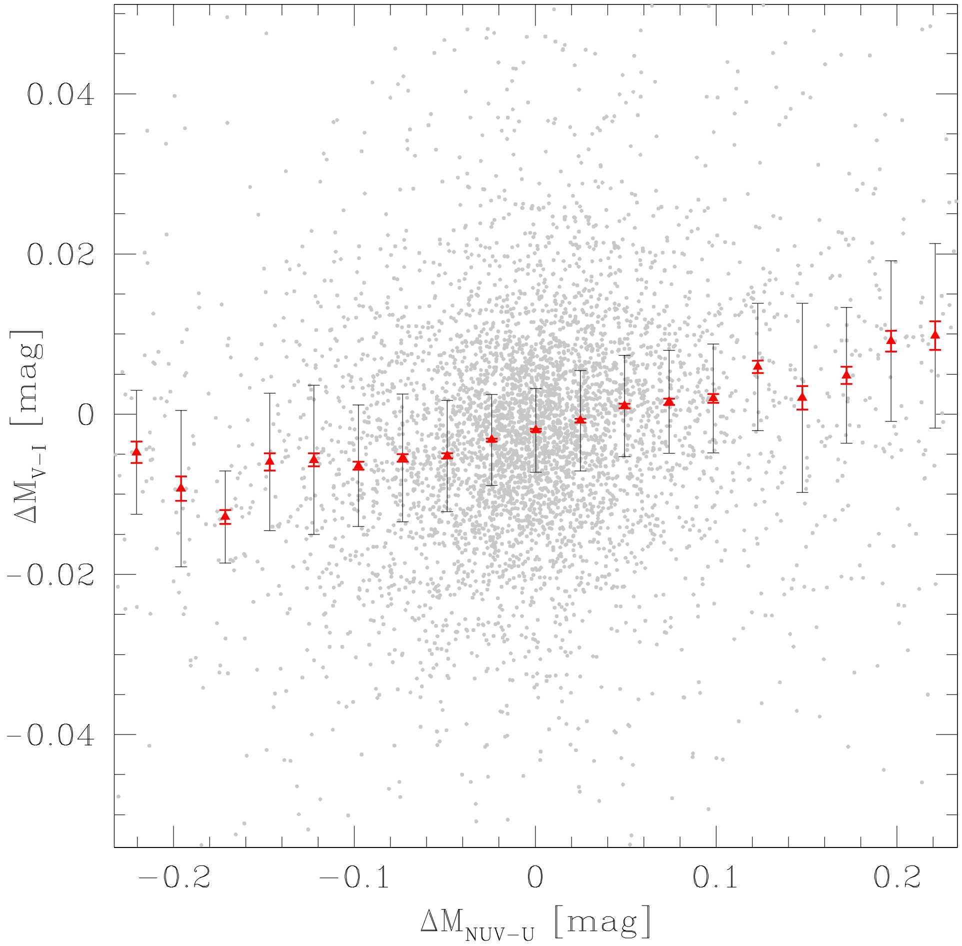

Figure 6.13: Grey points: ΔM_{NUV-U} against ΔM_{V-I} for all sources. Red triangles: median ΔM_{V-I} value for ΔM_{NUV-U} bins. The black bars show the standard deviation and the red bars indicate the error on the median value. There is a weak, but statistically significant, correlation between the ΔM_{V-I} and ΔM_{NUV-U} measurements.

created a set of intrinsic NUV - U broadening values by selecting values at random from a Gaussian distribution with width equal to the measured intrinsic broadening. The number of sources and intrinsic broadening measurements used were for I-band magnitude bins, so the change in broadening with magnitude was reflected in the simulation. A V- and I-band intrinsic broadening value was determined by multiplying the NUV - U value by the ratio of the measured broadening values in the two CMDs. Photometric errors were selected from Gaussian distributions with widths equal to the measured σ_{Error} in each CMD, in each I-band magnitude bin. The sum of these values formed the distance from the MSRL for each source, in each CMD. In Figure 6.14 I plot ΔM_{NUV-U} against ΔM_{V-I} for the simulated

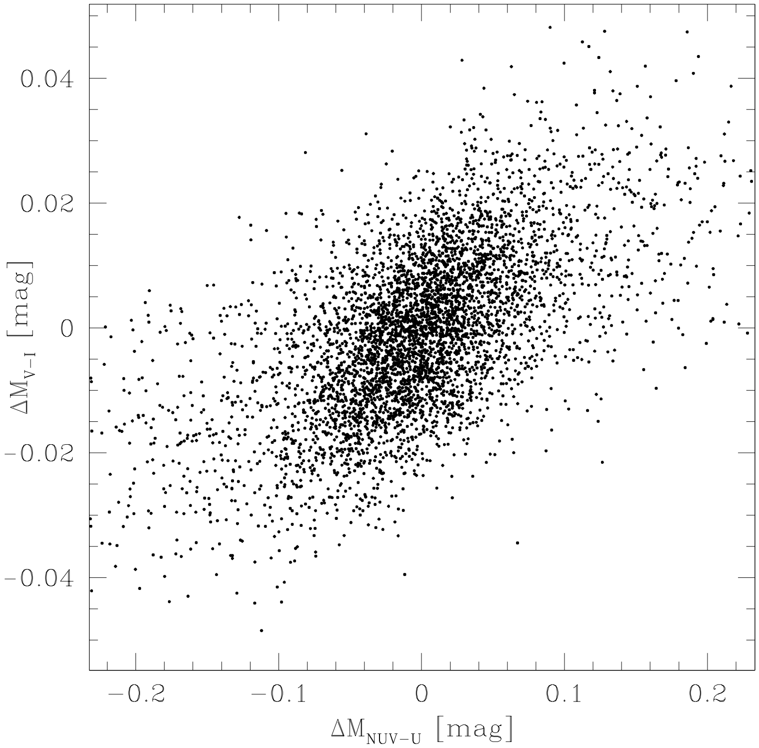

Figure 6.14: ΔM_{NUV-U} against ΔM_{V-I} for simulated data, assuming that a source's distance from the MSRL is a combination of its intrinsic broadening and photometric error. In this simulation, I assume that both of these factors are Gaussian distributed.

data. The changing ratio between the intrinsic broadening values, combined with the increase in intrinsic broadening with magnitude, leads to a change in gradient as one moves farther from the origin. The level of scatter in this simulation is clearly considerably smaller than that seen in the data (the grey points) in Figure 6.13. This is to be expected, since the broadening in the data is not well represented by a Gaussian distribution at larger distances from the MSRL.

To investigate further the difference between the real data and simulations, I created a second fake data set which reflected the real photometric errors, rather than assuming that they are Gaussian distributed. Each source's intrinsic broadening in NUV and U-band or V- and I-band were determined as before, but I then added the photometric error belonging to a real source, drawn at random from within the relevant I-band magnitude bin. As the NUV - U and V - I errors on each fake source came from the same (real) source, any correlations between the errors measured in the two colours (due to blends, for example) are reflected in the simulations. The resulting distances from the MSRLs are plotted in Figure 6.15. The differing

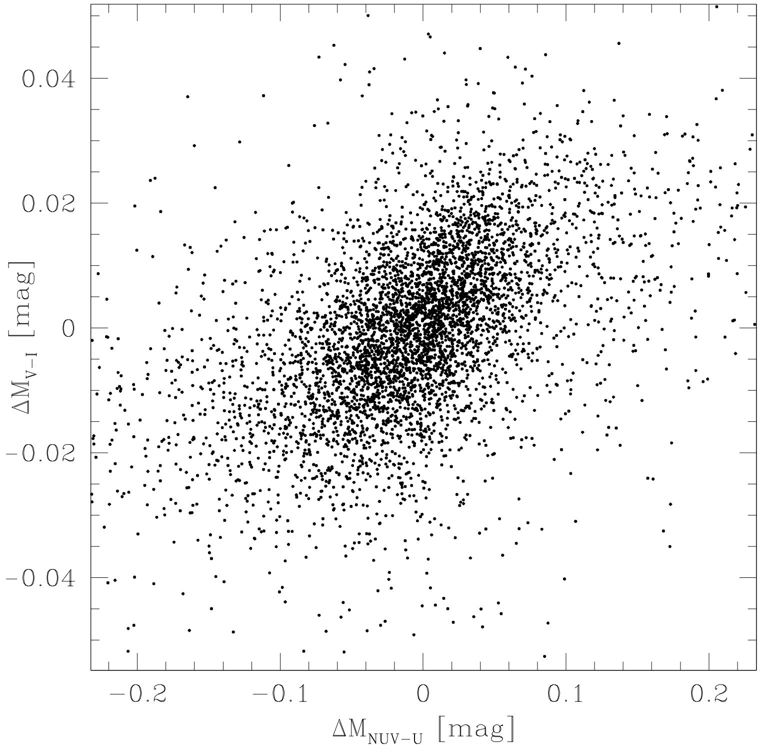

Figure 6.15: ΔM_{NUV-U} against ΔM_{V-I} for simulated data, assuming that a source's distance from the MSRL is a combination of its intrinsic broadening and photometric error. In this simulation, I assume that the mean distance from the MSRL can be well described by a Gaussian distribution, but I use the errors from real sources, drawn at random from the population.

gradients and distribution widths at different magnitudes are less apparent than in Figure 6.14, and there is substantially more scatter apparent here, which further indicates that the Gaussian distributed errors assumed in Figure 6.14 might not be a good reflection of the true errors. The correlation between the colours is still more obvious than in the data (Figure 6.13), however, suggesting that something else is affecting the distribution of the data, which is not accounted for in this simulation.

6.7.3 The Most Trusted Sources

As the sources' measured colours in the NUV - U and V - I CMDs are not as well correlated as one might expect from simulations, I now plot the correlation only for sources for which I should be able to be confident about the sign of the measured colours' offset from the MSRL. I select sources within each I-band magnitude bin which satisfy the the following criteria:

- Mean distance from ridge-line, defined as $(\Delta M_1 + \Delta M_2)/2$, $< 3 \times \sigma_{Mean}$, so the sources are not outliers in colour;

- Mean distance from ridge-line, defined as $(\Delta M_1 + \Delta M_2)/2$, $> 2 \times \sigma_{Error}$, so the distance from the MSRL is unlikely to be due to photometric error.

The top panel of Figure 6.16 shows the resulting plot of ΔM_{NUV-U} against ΔM_{V-I}. In the lower panel, I plot the result if I also specify that sources must satisfy an extra criterion:

- Mean distance from ridge-line, defined as $(\Delta M_1 + \Delta M_2)/2$, $> 2\times$ Error (defined as $(\Delta M_1 - \Delta M_2)/2$) for the source. This further enforces the rule that distance from the MSRL cannot be due to photometric error.

As I expect sources which are on the blue side of the MSRL in the NUV - U CMD to also lie on the blue side of the V - I MSRL, the sources should lie either in the lower left or upper right quadrants of these plots. In Figure 6.16, the number of sources falling in each quadrant is displayed, and shows that the majority of sources follow this trend. However, there are also a number of sources in the lower right and upper left quadrants, which lie to the blue of the MSRL in one CMD and red of the MSRL in the other. Some of these spurious colour measurements can be explained. For example, some might be unresolved binaries in which the red source dominates in the red (V- and I-band) filters, and the bluer source contributes most of the flux in the NUV and U-band. Another possibility is fast rotation of single stars; coronal mixing could cause the source to appear red in the redder (V- and I-band) filters, but the high temperature means that they appear blue in the bluer (NUV and U-band) filters. Of course, some sources might simply be erroneously positioned in one of the CMDs; I have selected sources based on the intrinsic photometric error, defined using the difference between the two measurements in either CMD, but it is possible that some sources are poorly measured in both groups of NUV and U-band, or V- and I-band images, leading to a poorly measured colour with a small measured error.

In order to assess the strength of the evidence for a correlation between the NUV - U and V - I data sets, Table 6.8 displays the probability of this ratio of ‘good’ to ‘bad’ sources occurring by chance. This is calculated by assuming that the distribution is binomial, and that in the limit that there was no correlation between the

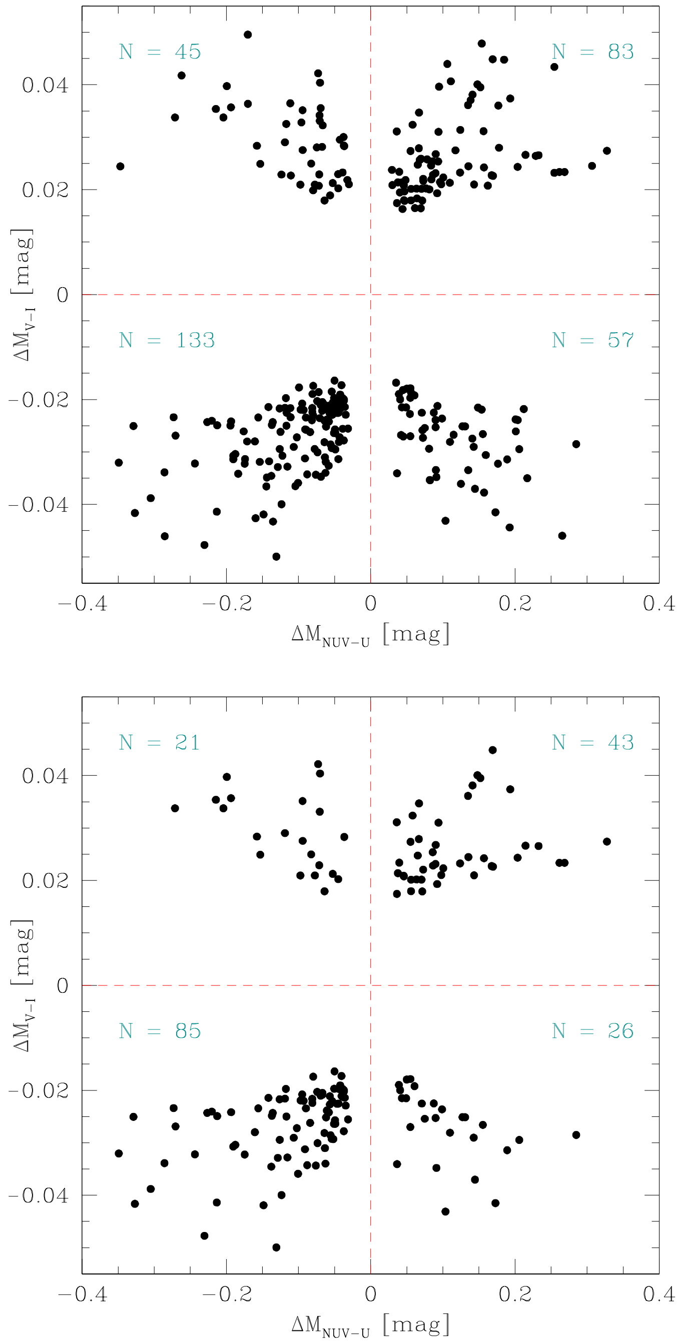

Figure 6.16: ΔM_{NUV-U} against ΔM_{V-I} for sources for which the colour determination is considered safe. Top: measurements are considered safe if the sources satisfies the following criteria: $(\Delta M_1 + \Delta M_2)/2 < 3 \times \sigma_{Mean}$; $(\Delta M_1 + \Delta M_2)/2 > 2 \times \sigma_{Error}$. Bottom: sources also satisfying $(\Delta M_1 + \Delta M_2)/2 > 2 \times (\Delta M_1 - \Delta M_2)/2)$. As I expect sources which are on the blue side of the MSRL in the NUV - U CMD to also lie on the blue side of the V - I MSRL, the sources should lie either in the lower left or upper right quadrants. The number of sources in each quadrant is shown.

Table 6.8: Results of a comparison between the position of sources relative to the MSRL in the NUV - U and V - I CMD. If the data is reliable, a source which is bluer than the MSRL in the NUV - U CMD should also be to the blue side of the MSRL in the V - I CMD. The first column gives the selection method used. See text for details. Columns 2 and 3 give the number of ‘good’ sources (those falling in the lower left or upper right quadrants) and the total number of sources considered. Column 4 lists the percentage of sources which are considered ‘good’. In the final column, I present the probability of this fraction of sources appearing in the ‘good’ quadrants (lower left and upper right, indicating blue-blue or red-red), if I assume that the distribution is binomial, and that 50% of the sources would fall in these quadrants if there was no correlation between the measurements in the two CMDs.

Method	N_{Good}	N_{Total}	$\%_{Good}$	$\text{Probability}_{Chance}$ [%]
1	216	318	68	4.029×10^{-9}
2	128	175	73	2.354×10^{-8}

colours, 50% of the sources would fall in the ‘good’ quadrants. The results show that there is a very small probability of finding as many sources as observed in the “correct” quadrants by chance, indicating that the correlation between the sources’ colours in the NUV - U and V - I CMDs is real.

6.7.4 The Result At Different Magnitudes

Having shown that the data set, as a whole, is behaving in a manner which is reasonable when compared to simulations, I now focus on sources at similar locations on the MS, as I did in the initial searches for broadening in Section 6.4 and 6.5.

In Figure 6.17, I plot ΔM_{NUV-U} against ΔM_{V-I}, for a range of I-band magnitude bins. The left panels show the plots for the real data, while the right panels show the result of simulations in which the assumed photometric errors are the errors of a real source drawn at random from within the relevant magnitude bin. In each plot, the dark green line shows the best-fit line to the data, and the cyan, dashed line shows the expected correlation (with gradient equal to the ratios of the intrinsic broadenings in each magnitude bin). In each bin I find a positive correlation in the real data, indicating that a source to the red of the MSRL in the NUV - U CMD is, in general, also red in the V - I CMD. The gradient of the best-fit line is always lower than expected from the ratio of the measured intrinsic broadening in each CMD, and is also lower than the gradient of the simulations. This might imply that using a Gaussian distribution to simulate the intrinsic broadening might not be a good representation of the real data, even allowing for non-Gaussian errors. An

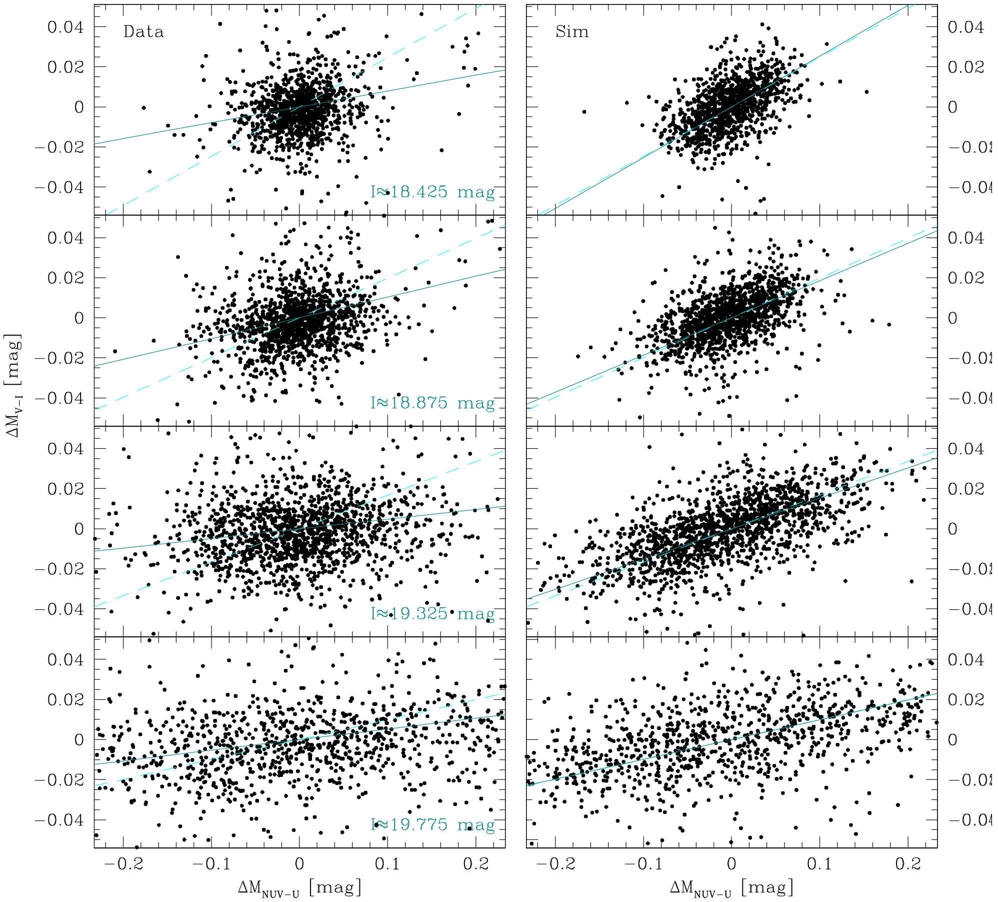

Figure 6.17: ΔM_{NUV-U} against ΔM_{V-I}, divided into I-band magnitude bins. Left panels: real data. Right panels: simulated data in which the assumed photometric errors are the errors of a real source drawn at random from within the relevant magnitude bin. Dark green, solid lines: best-fit line to the data. Cyan, dashed line: expected correlation (with gradient equal to the ratios of the intrinsic broadenings in each magnitude bin).

alternative explanation is that the position-dependent colour correction algorithm described in Section 6.3.1 is not 100% effective in removing spatial trends. This would explain why there is a good correlation within data sets (see Figure 6.4 and 6.5), but a less good correlation between the data sets. Spearman's rank tests show that the correlation seen in the data is significant in all magnitude bins. I conclude, therefore, that there is a correlation between the colour measurements, but that it is not as strong as I would expect. The spread in the MS appears to suggest that the broadening is real, but the levels of intrinsic broadening observed in either CMD should be viewed as upper limits.

6.8 Radial Trends in the MS Broadening

Milone et al. (2010) demonstrated that there is clear evidence for MS broadening in NGC 6752 between 1 and $\approx 2.2'$ from the centre. I have shown in this investigation that broadening can also be seen in the core region of the cluster. Milone et al. (2010) found no evidence for a difference in the radial distribution of the redder and bluer stars, with the Kolmogorov-Smirnov test indicating that there is a 49% chance that a difference this large between the radial distributions of two samples drawn from the same overall population. KS tests are straightforward to apply where a clear split sequence can be seen, and can be used to determine differences in the radial distribution of sources which clearly belong to each sequence. I note, however, that the KS test depends entirely on whether a source is marked as red or blue, so is very sensitive to the position of the MSRL. In the case of broadened sequences, a test which is less sensitive to the exact position of the MSRL might be better. One such test is to look at the size of the intrinsic broadening at different radial distances.

To search for radial trends, I split the data into radius bins such that there is an equal number of sources in each bin. Figure 6.18 shows the result for the NUV and U-band data, for different U-band magnitude bins. The left panels show the mean spread of the MS (cyan points) and the estimated intrinsic photometric error (magenta crosses). These are analogous to the σ values marked on Figure 6.5, but split into radial bins. In the right hand panels I present the estimated intrinsic broadening, defined as $\sqrt{\sigma^2_{Mean} - \sigma^2_{Error}}$. To estimate the uncertainties in the measurements, I used a bootstrapping technique involving sampling with replacement from the data to create 1000 fake catalogues and estimating the mean spread, error estimate, and broadening of each one. The standard deviation of these fake ‘measurements’ gives the error on the real measurement in each plot.

In all but the faintest magnitude bin, there is a strong suggestion that the broadening is greatest towards the centre of the cluster. The trend is less obvious in the faintest U-band magnitude bin, but the larger error bars mean that such a trend is not ruled out.

Figure 6.19 shows a sample of the results for the V- and I-band data. Four of the twelve I-band magnitude bins are shown for the sake of clarity, but the trends described here are apparent in all magnitude bins. In every magnitude bin, the extent of the intrinsic broadening is largest in the innermost radial bin. This cannot be explained simply in terms of crowding, because the intrinsic error has been taken into account.

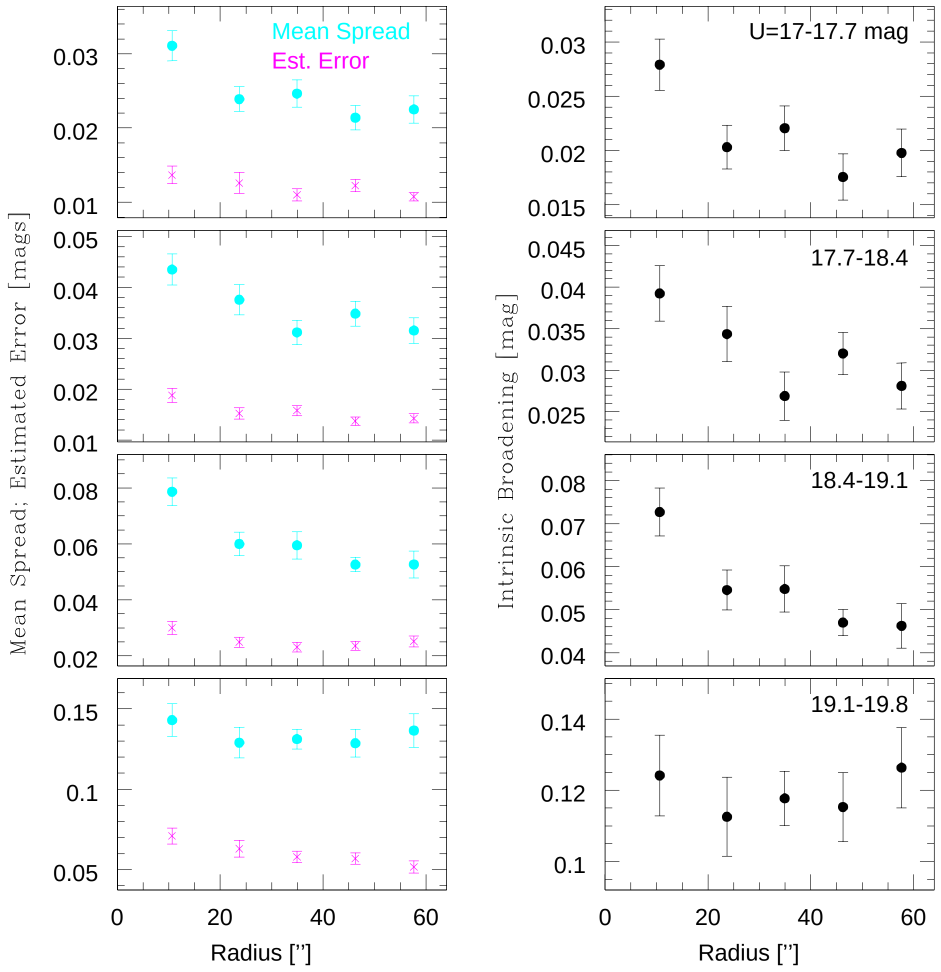

Figure 6.18: Radial distribution of intrinsic broadening in the NUV - U MS, at different magnitudes. Left: mean spread of the MS (cyan points) and error on the measured mean spread (magenta crosses). Right: upper limit on the intrinsic broadening.

Figures 6.18 and 6.19 imply that the level of intrinsic broadening decreases as one moves away from the centre of the cluster. I regard this as a preliminary result because, as stated in Section 6.4, I interpret my results as providing upper limits on the intrinsic broadening. Milone et al. (2010) searched for broadening in a region overlapping with, but extending further out than, the region considered here. Assuming the radial trend shown above continues to hold out to $\approx 2.2''$ from the centre, one would expect Milone et al. to have found smaller intrinsic broadening than measured in this investigation. This is not the case. In fact, the broadening measured by Milone et al. is twice as large as measured here, in all four of the magnitude bins that they considered. This is a very puzzling result which might suggest that the mean distances from the MSRL or the intrinsic errors reported in that paper

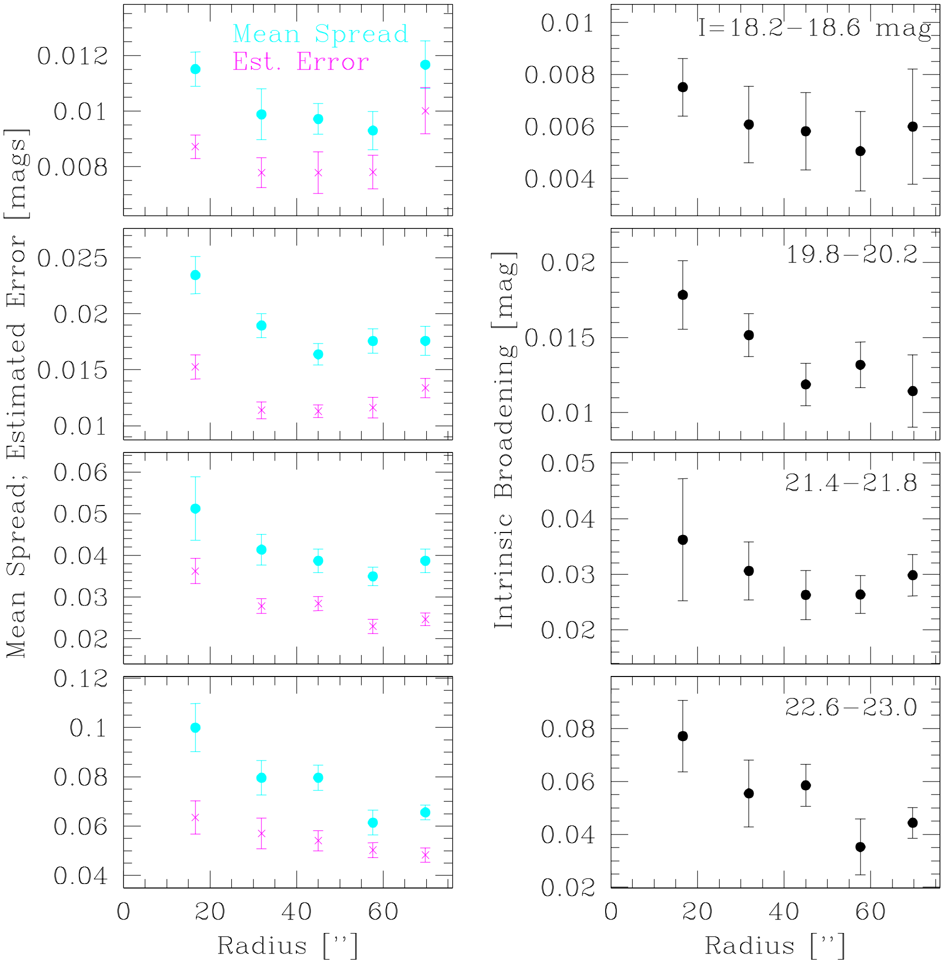

Figure 6.19: As Figure 6.18, for the V - I case. Four of the twelve magnitude bins are shown.

are incorrect. Nonetheless, further investigation into the radial trends at larger radii would probably be needed before conclusions can be drawn from the difference in the amount of broadening detected in the two investigations.

The radial trend in the level of broadening seen, with the widest intrinsic broadening found in the core of the cluster, implies that there is more variation in the metal abundances of sources in the core. Milone et al. (2012a) find a difference between the dominant population in the core of 47 Tuc and the outskirts ($R < \sim 2'$ and $R > \sim 15'$), but do not search for a trend on smaller scales. Given that NGC 6752 is thought to be a core-collapsed cluster (see Chapter 4), it would be interesting to know if similar trends are present in other clusters, and if they are a product of the dynamical processes involved in core-collapse, or if all clusters with multiple stellar populations exhibit such a trend.

6.9 A Note on The Sub-Giant Branch and Red Giant Branch

In addition to the MS broadening presented here and in Milone et al. (2010), previous studies have also found photometric and spectroscopic evidence for multiple populations in the red giant branch of NGC 6752 (Grundahl et al., 2002; Milone et al., 2010). Milone et al. (2010) studied the sub-giant branch and found no evidence for broadening. Unfortunately, while the correction algorithm described in Section 6.3.1 is able to correct for CTE errors in the MS, the small numbers of red giant branch stars in the NUV and U-band data mean that such a correction is not suitable for use in investigating broadening in the RGB. Furthermore, the F390W exposures used in observing the red giant branch stars are short (2 s) so have low background, making them more susceptible to CTE effects. As soon as CTE corrections become available, it should be possible to detect broadening in the RGB in the NUV and U-band, and perhaps trace the different populations through their evolution from MS to RGB. This is discussed further in Chapter 7.

6.10 Conclusions

I have searched for MS broadening in the NUV - U and V - I CMDs of NGC 6752. Having corrected for position-dependent colour trends in the data, I found that the MS in both the NUV - U and V - I CMDs exhibit broadening, and that this cannot be explained only in terms of intrinsic photometric errors. The broadening is more apparent in the NUV - U CMD than in the V - I, which is in line with the trend seen in helium enhancement models. A small helium enhancement of Y$\approx$ 8% (ΔY $\approx$ 0.02) is enough to produce broadening at the level seen here.

Taking advantage of the two completely independent data sets (NUV and U-band, and V- and I-band), I assessed the extent to which the apparent broadening can be trusted. Comparisons between the two sets of colours (ΔM_{NUV-U} vs ΔM_{V-I}) do not have as high a gradient as one would expect from the ratio of intrinsic broadening measurements, leading me to conclude that the intrinsic broadening measured in each CMD should be considered to be an upper limit. The comparisons do, however, show a significant correlation in all I-band magnitude bins considered, indicating that, in general, a source which is found to the blue side of the MSRL in the NUV - U CMD also lies to the blue of the MSRL on the V - I CMD. Using only the sources for which the colour determination can be trusted most, I found that the correlation between colours is strongly significant and the probability of the measured colours matching in as many cases as they do by chance is almost zero.

I conclude, therefore, that there is evidence for some broadening in the MS of NGC 6752, but that it is small. I have determined upper limits on the amount of broadening in the NUV - U and V - I CMD and found that a small difference in helium abundance of (ΔY $\approx$ 0.02) is sufficient to produce the observed levels of broadening.

I have found hints of a radial trend in the level of broadening in each CMD, with more broadening in the core of the cluster than further out. This contradicts the result of Milone et al. (2010), who considered a region overlapping with, but extending further out than, the region considered in this investigation. If the radial trend found here is extrapolated to cover the region considered by Milone et al., I would expect the broadening found in their investigation to be lower than the results shown here; in fact, they found twice as much intrinsic broadening as in this investigation.

...And whether or not it is clear to you, no doubt the Universe is unfolding as it should.

M. EHRMANN (1872 – 1945)

7

Summary and Further Work

In this thesis I have discussed surveys of two GCs: Chapter 3 describes an FUV survey of M 80, and Chapters 4 to 6 present an in-depth, multi-wavelength study of NGC 6752. In this chapter, I will summarise the main conclusions of both investigations, highlight the key outstanding issues, and suggest some of the ways in which they might be addressed.

7.1 The Colour-Magnitude Diagram and Stellar Populations

The colour-magnitude diagrams of M 80 and NGC 6752 are shown in Figures 3.15, 4.1 and 4.2. In M 80's case, the CMDs were created using FUV - NUV and V - I colours; in the case of NGC 6752, NUV - U, V - I and FUV - NUV measurements were used. The CMDs exhibit the main types of stellar populations found in GCs, and demonstrate the differences between using UV and optical wavelengths. In the UV CMDs, gap sources and white dwarfs are found easily, while in the optical CMD in each case, the vast majority of sources are main-sequence and red giant branch stars.

7.1.1 The Horizontal Branch

In both clusters' CMDs, the horizontal branches are well populated and can be divided into BHB and EHB populations. Neither cluster exhibits any HB sources to the red side of the instability strip ('red HB stars'). This is as expected and follows from the so-called 'first parameter' in HB morphology: more metal poor clusters tend to have bluer HBs, and both of these clusters have low metallicity (M 80 and NGC 6752 have $[\mathrm{Fe/H}] = -1.7$ dex and -1.54 dex, respectively). While the colours of stars distributed along the HB is understood to be due to differences in the envelope masses of stars when they leave the RGB (e.g. Fusi Pecci et al. 1993), a number of clusters are known to exhibit complex morphologies such as gaps, whose physical origins are not understood. Accurately establishing the detailed morphology of the HB populations in GCs is important in the context of refining stellar evolution models. This is highlighted in Section 3.1.4, in which the positions of gaps found in the HB of M 80 are compared with those found in a previous survey, demonstrating the difficulties in using models to accurately convert from temperature to magnitude.

One of the key unresolved mysteries in GC astronomy is the 'second parameter' problem, which concerns what, aside from metallicity, governs the morphology of a GC's horizontal branch. Current theories suggest that cluster age or central density are likely to determine the morphology, but this problem is far from resolved. Furthermore, as outlined in Sections 1.3.2.4 and 2.1.3, HB morphology is linked to the presence of multiple populations, but the nature of the connection is unclear.

It is likely that the solutions to the 'second parameter' and multiple population mysteries will be intrinsically linked, and investigations into both topics can be aided by deeper and more precise CMDs of individual GCs. UV observations will be key here, since HB stars are most easily distinguished in UV CMDs. Comparisons between the HB morphologies of a number of clusters might then be done in a way similar to that employed by Ferraro et al. (1998), who compared the position of gaps in the HB of M 3, M 13 and M 80. Another option is to investigate the size and radial distributions of HB populations found in clusters of different masses. Leigh et al. (2011) found that the number of HB stars scale with GC mass, but also suggest that the radial distribution in lower mass GCs might be more extended. In order to clarify this relationship, surveys of more GCs are required which are deep enough to measure the whole horizontal branch ($V_{STMAG} \approx 19$ mag, $FUV_{STMAG} \approx 16$ mag is sufficient for nearer GCs such as NGC 6752, but completeness in the cluster core to a level of $V_{STMAG} \approx 21$ mag and $FUV_{STMAG} \approx 18$ mag are required for more distant

GCs like M 80). These surveys must also cover sufficient areas of the cluster that the HB population can be accurately measured.

An ongoing issue is that theoretical isochrones are highly uncertain in the HB. This makes consistently determining what defines an HB star something of a challenge at present; improved theoretical models will allow a more consistent approach to be used in comparing HBs of different clusters, both in terms of numbers and morphologies.

In terms of the link with multiple populations, specifically, spectra can be used to establish the abundances of a number of HB stars within a single cluster, and used to search for evidence of multiple populations of stars. For example, Peterson et al. (1995) found that oxygen abundance decreases with temperature along the HB of each cluster that they studied. Searches have also been carried out for anticorrelations between sodium and oxygen in stars of similar helium abundance (see, for example, Villanova et al. 2009, 2012; Marino et al. 2011b), and redder and bluer parts of the HB have recently been linked with different main-sequences in NGC 2808 (Gratton et al., 2011). Most of these surveys use only a few stars each (Gratton et al. (2011) is the exception, with a few tens of stars). Surveys including larger numbers of stars will allow stronger conclusions to be drawn regarding these anticorrelations, and connections to be drawn between spectroscopic and photometric features.

7.1.2 The Blue Hook

Only one candidate blue hook star (which may actually be an EHB star) was found in M 80. This was contrary to a prediction by Momany et al. (2004), who suggested that M 80 may house a BHk population. No blue hook stars were found in NGC 6752.

Debate continues over whether BHk stars can exist in all GCs or if there is a lower mass limit and only the most massive clusters contain any BHk stars. Both M 80 and NGC 6752 can be considered to be relatively low mass (Brown et al., 2010), so the lack of observable BHk stars is in line with the theory that lower mass GCs do not house BHk populations. To date, no BHk stars have been found in any low mass clusters. However, as argued by Dieball et al. (2009), this may be due to selection effects and may not be a physical mass limit. The sample of GCs for which surveys capable of identifying BHk stars have been completed is small, and skewed towards more massive clusters (see Dieball et al. (2009), their Table 2). Deep, ultraviolet surveys of a number of low-mass clusters are needed to address this imbalance and allow proper statistical analyses of the types of clusters that house BHk stars. Similarly, it should be noted that no BHk stars have been found in 47 Tuc or NGC 6441, which are both massive clusters. This may be indicative that it is possible for massive clusters to not house any BHk stars, but of course, it may simply be that they are yet to be found.

Once a blue hook population has been convincingly found in a number of clusters and the relationship between the presence of BHk stars and GC mass is resolved, attention will turn to the size of the BHk populations. Comparisons could be drawn between the size of the population and various GC parameters such as concentration parameter or core radius. A more uniform data set would be required for this survey; at present, only lower limits on the numbers of BHk stars are available. A number of clusters would need to be studied using observations that were deep enough to reliably reveal the BHk population. The radial profile of all of the clusters would also be needed, in order to determine the core radius in a self-consistent way (observations of the outskirts of the cluster would also be needed if the concentration parameter were to be used, as this requires knowledge of the tidal radius).

7.1.3 Pulsating Stars

This thesis includes a search for variable sources in the catalogues of both GCs. In M 80, three variable sources were found, including an RR Lyrae source of type ab. This source was observed around the peak of the light curve, and demonstrates the extreme magnitude variation exhibited by RR Lyrae at short wavelengths. In NGC 6752, a number of candidate variable sources were identified.

Ultraviolet observations are excellent tools in the search for variable sources: as well as the ability to resolve bluer stars in the dense core of GCs, the magnitude variation in pulsating stars is larger at UV wavelengths than optical. Searches for periods among such sources tend to be limited by the number of observations. Surveys which are deep enough to reliably find pulsating sources, yet include large numbers of individual exposures are needed in order to accurately measure periods and categorise pulsating stars correctly. Surveys capable of locating instability strip sources (such as RR Lyrae stars) in GCs would be useful in aiding understanding of pulsating stars themselves, since GCs present the opportunity to study a number of these stars simultaneously. Surveys capable of achieving this would also be deep enough to be useful in studies of HB stars, as described above. At present, observing programmes tend to be skewed to preferentially find short period variables; observations over longer time-scales are needed to measure periods in longer period variables such as TDK 3, described in Chapter 3.

7.1.4 Blue Straggler Stars

Blue straggler stars were found in both of the clusters studied in this thesis. BSs are abnormally massive stars that lie above the MSTO on the CMD. The formation mechanism (or mechanisms) responsible for BSs is not yet well understood and a topic of current debate (see Section 2.1.8). It is likely that they form from either direct stellar collisions (Hills & Day, 1976) or coalescing primordial binaries (McCrea, 1964), or a combination of the two (Knigge et al., 2009; Ferraro et al., 2009). Comparing the NUV - U and V - I CMDs shown in Figure 4.1 demonstrates how much easier it is to separate BS stars from the MSTO region using UV observations. As shown in Chapters 3 and 4, studies using UV images are valuable tools in searches for BSs, especially in the dense globular cluster cores. They could play a vital role in establishing correlations between BS population sizes and cluster core mass, collision rate and binary fraction, and shed much needed light on the formation mechanisms at work. In turn, the formation mechanism is closely linked to the dynamical status of the host GC, since a large binary fraction can delay core-collapse (e.g. Ferraro et al. 1999), while core-collapse increases the number of collisions and hardens existing binaries (e.g. Ferraro et al. 2009).

In an earlier study, Ferraro et al. (1999) found that M 80 housed a large, centrally concentrated blue straggler population and suggested that the interactions which formed the BS stars was also delaying core-collapse. In the study described in Section 3.1.4, the BS population of M 80 is the most centrally concentrated population, but it does not appear unusually large, when compared to that of M 15 (Dieball et al., 2007) or the numbers expected from the number of horizontal branch stars. What was found to be unusual about M 80's BSs, however, was the radial distribution of the brighter and fainter BSs. Brighter and bluer BSs are thought to be younger (Ferraro et al., 2003b) and more massive (Sills et al., 2000) than faint, red BSs, so are expected to be more centrally concentrated. As Figure 3.6 shows, the opposite was found in M 80: the redder and fainter BSs were more centrally concentrated, and the KS test showed just a 3.5% probability that the two groups were from the same underlying population. This might suggest that the BSs in this cluster receive a 'kick' at their formation, moving them towards the cluster outskirts, and they then sink back towards the core. The younger, bright BSs could then be found further out in the cluster because (assuming that the relaxation time-scale of the cluster is longer than the typical age of a bright BS) they have not yet had time to settle back to the expected distribution. In NGC 6752 (see Figure 4.10), the distributions were found to be in line with expectation, with no significant difference between the two.

The intriguing result found in M 80, and the contrast between the radial distributions of M 80 and NGC 6752's BSs could be further investigated using comparisons with other GCs. Leigh et al. (2011) present a homogeneous catalogue of RGB, MSTO, HB and BS stars in 35 Galactic GCs, which was constructed using data taken from the ACS Survey for Globular Clusters (Sarajedini et al., 2007). This catalogue includes V- and I-band measurements for sources down to at least 7 mag below the MSTO and is complete above at least 0.5 mag below the MSTO, so should include all (detectable) blue stragglers. The GCs are centred in the ACS field, and the field extends several core radii from the cluster centre in each case. The catalogue includes M 80, but not NGC 6752. Exploiting this catalogue to investigate the radial distributions of redder and bluer BSs seems a natural extension to the work presented in this thesis.

Knigge et al. (2009) and Leigh et al. (2011) found that the number of BSs scales (sub-linearly) with cluster mass, and that the number of BSs found within a given radius scales with the total mass enclosed in that radius, as expected. They did not, however, consider sub-populations of BSs. It would be interesting to use their catalogue to construct radial profiles for redder and bluer (fainter and brighter) BSs to see if the radial distributions differ in other GCs or if M 80 is unique in exhibiting such a trend. It would also be worth seeing if the presence of differences in radial distributions are correlated with GC parameters like GC mass, core density, or collision rate.

7.1.5 X-ray Sources and Compact Objects

One of the key questions in GC astronomy at present is how and why (and, indeed, if) X-ray sources in globular clusters are fundamentally different from those found in the field. In order to help address this problem, this thesis includes searches for optical counterparts to X-ray sources in M 80 and NGC 6752.

Cataclysmic variables in the field are known to have a period distribution which has a gap; very few field CVs have orbital periods of $2-3$ hours (e.g. Knigge 2012). In the (small) sample of known GC CVs, this period gap is not seen. It is not yet known if this is due to physical differences between GC and field CVs, or if it is simply a selection effect. Observing CVs in globular clusters and ascertaining their orbital periods is vital if we are to understand if the apparent difference is real. Previously unknown counterparts to X-ray sources were found in both clusters studied in this thesis, and candidate CVs were identified based on their CMD positions. In neither cluster did I detect any CVs with orbital periods in the 2 – 3 hour range, but the number of CVs with known periods in both clusters is very small; further studies, with multiple observations taken over several hours, are needed to establish the period distribution of the CVs in these and other globular clusters.

Edmonds et al. (2003a,b) used an extensive WFPC2 study in combination with a *Chandra* X-ray survey to search for CVs in 47 Tuc, and determined reliable periods for six CVs (compared to a total of fifteen GC CVs with known periods). Their study used over 120 orbits of V- and I-band observations, comprising over 600 images in each band, and a limited number of short U-band exposures. Crowding was acknowledged to be a limiting factor in this study. A study of similar scale, using deep observations taken over many orbits, but using the newer WFC3 rather than WFPC2 might prove even more enlightening; WFC3 has a smaller pixel scale than WFPC2 ($0.''04$ per pixel vs. $0.''1$ per pixel; see Appendix B), so crowding will be less of an issue. Furthermore, one could take advantage of WFC3's UV filters, to further reduce crowding in the core of the cluster and allow for likely counterparts to X-ray sources to be categorised more clearly based on CMD position.

In M 80, it was discovered that the brightest X-ray source, which was known to lie close to the location of the classical nova T Scorpii, was in fact the nova remnant. The optical counterpart was also recovered and found to be undergoing a dwarf nova outburst during the FUV observations, leading to the suppression of the expected flickering (Bruch, 1992; Warner, 2003). In this cluster, five further optical counterparts to known CVs were recovered, as well as the faint optical counterpart to the known dwarf nova, DN 1. NGC 6752 was already known to harbour at least one dwarf nova, which was known to have an orbital period of 5.1 hours. In the search described in Section 5.1, I discovered that two X-ray sources which were previously categorised as CVs were, in fact, DNe, which underwent outbursts in my observations. This takes the number of known DNe in NGC 6752 to three, more than any other globular cluster. Observations like these, which add to the list of known GC DNe, are invaluable in discovering if there really is a lack of DNe in globular clusters, or if they simply have not been discovered yet.

Theoretical evolutionary scenarios suggest that the majority of CVs in globular clusters should be dwarf novae (Knigge et al., 2011). Observations, however suggest that dwarf novae are unexpectedly rare in GCs (Pietrukowicz et al., 2008). Again, this may be due to a selection effect, as the fraction of a cluster's dwarf novae that should be detected in a survey depends strongly on the duty cycle of dwarf novae, which is not well known (Knigge et al., 2011). As with other CVs, ‘collecting’ observations of dwarf novae is important in understanding more about the intrinsic properties of individual dwarf novae and the dwarf nova populations of GCs in general. This can be done in the same way as searches for other CVs, by detecting and then studying optical counterparts to X-ray sources. Interpreting these results in terms of the overall dwarf novae population then requires knowledge of the completeness of the survey, the determination of which is proving to be something of a challenge (Knigge, 2012).

Previous attempts to estimate the fraction of a GC’s dwarf novae population that should be detectable in a survey have used Monte Carlo simulations and templates taken from light curves of field DNe (see Shara et al. (1996); Pietrukowicz et al. (2008)). Of course, this immediately relies on the assumption that the field DNe used in the models and the GC DNe found in a given survey are essentially the same, which is a contentious assumption in itself. The well-known field DNe that they chose are likely to be well-known precisely because they are bright and frequently erupting (which means they have long periods but high duty cycles). In reality, however, the vast majority of DNe are thought to be short period, faint sources like WZ Sge, whose duty cycle is just 0.4% (Knigge, 2012), while GC surveys conducted so far tend to preferentially pick out short period variable sources. Observations taken over a large number of epochs (with observations frequent enough to ensure that DNe are caught in their high state if they erupt during the survey), or very deep, shorter surveys (down to $m_V \approx 28$) are needed in order to guarantee detection of at least some WZ Sge type objects, if they exist in GCs.

In NGC 6752, the previously unknown optical counterpart to one of the X-ray sources appears to be consistent with an SX Phoenicis star with a WD companion. If true, this would be the second BS-WD system identified in a GC (the first was found in 47 Tuc by Knigge et al. 2008). Such systems are expected to exist in GCs, either as the result of stellar evolution in an MS-MS binary or through dynamical interactions. Confirmation of the nature of this system would require knowledge of the spectral energy distribution and/or spectral measurements. SX Phoenicis stars in binary systems would be of interest not only in terms of X-ray astronomy and stellar dynamics, but also in terms of the study of SX Phoenicis stars themselves. Models of SX Phoenicis stars are not well constrained by current theory, and further observations are required in order to better understand the physical mechanisms at work (see, for example, Bruntt et al. 2001).

7.2 Globular Cluster Morphology

7.2.1 Dynamical Status

In Section 4.4, I investigated the dynamical status of NGC 6752. Even though this cluster has been studied frequently, its dynamical status has never been indisputably determined. Previous studies have concluded both that the cluster is core-collapsed (Djorgovski & King, 1986; Auriere & Ortolani, 1989; Ferraro et al., 2003a) and not core-collapsed (Lugger et al., 1995), based on comparisons of the stellar density or surface brightness profile with models. King (1966) models can be used to model clusters whose radial profiles flatten towards the core. Such clusters are thought to be pre-core-collapse (see Section 1.3.3.1), although recent work by Heggie & Giersz (2009) has shown that clusters whose cores have expanded in a post-core-collapse bounce might be indistinguishable from pre-collapse clusters. Radial profiles whose density or surface brightness increases into the core are thought to be about to undergo collapse, in the process of collapsing, or entering a post-collapse bounce phase. The radial profile does not allow us to distinguish between these phases. In this study, I found that NGC 6752's stellar density profile cannot be well fitted using a single 'King' profile and concluded that the cluster is in a state of core-collapse.

The fact that so many studies can look at the same cluster and reach different conclusions indicates that further work is needed for a consensus to be reached on the best approach. The key to creating precise stellar density profiles is the ability to resolve sources in the cluster core, which can be solved using new instruments such as WFC3 and bluer wavebands where the crowding is less of a problem. Of course, this relies on the assumption that the sources surveyed have the same radial profile, regardless of colour used; in the investigation described in Section 4.4, I used U-band observations of main sequence stars. Resolution is also key to surface brightness profiles, since measurements are needed in small annuli in the core region in order to establish the gradient of the profile near the centre. Past surveys such as that by Noyola & Gebhardt (2006) show that dividing radial profiles into those with 'flat' and 'steep' central profiles is complicated; in reality, profiles span a range of central gradients. Numerical simulations which can more precisely show what gradients to expect in different dynamical regimes are key to distinguishing between core-collapse phases in observations. All radial profile measurements depend on accurately and precisely locating the centre position of the cluster. Estimates of the cluster centre are limited by crowding in the core; again, deep UV observations can assist in establishing reliable measurements.

Establishing the shape of the radial profile accurately not only tells us the dynamical status, but might also hint at the presence of black holes in GCs, since a ‘cusp’ in the central region of the radial profile might indicate the presence of a central black hole. This is a topic which is a key area of research at present (see Sections 1.4.3 and 2.3.4).

Determining the binary fraction of clusters with central cusps might help to rule in or out the presence of an IMBH (Beccari et al., 2010). Reliable binary fraction estimates are only available for a few GCs, however (e.g. Sollima et al. 2007; Milone et al. 2008b). The most robust way to estimate the binary fraction of a cluster is using the colour distribution of MS stars (e.g. Hut et al. 1992). Such investigations require deep CMDs, preferably with wide colour baselines where the distribution of stars across the MS is most apparent. Care must be taken to fully understand the effects of differential reddening and photometric errors, so a large survey of many GCs, using instruments for which differential reddening is understood (e.g. ACS) which can be analysed in a consistent way are the best option here. The ACS Survey of Galactic Globular Clusters allowed for such a study (Milone et al., 2008b), but more are needed if the link between IMBHs, binary fraction and dynamical status is to be fully understood (Beccari et al., 2010).

7.2.2 Multiple Stellar Populations

One of the most important developments in GC astrophysics in recent times is the discovery that GCs are not made up of simple, single stellar populations, but that multiple generations of stars were formed. These multiple populations exhibit photometric evidence in the form of broadened or split CMD sequences. In Chapter 6, I described a search for intrinsic broadening along the main-sequence of the NGC 6752 CMD. Having corrected the catalogue for position-dependent colour errors, I found evidence for broadening and estimated (or, strictly speaking, determined an upper limit to) the amount of broadening present. A very modest difference in helium abundance of $\Delta Y < 0.02$ would be enough to account for the small level of broadening detected in both the NUV - U and V - I CMDs.

An important mystery in the understanding of multiple populations is the observed range of helium enhancements needed to recreate the different sequence widths seen in different GCs. In NGC 6752, a very small helium enhancement would be sufficient to explain the MS broadening, but other GCs require very large spreads, as well as very large absolute helium abundances. Furthermore, the possible radial trend might suggest that the formation mechanisms are linked to radial positions or density. Searches for similar trends in other clusters are needed to establish if this pattern is seen elsewhere or if NGC 6752 is atypical.

In Section 7.1.1, I discussed using spectroscopy to investigate the link between chemical abundance anticorrelations among HB stars and multiple populations. Spectral analysis of larger numbers of sources, and surveys which search for chemical anomalies among HB, RGB and MS stars in a self-consistent way are vital if we are to establish the connection between multiple stellar populations at different stages of stellar evolution. Abundance patterns in other elements (e.g. helium, lithium, aluminium and fluorine) are also possible with current spectroscopic instruments, and have not been fully explored. Gratton et al. (2011) found that "prohibitively long" exposures would be needed in order to accurately determine the helium abundance of large numbers of HB stars, since the required signal-to-noise ratio is higher for absolute helium abundances than for ratios of sodium and oxygen. If achieved, however, this could allow one to determine the helium abundances of first and second generation HB stars, and connect these to the different generations in other parts of the CMD.

As described in Section 6.8, I found hints of a radial trend in the level of broadening detected in NGC 6752, with a wider MS towards the core of the cluster. Spectroscopic surveys including a significant fraction of the HB population could also be used to search for radial trends in the chemical abundances. As explained in Section 1.3.2.6, most proposed multiple population formation mechanisms would lead to the second generation preferentially forming in the core. Vesperini et al. (2013) recently used simulations to show that the second generation is expected to be more centrally concentrated that the first generation, while observational evidence for this has been found among RGB stars (Kravtsov et al., 2011). However, a link between radial trends in the first and second generation and the radial trends in the absolute observed width of the broadening has not yet been determined. Investigating radial trends in both cases would require accurate positions as well as clearly defined sequences. It might not, however, need vast numbers of stars, as long as those included were well above the confusion limit (so stars close to the core were not preferentially lost). This could be performed using either accurate, deep photometric measurements or spectral surveys.

7.3 A Final Remark

In this chapter I have summarised some of the main results of this thesis and outlined some of the key, outstanding questions. I have also given examples of ways in which future studies of GCs might yield new and interesting results, which might help us to understand the nature not only of the populations present in GCs, but also of GCs as a whole. The concepts described here approach the outstanding questions in two ways: studying the stellar populations contained in individual GCs, and studying the overall parameters of GCs, in terms of their morphology and dynamical status. While each is interesting, it is combining the results from the two strands that will allow us to fully understand the nature of the binary populations, their origins and evolution. It will also allow for better understanding of the nature of GCs, including the nature of the multiple generations of stars which have recently been found, the dynamical evolutionary processes experienced by GCs, and their place in the study of wider topics such as galaxy formation.

APPENDICES

A

List of Abbreviations

AB – active binary

ACS[1] – Advanced Camera for Surveys

AGB – asymptotic giant branch

AGN – active galactic nucleus/nuclei

BH – black hole

BHB – blue horizontal branch

BHk – blue hook

BS – blue straggler

BY Dra – BY Draconis

CCD – charge-coupled device

Chandra – Chandra X-Ray Observatory

CMD – colour-magnitude diagram

COS[1] – Cosmic Origins Spectrograph

COSPAR[1] – Corrective Optics Space Telescope Axial Replacement

CTE – charge-transfer efficiency

---

[1] *Hubble Space Telescope* instrument; see Appendix B for details

CV – cataclysmic variable
DN(e) – dwarf nova(e)
EHB – extreme/extended horizontal branch
EW – equivalent width
FAP – false alarm probability
FGS[1] – Fine Guidance Sensor
FOC[1] – Faint Object Camera
FOS[1] – Faint Object Spectrograph
FUV – far ultraviolet
GC – globular cluster
GSC1 – Guide star catalogue 1
HB – horizontal branch
He WD – helium white dwarf
HRC[2] – high resolution channel
HRS[1] – High Resolution Spectrograph
HSP[1] – High Speed Photometer
HST – *Hubble Space Telescope*
IMBH – intermediate mass black hole
IMF – initial mass function
JVLA – Jansky Very Large Array
KS – Kolmogorov-Smirnov (test)
LMXB – low-mass X-ray binary
MAMA[1] – Multi-Anode Microchannel Array
mas – milli-arcsecond
MS – main-sequence
MSRL – main-sequence ridge-line
MSP – millisecond pulsar
MSTO – main-sequence turn-off
NICMOS[1] – Near Infrared Camera and Multi-Object Spectrometer
NS – neutron star
NUV – near ultraviolet
PSF – point-spread function
qLMXB – quiescent low-mass X-ray binary

---

[1] *Hubble Space Telescope* instrument; see Appendix B for details

[2] Relates to ACS (*Hubble Space Telescope* instrument); see Appendix B for details

r_c – core radius
r_h – half-light radius
r_m – half-mass radius
r_t – tidal radius
RG – red giant
RGB – red giant branch
RHB – red horizontal branch
RL – ridge line
RS CVn – RS Canum Venaticorum
SBC[2] – solar blind channel
SED – spectral energy distribution
SGB – sub-giant branch
STIS[1] – Space Telescope Imaging Spectrograph
t_{cross} – crossing time
t_{evap} – evaporation time
t_{relax} – relaxation time
UCAC2/3 – Second US Naval Observatory CCD Astrograph Catalog version 2/3
UCXB – ultra-compact X-ray binary
UV – ultraviolet
WD – white dwarf
WCS – world coordinate system
WFC[1] – Wide Field Camera
WFC3[1] – Wide Field Camera 3
WF/PC(1)[1] – Wide Field/Planetary Camera(1)
WFPC2[1] – Wide Field Planetary Camera 2
ZAHB – zero-age horizontal branch
ZAMS – zero-age main-sequence

---

[1] *Hubble Space Telescope* instrument; see Appendix B for details

[2] Relates to ACS (*Hubble Space Telescope* instrument); see Appendix B for details

B

The Hubble Space Telescope

The data used throughout this thesis were obtained using the *Hubble Space Telescope* (*HST*). In this section, I briefly introduce *HST* and its instruments and, for convenience, I list the instruments and filters used in this thesis, along with some important parameters.

The idea of positioning a telescope in space was first proposed (with little success) by Hermann Oberth in 1923, and more influentially suggested by Lyman Spitzer in 1946 (O'Dell, 2009). *HST* was designed and built in the 1970s and 1980s, and launched, after some delay, in 1990.

Its position in orbit around the Earth makes *HST* unique in its capability to observe the Universe in wavelengths from UV (which cannot be viewed from the ground as UV radiation is stopped by the atmosphere), through the optical wavelengths (without the problem of atmospheric distortion), to the infrared (without the immense background radiation from the Earth's atmosphere itself that affects ground-based telescopes). It does so using a number of instruments, which were updated during the service missions as old instruments failed or new technology became available.

As this thesis involves data from both current and "previously flown" instruments, it is worth briefly listing them all. The details of the instruments and specific filters used in this thesis are then summarised in Table B.1.

B.1 Current Instruments

- The Space Telescope Imaging Spectrograph (STIS) is a two-dimensional spectrograph consisting of three detectors: a charge-coupled device (CCD) and two Multi-Anode Microchannel Array (MAMA) detectors. The MAMA detectors (one FUV and one NUV) have plate scales of $\approx 0\farcs024$ per pixel, making them excellent tools for use in resolving stars in crowded fields, but the small field of view ($25 \times 25''$) means STIS MAMAs can only view part of the core of a GC at one time. STIS was rendered inoperable by a power supply failure in 2004, and was repaired in 2009. It is currently in operation.

- The Near Infrared Camera and Multi-Object Spectrometer (NICMOS) is an infrared imaging and spectroscopic instrument, with wavelength range $0.8 - 2.5\mu m$ (8000 – 25000Å). NICMOS detectors must be maintained at $\approx 77\,$K. It was unusable from 1999 when the nitrogen ice used to cool the detectors was exhausted, to 2002 when a mechanical cooler was installed. Since 2008, the cooling system has been experiencing difficulties. At the time of writing, NICMOS is unavailable for use and a decision on the future of the instrument has not yet been reached.

- The Advanced Camera for Surveys (ACS) was installed in 2002 and is *HST*'s most heavily used instrument to date. It was designed to provide deep, wide-field capability and is a substantial improvement on earlier instruments in terms of imaging and instrument throughput. The ACS has three channels, each optimised for specific tasks: the Wide Field Channel (WFC) consists of two CCDs with a plate scale of $0\farcs05$ per pixel and a large field of view ($202 \times 202''$) and is capable of observing from 3500 to 11000Å; the High-Resolution Channel (HRC) has a smaller field of view than WFC ($26 \times 29''$), but twice the spatial sampling capabilities ($0\farcs025$ per pixel), and is more sensitive at NUV wavelengths; finally, the Solar Blind Channel (SBC) is a photon-counting device used in the FUV range of 1150 – 1700Å. The ACS suffered electronic failures, rendering it out of action for brief periods in 2006. One of these failures, in September 2006, proved more serious. The SBC was returned to operation in early 2007, followed by the WFC in 2009. The HRC, however, remains offline.

- The Fine Guidance Sensors (FGS), in addition to being part of the *HST* pointing control system, can be used for precision astrometry and have been used in the study of binary star systems.

- The Cosmic Origins Spectrograph (COS) is one of the newest instruments on *HST*, installed during the 2009 service mission. It is a high-sensitivity, moderate- and low-resolution spectrograph, operating in the FUV and NUV range, useful in studying the origins of large scale structure in the Universe, the formation and evolution of galaxies, and the origin of planetary and stellar systems. At the time of writing, the NUV instrument is operational, but the FUV detector is suspended following shut-down due to an anomalous, abnormally high count rate, pending investigation and recovery.

- The Wide Field Camera 3 (WFC3) was also installed in 2009. It is designed to provide wide-field imaging with coverage from the NUV to infrared. It consists of two channels: the UVIS channel covers the UV and visible range, from 2000 to 10000 Å, and the IR channel, operating in the infrared (9000 – 17000 Å).

B.2 Previous Instruments

- The Wide Field/Planetary Camera (WF/PC or WF/PC1) was one of *HST*'s initial instruments, and was used from 1990 to 1993. It was designed as a wide field camera with high resolution.

- The Wide Field Planetary Camera 2 (WFPC2) replaced WF/PC1. It was the first instrument to include a correction for the spherically aberrated primary mirror, and consisted of four cameras. Three "WF" cameras are positioned in an "L"-shape with sides of length $150 \times 150''$, and have pixel scales of $0\farcs1$ per pixel, while a smaller "PC" chip has a smaller, $34 \times 34''$ field of view but finer pixel scale of $0\farcs046$ per pixel. The WFPC2 worked in the same wavelength range as WF/PC1 (1150 – 11000 Å). The WFPC2 was removed in the May 2009 servicing mission, when it was replaced by the WFC3.

- The Faint Object Spectrograph (FOS) was one of the original *HST* spectrographs, and was designed to examine faint objects, in a wide spectral range (1150 – 8000 Å). In its low-resolution mode, FOS could reach magnitude 26 in one hour of observing. In high resolution mode, it could reach 22 magnitude in one hour, but with far better resolving power. FOS was replaced by NICMOS in 1997.

- The Goddard High Resolution Spectrograph (HRS) was the other original spectrograph. It contrasted with FOS in that it was designed to examine objects in fine spectral detail, at UV wavelengths. The two detectors were sensitive to light at $1050 - 1700\,\text{Å}$ and $1150 - 3200\,\text{Å}$. The HRS could also discriminate variations in light from objects as rapid as 100 milliseconds apart. The HRS failed in 1997, shortly before being replaced by STIS.

- The Faint Object Camera (FOC) was built by the European Space Agency. It was designed to take high resolution images in the NUV to infrared range. It had a small field of view ($14 \times 14''$), and a pixel scale down to $0.''014$ per pixel, giving it better spatial resolution than the WFPC2. FOC was replaced by the ACS in 2002.

- The High Speed Photometer (HSP) was one of *HST*'s original instruments and was removed in 1993. It was designed to make very rapid photometric observations in a variety of wavebands from UV to visible.

- Corrective Optics Space Telescope Axial Replacement (COSPAR) was not actually a science instrument; it was the package that corrected the aberration of the primary mirror of *HST*. COSPAR was used in correcting the optics for the FOC, HRS and FOS. All instruments installed since *HST*'s initial deployment have had built-in corrective optics. COSPAR was removed in 2009 as it was no longer needed.

Table B.1: A summary of the *HST* instruments used in this thesis. The first column lists the instruments used. Columns 2 and 3 give the field of view and pixel size. The next two columns list the specific filters, and the final column indicates in which part of the thesis the data is used.

Instrument	FoV [$''$]	Pixel Size [$''$]	Filter	Waveband	Chapter
ACS/SBC	35×31	0.034×0.030	F140LP	FUV	3
			F150LP	FUV	3
			F165LP	FUV	3
ACS/HRC	29×26	0.028×0.025	F250W	NUV	3
ACS/WFC	202×202	0.05×0.05	F435W	B	3
			F606W	V	4−6
			F814W	I	4−6
STIS	25.1×25.3	0.025×0.025	F25QTZ	FUV	4−5
WFC3/UVIS	162×162	0.04×0.04	F225W	NUV	4−6
			F390W	U	4−6
			F410M	B	5
WFPC2/PC	34×34	0.046×0.046	F439W	B	3
			F555W	V	3
			F656N	$H\alpha$	3
			F675W	R	3

C

Preliminary Work Towards Further Investigation of Broadening in the NGC 6752 CMD

In Chapter 6, I showed evidence of broadening in the main-sequence of NGC 6752 and suggested that the CMD shown in Chapter 4 shows hints of a broadened red giant branch, while the sub-giant branch appears to be narrow. Preliminary investigations into these CMD sequences suggest that it would be interesting to study the photometric characteristics of these branches further. In this appendix, I discuss the investigations carried out so far and how the work might be continued in future.

C.1 The Red Giant Branch

Correlations between colours of red giant branch stars and spectroscopic features (Na and O abundance, for example) have been found by Grundahl et al. (2002), Yong et al. (2008) and Milone et al. (2010). In theory, it should be possible to carry out a full photometric investigation of the suspected broadening in the RGB using the same technique as that employed in my study of the main-sequence in

Table C.1: Summary of observations used in preliminary investigations of broadening in the SGB and RGB. All observations were taken with the WFC3/UVIS detector, which has a field of view of 162″ × 162″ and a plate scale of 0.″04 per pixel.

Waveband	Filter	Date	Number × Exptime Overall	Number × Exptime Per Group
NUV	F225W	2010 July 31, August 7, 21	18 × 120 s	9 × 120 s
U	F390W	2010 January 5	2 × 2 s	1 × 2 s
B	F410M	2010 May 5	2 × 800 s	1 × 800 s

Chapter 6. Searching for RGB broadening using photometry, without the need for comparisons with spectroscopy results, would mean that all observable stars could be used; not only those with available spectra. It would also allow for a quantitative analysis of the level of broadening, which could then be compared to models to estimate the levels of light-element enhancement required. Finally, this could be compared to results from spectroscopy to demonstrate how reliable the photometry is, or to help refine the theoretical models. In practice, photometric measurements of RGB broadening are complicated by the need for precise photometry and a large enough population of RGB stars. The WFC3 might be useful in this type of study, because the wide field of view allows for many RGB stars to be observed at once (see Table B.1), while the excellent resolution and availability of NUV and U-band filters allow RGBs to be resolved in the GC core.

Using a method analogous to that used in studying the MS, I have carried out preliminary work using WFC3 images of NGC 6752, in order to search for evidence of RGB broadening. I used images taken with the WFC3, using the F225W (NUV) and F390W (U-band) filters. The NUV images were the same images that I used when studying the MS. The U-band data set comprised a pair of 2 s images, in which RGB stars were not saturated. As before, I used `DOLPHOT` to carry out photometry on two groups of images, and compared the colours measured in the two groups. Table C.1 lists the observations used, and Figure C.1 shows the results.

The figure was created in the same way as Figure 6.4: In panel (a), sources are coloured red or blue depending on their colour relative to a ridge-line (RL) which was created using the Group 1 CMD; panel (b) shows the colour relative to Group 2 RL, with sources retaining the red/blue classification given in panel (a); in panel (c) I compare the two results. The gradient of the best fit line (dark green) is close to 1 in all magnitude bins, even though the small number of stars would make the fit susceptible to influence from outliers. This suggests that the colours measured

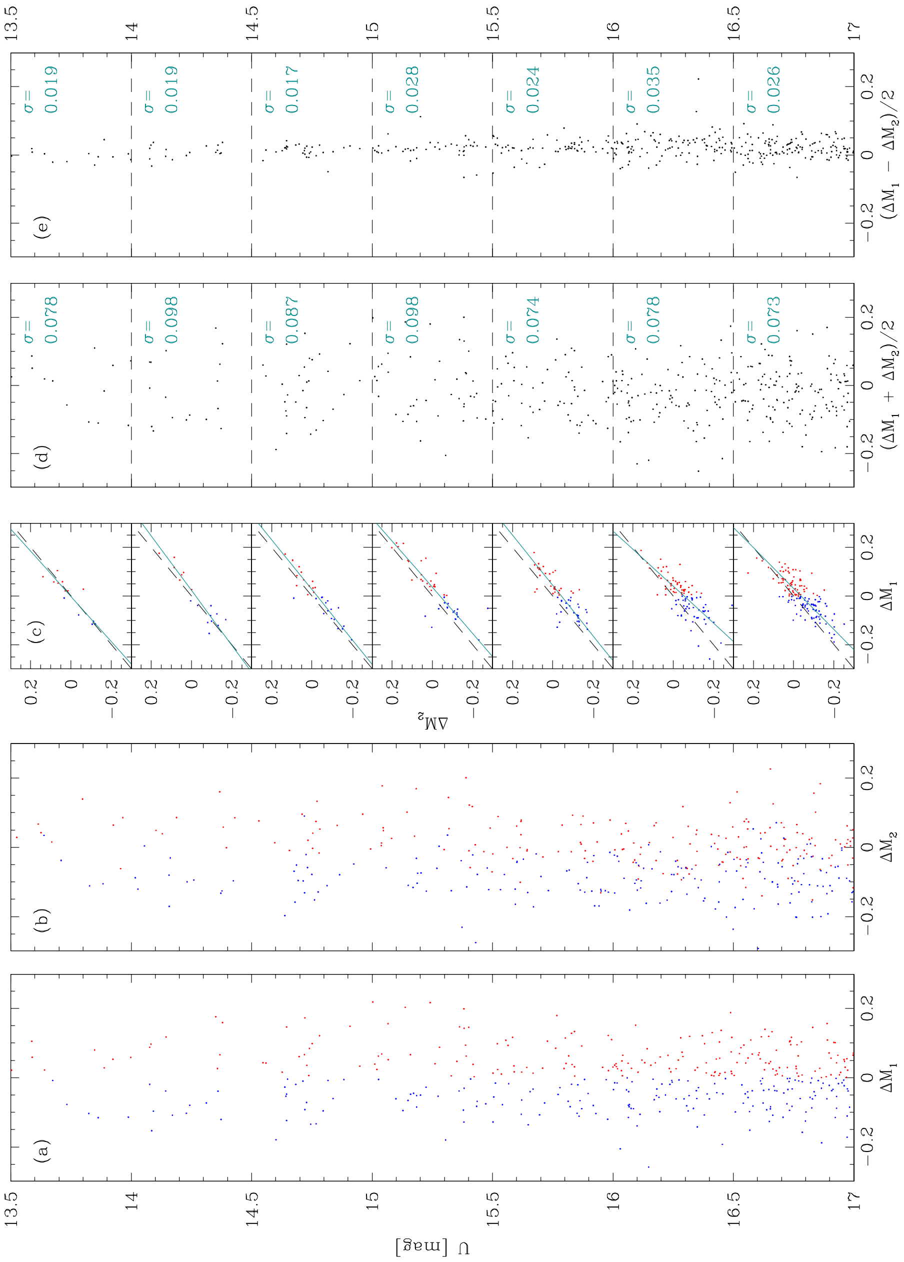

Figure C.1: Preliminary evidence for RGB broadening using NUV - U data. I caution that the result is unlikely to be entirely due to real broadening; it is likely that position-dependent errors have a significant effect. Panel (a): Straightened RGB for Group 1 data. Stars are coloured blue or red depending on their colour relative to the ridge-line (RL). Panel (b): Straightened RGB for Group 2 data. Each source is plotted with the colour assigned to it in panel (a). Panel (c): Correlations between the two measurements, in U-band magnitude bins. The black, dashed line has a gradient of 1 and is the expected result if there was a perfect correlation between the measurements, with no photometric errors. The dark green, solid line shows the actual best-fit line to the data. Panel (d): The mean distance of each source from the RLs. Panel (e): Estimates of errors in the mean colour.

in the two groups are strongly correlated. Interestingly, the best fit line in panel (c) often sits below the ‘expected result’ (black, dashed line), suggesting that there is a systematic shift between the two measurements. Upon inspection, I found that ΔM_1 is, on average, approximately 0.02 mag larger (redder) than ΔM_2. This might be due to PSF changes due to telescope breathing.[1] In panel (d) and (e) of Figure C.1, I plot the mean distance from the ridge-line and the minimum error. There appears to be strong evidence that the broadening shown in panel (d) cannot be due to photometric errors.

I caution, however, that the RGB catalogues have not been processed using a position-dependent error correction algorithm like the one described in Chapter 6. The Group 1 and 2 RGB images are taken at the same alignment (like the NUV and U-band images used in studying the MS), making the measured colours strongly susceptible to the sorts of errors that were explored in that chapter. In fact, the low background in the U-band images makes CTE effects even more of an issue here than in the MS investigation. As there are far fewer RGB stars than MS stars, the position-dependent trends are far less obvious, which demonstrates the risk involved in using techniques like these which rely on precision photometry. Unfortunately, a colour correction like that applied in Chapter 6 cannot be used here because the sparsity of the stars means that sources do not have enough close neighbours to make the correction reliable. CTE corrections for the WFC3 are necessary for this investigation to be completed. Further caution should be taken, however, as CTE corrections alone might not be enough to account for position-dependent errors. If the remaining spatial trends are purely spatial, and do not depend on source flux or background level, the correction determined using the MS stars may be extended to correct the colours of the RGB stars; this is something that should be investigated once the CTE effects are taken care of. The apparent broadening is certainly intriguing, and as soon as a pixel based CTE correction becomes available for this instrument, a full, quantitative analysis of the RGB broadening should be possible using this method.

C.2 The Sub-Giant Branch

At first glance, the SGB shown in Figure 4.1 looks very narrow compared to the other CMD sequences. Milone et al. (2010) found very little evidence of broadening on the SGB and concluded that any broadening must be smaller than a few

---

[1] “Telescope breathing” is the name given to variations in the focus of *HST* instruments due to temperature changes as the telescope orbits the Earth (e.g. Sabbi 2009).

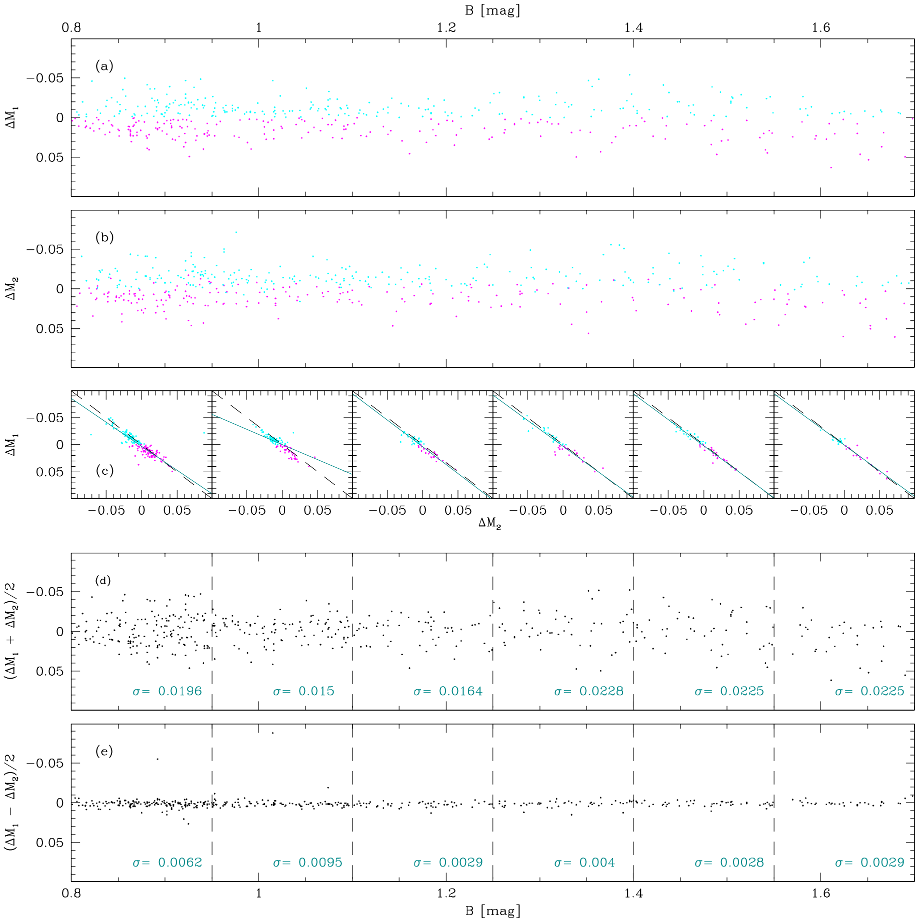

Figure C.2: Preliminary evidence for SGB broadening using NUV - B data. I caution that the result is unlikely to be entirely due to real broadening; it is likely that position-dependent errors have a significant effect. Panel (a): Straightened SGB for Group 1 data. Stars are coloured cyan or magenta depending on their brightness relative to the ridge-line (RL). Panel (b): Straightened SGB for Group 2 data. Each source is plotted with the colour assigned to it in panel (a). Panel (c): Correlations between the two measurements, in NUV - B colour bins. The black, dashed line has a gradient of 1 and is the expected result if there was a perfect correlation between the measurements, with no photometric errors. The dark green, solid line shows the actual best-fit line to the data. Panel (d): The mean (magnitude) distance of each source from the RLs. Panel (e): Estimates of errors in the mean brightness.

hundredths of a magnitude. As in the RGB case, I completed a preliminary investigation into broadening of this sequence, and found what appears to be strong evidence that a spread exists, but that it is very small. Again, I cannot rule out that systematic effects may have caused the apparent results. In studying the SGB, I used the same NUV images as before, and combined them with 800 s B-band exposures taken using the F410M filter with the WFC3 (see Table C.1). These images are deep enough to show the SGB, but not so deep that saturation becomes an issue.

As the SGB is near-horizontal in the NUV - B CMD, I searched for a spread in NUV magnitude, rather than colour, and binned the points according to NUV - B colour, rather than magnitude. The result is shown in Figure C.2. It appears that there is clear evidence of very small scale broadening of the SGB, of $\approx 0.012 - 0.022$ mag.

A preliminary search for a radial trend in sources brighter and fainter than the ridge-line indicates that the brighter sources are marginally more centrally concentrated than the fainter ones; a KS test resulted in a 6.8% probability that the brightest and faintest 20% of the SGB sources are from the same underlying distribution. This contradicts the radial distributions found by Kravtsov et al. (2011) and Milone et al. (2010). Kravtsov et al. (2011) found that fainter SGB sources in their B - I vs. U CMD were more centrally concentrated than brighter sources with a confidence level of greater than 99.9%, while Milone et al. (2010) used V- and I-band data to show that, again, the fainter sources were more centrally concentrated, with only a 4% probability that they are from the same distribution. With so few sources, it is difficult to pick out spatial trends in the data, but the fact that the radial distributions do not resemble those of previous work suggests the result is at least partly due to systematic effects.

The near-horizontal appearance of the SGB in the NUV - B CMD means that errors in colour, like those seen in the MS study, would move sources along the SGB, rather than away from it. The broadening in the SGB, if due to CTE problems, would be almost entirely due to sources appearing brighter or fainter than they should in the NUV images, with almost no dependence on the B-band observations' CTE. In theory, this should make any position-dependent problems simpler to correct. To use a similar correction algorithm to that described in Chapter 6, one would still need a number of sources of similar magnitude, within the vicinity of each 'target' source (since CTE effects are strongly dependent on source brightness). This is not feasible as sources brighter than the MSTO are quite scarce. Furthermore, the apparent effects of CTE, while certainly the dominant source of error, might be masking other, more subtle effects, which also need to be corrected. These cannot be assessed until the CTE problems are fixed. As with the RGB, it is possible that the trends determined using the MS sources could be used as a starting point for correcting position-dependent errors in the SGB.

These investigations demonstrate a number of key points which must be considered in using precise photometric studies to search for sequence broadening. First, CTE corrections for the WFC3 are essential if WFC3 data, which should be ideal for these investigations, are to be used to their full potential. Second, due to the small number of sources available for the position-dependent corrections, a number of images taken at different alignments would be ideal for this study. The colour correction algorithm could then be run on images taken at each pointing to remove the worst of the position-dependent effects, while comparisons between different alignments could be used to correct for any residual effects. Finally, consistency across many data sets is key: In terms of radial distributions, Kravtsov et al. (2011) found a much stronger radial effect than Milone et al. (2010), while this preliminary investigation found a contradictory effect; in the MS, Milone et al. (2010) found a level of broadening which was twice as large as the upper limit that I found. Further study of these aspects is clearly required before we can claim to truly understand the nature (or, indeed, the presence) of broadening of CMD sequences in NGC 6752.

BIBLIOGRAPHY

Alcaino G., Liller W., Alvarado F., Kravtsov V., Ipatov A., Samus N., Smirnov O., 1998, AJ, 116, 2415

Altamirano D., Casella P., Patruno A., Wijnands R., van der Klis M., 2008, ApJL, 674, 45

Altamirano D., Patruno A., Heinke C. O., 2010, ApJL 712, 58

Anderson J., Bedin L. R., 2010, PASP, 122, 1035

Anderson J., van der Marel R. P. 2010, ApJ, 710, 1032

Anderson J., Sarajedini A., Bedin L. R. et al., 2008, AJ, 135, 2055

Anderson J., Piotto G., King I. R., Bedin L. R., Guhathakurta P., 2009, ApJ, 697, L62

Armandroff T. E., 1989, AJ, 97, 375

Arnould M., Goriely S., Jorissen A., 1999, A&A, 347, 572

Ashman K. M., 1990, MNRAS, 247, 662

Ashman K. M., Zepf S. E., 1992, ApJ, 384, 50

Ashman K. M., Zepf S. E., 1998, Globular Cluster Systems, CAS,

Ashman K. M., Zepf S. E., 2001, ApJ, 122, 1888

Auriere M., Ortolani S., 1989, A&A, 221, 20

Bahcall J. N., Ostriker J P., 1975, Nature, 256, 23

Bailyn C. D., Rubenstein E. P., Slavin S. D., Cohn H., Lugger P., Cool A. M., Grindlay J. E., 1996, ApJ, 473, L31

Barnes J. E., Hernquist L., 1996, ApJ, 471, 115

Bassa C. G., Verbunt F., van Kerkwijk M. H., Homer L., 2003, A&A, 409, L31

Bassa C. G., Pooley D., Homer L., 2004, ApJ, 609, 755

Bassa C. G., van Kerkwijk M. H., Koester D., Verbunt F., 2006, A&A, 456, 295

Baumgardt H., Makino J., Hut P., 2005, ApJ, 620, 238

Beasley M. A., Baugh C. M., Forbes D. A., Sharples R. M., Frenk C. S., 2002, MNRAS, 333, 383

Beccari G., Pasquato M., De Marchi G., Dalessandro E., Trenti M., Gill M., 2010, ApJ, 713, 194

Bedin L. R, Piotto G., Anderson J., Cassisi S., King I. R., Momany Y., Carraro G., 2004, ApJ, 605, L125

Bekki K., 2011, MNRAS, 412, 2241

Bekki K., Yong D., 2012, MNRAS, 419, 2063

Benacquista M. J., 2006, Living Reviews in Relativity, 9, 2

Binney J., Tremaine S., 1987, Galactic Dynamics, Princeton University Press

Bogdanov S., Grindlay J. E., van den Berg M., 2005, ApJ, 630, 1029

Bogdanov S., Grindlay J. E., Heinke C. O., Camilo F., Freire P. C. C., Becker W., 2006, ApJ, 646, 1104

Bonnell J. T., Bell R. A., 1985, PASP, 97, 236

Bono G., Caputo F., Stellingwerf R. F., 1994, ApJ, 423, 294

Bragaglia A., Carretta E., Gratton R., DOrazi V., Cassisi S., Lucatello S., 2010, A&A, 519, A60

Brassington N. J., Fabbiano G., Blake S. et al., 2010, ApJ, 725, 1805

Brocato, E., Castellani, V., Scotti, G. A., Saviane, I., Piotto, G., Ferraro, F. R., 1998, A&A, 335, 929

Brodie J. P., Strader J., 2006, ARA&A, 44, 193

Brodie J. P., Romanowsky A. J., Strader J., Forbes D. A., 2011, AJ, 142, 199

Brown T. M., Sweigart A. V., Wayne B. L., Hubeny I., 2001, ApJ, 562, 368

Brown T. M., Sweigart A. V., Lanz T., Smith E., Landsman W. B., Hubeny I., 2010, ApJ, 718, 1332

Bruch A., 1992, A&A, 266, 237

Bruntt H., Frandsen S., Gilliland R. L. et al., 2001, A&A, 371, 614

Caloi V., D'Antona F., 2011, MNRAS, 417, 228

Calzetti D., de Marchi G., Paresce F., Shara M., 1993, ApJ, 402, L1

Capaccioli M., Piotto G., Stiavelli M., 1993, MNRAS, 261, 819

Carretta E., Gratton R. G., Clementini G., Fusi Pecci F., 2000, ApJ, 533, 215

Carretta E., Bragaglia A., Gratton R. G., Leone F., Recio-Blanco A., Lucatello S., 2006, A&A, 450, 523

Carretta E., Bragaglia A., Gratton R. G., Lucatello S., Momany Y., 2007a, A&A, 464, 927

Carretta E., Recio-Blanco A., Gratton R. G., Piotto G., Bragaglia A., 2007b, ApJ, 671, 125

Carretta E., Bragaglia A., Gratton R. G., Recio-Blanco A., Lucatello S., DOrazi V., Cassisi S., 2010, A&A, 516, A55

Carretta E., Lucatello S., Gratton R., Bragaglia A., DOrazi V., 2011, A&A, 533, 69

Cavallo R. M., Suntzeff N. B., Pilachowski C. A., 2004, AJ, 127, 3411

Cho D. H., Lee S. G., 2002, AJ, 124, 977

Clark G., 1975, ApJ, 199, 143L

Clement, C. M., Walker, I. R., 1991, AJ, 101, 1352

Clement, C., Muzzin, A., Dufton, Q. et al., 2001, AJ, 122, 2587

Cocozza G., Ferraro F. R., Possenti A., D'Amico N., 2006, ApJ, 641, L129

Cohen J. G., 1999a, AJ, 117, 2428

Cohen J. G., 1999b, AJ, 117, 2434

Cohen J. G., 2004, AJ, 127, 1545

Cohn H. N., Lugger P. M., Couch S. M. et al., 2010, ApJ, 722, 20

Cole S., Lacey C. G., Baugh C. M., Frenk C. S., 2000, MNRAS, 319, 168

Colpi M., Possenti A., Gualandris A., 2002, ApJ, 570, L85

D'Amico N., Possenti A., Fici L., Manchester R. N., Lyne A. G., Camilo F., Sarkissian J., 2002, ApJ, 570, L89

DAntona F., Bellazzini M., Caloi V., Fusi Pecci F., Galleti S., Rood R. T., 2005, ApJ, 631, 868

DAntona F., Caloi V., 2004, ApJ, 611, 871

DErcole A., Vesperini E., DAntona F., McMillan S. L. W., Recchi S., 2008, MNRAS, 391, 825

Decressin T., Meynet G., Charbonnel C., Prantzos N., Ekström S., 2007, A&A, 464, 1029

Di Cecco A., Becucci R., Bono G., 2010, PASP, 122, 991

Dieball, A., Knigge, C., Zurek, D., Shara, M. M., Long, K. S., 2005a, ApJL, 634, L105

Dieball, A., Knigge, C., Zurek, D., Shara, M. M., Long, K. S., 2005b, ApJ, 625, 156

Dieball A., Knigge C., Zurek D. R., Shara M. M., Long K. S., Charles P. A., Hannikainen D., 2007, ApJ, 670, 379

Dieball A., Knigge C., Maccarone T. J., Long K. S., Hannikainen D., Zurek D. R., Shara M. M., 2009, MNRAS, 394, L56

Dieball A., Long K. S., Knigge C., Thomson G. S., Zurek D. R., 2010, ApJ, 710, 332

Di Stefano, R., Rappaport, S., 1994, ApJ, 423, 274

Djorgovski S. G., 1988, The Harlow-Shapley Symposium on Globular Cluster Systems in Galaxies; Proceedings of the 126th IAU Symp., 126, 333

Djorgovski S. G., King I. R., 1986, ApJ, 305, L71

Djorgovski S. G., Meylan G., 1994, AJ, 108, 1292

Djorgovski S. G., Piotto G., Capaccioli M., 1993, AJ, 105, 2148

Dobrotka A., Lasota J.-P., Menou K., 2006, ApJ, 640, 288

Dolphin A. E., 2000, PASP, 112, 1383

Dorman B., Rood, R. T., O'Connell, R. W., 1993, ApJ, 419, 596

Dotter A., Sarajedini A., Anderson J., et al., 2010 ApJ 708 698

Downes R. A., Margon B., Homer L., Anderson S. F., 2004, AJ, 128, 2288

Dziembowski W. A., Mizierski T., 2004, Acta Astron., 54, 363

Edmonds P. D., Gilliland R. L., Heinke C. O., Grindlay J. E., Camilo F., 2001, ApJ, 557, L57

Edmonds P. D., Gilliland R. L., Heinke C. O., Grindlay J. E., 2003a, ApJ, 596, 1177

Edmonds P. D., Gilliland R. L., Heinke C. O., Grindlay J. E., 2003b, ApJ, 596, 1197

Elmegreen B. G., 2010, ApJ, 712, L184

Elmegreen B. G., Efremov Y. N., 1997, ApJ, 480, 235

Elson, R., Hut, P., Inagaki, S., 1987, ARA&A, 25, 565

Engle S. G., Guinan E., Evans N., DePasquale J., 2009, Bulletin of the American Astronomical Society, 41, 303

Fabian A. C., Pringle J. E., Rees M. J., 1975, MNRAS, 172, 15

Fall S. M., Chandar R., 2012, ApJ, 752, 96

Fall S. M., Rees M. J., 1985, ApJ, 298, 18

Fall S. M., Zhang Q., 2001, ApJ, 561, 751

Ferraro, F. R., Paltrinieri, B., Fusi Pecci, F., Rood, R. R., Dorman, B., 1998, ApJ, 500, 311

Ferraro, F. R., Paltrinieri, B., Rood, R., Dorman, B., 1999, ApJ, 522, 983

Ferraro F. R., Possenti A., Sabbi E., Lagani P., Rood R. T., D'Amico N., Origlia L., 2003a, ApJ 595 179

Ferraro, F. R., Sills, A., Rood, R., Paltrinieri, B., Buonanno, R., 2003b, ApJ, 588, 464

Ferraro F. R., Beccari G., Rood R., Bellazzini M., Sills A., Sabbi E., 2004, ApJ, 603, 127

Ferraro F. R., Beccari G., Dalessandro E., 2009, Nature, 462, 1028

Fernley J. A., Skillen I., Jameson R. F., Longmore A. J., 1990, MNRAS, 242, 685

Forbes D. A., Brodie J. P., Grillmair C. J., 1997, AJ, 113, 1652

Freeman K. C. 1993, ASPC, 48, 608

Freire P. C., Camilo F., Kramer M., Lorimer D. R., Lyne A. G., Manchester R. N., D'Amico N., 2003, MNRAS, 340, 1359

Fusi Pecci F., Ferraro F. R., Bellazzini M., Djorgovski S., Piotto G., Buonanno R., 1993, AJ, 105, 1145

Georgiev I. Y., Hilker M., Puzia T. H., Goudfrooij P., Baumgardt H., 2009, MNRAS, 396, 1075

Gerssen J., van der Marel R. P., Gebhardt K. et al. 2003, AJ, 125, 376

Gieles M., Portegies Zwart S. F., Baumgardt H., Athanassoula E., Lamers H. J. G. L. M., Sipior M., Leenaarts J., 2006, MNRAS, 371, 793

Gillett F. C., Jacoby G. H., Joyce R. et al., 1989, ApJ, 338, 862

Gnedin O. Y., Ostriker J. P., 1997, ApJ, 474, 223

Gnedin O. Y., Lee H. M., Ostriker J. P., 1999, ApJ, 522, 935

Goldsbury R., Richer H. B., Anderson J., Dotter A., Sarajedini, A., Woodley K., 2010, AJ, 140, 1830

Goodwin S. P., 1997, MNRAS, 286, L39

Gratton R. G., Bonifacio P., Bragaglia A., et al., 2001, A&A, 369, 87

Gratton R. G., Sneden C., Carretta E., 2004, ARA&A, 42, 385

Gratton R. G., Bragaglia, A., Carretta, E., de Angeli, F., Lucatello, S., Piotto, G., Recio Blanco, A., 2005, A&A, 440, 901

Gratton R. G., Carretta E., Bragaglia A., Lucatello S., D'Orazi V., 2010, A&A, 517, 81

Gratton R. G., Lucatello S., Carretta E., Bragaglia A., D'Orazi V., Momany Y. A., 2011, A&A, 534, A123

Gratton R. G., Carretta E., Bragaglia A., 2012, A&ARev, 20, 50

Grindlay J., Gursky H., Schnopper H., Parsignault D. R., Heise J., Brinkmann A. C., Schrijver J., 1976, ApJ, 205, L127

Grindlay J. E., Heinke C., Edmonds P. D., Murray S. S., 2001, Sci, 292, 2290

Grundahl F., Briley M., Nissen P. E., Feltzing S., 2002, A&A, 385, L14

Gunn J. E., Griffin R. F., 1979, AJ, 84, 752

Haggard D., Cool A. M., Arias T., Brochmann M. B., Anderson J., Davies M. B., 2010, AIPC, 1314, 157

Hansen M. S., Anderson J., Brewer J., 2007, ApJ, 671, 380

Harris W. E., 1991, ARA&A, 29, 543

Harris W. E., 1996, AJ, 112, 1487

Harris W. E., 1996, AJ, 112, 1487, 2010 edition

Heggie D. C., Giersz M., 2009, MNRAS, 397, L46

Harris W. E., Racine R., 1979, ARA&A, 17, 241

Heggie D., Hut P., 2003, The Gravitational Million-Body Problem: A Multidisciplinary Approach to Star Cluster Dynamics, Cambridge: Cambridge Univ. Press

Heinke C. O., 2010, AIPC, 1314, 135

Heinke C. O., Grindlay J. E., Edmonds P. D., Lloyd D. A., Murray S. S., 2003, ApJ, 598, 516

Heinke C. O., Grindlay J. E., Edmonds P. D. et al., 2005, ApJ, 625, 796

Heinke C. O., Cohn H. N., Lugger P. M., 2009, ApJ, 692, 584

Hernquist L., 1989, Nature, 340, 687

Hesser J. E., Bell R. A., 1980, ApJ, 238, L149

Hilker M., Richtler T., 2000, A&A, 362, 895

Hills J. G., 1976, MNRAS, 175, 1

Hills J. G., Day C. A., 1976, ApJL, 17, 87

Holtzman J. A., Faber S. M., Shaya E. J. et al., 1992, AJ, 103, 691

Holtzman J. T., Hester J., Casertano S. et al., 1995, PASP, 107, 156

Hut P., McMillan S., Goodman J., et al., 1992, PASP, 104, 981

Irwin J. A., Brink T. G., Bregman J. N., Roberts T. P., 2010, ApJ, 712, L1

Ivanova, N., Heinke, C. O., Rasio, F. A. et al., 2006, MNRAS, 372, 1043

Ivanova N., Heinke C. O., Rasio F. A., Belczynski K., Fregeau J. M., 2008, MNRAS, 386, 553

Jacoby G. H., Morse J. A., Fullton L. K., Kwitter K. B., Henry R. B. C., 1997, AJ, 114, 2611

Jeon Y.-B., Kim S.-L., Lee H., Lee M. G., 2001, AJ, 121, 2769

Johnston H. M., Verbunt F., Hasinger G., 1994, A&A, 289, 763

Kalirai J. S., MacKenty J., Rajan A., 2009, Instrument Science Report WFC3 2009-31

Kaluzny J., Thompson I. B., 2009, Acta Astron., 59, 273

Katz J., 1975, Nature, 253, 698

Kim M., Kim D.-W., Wilkes B. J. et al., 2007, ApJ, 169, 401

King I. R., 1966, AJ, 71, 64

Knigge C., 2012, MmSAI, 83, 549

Knigge C., Zurek D. R., Shara M. M., Long K. S., 2002, ApJ, 579, 752

Knigge, C, Zurek D. R., Shara M. M., Long K. S., Gilliland R. L., 2003, ApJ, 599, 1320

Knigge C., Dieball A., Maz Apellniz J., Long K. S., Zurek D. R., Shara M. M., 2008, ApJ, 683, 1006

Knigge C., Leigh N., Sills, A., 2009, Nature, 457, 288

Knigge C., Baraffe I., Patterson J., 2011, ApJS, 194, 28

Kolenberg K., Szabó R., Kurtz D. W. et al., 2010, ApJ, 713, L198

Kopacki G., 2009, American Institute of Physics Conference Series, 1170, 194

Krauss L. M., Chaboyer B., 2003, Science, 299, 65

Kravtsov V., Alcano G., Marconi G., Alvarado F., 2011, A&A, 527, L9

Kruijssen J. M. D., Pelupessy F. I., Lamers H. J. G. L. M., Zwart S. F. P., Bastian N., Icke V., 2012, MNRAS, 421, 1927

Kulkarni S. R., Hut P., McMillan S., 1993, Nature, 364, 421

Kundic T., Ostriker J. P., 1995, ApJ, 438, 702

Kurucz R. L., 1993, VizieR Online Data Catalog, 6039, 0

Larson R. B., 1993, ASPC, 48, 675

Lázaro C., Ferro A. A., Arévalo M. J., Bramich D. M., Giridhar S., Poretti E., 2006, MNRAS, 372, 69

Le Borgne J.-F., Klotz A., Poretti E. et al., 2012, AJ, 144, 39L

Lee J.-W., Kang Y.-W., Lee J., Lee Y.-W., 2009, Nature, 462, 480

Leigh N., Sills A., Knigge C., 2007, ApJ, 661, 210221; Erratum 2008, ApJ, 678, 564

Leigh N., Sills A., Knigge C., 2011, MNRAS, 416, 1410

Lomb N. R., 1976, Ap&SS, 39, 447

Lu T.-N., Kong A. K. H., Verbunt F., Lewin W. H. G., Anderson S. F., Pooley D., 2011, ApJ, 736, 158L

Lugger P. M., Cohn H. N., Grindlay J. E., 1995, ApJ, 439, 191

Maccarone T., Knigge C., 2007, A&G, 48, 5.12

Maccarone T. J., Peacock M. B., 2011 MNRAS, 415, 1875

Maccarone T. J., Servillat M., 2008, MNRAS, 389, 379; Erratum 2010, MNRAS, 408, 2511

Maccarone T. J., Zurek D. R., 2012, MNRAS, 423, 2

Maccarone T. J., Kundu A., Zepf S. E., Rhode K. L., 2007, Nature, 445, 183

Maccarone T. J., Kundu A., Zepf S. E., Rhode K. L., 2010a, MNRAS, 410, 1655

Maccarone T. J., Long K. S., Knigge C., Dieball A., Zurek D. R., 2010b, MNRAS, 406, 2087

Mackey A. D., Wilkinson M. I., Davies M. B., Gilmore G. F., 2007, MNRAS, 379, L40

Mapelli M., Sigurdsson S., Ferraro F. R., Colpi M., Possenti A., Lanzoni B., 2006, MNRAS, 373, 361

Marin-Franch A., Aparicio A., Piotto G. et al. 2009, 694, 1498

Marino A. F., Milone A. P., Piotto G. et al. 2011a, ApJ, 731, 64

Marino A. F., Villanova S., Milone A. P., Piotto G., Lind K., Geisler D., Stetson P. B., 2011b, ApJ, 730, L16

McCrea W. H., 1964, MNRAS, 128, 147

McLaughlin D. E., van der Marel R. P., 2005, ApJ, 161, 304

McNamara B. J., McKeever J., 2011, AJ, 142, 163

McNamara B. J., Harrison T. E., Anderson J., 2003, ApJ, 595, 187

Mendel J. T., Proctor R. N., Forbes D. A., 2007, MNRAS, 379, 1618

Meylan G., Heggie D. C., 1997, A&A Rev., 8, 1

Michie R. W., 1963, MNRAS, 126, 499

Mihos J. C., Hernquist L., 1996, ApJ, 464, 641

Milone A. P., Bedin L. R., Piotto G. et al., 2008a, ApJ, 673, 241

Milone A. P., Piotto G., Bedin L. R., Sarajedini A., 2008b, MmSAI, 79, 623

Milone A. P., Stetson P. B., Piotto G., Bedin L. R., Anderson J., Cassisi S., Salaris M., 2009, A&A, 503, 755

Milone A. P., Piotto G., King, I. R. et al., 2010, ApJ, 709, 1183

Milone A. P., Piotto G., Bedin, L. R. et al., 2012a, ApJ, 744, 58

Milone A. P., Marino A. F., Piotto G. et al. 2012b, ApJ, 745, 27

Milone A. P., Marino A. F., Cassisi S. et al. 2012c, ApJ, 754, L34

Moffett T. J., Gieren W. P., Barnes III T. G., Gomez M., 1998, APJS, 117, 135

Momany Y., Bedin, L. R., Cassisi, S., et al., 2004, A&A, 420, 605

Montegriffo P., Ferraro F. R., Fusi Pecci F., Origlia L., 1995, MNRAS, 276, 739

Moore B., 1996, ApJ, 416, L13

Moretti A., Piotto G., Arcidiacono C. et al., 2009, A&A, 493, 539

Nataf D. M., Gould A., Pinsonneault M. H., Stetson P. B., 2011, ApJ, 736, 94

Nelemans G., Jonker P. G., 2010, NewAR, 54, 87

Nemec J. M., 1985, AJ, 90, 204

Norris J. E., 2004, ApJ, 612, L25

Norris J. E., Da Costa G. S., 1995, ApJ, 447, 680

Norris J. E., Cottrell P. L., Freeman K. C., Da Costa G. S., 1981, ApJ, 244, 205

Noyola E., Gebhardt K., 2006, AJ, 132, 447

Noyola E., Gebhardt K., Bergmann M., 2008, ApJ, 676, 1008

ODell C. R., 2009, Experimental Astronomy, 25, 261

Olech A., Moskalik P., 2009, A&A, 494, 17OL

Oosterhoff P. T., 1939, The Observatory, 62, 104

Osborn W., 1971, Obs, 91, 223

Ostriker J. P., Spitzer L. Jr., Chevalier R. A., 1972, ApJ, 176, L51

Olszewski E. W., Saha A., Knezek P., Subramaniam A., de Boer T., Seitzer P., 2009, AJ, 138, 1570

Padmanabhan T., 2001, Theoretical Astrophysics, Volume 2, Stars and Stellar Systems, Cambridge: Cambridge Univ. Press

Pasquini L., Ecuvillon A., Bonifacio P., Wolff B., 2008, A&A, 489, 315

Patterson J., 1994, PASP, 106, 209

Paust N. E. Q., Reid N., Piotto G., 2010, AJ, 139, 476

Peacock M B., Maccarone T J., Knigge C., Kundu A., Waters C Z., Zepf S E., Zurek D R., 2010, MNRAS, 402, 803

Pease F. G. 1928, PASP, 40, 342

Peebles P. J. E., Dicke R. H., 1968, ApJ, 154, 891

Peña J. H., Chow M., Peña R., Arellano Ferro A., Alvarez M., Torres E., 2008, Communications in Asteroseismology, 157, 357

Peña J. H., Arellano Ferro A., Peña Miller R., Sareyan J. P., Álvarez M., 2009, Revista Mexicana de Astronomia y Astrofisica, 45, 191

Peterson R. C., Rood R. T., Crocker D. A., 1995, ApJ, 453, 214

Pietrukowicz P., Kaluzny J., Schwarzenberg-Czerny A., Thompson I. B., Pych W., Krzeminski W., Mazur B., 2008, MNRAS, 388, 1111

Piotto G., King I. R., Djorgovski S. G. et al., 2002, A&A, 391, 945

Piotto, G., De Angeli F., King I. R. et al., 2004, ApJ, 604, L109

Piotto G., Villanova S, Bedin L. R. et al., 2005, ApJ, 621, 777

Piotto G., Bedin L. R., Anderson J. et al., 2007, ApJ, 661, L53

Piotto G., 2009, IAUS, 258, 233

Pogson N., 1860, MNRAS, 21, 32

Pooley D., 2010, PNAS, 107, 7164

Pooley D., Hut P., 2006, ApJ, 646, L143

Pooley D., Lewin W. H. G., Homer L. et al., 2002, ApJ, 569, 405

Pooley, D., Lewin W. H. G., Anderson S. F. et al. 2003, ApJ, 591, L131

Portegies Zwart S. F., McMillan S. L. W., Gieles M., 2010, ARA&A, 48, 431

Press W. H., Teukolsky S. A., Vettering V. T., Flannery B. P., 2007, Numerical Recipes 3rd Edition: The Art of Scientific Computing, Cambridge: Cambridge Univ. Press

Recio-Blanco A., Aparicio A., Piotto G., de Angeli F., Djorgovski S. G., 2006, A&A, 452, 875

Rodríguez E., López-González M. J., 2000, A&A, 359, 597

Rodgers A. W., Paltoglou G., 1984, ApJ, 283, L5

Rosenberg A., Piotto G., Saviane I., Aparicio A., 2000, A&AS, 144, 5

Rutledge R. E., Fox D. W., Kulkarni S. R., Jacoby B. A., Cognard I., Backer D. C., Murray S. S., 2004, ApJ, 613, 522

Sabbi E., 2009, WFC3 SMOV Program 11798: UVIS PSF Core Modulation, WFC3 ISR 2009-20. (Baltimore: STScI)

Sandage A., Wildey R., 1967, ApJ, 150, 469

Sarajedini A., 2008, Proceedings of the International Astronomical Union, 4, 221

Sarajedini A., Norris J. E., 1994, ApJS, 93, 161

Sarajedini A., Bedin L. R., Chaboyer B. et al., 2007, AJ, 133, 1658

Sbordone L., Bonifacio P., Marconi G., Buonanno R., Zaggia S., 2005, A&A, 437, 905

Scargle J. D., 1982, ApJ, 263, 835

Servillat M., Webb N. A., Lewis F., Knigge C., van den Berg M., Dieball A., Grindlay J., 2007, ApJ, 773, 106

Servillat M., Dieball A., Webb N. A. et al. 2008, A&A, 490, 641

Shapley, H., 1918, PASP, 30, 42

Shara M. M., Drissen L., 1995, ApJ, 448, 203

Shara, M. M., Hurley, J. R., 2006, ApJ, 646, 464

Shara M, M., Bergeron L. E., Gilliland R. L., Saha A., Petro L., 1996, ApJ, 471, 804

Shara M. M., Hinkley S., Zurek, D., 2005a, ApJ, 634, 1272

Shara M. M., Hinkley S., Zurek D. R., Knigge C., Dieball A., 2005, AJ, 130, 1829

Shawl, S. J., White, R. E., 1986, AJ, 91, 312

Shibahashi H., 2000, ASPC, 203, 299

Shih I. C., Kundu A., Maccarone T. J., Zepf S. E., Joseph T. D., 2010, ApJ, 721, 323

Sigurdsson S., Hernquist L., 1993, Nature, 364, 423

Sills A., Bailyn C. D., Edmonds P. D., Gilliland R. L., 2000, ApJ, 535, 298

Sirianni, M., Jee, M.J., Benítez, N. et al., 2005, PASP, 117, 1049

Smith G. H., Norris J. E., 1982, ApJ, 254, 594

Smith H. A., 1995, RR Lyrae Stars, Cambridge: Cambridge Univ. Press)

Smith M. A., Sterken C., Fullerton A. W., 2005, APJ, 634, 1300

Sódor Á., Jurcsik J., Szeidl B., 2009, MNRAS, 394, 261

Sollima A., Beccari G., Ferraro F. R., Fusi Pecci F., Sarajedini A., 2007, MNRAS, 380, 781

Spitler L. R., Forbes D. A., 2009, MNRAS, 392, L1

Spitzer L., 1940, MNRAS, 100, 396

Spitzer L., Jr, 1958, ApJ, 127, 17

Spitzer L., 1969, ApJ, 158, L139

Staneva A., Spassova N., Golev V., 1996, A&AS, 116, 447

Stetson P. B., 1991, in 3rd ESO/ST-ECF Garching - Data Analysis Workshop, eds. Grosbøl P. J., Warmels R. H., p. 187

Stothers R. B., 2006, ApJ, 652, 643

Strader J., Romanowsky A J., Brodie J P., 2011, ApJS, 197, 33

Strader J., Chomiuk L., Maccarone T. J., Miller-Jones J. C. A., Seth A. C., 2012a, Nature, 490, 71

Strader J., Chomiuk L., Maccarone T. J., Miller-Jones J. C. A., Seth A. C., Heinke C. O., Sivakoff G. R., 2012b, ApJL, 750, 27

Sutantyo W., 1975, A&A, 44, 227

Thomson G. S., Dieball, A., Knigge, C., Long, K. S., Zurek, D. R., 2010, MNRAS, 406, 1084

Thomson G. S., Knigge, C., Dieball, A. et al., 2012, 423, 2901

Trager S. C., Djorgovski S., King, I. R., 1993, Structure and Dynamics of Globular Clusters (ASP Conf. Ser. 50), ed. S. G. Djorgovski & G. Meylan (San Francisco, CA: ASP), 347

Ubeda L., Anderson J., 2012, Instrument Science Report ACS 201203, Baltimore: STScI

Ventura P., D'Antona F., Mazzitelli I., Gratton R., 2001, ApJ, 550, L65

Verbunt F., 2005, AIPC, 797, 30

Vesperini E., McMillan S. L. W., D'Antona F., D'Ercole A., 2013, MNRAS, 442

Villanova S., Piotto G., King I. R. et al., 2007, ApJ, 663, 296

Villanova S., Piotto G., Gratton R. G., 2009, A&A, 499, 755

Villanova S., Geisler D., Piotto G., Gratton R. G., 2012, ApJ, 748, 62

Volonteri M., Perna R., 2005, MNRAS, 358, 913

Warner B., 2003, Cataclysmic Variable Stars, Cambridge: Cambridge Univ. Press

Webb N. A., 2006, ESASP, 604, 177

Webb N. A., Serre D., Gendre B., Barret D., Lasota J.-P., Rizzi L., 2004a, A&A, 424, 133

Webb N. A., Gendre B., Barret D., 2004b, RMxAC, 20, 75

Webb N. A., Wheatley P. J., Barret D., 2006, A&A, 445, 155

Wehlau A., Butterworth S., Hogg H. S., 1990, AJ, 99, 1159

Wheatley J. M., Welsh B. Y., Oswald H. W. S. et al., 2005, APJ, 619, 123

White S. D. M., Rees M. J., 1978, MNRAS, 183, 341

Whitney J. H., Rood R. T., O'Connell R. W., et al., 1998, ApJ, 495, 284

Whitmore B. C., Zhang Q., Leitherer C., Fall S. M., Schweizer F., Miller B. W., 1999, AJ, 118, 1551

Williams L. L. R., Barnes E. I., Hjorth J., 2012, MNRAS, 423, 3589

Wilson C. P., 1975, AJ, 80, 175

Wood M. A., 1995, in White Dwarfs, ed. D. Koester & K. Werner (Berlin: Springer), 41

Woosley S. E., Taam R. E., 1976, Nature, 263, 101

Yong D., Grundahl F., 2008, ApJ, 672, L29

Yong D., Grundahl F., Johnson J. A., Asplund M., 2008, ApJ, 684, 1159

Zacharias, N., Urban, S. E., Zacharias, M. I., Wycoff, G. L., Hall, D. M., Monet, D. G., Rafferty, T. J., 2004, AJ, 127, 3043

Zacharias N., Finch C., Girard T. et al., 2009, VizieR Online Data Catalog, 1315, 0

Zepf S. E., Maccarone T. J., Bergond G., Kundu A., Rhode K. L., Salzer J. J., 2007, ApJ, 669, L69

Zepf S. E., Stern D., Maccarone T. J. et al., 2008, ApJ, 683, L139

Zhang Q., Fall S. M., 1999, ApJ, 527, L81

Zhao B., Bailyn C. D., 2005, AJ, 129, 1934

Zinn R., 1985, ApJ, 293, 424

Zoccali M., Pancino E., Catelan M., Hempel M., Rejkuba M., Carrera R., 2009, ApJ, 697, 22

Zurek D. R., Knigge C., Maccarone T. J., Dieball A., Long K. S., 2009, ApJ, 699, 1113